SIMON LAPOINTE

Numerical study of self-sustained oscillations in transitional flows

Mémoire présenté
à la Faculté des études supérieures et postdoctorales de l'Université Laval
dans le cadre du programme de maîtrise en génie mécanique
pour l'obtention du grade de Maître ès sciences (M. Sc.)

FACULTÉ DES SCIENCES ET DE GÉNIE
UNIVERSITÉ LAVAL
QUÉBEC

2012

Résumé

Ce mémoire présente une étude numérique du phénomène d'oscillations auto-induites d'une aile rigide montée sur un support élastique. Ces oscillations ont été rapportées expérimentalement au Collège Militaire Royal du Canada par l'équipe du professeur Poirel. Ils ont montré que le phénomène a lieu dans une plage de nombres de Reynolds spécifique où la transition de la couche limite peut survenir : $5 \times 10^4 < \mathrm{Re}_c < 1.3 \times 10^5$. Des oscillations en tangage seulement ainsi qu'en tangage et pilonnement ont été observées. Les oscillations en tangage seulement ont une amplitude d'environ 5 degrés et une fréquence aux alentours de 3 Hz. Les oscillations en tangage et pilonnement ont des amplitudes de tangage pouvant atteindre 65 degrés selon la rigidité structurale et des fréquences allant de 3 à 5 Hz.

Le phénomène a été étudié ici par la mécanique des fluides numérique. Le code libre *OpenFOAM* utilisant la méthode des volumes finis a été utilisé pour simuler le problème aéroélastique. Dans le cas des oscillations en tangage, une très bonne comparaison entre les résultats numériques et expérimentaux a été obtenue. L'utilisation d'un modèle de transition a entraîné une amélioration par rapport aux simulations numériques réalisées dans le passé et a contribué à mieux élucider la physique en jeu. La séparation de la couche limite laminaire étant le mécanisme déclencheur du phénomène, ces oscillations sont appelées flottement de séparation laminaire. L'impact de l'intensité turbulente de l'écoulement sur les oscillations a été étudié et s'est révélé jouer un rôle très important: un haut niveau empêchant l'apparition des oscillations. Le caractère secondaire du rôle joué par les structures d'écoulement à haute fréquence a été démontré ainsi que les différents mécanismes de dissipation d'énergie en jeu.

Les oscillations auto-induites en tangage et pilonnement combinés ont également été simulées. La comparaison entre les résultats numériques et expérimentaux n'est pas aussi bonne que dans le cas de oscillations en tangage, mais des tendances similaires sont tout de même observées. Lorsque la rigidité structurale en pilonnement est petite, des oscillations de faibles amplitudes en tangage et pilonnement sont obtenues, tel que dans le cas en tangage pure. Lorsque la rigidité structurale est grande, d'importantes amplitudes de tangage sont obtenues qui s'avèrent du même ordre de grandeur que celles observées en expérimental. Ces oscillations diffèrent du cas en tangage puisqu'elles sont caractérisées par un flottement de coalescence plutôt qu'un flottement de séparation laminaire.

Abstract

This thesis presents a numerical study of the phenomenon of self-sustained oscillations of an elastically mounted rigid wing. These oscillations were reported experimentally at the Royal Military College of Canada by the team of professor Poirel. They showed that the phenomenon is observed in a specific range of Reynolds numbers where the transition of the boundary layers can occur: $5 \times 10^4 < \mathrm{Re} < 1.3 \times 10^5$. Both pitch-only and pitch-heave oscillations were observed. The pitch-only oscillations have an amplitude of approximately 5 degrees and a frequency of about 3 Hz. The pitch-heave oscillations have pitching amplitudes reaching up to 65 degrees depending on the structural stiffness coefficients and frequencies in the range of 3 to 5 Hz.

The phenomenon has been studied in this thesis through the means of Computational Fluid Dynamics. Using the open-source finite volumes code *OpenFOAM*, simulations of the aeroelastic problem were performed. In the case of the pitch-only oscillations, a very good agreement between the numerical and experimental results was obtained. The use of a transition model was an improvement over previous numerical simulations and contributed to a better understanding of the flow physics involved. Since the separation of the laminar boundary layer is the trigger mechanism of the phenomenon, these oscillations are labelled as laminar separation flutter. The impact of freestream turbulence intensity on the oscillations has also been investigated and found to play an important role, suppressing the oscillations at high levels. The secondary role played by the high-frequency flow structures was demonstrated as well as the different energy dissipation mechanisms involved.

Self-sustained pitch-heave oscillations were also simulated numerically. The quantitative comparison with experimental results is not as good as the pitch-only oscillations but similar trends are observed. When a small heave stiffness is used, small pitching and heaving amplitudes are obtained in a similar fashion as for the pitch-only case. When a large heave stiffness is used, large pitching oscillations are obtained of the same order of magnitudes as the experimental results. These oscillations differ from the pitch-only case since they are characterized by coalescence flutter rather than laminar separation flutter.

Avant-propos

J'aimerais d'abord exprimer ma reconnaissance envers tous les gens qui m'ont soutenu au cours de mes études de maîtrise. Je remercie particulièrement mon directeur de recherche, le professeur Guy Dumas, pour la qualité de son enseignement et de son encadrement. Sa bonne humeur, son expertise et sa rigueur en font une personne très agréable et un excellent superviseur. Il a su me transmettre sa passion pour la mécanique des fluides et je lui en serai toujours reconnaissant.

Le succès de ma maîtrise est en grande partie dû à mes collègues avec qui j'ai partagé le LMFN durant ces deux années. Merci à Steve Julien, Mathieu Olivier, Julie Lefrançois, Thomas Kinsey, Guillaume Boutet-Blais, Marc-André Plourde-Campagna, Frédérik Chan, Carl-Anthony Beaubien, Rémi Gosselin et Étienne Gauthier. Votre aide ainsi que l'ambiance chaleureuse qui règne au laboratoire ont été très appréciées. Je désire également souligner le plaisir que j'ai eu à superviser deux étudiants de premier cycle, Maxime Picard-Deland et Jean-Christophe Veilleux. Bonne chance dans vos projets futurs.

Ce travail a été rendu possible grâce au support financier du Conseil de Recherches en Sciences Naturelles et en Génie du Canada (CRSNG) et du Fonds Québécois de la Recherche sur la Nature et les Technologies (FQRNT). Leur appui a été grandement apprécié.

Finalement, je voudrais exprimer ma reconnaissance envers mes parents, mon frère et toute ma famille qui m'ont toujours encouragé et supporté dans mes études.

Contents

List of Tables

List of Figures

Nomenclature

List of symbols used.

c = chord length
AR = wing aspect ratio
C_f = skin friction coefficient, $\frac{\tau_w}{\frac{1}{2}\rho U_\infty^2}$
$C_{\mathcal{L}}$ = instantaneous lift coefficient
C_p = surface pressure coefficient, $\frac{p-p_\infty}{\frac{1}{2}\rho U_\infty^2}$
C_{Mea} = aerodynamic moment coefficient about the elastic axis
C_P = instantaneous power coefficient normalized by chord, $\frac{P}{\frac{1}{2}\rho U_\infty^3 c}$
$C_{P\theta}$ = instantaneous rotational power coefficient, $\frac{P_\theta}{\frac{1}{2}\rho U_\infty^3 c}$
$\bar{C}_{P\theta}$ = average rotational power coefficient, $\frac{\bar{P}_\theta}{\frac{1}{2}\rho U_\infty^3 c}$
C_{Py} = instantaneous vertical power coefficient, $\frac{P_y}{\frac{1}{2}\rho U_\infty^3 c}$
$\bar{C}_{Py}$ = average vertical power coefficient, $\frac{\bar{P}_y}{\frac{1}{2}\rho U_\infty^3 c}$
C_P^* = average power coefficient, normalized by vertical displacement of pivot point, $\frac{\bar{P}}{\frac{1}{2}\rho U_\infty^3 (2y_{max}}$
C_y = instantaneous vertical force coefficient
d = distance between highest and lowest point of airfoil's profile
D_θ = rotational damping coefficient
D_h = vertical damping coefficient
E = turbulent energy
f = frequency of oscillation
f_c = cut-off frequency used for the estimation of the experimental coefficient of moment
$f_{ae,qs}$ = aeroelastic natural frequency (inviscid quasi-steady theory)
I_{axis} = moment of inertia about the elastic axis
k = wavenumber
K_θ = torsional stiffness coefficient
K_h = vertical stiffness coefficient
$\mathcal{L}$ = lift for span of unity
l_0 = integral length scale
l_n = Kolmogorov length scale
M_{axis} = moment of force about the elastic axis for span of unity
m = mass of the moving parts of the apparatus

p = pressure
P = instantaneous power
$\bar{P}$ = mean power in a cycle
P_y = instantaneous vertical power
$\bar{P}_y$ = mean vertical power in a cycle
P_θ = instantaneous rotational power
$\bar{P}_\theta$ = mean rotational power in a cycle
Q = vortex identification criterion
Re_c = Reynolds number, $U_\infty c / \nu$
R_k = low-Reynolds number correction constant
s = span of the wing
t = time
T = period
Tu = freestream turbulence intensity
u_0 = integral velocity scale
u_n = Kolmogorov velocity scale
u_τ = friction velocity
u^+ = velocity in wall units
U_i = velocity vector
U_∞ = freestream velocity
$\overline{u'v'}$ = Reynolds stresses
v_y = vertical velocity of the airfoil
x_{CM} = chordwise position of the center of mass
x_{EA} = chordwise position of the elastic axis
x_r = chordwise position of re-attachment
x_{sep} = chordwise position of separation
x_{tr} = chordwise position of transition
x_θ = distance between pivot point and center of mass, $x_{CM} - x_{EA}$
y = vertical position
$\dot{y}$ = vertical velocity
$\ddot{y}$ = vertical acceleration
y_{max} = highest or lowest position of pivot point
y^+ = distance in wall coordinates
δ = boundary layer thickness
Δx^+ = streamwise spacing in wall coordinates
Δz^+ = spanwise spacing in wall coordinates
θ_{max} = maximum pitch amplitude
θ = instantaneous pitch angle
$\dot{\theta}$ = instantaneous pitch angular velocity
$\ddot{\theta}$ = instantaneous pitch angular acceleration

Δt = timestep
Δt^* = non-dimensional convective timestep $\Delta t U_\infty / c$
Δt = timestep
η = efficiency, normalized by total flow window
ϕ = phase-shift
ρ = density of the fluid
ν = kinematic viscosity of the fluid
ν_t / ν = turbulent viscosity ratio
τ_0 = integral time scale
τ_n = Kolmogorov time scale
ω = vorticity vector

Chapter 1

Introduction

1.1 Context

Over the course of the last decades, there has been an increasing interest in the development of unmanned aerial vehicles (UAVs) and micro-air vehicles (MAVs). These vehicles can be used in a large variety of applications and can be either remotely piloted or autonomous. As typical commercial aircrafts usually fly at high Reynolds number $O(10^7)$, the small length scale and low velocities of UAVs and MAVs result in a flight regime with low-to-moderate chord Reynolds numbers (15,000 to 500,000) [49].

The flow at these Reynolds numbers is highly nonlinear and complex viscous phenomena are present. One could observe for example an extensive region of laminar flow in the boundary layer up to a separation point. A transition of the laminar shear layer would then follow with a possible reattachment of the turbulent shear layer, thus forming a laminar separation bubble (LSB) on the surface of the airfoil [26, 87].

Often responsible of triggering instabilities, nonlinear effects can also attenuate the growing oscillations of an unstable system, resulting in finite amplitude, steady-state oscillations. In aeroelasticity, these are called limit-cycle oscillations (LCO) [9] and can be of crucial importance since, in their absence, instabilities such as flutter could ultimately lead to structural failure. Therefore, nonlinear phenomena in aeroelastic systems must be included in safety and performance analyses for aerospace crafts. It is hence of crucial importance to develop reliable tools to predict these nonlinear effects as they can have favorable or unfavorable impacts on the system.

Recently, Poirel's group [19, 59, 61] has worked on a series of experimental studies on a

free pitching NACA0012 wing at Reynolds numbers in the range $5.0\times10^4 < \mathrm{Re}_c < 1.3\times10^5$. Wind tunnel experiments have shown that the elastically mounted rigid airfoil in this transitional flow regime becomes unstable and undergoes self-sustained or limit-cycle oscillations.

Mendes *et al.* [39] also conducted wind tunnel experiments of a NACA0012 in the same Reynolds numbers range allowing a two-degree-of-freedom motion in both the pitching and heave directions. Two types of LCOs were also observed for this case.

In the past, our CFD research group has collaborated with Dr. Poirel's experimental group at the Royal Military College of Canada for both experimental [51] and numerical [62] studies.

1.2 Previous experimental results

The experiments with the NACA0012 wing were carried out in the low-speed wind tunnel of the RMC, as shown in Fig. 1.1. The close circuit wind tunnel has a test section that measures 0.76 m by 1.08 m. Velocities from 4 to 60 m/s can be reached by varying the fan speed, which results in a Reynolds number ranging from 40 000 to 630 000. The solid blockage ratio is 5%. In the test section, the maximum turbulence intensity level is reported as less than 0.2% for the range of airspeeds considered in this work.

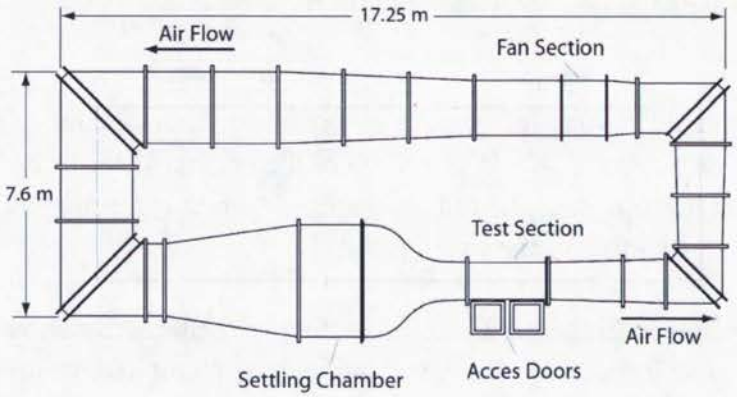

Figure 1.1: The low-speed wind tunnel of the Royal Military College of Canada [61].

In the wind tunnel, the wing is vertically mounted so the motion is unaffected by the effect of gravity. Particular care was taken to truly achieve this since the features of the oscillations may be quite sensitive to misalignment. As shown in Fig. 1.2, end plates are installed to minimize 3-D effects. The wing has rectangular planform of $AR = 3.9$ and is made of a solid foam core encased within an aluminium frame, the exterior of which is covered by fibreglass-

epoxy. The free-stream velocity is measured with a pitot-static tube located at the entrance of the test section and linked to a manometer, also shown on the figure.

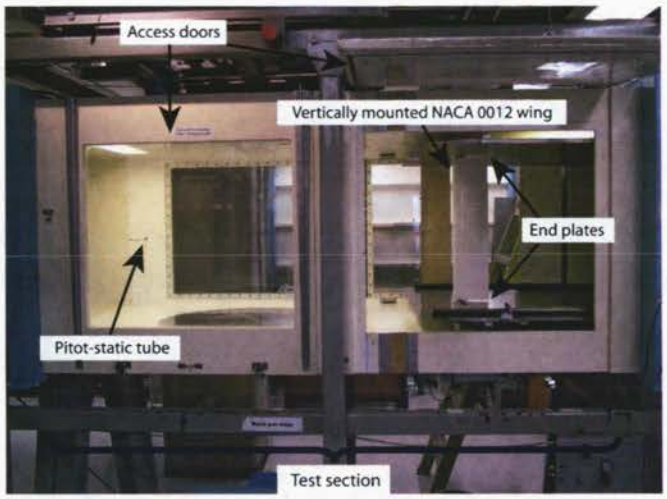

Figure 1.2: The vertically mounted NACA 0012 in the wind tunnel [51].

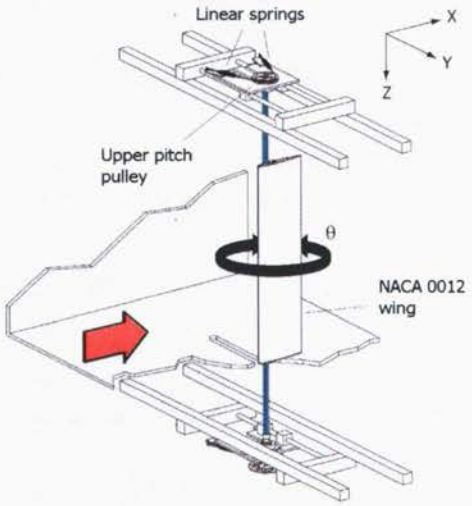

Figure 1.3: Schematic of the apparatus, showing the pitch degree of freedom, adapted from Harris [19].

Fig. 1.3 shows a schematic of the aeroelastic apparatus, highlighting the pitch degree of freedom of the setup. Linear springs are fixed to pulleys to provide the torsional stiffness. They are adjusted to set the equilibrium position at zero incidence. The pulleys convert the wing rotational motion into spring elongation. Dry friction in the ball bearings and spring compression causes dissipation and the overall system is not without damping, which is estimated from decaying time-scale of free oscillations. The heaving motion is constrained by another pulley system. Different stiffnesses were tested for the plunging springs: a low stiffness of 75 N/m and a high stiffness of 371 N/m [39].

The measured frequency of oscillation being of the order of 3 Hz, the pitching position data were recorded in each experiment for at least 20 cycles of oscillation and the sampling frequency was set to a nominal value of 1 kHz.

In the periodic response regime, the oscillations observed are essentially simple harmonic motions at all airspeeds [61]. The frequency of oscillation can be related to the aeroelastic natural frequency, and it does not coincide with a simple von Kármán vortex shedding mechanism. Pitch-only oscillations observed in that range have low amplitudes ($\theta_{max} < 5^{\circ}$). Typical results are shown in Fig. 1.4. There is a maximum pitch amplitude at $\mathrm{Re}_c \approx 80000$ and the reduced pitch frequency (fc/U_∞) is slightly decreasing with Reynolds number.

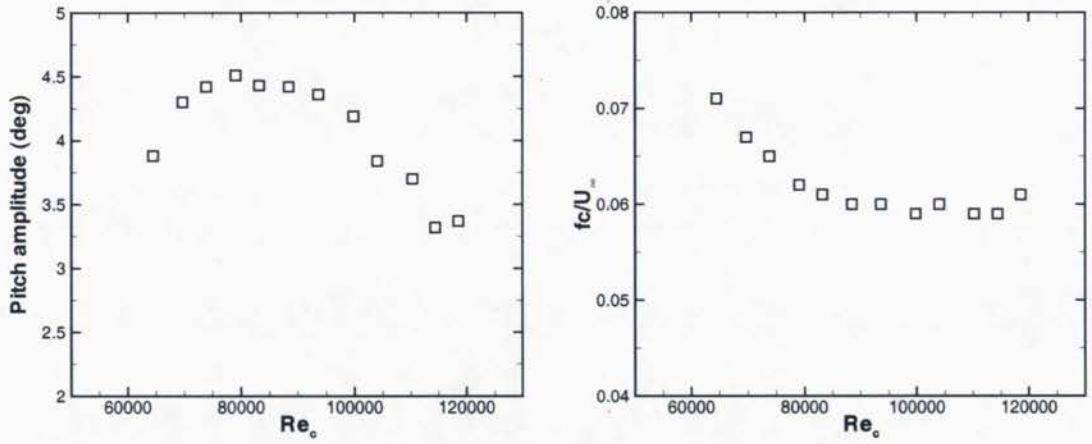

Figure 1.4: Reynolds number effect. Left: Amplitude as a function of Re_c. Right: Reduced pitch frequency as a function of Re_c [52].

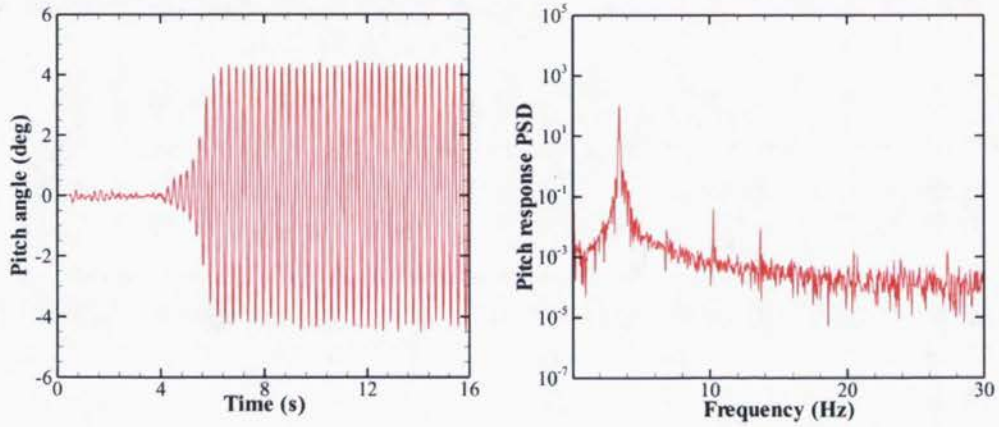

(a) Wing response in the one DOF setup

(b) Pitch response frequency spectrum

Figure 1.5: Nominal experimental configuration, Re_c = 94 000 [51].

Figure 1.5a shows the typical time evolution of the pitch response in the one DOF setup. Early on after initiating the flow, one observes a loss of stability of the equilibrium position ($\theta = 0^{\circ}$) which yields an oscillatory motion that is growing, and then saturating and settling on a limit cycle oscillation. As shown in Fig. 1.5b, there is a single dominant frequency (at 3 Hz) as well as weaker super-harmonics. Oscillations appear for Reynolds numbers between $5.0 \times 10^4 < Re_c < 1.2 \times 10^5$. Outside this range, pitch-only oscillations are not sustained.

Based on those experimental results, it has been proposed that unsymmetrical laminar trailing edge separation initiates the oscillations when upstream and airfoil conditions are essentially unperturbed. Additionally, Poirel *et al.* [61] suggest that the presence of a laminar separation bubble might be responsible for limiting the oscillations amplitude. The presence of a turbulence-generating grid placed upstream and the use of a trip wire close to the leading edge have also proved to suppress the oscillations, suggesting that the presence of turbulent and robust boundary layers is sufficient to prohibit the appearance of oscillations.

Concerning the pitch-heave oscillations for the two DOF setup, the experimental results are summarized in Fig. 1.6. Two types of oscillating amplitudes have been observed: small and large. Although both small and large oscillations were measured using a high plunge stiffness, only relatively small oscillation amplitudes were obtained when a low plunge stiffness was used. Additionally, it was necessary to provide an external perturbation to obtain the large amplitude oscillations. The large plunge stiffness corresponds to a natural frequency ratio greater than one ($\frac{\omega_h}{\omega_\theta} > 1$) while the low stiffness corresponds to a ratio smaller than one. In this case, the addition of a trip wire close to the leading edge did not inhibit the appearance of the large oscillations suggesting that these large oscillations are not associated with laminar separation flutter but rather with coalescence flutter. Coalescence flutter is known as a dynamic instability leading to exponentially growing oscillations until aerodynamic or structural forces impede this growth which creates the LCO behavior [39]. The instability responsible for this flutter phenomenon occurs through the nonlinear coupling effect between the pitching and heaving motions [63].

1.3 Previous numerical results

Numerical studies performed in our research group at the LMFN with the CFD software *ANSYS FLUENT* and a RANS turbulence model in 2D, confirmed that laminar separation of the boundary layers near the trailing edge plays a critical role in initiating the pitch oscillations [50, 62]. It was also found that the high-frequency shear instabilities present in the flow, in the separated boundary layers and wake, are not crucial nor necessary to the maintaining mechanism of the self-sustained oscillations. In addition, wake measurements

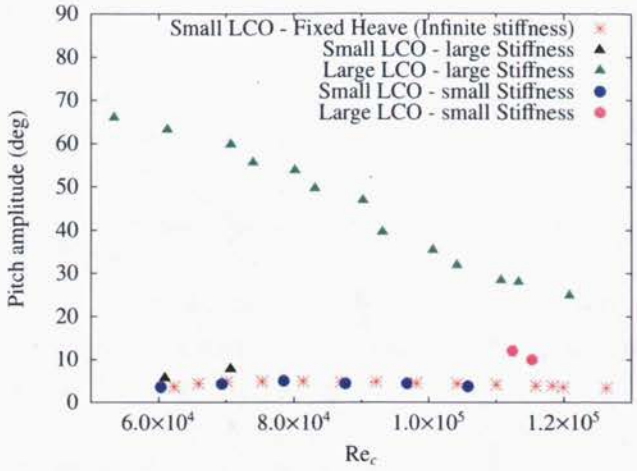

(a) Amplitudes

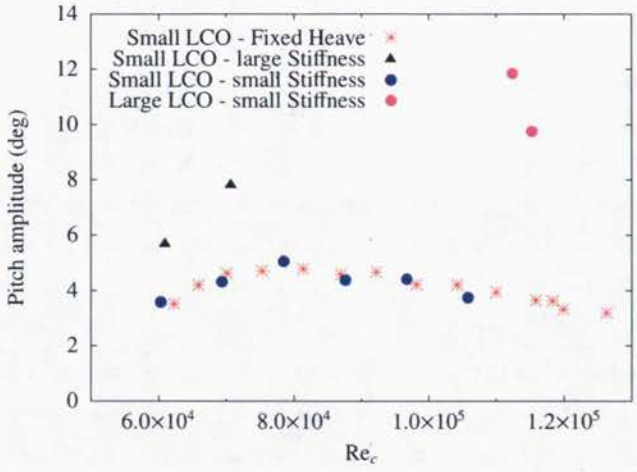

(b) Amplitudes small LCOs

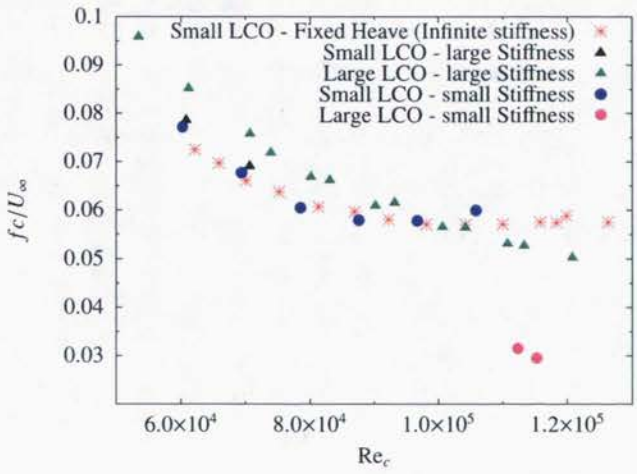

(c) Frequencies

Figure 1.6: Two DOF self-sustained oscillations characteristics results from Mendes *et al.* [39].

confirmed that the phenomenon was not associated with a vortex lock-in mechanism, because the pitch degree of freedom did not respond to a basic von Kármán vortex shedding excitation. The predicted pitch amplitudes and frequencies of the early numerical simulations [50] are shown in Fig. 1.7. They are generally close to the experimental results as they predict the main tendencies of amplitudes and frequencies. However, they do not reproduce them with great accuracy, especially with respect to the amplitude damping at higher Reynolds numbers. These computations were performed with the commercial software *Fluent* and used the SST $k-\omega$ turbulence model [40] with a low-Reynolds number correction [90]. Based on these results, Métivier [44] recommends in his thesis conclusion the use of a transition model and/or of a Large Eddy Simulations approach in future studies to improve on these results and gain physical insight since adequate resolution of the boundary layer phenomena is crucial. No previous numerical simulations known to the authors exist for the two degrees of freedom LCOs.

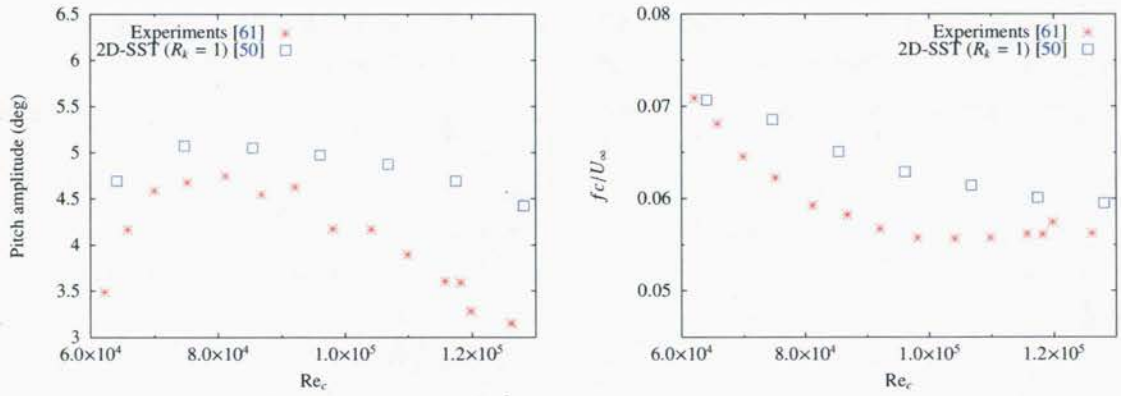

(a) Amplitudes (b) Frequencies

Figure 1.7: Comparison of self-sustained oscillations characteristics from numerical simulations and experiments.

1.4 Objectives and structure

The objectives of this master's thesis may thus be formulated as:

- To develop a numerical methodology to simulate pitch and pitch-heave aeroelastic oscillations.
- To investigate different turbulence modeling strategies and their ability to adequately capture self-sustained pitch oscillations.

- To simulate two DOF pitch-heave oscillations using different turbulence models and investigate the potential for energy extraction.

The first part in the presentation of this thesis concerns the physical context of the aeroelastic phenomenon studied, presented in Chapter 2. It reveals a rich flow physics which involves a complex interaction between the oscillating wing and the flow. Understanding basic aerodynamics characteristics as well as some important aspects of turbulence, the different modes of transition and the governing equations of the problem is key to determining the requirements of the numerical model better suited to represent the aeroelastic behaviour of an airfoil at low-to-moderate Reynolds numbers.

Based on the physical considerations presented, Chapter 3 focuses on the computation techniques used. Discretization practices and other numerical concerns are presented and the governing equations of different turbulence modeling approaches considered are explained. An overview of the advantages and drawbacks of each method is given, leading finally to the choices of turbulent and sub-grid scale models and wall treatments used during the current investigation. A section of this chapter explains the numerical procedure allowing the interaction between the fluid flow and the solid region's motion.

Chapter 4 deals with the validation and comparison of the different models described earlier through pertinent test cases. The different turbulence modeling approaches are applied to three different cases to assess their performances in the simulation of transitional flows. A test case to validate the fluid-structure interaction is also presented.

In Chapter 5, results concerning the problem of interest, namely the self-sustained pitch oscillations of the NACA0012 airfoil, are described in details. Computations are performed with two different turbulence modeling approaches, and both 2D and 3D flows are studied. Comparisons with experimental work and previous numerical results are presented.

Chapter 6 presents the results of the pitch-heave self-sustained oscillations obtained with different turbulence models. These are compared with available, preliminary experimental data and the power extraction performance of the two DOF setup is discussed.

Chapter 2

Physical aspects

The purpose of this chapter is to review the different physical aspects of the problem. In the first section, a brief overview of the basics of the vast subject of turbulence is presented. The second section describes the various modes of transition from laminar to turbulent flow to provide some insights into the formidable challenge of modeling reliably the transition occurence and physical impact in the context of a RANS approach. The third section presents the governing equations of the problem including the equation of motion for the wing and a dimensional analysis is performed to determine the main non-dimensional parameters governing this fluid-structure interaction. Finally, the present aeroelastic problem is briefly considered using some basic results of the aerodynamic theory.

2.1 Turbulence

Turbulence in fluid flows is a very complex phenomenon, such that no universal theory or global understanding is available. It is hence considered as one of the last open problems of classical physics. Since a simple or unique definition of turbulence cannot be formulated, it is often presented by its main features. Occurring at high Reynolds number, a turbulent flow is necessarily rotational, unsteady and three-dimensional. It is characterized by an irregular motion in space and time, often depicted as random or chaotic, but it also presents coherent large scale structures. Turbulence is also a very diffusive and dissipative mechanism, enhancing heat transfer and wall shear stress and transforming kinetic energy into heat by the means of viscous stresses.

As turbulence is such a vast subject, this section only covers briefly some basic aspects

that are most relevant to the physical analysis and numerical simulations of the problem studied.

2.1.1 Turbulence energy cascade and length scales

Turbulence is characterized by the presence of eddies of different sizes or scales. The larger eddies are the most energetic ones, containing most of the kinetic energy created by the velocity gradients of the mean turbulent motion, and their size is of the order of the dimension of the flow feature itself or the turbulent region studied. This size is often given by the integral length scale l_0. The energy contained in those large eddies is then transferred to smaller scales by a cascade process where the large eddies breakdown to form smaller eddies which, when small enough, succeed to dissipate the energy by the action of molecular viscosity.

The scales distribution in the turbulence cascade can be described by Kolmogorov's theory [31], expressed as three hypotheses.

1. Hypothesis of local isotropy: At high Reynolds number, the small-scale motions are isotropic. This suggests that the smallest-scale motions have a universal character.

2. First similarity hypothesis: At high Reynolds number, the universal character of the small-scale motions is determined by the kinematic viscosity, ν, and the dissipation rate, ϵ, uniquely. The Kolmogorov length, velocity and time scales, associated with the smallest eddies, are thus expressed as:

$$l_n \equiv (\frac{\nu^3}{\epsilon})^{1/4}, \tag{2.1}$$

$$u_n \equiv (\epsilon\nu)^{1/4}, \tag{2.2}$$

$$\tau_n \equiv (\frac{\nu}{\epsilon})^{1/2}. \tag{2.3}$$

It is revealing to compare the ratios of the Kolmogorov scales to those of the largest scales as a function of the Reynolds number [83]:

$$\frac{\eta}{l_0} \sim \mathrm{Re}^{-3/4}, \tag{2.4}$$

$$\frac{u_\eta}{u_0} \sim \mathrm{Re}^{-1/4}, \tag{2.5}$$

$$\frac{\tau_\eta}{\tau_0} \sim \mathrm{Re}^{-1/2}, \tag{2.6}$$

which show the wide ranges of the length scales at high Reynolds number making Direct Numerical Simulation of turbulent flows a formidable challenge.

3. Second similarity hypothesis: At high Reynolds number, there exists a motion within a range of scales l in the range $l_n << l << l_0$ which has a universal form depending only on ϵ. This means that in this certain range of length scales (referred to as the inertial sub-range), turbulence is independent of the formation mechanism. This is associated with the constant slope portion on the turbulent energy spectrum, as depicted in Fig. 2.1, and expressed by:

$$E(k) = C_k \epsilon^{2/3} k^{-5/3}. \tag{2.7}$$

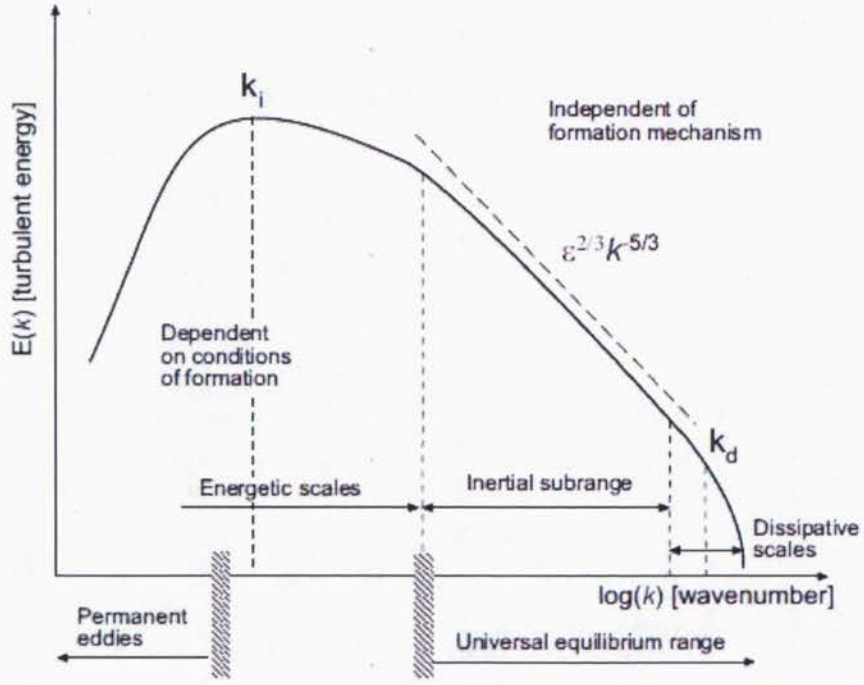

Figure 2.1: The turbulence energy spectrum, adapted from de Villiers [7].

2.1.2 Near-wall region

Among the three types of turbulent flows (homogeneous, free-shear and wall-bounded), wall-bounded flows are the primary concern of this study. The presence of solid boundaries, typically named walls in this context, is an important cause of anisotropy. Close to the wall within

the boundary layer, the wall-normal fluctuations are damped and their energy is redistributed in the other directions. Therefore, turbulence in the flow is in a relatively isotropic state in the free stream region and becomes more and more anisotropic as we approach the walls. In the very near-wall region, the turbulent motions become insignificant and the energy is mainly dissipated by molecular viscosity.

The behavior of the flow very close to a wall can be described as a function only of the wall scales, as it becomes independent of external or free stream parameters. This is called the "law of the wall". To express the velocity profile in this region, the flow and geometric quantities are normalized by the wall shear stress τ_w which remains the only flow-dependent variable. The friction velocity is defined as :

$$u_\tau = \sqrt{\frac{\tau_w}{\rho}} \tag{2.8}$$

and is used to normalize the velocity and wall-normal distance as follows :

$$u^+ = \frac{\overline{U}}{u_\tau}, \qquad y^+ = \frac{y u_\tau}{\nu}. \tag{2.9}$$

There exists many regions in the boundary layer of thickness δ which display different flow behaviors. The description of these regions and their corresponding u^+ and y^+ values is summarized below (from Pope [65]) and depicted in Fig. 2.2:

- Inner layer ($y/\delta < 0.1$): The velocity profile depends on u_τ and y^+ and is not affected by the boundary layer thickness.
- Viscous wall region ($y^+ < 50$): The velocity profile is primarily influenced by the molecular viscosity.
- Outer layer ($y^+ > 50$): The effect of molecular viscosity is insignificant.
- Overlap region ($y^+ < 50$ and $y/\delta < 0.1$): The inner and outer layers overlap.
- Viscous sublayer ($y+ < 5$): The viscous shear stress is dominant and the velocity profile is linear:

$$u^+ = y^+. \tag{2.10}$$

- Log-law region ($y^+ > 30$ and $y/\delta < 0.3$): The velocity profile is given by the log-law:

$$u^+ = \frac{1}{\kappa} \ln y^+ + B \tag{2.11}$$

  where the constants have approximate values of $B \approx 5.2$ and $\kappa \approx 0.41$, as determined by experimental and DNS data.

- Buffer layer ($5 < y^+ < 30$): The transition zone between the viscous sublayer and log-law region.

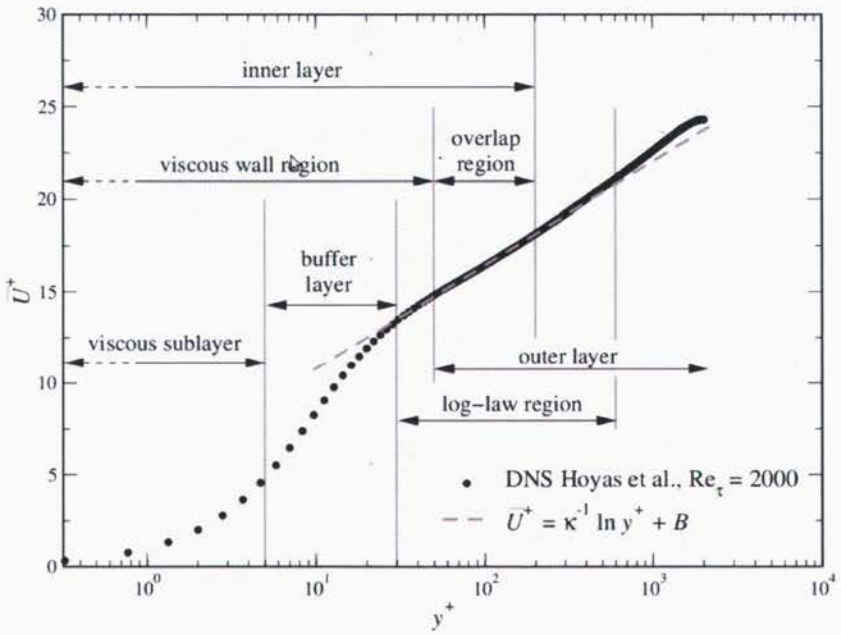

Figure 2.2: Different regions of the boundary layer, from [45].

This near-wall behavior is of great importance in turbulence modeling. Some turbulence models use the log-law approach, meaning that the viscous sublayer and buffer layer are modeled by empirical correlations and hence not resolved. Other turbulence models do not make use of the velocity profile described above and solve the Navier-Stokes equations up to the wall. As the second approach is more precise but has a higher computational cost, the choice of the turbulence model has to be made according to the flow studied and the importance of the near-wall region. It is important to note that this near-wall behavior does not necessarily hold true for large-defect boundary layers, near detachment and in separated regions. Hence a turbulence model that resolves the near-wall region is better suited in those cases.

2.1.3 Vortex identification

Since we are dealing with turbulent flows, or flows transitioning from laminar to turbulent regime, and which are characterized by the presence of vortex roll-up and vortex shedding, it is of outmost importance to be able to clearly identify vortical structures since their presence may dictate the type of flow regime we are dealing with. This section briefly describes the different methods used to achieve this task.

Two of the most intuitive ways to identify vortices are the local pressure minimum and the vorticity magnitude. A local pressure minimum is often observed along the axis of circulation of vortices and it has been shown that some vortex cores can be highlighted using this method. However, in most cases there is not a single appropriate pressure level that enables to capture all the vortical regions. Jeong and Hussain [25] also show situations where a pressure minimum falsely indicate a vortex core region. Vorticity magnitude (ω criteria) is also a popular method to represent vortex cores. However, in wall-bounded flows, the vorticity magnitude is maximum at the wall surface due to the shear created by the no-slip condition. This makes the criterion unsuitable to identify coherent vortices in a boundary layer since a vortex core cannot coincide with the wall. It is also unsuitable in free shear flows since pure planar shear has vorticity and is not a rotational region.

In order to alleviate the shortcomings of those two methods, other criteria were developped to define a vortical region.

The Q-criterion, proposed by Hunt *et al.* [22], is named after the second invariant of the velocity gradient tensor $\nabla\mathbf{u}$:

$$Q = \frac{1}{2}(\Omega_{ij}\Omega_{ij} - S_{ij}S_{ij}) \tag{2.12}$$

where S_{ij} and Ω_{ij} are the symmetric and antisymmetric components of $\nabla\mathbf{u}$. Q is then the balance between the rotation rate and the strain rate. Hence, positive values of Q mark regions where the rotation rate is greater than the strain rate. An isosurface of positive Q is thus eligible as a vortex envelope. Dubief and Delcayre [12] used the Q criterion to investigate coherent vortices in DNS and LES simulations of different types of flow and showed its superiority over ω and low-pressure criteria.

The λ_2-criterion, proposed by Jeong and Hussain [25], is based on $\Omega_{ij}\Omega_{ij} + S_{ij}S_{ij}$, which determines the presence of a local pressure minimum if the tensor has two negative eigenvalues. Thus, a vortex is present if the second largest eigenvalue of $\Omega_{ij}\Omega_{ij} + S_{ij}S_{ij}$ is less than zero.

These two methods are the most commonly used in the litterature. In many circumstances,

the Q-criterion and λ_2-criterion yield very similar results and are both considered efficient for the current study. As a matter of consistency, the Q-criterion is used in this work.

2.2 Laminar to turbulent transition

2.2.1 Kelvin-Helmholtz instability

The Kelvin-Helmholtz instability is the famous instability of a free shear layer. It is a phenomenon of great importance in fluid mechanics as it can influence the transition process of jets, mixing layers, separated layers and wakes.

A typical case of this instability occurs when fluids moving at different speeds form a shear layer (this is often the case in atmospheric boundary layers). The process of evolution of the instability is depicted in Fig. 2.3. The shear layer (or vortex layer) is very sensitive to perturbations, which can create an oscillation of the vortex sheet. One can imagine a flat vorticity layer being subjected to an infinitesimal sinusoidal perturbation. There will be induced velocity at the concavities and convexities due to the perturbation, which will create a roll-up of the vorticity layer leading to larger structures as can be seen in Fig. 2.4.

Figure 2.3: Evolution of the Kelvin-Helmholtz instability.

In the particular case of the flow around an airfoil, the Kelvin-Helmholtz instability can appear when the boundary layer separates over the airfoil. The separation generates a free shear layer between the external main high speed flow and the internal slow, recirculating flow close to the airfoil. The instability may produce vortex roll-up and may contribute to the transition from laminar to turbulent flow.

2.2.2 Natural transition

The term natural transition in the context of wall-bounded flows describes the process occurring when, subjected to a low free stream turbulence level (below 1 %), a laminar boundary layer can be perturbed by the presence of viscous instability waves, often referred to as

Figure 2.4: A typical case of Kelvin-Helmholtz instability.

Tollmien-Schlichting waves, or other types of disturbances. Beyond a critical Reynolds number, the Tollmien-Schlichting waves begin to grow and the boundary layer becomes unstable. The waves grow slowly, forming spanwise vortices which will cause three-dimensional disturbances of the flow. Turbulent spots then begin to appear and they grow in the surrounding laminar layer, ultimately forming a turbulent boundary layer. These steps of the phenomenon of natural transition are represented on Fig. 2.5.

It is of interest to note that, in some cases, Tollmien-Schlichting waves are not the only instability that can cause transition. Other types of disturbances, namely stationary and traveling cross flow instabilities, can occur separately or simultaneously, and interact with Tollmien-Schlichting waves.

2.2.3 Bypass transition

Bypass transition denotes the transition process at higher free stream turbulence levels (above 1%), where the first three stages of the natural transition process described earlier are not observed (they are "bypassed"). In such cases, turbulent spots are directly produced within the boundary layer by the influence of free stream disturbances. The free stream turbulence

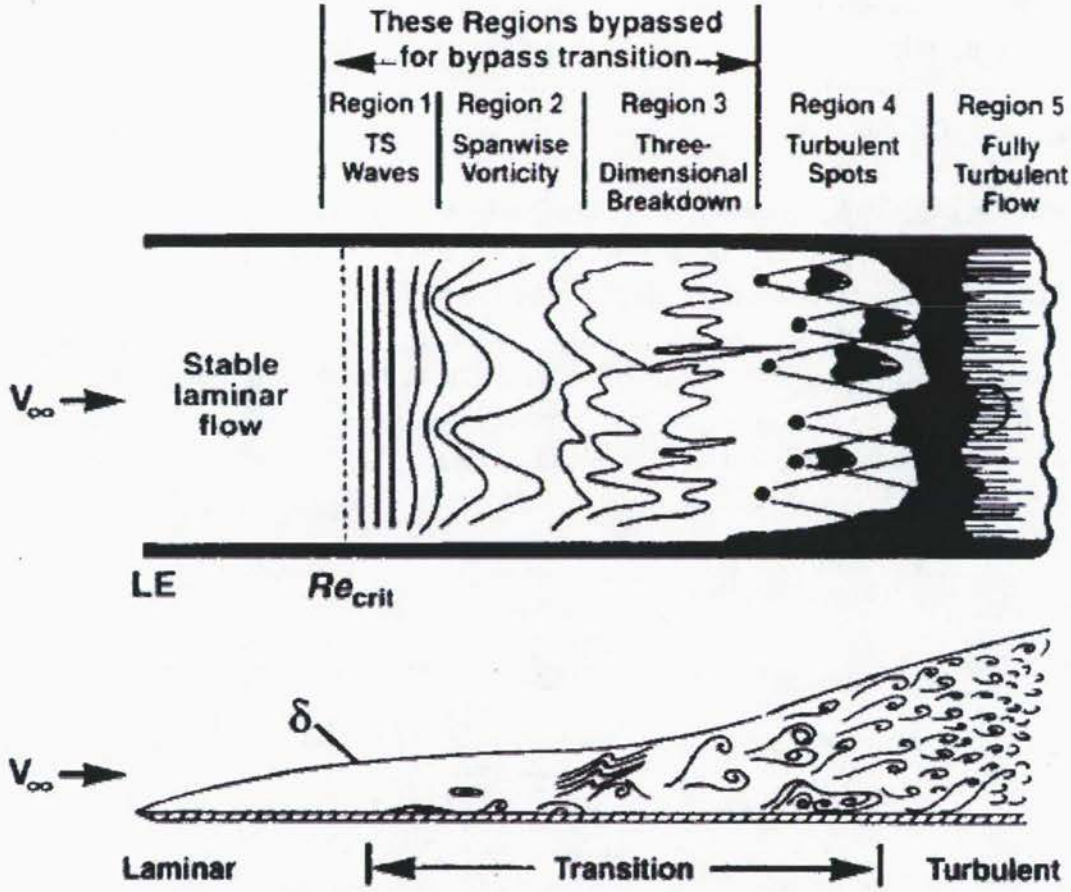

Figure 2.5: The process of natural transition, from Schlichting and Gersten [72].

level value of 1% is taken as the limit between natural and bypass transition because Tollmien-Schlichting waves have never been reported when the turbulence level was greater than 1% [37]. However, high free stream turbulence levels are not the only cause of bypass transition. The phenomenon can also be caused by surface roughness. In that case, turbulent spots will be produced by perturbations at the wall instead of free stream disturbances.

2.2.4 Separation induced transition

The term separation induced transition refers to the case where, following the separation of the laminar boundary layer, transition occurs in the shear layer of the separated flow as a result of some inviscid instability mechanisms such as Kelvin-Helmholtz. Following transition, the presence of turbulence increases mixing in the shear layer and can cause the reattachment of the boundary layer, thus forming a laminar separation with turbulent reattachment bubble

on the surface. This type of transition is often observed on airfoils when separation is provoked by the presence of a strong adverse pressure gradient. It can also appear at the leading edge of an airfoil if the leading edge radius is small enough. The structure of a time-averaged bubble was given by Horton [21] and is shown on Fig. 2.6. Downstream of the separation point, there is a zone close to the wall where the fluid is almost stationary, referred to as the "dead-air" region. The center of the recirculation vortex is located near the reattachment point where higher recirculation velocities are observed. At the point of separation, the dividing streamline detaches from the wall and quickly reattaches following the transition from laminar to turbulent flow. Inside the separated region, the wall pressure remains constant near the separation point and the reverse-flow vortex region near the reattachment point is characterized by a strong pressure gradient. Tani [82] noted that the length of the separated region was reduced as the adverse pressure gradient increased, and suggested that this was due to more rapid transition of the separated laminar boundary layer.

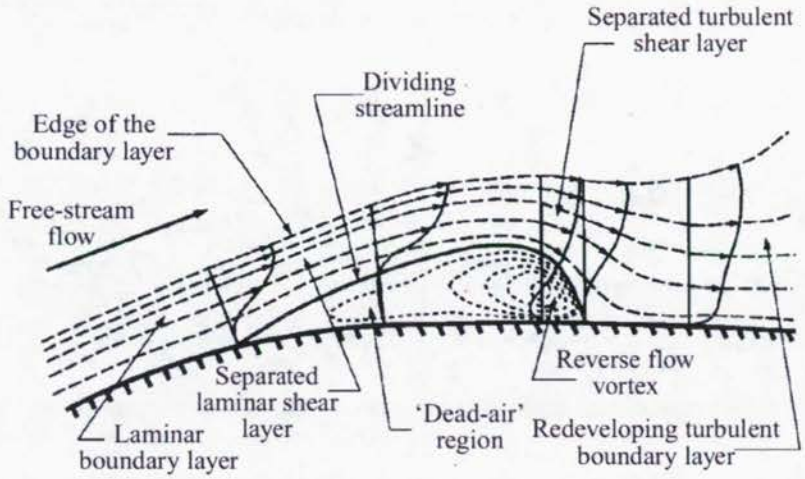

Figure 2.6: The mean flow structure of a laminar separation bubble, from Horton [21].

The behavior of laminar separation bubbles (LSB) is of importance in aerodynamics because they play a crucial role in leading-edge stall and thin-airfoil stall. An important characteristic of laminar separation bubbles is their length. They have been classified as "long" or "short" based on their effect on the pressure distribution around an airfoil. Short bubbles reattach rapidly after their separation and thus only have a small, local effect on the pressure distribution. This can be benefiting in some cases as the resulting turbulent boundary layer can sustain a larger adverse pressure gradient. On the other hand, longer laminar separation bubbles modify significantly the pressure distribution around the airfoil (through modification of the effective airfoil shape), causing large pressure losses and should generally be avoided. The prediction of bubble length is a challenge since the length is influenced by the free stream turbulence level, the Reynolds number and the angle of attack. A small, rapid change of these last two parameters can cause a bubble to suddenly grow from small to long. This phenomenon is called bursting and can cause an important loss of lift or even stall. Pa-

rameters playing an important role in the bursting have been identified by Gaster [17] and Horton [20] who developed a semi-empirical method for predicting the growth and bursting of bubbles. Numerical simulations of laminar boundary layers subjected to adverse pressure gradients by Pauley *et al.* [56] have shown the presence of periodic shedding from the separation point. This unsteady separation, arising from inviscid instability of the separated shear layer, turns out to be the cause of the bursting as the shedding reported in this study was consistent with the empirical results of Gaster.

A point relevant to CFD simulations of LSB was highlighted by Alam and Sandham [1] who performed two and three-dimensional direct numerical simulations of short laminar separation bubbles. Their study showed that the transition to turbulence was characterized by the breakdown of Λ-vortices and that three-dimensional simulations were required for accurate results since two-dimensional simulations did not properly represent the characteristics of short separation bubbles.

The importance of laminar separation bubbles in flows at transitional Reynolds numbers was also underlined by Radespiel *et al.* [66]. They performed unsteady simulations of moving airfoils at $\mathrm{Re}_c = 60000$ and observed the presence of laminar separation bubbles and their significant impact on the aerodynamics of the airfoil. Although they employed a relatively simple numerical methodology (2D RANS simulations combined with a stability analysis), they captured the main transitional flow features and obtained a good comparison with experimental measurements.

2.3 Governing equations

2.3.1 Equations of motion

In this section we consider an elastically-mounted rigid body with two degrees of freedom in pitching and heaving. The problem is sketched in Fig. 2.7 and forces acting on the body are shown in Fig. 2.8. A Cartesian coordinate system is used with the y axis defined positive downward and the x axis positive towards the right, in order to respect the aerodynamic convention concerning the sign of the pitching angle θ.

Equations of motion can be obtained by applying the summation of forces and moments

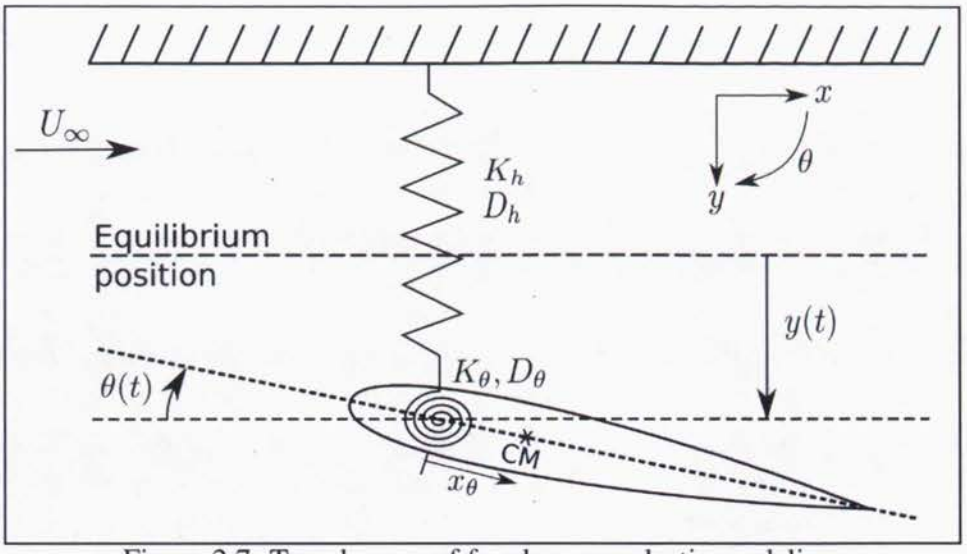

Figure 2.7: Two degrees of freedom aeroelastic modeling.

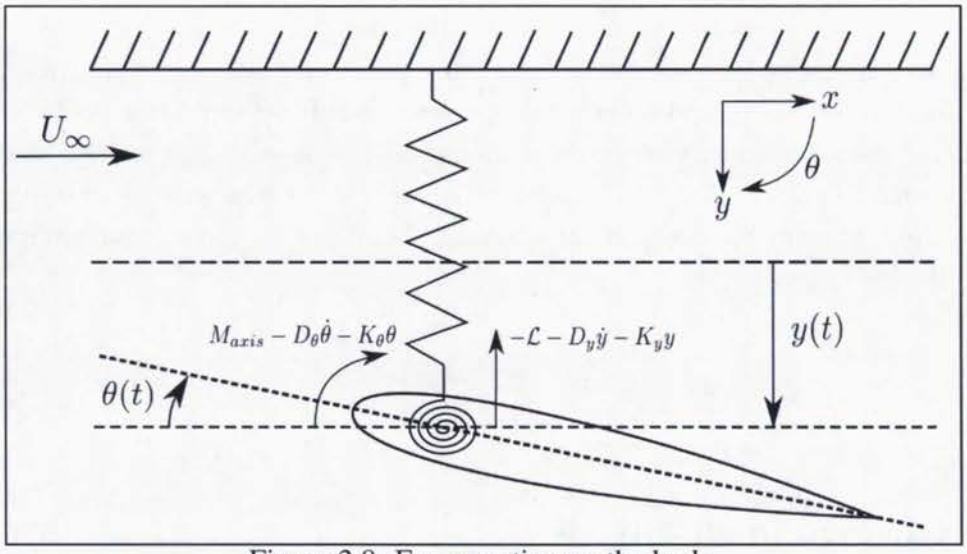

Figure 2.8: Forces acting on the body.

acting on the body:

$$\sum \vec{F} = m\vec{a}_{CM}, \tag{2.13}$$

$$\sum \vec{M}_{/AXIS} = I_{axis}\vec{\ddot{\theta}} + \vec{r}_{\frac{CM}{AXIS}} \times m\vec{a}_{AXIS}. \tag{2.14}$$

In the case of the two degrees of freedom pitch and plunge motion studied here, the equations of motion are:

$$M_{axis} = I_{axis}\,\ddot{\theta} + D_\theta\,\dot{\theta} + K_\theta\,\theta + m\ddot{y}x_\theta\,cos(\theta) \tag{2.15}$$

$$-\mathcal{L} = m[\ddot{y} + x_\theta\,cos(\theta)\,\ddot{\theta} - x_\theta\,sin(\theta)\,\dot{\theta}^2] + D_h\dot{y} + K_h y. \tag{2.16}$$

where M_{axis} and $\mathcal{L}$ are respectively the moment exerted around the pitching axis and the vertical force exerted on the airfoil, for a domain depth of unity, caused by the unsteady aerodynamics. The mass m is the total mass of the system as no distinction is made between the heaving mass and the rotating mass. The equilibrium in the x direction is implicit since no motion is allowed in that direction. These equations are coupled in the case where the pitching axis is not coincident with the center of mass ($x_\theta \neq 0$, $x_\theta > 0$ if the axis is before the center of mass).

In the case where the motion is restricted to pitching only, we obtain a single differential equation for θ:

$$\boxed{M_{axis} = I_{axis}\,\ddot{\theta} + D_\theta\,\dot{\theta} + K_\theta\,\theta.} \tag{2.17}$$

2.3.2 Non-dimensional formulation

One degree of freedom

If we consider the case where the wing is restricted to a pitching motion, the governing equations are the continuity equation, Navier-Stokes equation and the equation of motion of a rotating body as seen in Eq. (2.17). Thus, we have :

$$\frac{\partial U_i}{\partial x_i} = 0, \tag{2.18}$$

$$\frac{\partial U_i}{\partial t} + U_j\frac{\partial U_i}{\partial x_j} = -\frac{1}{\rho_f}\frac{\partial p}{\partial x_i} + \nu\frac{\partial^2 U_i}{\partial x_j^2}\,. \tag{2.19}$$

and

$$I_{axis}\ddot{\theta} + D_\theta\dot{\theta} + K_\theta\theta = M_{axis}. \tag{2.20}$$

In order to obtain a non-dimensional formulation, we enter the following reference quantities:

T_{ref}	:	time of reference	(sec)
L_{ref}	:	length of reference	(m)
U_{ref}	:	speed of reference	(m/sec)
P_{ref}	:	pressure of reference	(N/m^2)
M_{ref}	:	moment of reference	$(N \cdot m)$

and we define the following non-dimensional variables:

$$t^* = \frac{t}{T_{ref}} \qquad x_i^* = \frac{x_i}{L_{ref}} \qquad U_i^* = \frac{U_i}{U_{ref}} \qquad p^* = \frac{p}{P_{ref}} \qquad M^* = \frac{M_{axis}}{M_{ref}}. \tag{2.21}$$

Introducing these in Eq. (2.18) and Eq. (2.19), we obtain:

$$\frac{U_{ref}}{L_{ref}} \frac{\partial U_i^*}{\partial x_i^*} = 0, \tag{2.22}$$

$$\frac{U_{ref}}{T_{ref}} \frac{\partial U_i^*}{\partial t^*} + \frac{U_{ref}^2}{L_{ref}} U_j^* \frac{\partial U_i^*}{\partial x_j^*} = -\frac{P_{ref}}{\rho_f L_{ref}} \frac{\partial p^*}{\partial x_i^*} + \frac{U_{ref}}{L_{ref}^2} \nu \frac{\partial^2 U_i^*}{\partial x_j^{*2}}, \tag{2.23}$$

which can be easily manipulated into the following non-dimensional form:

$$\frac{\partial U_i^*}{\partial x_i^*} = 0, \tag{2.24}$$

$$\frac{L_{ref}}{U_{ref} T_{ref}} \frac{\partial U_i^*}{\partial t^*} + U_j^* \frac{\partial U_i^*}{\partial x_j^*} = -\frac{1}{\rho_f} \frac{P_{ref}}{U_{ref}^2} \frac{\partial p^*}{\partial x_i^*} + \frac{\nu}{U_{ref} L_{ref}} \frac{\partial^2 U_i^*}{\partial x_j^{*2}}. \tag{2.25}$$

In a similar fashion, equation Eq. (2.20) becomes:

$$\frac{I_{axis}}{T_{ref}^2} \ddot{\theta} + \frac{D_\theta}{T_{ref}} \dot{\theta} + K_\theta \theta = M_{ref} M^*, \tag{2.26}$$

which, dividing by M_{ref}, we rewrite as:

$$\frac{I_{axis}}{M_{ref} T_{ref}^2} \ddot{\theta} + \frac{D_\theta}{M_{ref} T_{ref}} \dot{\theta} + \frac{K_\theta}{M_{ref}} \theta = M^*. \tag{2.27}$$

If we choose the following reference quantities pertaining to our problem:

$$L_{ref} = c, \tag{2.28}$$
$$U_{ref} = U_\infty, \tag{2.29}$$
$$P_{ref} = \rho_f U_{ref}^2 = \rho_f U_\infty^2, \tag{2.30}$$
$$T_{ref} = L_{ref} / U_{ref} = c \,/\, U_\infty, \tag{2.31}$$
$$M_{ref} = \rho_f U_\infty^2 c^3, \tag{2.32}$$

and substitute these in Eq. (2.25), we obtain:

$$\frac{\partial U_i^*}{\partial t^*} + U_j^* \frac{\partial U_i^*}{\partial x_j^*} = -\frac{\partial p^*}{\partial x_i^*} + \frac{\nu}{U_\infty c} \frac{\partial^2 U_i^*}{\partial x_j^{*2}} . \tag{2.33}$$

Introducing the Reynolds number $Re_c = \frac{U_\infty c}{\nu}$, the last equation can be rewritten to finally obtain the non-dimensional form of the Navier-Stokes equation :

$$\boxed{\frac{\partial U_i^*}{\partial t^*} + U_j^* \frac{\partial U_i^*}{\partial x_j^*} = -\frac{\partial p^*}{\partial x_i^*} + \frac{1}{Re_c} \frac{\partial^2 U_i^*}{\partial x_j^{*2}} .} \tag{2.34}$$

Substituting the reference quantities in Eq. (2.27), the equation now becomes:

$$\frac{I_{axis}}{\rho_f c^5} \ddot{\theta} + \frac{D_\theta}{\rho_f U_\infty c^4} \dot{\theta} + \frac{K_\theta}{\rho_f U_\infty^2 c^3} \theta = M^* . \tag{2.35}$$

It is now possible to identify the non-dimensional parameters of importance in our problem. First of all, the non-dimensional inertia about the rotating axis is defined as :

$$I_{axis}^* = \frac{I_{axis}}{\rho_f c^5} .$$

The non-dimensional damping is defined as :

$$D_\theta^* = \frac{D_\theta}{\rho_f U_\infty c^4} ,$$

and the non-dimensional stiffness is :

$$K_\theta^* = \frac{K_\theta}{\rho_f U_\infty^2 c^3} .$$

The equation of motion can finally be rewritten as:

$$\boxed{I_{axis}^* \ddot{\theta} + D_\theta^* \dot{\theta} + K_\theta^* \theta = M^* .} \tag{2.36}$$

Hence, the non-dimensional parameters of interest in the aeroelastic problem of a given rigid airfoil in pitching motion are :

$$Re_c , \; I_{axis}^* , \; D_\theta^*, \; K_\theta^* .$$

Two degrees of freedom

In the case where the airfoil is allowed to pitch and plunge, there are four equations to work with. The continuity Eq. (2.18) and Navier-Stokes Eq. (2.19) equations and the following two equations of motion:

$$I_{axis}\,\ddot{\theta} + D_\theta\,\dot{\theta} + K_\theta\,\theta + m\ddot{y}x_\theta\,cos(\theta) = M_{axis} \tag{2.37}$$

and

$$m[\ddot{y} + x_\theta\,cos(\theta)\,\ddot{\theta} - x_\theta\,sin(\theta)\,\dot{\theta}^2] + D_h\dot{y} + K_h y = -\mathcal{L}. \tag{2.38}$$

To the reference quantities previously introduced, we need to add a lift of reference:

$$\mathcal{L}_{ref} \quad : \quad \text{lift of reference} \quad (N)$$

and define the non-dimensional variable: $\mathcal{L}^* = \frac{\mathcal{L}}{\mathcal{L}_{ref}}$.

From there we procede in the same way as the one DOF case. The non-dimensional continuity and Navier-Stokes equations do not change, remaining Eq. (2.24) and Eq. (2.34). Introducing the non-dimensional variables in Eq. (2.37) and Eq. (2.38), we obtain:

$$\frac{I_{axis}}{T_{ref}^2}\ddot{\theta} + \frac{D_\theta}{T_{ref}}\dot{\theta} + K_\theta\theta + \frac{mL_{ref}}{T_{ref}^2}\ddot{y}\,x_\theta\,cos(\theta) = M_{ref}M^*, \tag{2.39}$$

which, dividing by M_{ref}, we rewrite as:

$$\frac{I_{axis}}{M_{ref}T_{ref}^2}\ddot{\theta} + \frac{D_\theta}{M_{ref}T_{ref}}\dot{\theta} + \frac{K_\theta}{M_{ref}}\theta + \frac{mL_{ref}}{M_{ref}T_{ref}^2}\ddot{y}\,x_\theta\,cos(\theta) = M^*. \tag{2.40}$$

and

$$m\left(\frac{L_{ref}}{T_{ref}^2}\ddot{y} + \frac{x_\theta\,cos(\theta)}{T_{ref}^2}\,\ddot{\theta} - \frac{x_\theta\,sin(\theta)}{T_{ref}^2}\,\dot{\theta}^2\right) + \frac{D_hL_{ref}}{T_{ref}}\dot{y} + K_hL_{ref}y = -\mathcal{L}\mathcal{L}_{ref}, \tag{2.41}$$

which, dividing by $\mathcal{L}_{ref}$, we rewrite as:

$$\frac{m}{T_{ref}^2\mathcal{L}_{ref}}\left(L_{ref}\ddot{y} + x_\theta\,cos(\theta)\,\ddot{\theta} - x_\theta\,sin(\theta)\,\dot{\theta}^2\right) + \frac{D_hL_{ref}}{T_{ref}\mathcal{L}_{ref}}\dot{y} + \frac{K_hL_{ref}}{\mathcal{L}_{ref}}y = -\mathcal{L}. \tag{2.42}$$

We make the same choice of reference quantities as for the one DOF case, to which we add $\mathcal{L}_{ref} = \rho_f U_\infty^2 c^2$. We substitute these in Eq. (2.40) and Eq. (2.42) to obtain:

$$\frac{I_{axis}}{\rho_f c^5}\ddot{\theta} + \frac{D_\theta}{\rho_f U_\infty c^4}\dot{\theta} + \frac{K_\theta}{\rho_f U_\infty^2 c^3}\theta + \frac{m}{\rho_f c^3}\ddot{y}\frac{x_\theta}{c}cos(\theta) = M^*, \tag{2.43}$$

and

$$\frac{m}{\rho_f c^3}\left(\ddot{y} + \frac{x_\theta}{c}cos(\theta)\,\ddot{\theta} - \frac{x_\theta}{c}sin(\theta)\,\dot{\theta}^2\right) + \frac{D_h}{\rho_f U_\infty c^2}\dot{y} + \frac{K_h}{\rho_f U_\infty^2 c}y = -\mathcal{L}. \tag{2.44}$$

We can now define the non-dimensional parameters of the two DOF problem. The non-dimensional rotational inertia, damping and stiffness do not change from the one DOF case. However, we now also have the non-dimensional mass:

$$m^* = \frac{m}{\rho_f c^3}.$$

the non-dimensional heaving damping is defined as:

$$D_h^* = \frac{D_h}{\rho_f U_\infty c^2},$$

the non-dimensional heaving stiffness is:

$$K_h^* = \frac{K_h}{\rho_f U_\infty^2 c}$$

and non-dimensional distance between the pitching axis and center of mass:

$$x_\theta^* = \frac{x_\theta}{c}.$$

The equations of motion can then be rewritten as:

$$I_{axis}^*\ddot{\theta} + D_\theta^*\dot{\theta} + K_\theta^*\theta + m^*\ddot{y}\,x_\theta^*\,cos(\theta) = M^*, \tag{2.45}$$

and

$$m^*\left(\ddot{y} + x_\theta^*\,cos(\theta)\,\ddot{\theta} - x_\theta^*\,sin(\theta)\,\dot{\theta}^2\right) + D_h^*\dot{y} + K_h^* y = -\mathcal{L}. \tag{2.46}$$

Hence, the non-dimensional parameters of interest in the aeroelastic problem of a rigid airfoil in pitching and heaving motion are :

$$Re_c\,,\ I_{axis}^*\,,\ D_\theta^*\,,\ K_\theta^*\,,\ m^*\,,\ D_h^*\,,\ K_h^*\,,\ x_\theta^*.$$

2.4 Aerodynamic theory

The phenomenon of the airfoil undergoing self-sustained oscillations in the transitional flow regime is clearly a case of unsteady aerodynamics where important viscous effects occur. However, it is still of interest to use the inviscid quasi-steady aerodynamic theory [15] to produce a preliminary prediction of the aeroelastic frequency.

Considering a symmetrical airfoil, the aerodynamic lift and moment coefficients obtained from the quasi-steady theory are:

$$C_L = \frac{dC_L}{d\theta}\left[\theta + \frac{1}{U_\infty}\left(\frac{3c}{4} - x_{EA}\right)\dot{\theta}\right], \tag{2.47}$$

where x_{EA} is the chordwise position of the elastic axis and

$$\begin{aligned} C_{Mea} &= -\frac{c\pi}{8U_\infty}\dot{\theta} + C_L\left(\frac{x_{EA}}{c} - \frac{1}{4}\right) \\ &= -\frac{c\pi}{8U_\infty}\dot{\theta} + \frac{dC_L}{d\theta}\left[\theta + \frac{1}{U_\infty}\left(\frac{3c}{4} - x_{EA}\right)\dot{\theta}\right]\left(\frac{x_{EA}}{c} - \frac{1}{4}\right) \\ &= -\left[\frac{c\pi}{8U_\infty} + \frac{dC_L}{d\theta}\frac{1}{U_\infty}\left(\frac{3c}{4} - x_{EA}\right)\left(\frac{1}{4} - \frac{x_{EA}}{c}\right)\right]\dot{\theta} + \left[\frac{dC_L}{d\theta}\left(\frac{x_{EA}}{c} - \frac{1}{4}\right)\right]\theta, \end{aligned} \tag{2.48}$$

where $\frac{dC_L}{d\theta} = 2\pi$, if we restrict ourselves to the case of thin airfoils.

To analyze the dynamic of an airfoil subjected to this aerodynamic theory, we substitute the moment around the elastic axis in Eq. (2.36):

$$\begin{aligned} I_{axis}\ddot{\theta} + D_\theta\dot{\theta} + K_\theta\theta &= \frac{1}{2}\rho U_\infty^2 c^2 s\, C_{Mea}, \\ &= -\frac{1}{2}\rho U_\infty^2 c^2 s\left[-\frac{c\pi}{8U_\infty} + 2\pi\left(\frac{x_{EA}}{c} - \frac{1}{4}\right)\frac{1}{U_\infty}\left(\frac{3c}{4} - x_{EA}\right)\right]\dot{\theta} \\ &\quad + -\frac{1}{2}\rho U_\infty^2 c^2 s\, 2\pi\left(\frac{x_{EA}}{c} - \frac{1}{4}\right)\theta. \end{aligned} \tag{2.49}$$

Reformulating, this yields:

$$I_{axis}\,\ddot{\theta} + \{D_\theta \overbrace{-\frac{1}{2}\rho U_\infty^2 c^2 s\left[-\frac{c\pi}{8U_\infty} + 2\pi\left(\frac{x_{EA}}{c} - \frac{1}{4}\right)\frac{1}{U_\infty}\left(\frac{3c}{4} - x_{EA}\right)\right]}^{D_{a,qs}}\}\,\dot{\theta} + \left[K_\theta \overbrace{-\frac{1}{2}\rho U_\infty^2 c^2 s 2\pi\left(\frac{x_{EA}}{c} - \frac{1}{4}\right)}^{K_{a,qs}}\right]\theta = 0, \quad (2.50)$$

where $D_{a,qs}$ is the aerodynamic damping and $K_{a,qs}$ the aerodynamic stiffness as predicted by the inviscid quasi-steady theory.

Considering an oscillatory solution of the form $\theta(t) = \theta_0\, e^{i\omega t}$, we obtain a quadratic equation for ω:

$$-\omega^2 I_{axis} + i\omega(D_\theta + D_{a,qs}) + (K_\theta + K_{a,qs}) = 0. \quad (2.51)$$

Solving for ω and taking magnitude of the real part divided by 2π, the aeroelastic natural frequency is obtained:

$$f_{ae,qs} \equiv \frac{1}{2\pi}\sqrt{\frac{K_\theta + K_{a,qs}}{I_\theta} - \frac{D_\theta + D_{a,qs}}{4I_\theta^2}}. \quad (2.52)$$

The above theory is certainly deficient since it takes into account the motion of the symmetric thin airfoil instead of the actual unsteady effective body. In the case of interest here, viscous effects such as trailing edge separation and laminar separation bubble are present and have important repercussions on the forces exerted by the flow on the wing as well as on the shape of the effective body. However, the expression for frequency obtained in Eq. (2.52) yields a reasonable prediction since it includes the dominant effect of the stiffness K_θ in the present case. Fig. 2.9 shows the comparison between $f_{ae,qs}$ calculated by the inviscid quasi-steady theory using the same parameters as the experiments and the experimental frequency (both in non-dimensionnal form) over the Reynolds number range where oscillations are observed. The trend of the decreasing frequency with increasing Reynolds number from 60,000 to 100,000 is present but not the plateau at the higher Reynolds numbers. Furthermore, the quasi-steady aerodynamic theory cannot predict the oscillations amplitudes. It appears as though CFD simulations are necessary to improve the prediction of the frequency as well as the amplitudes of the limit-cycle oscillations.

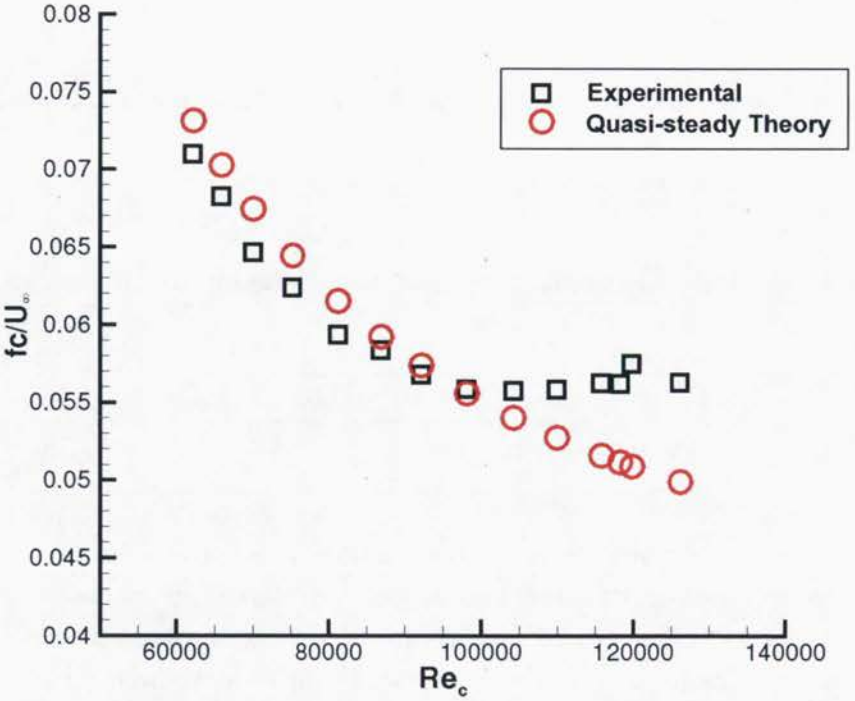

Figure 2.9: Comparison of experimental [61] and theoretical frequencies.

Chapter 3

Computational methodology

3.1 General formulation

3.1.1 Navier-Stokes and continuity

Fluid being a continuum material, the fundamental physical laws used in continuum mechanics, such as the conservation of mass, the conservation of momentum, and the conservation of energy, may be applied to derive the governing differential equations used in computational fluid dynamics.

The continuity equation is the result of the conservation of mass principle applied to a control volume. In the case of an incompressible and isothermal fluid, the equation can be further simplified:

$$\frac{\partial \rho}{\partial t} + \frac{\partial \rho U_i}{\partial x_i} = 0 \quad \overset{incompressible}{\longrightarrow} \quad \frac{\partial U_i}{\partial x_i} = 0 \,, \tag{3.1}$$

From the conservation of momentum, we obtain the famous Navier-Stokes equations which govern the dynamics of the flow:

$$\frac{\partial U_i}{\partial t} + U_j \frac{\partial U_i}{\partial x_j} = -\frac{1}{\rho}\frac{\partial p}{\partial x_i} + \nu \frac{\partial^2 U_i}{\partial x_j^2} \,. \tag{3.2}$$

The form presented in Eq. (3.2) is valid in the case of an incompressible fluid with constant and uniform properties. On the left-hand side are the terms related to the acceleration of the fluid and representing the inertial forces with in an unsteady and a convective part. On the right-hand side, the terms represent the net pressure and viscous forces.

3.1.2 Finite volume method

The finite volumes method considers the integral form of the governing equations applied over an arbitrary control volume V bounded by a closed surface S. For a general scalar field ϕ, the transport equation is:

$$\frac{\partial}{\partial t}\int_V \rho\,\phi\,dV + \int_S \rho\,\mathbf{n}\cdot\mathbf{u}\,\phi\,dS - \int_S \rho\,\gamma_\phi\,\mathbf{n}\cdot\nabla\phi\,dS = \int_V s_\phi\,dV, \tag{3.3}$$

where ρ is the density, $\mathbf{n}$ is the outward pointing unit normal vector on the surface, $\mathbf{u}$ is the fluid velocity, γ_ϕ is the diffusion coefficient and s_ϕ is a source term of ϕ.

Space is discretized using a mesh of small discrete control volumes, labelled as cells. The information of the physical fields can be stored either at the center of cells, at the faces or at the nodes. In the *OpenFOAM* software, values are stored at cells centers. Fig. 3.1 shows two neighboring cells along with the nomenclature of the spatial discretization.

Discretization of a convective term

A convective term is discretized by applying the divergence theorem and approximating the integrals as sums on the faces:

$$\int_V \nabla\cdot(\rho\mathbf{v}\phi)\,dV = \int_S d\mathbf{S}\cdot(\rho\mathbf{v}\phi) = \sum_{\text{Faces}} \mathbf{S}_f\cdot(\rho\mathbf{v})_f\,\phi_f = \sum_{\text{Faces}} F\phi_f, \tag{3.4}$$

where the mass flux F is defined as :

$$F = \mathbf{S}_f\cdot(\rho\mathbf{v})_f\,. \tag{3.5}$$

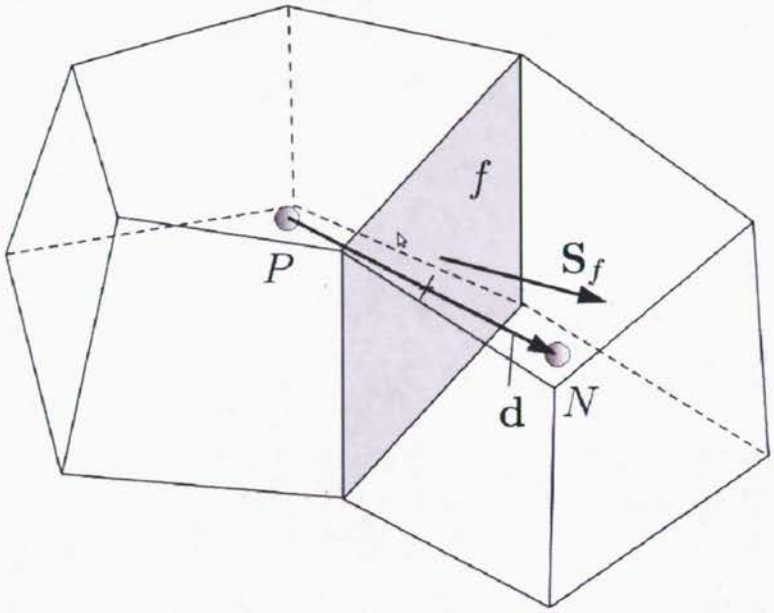

Figure 3.1: Cells and spatial discretization nomenclature, adapted from [54].

The mass flux is determined by the velocity field. In the case of the momentum equations, the velocity field is unknown and thus an initial prediction is needed. Typically the values of the previous iteration or time step are used. Eqs. (3.4) and (3.5) also require the face value of the variable ϕ calculated from the values in the cell centres, which is obtained using the convection differencing scheme.

There is a large variety of numerical interpolation schemes available. Among those, the Central Difference Scheme (CDS) consists of approximating the value by linear interpolation of the two closest centroids:

$$\phi_f = f_x \phi_p + (1 - f_x)\phi_N, \tag{3.6}$$

where the interpolation factor f_x is the ratio of distances between the faces and the centers:

$$f_x = \frac{x_N - x_f}{x_N - x_P}. \tag{3.7}$$

This schemes is second order accurate but is has been reported to cause unphysical oscillations in convection-dominated problems, thus violating the boundedness of the solution and sometimes creating numerical instabilities.

The Updwind Difference Scheme (UDS) is an alternative that guarantees boundedness of the solution, at the expense of a loss of order of accuracy. The face value of ϕ is here determined according to the direction of the flow:

$$\phi_f = \begin{cases} \phi_P & \text{if } F \geq 0 \\ \phi_N & \text{if } F < 0 \end{cases}. \tag{3.8}$$

Discretization of a diffusive term

A diffusive term can be discretized in a similar fashion as the convective term by applying the divergence theorem and approximating the integrals as sums on the surfaces:

$$\int_V \nabla \cdot (\Gamma \nabla \phi)\, dV = \int_S d\mathbf{S} \cdot (\Gamma \nabla \phi) = \sum_{\text{Faces}} \Gamma_f \mathbf{S}_f \cdot (\nabla \phi)_f . \tag{3.9}$$

An interpolation scheme is requiered to evaluate the gradient of ϕ at the cell's faces. If the mesh is orthogonal, it is possible to use the following expression:

$$\mathbf{S}_f \cdot (\nabla \phi)_f = |\mathbf{S}_f| \frac{\phi_N - \phi_P}{|\mathbf{d}|} . \tag{3.10}$$

In the case of a non-orthogonal mesh, the discretization of a diffusive term includes explicit terms and it might be necessary to apply correction loops in order to reduce the error produced by these terms [24].

Discretization of a source term

Sources terms include all terms of the original equation that cannot be written as convection, diffusion or temporal terms. When the source term is a function of ϕ, it is discretized as:

$$\int_V S \phi dV = V_P S_P \phi_P, \tag{3.11}$$

where S is a constant which depends on ϕ in the case of a non-linear source term. This allows to treat the source terms in an implicit or semi-implicit (in the case of a non-linear term) way.

Discretization of a temporal derivative

Temporal discretization is done by advancing the solution in time, using a time step. The treatment of the convective and diffusive spatial operators is done the same way in both steady and unsteady simulations. The temporal discretization requires to decide at what time these terms are actually evaluated. In the case of an explicit scheme, the terms are evaluated at past times where all the information is known. In the case of an implicit scheme, the terms need to be obtained for the present time, where all the information is not known a priori.

In the current projet, the second order backward differencing scheme is used. It is an implicit scheme which uses three time levels to obtain a second order accurate solution.

3.1.3 FVM on a moving mesh

When applied to a moving grid, the integral form of the Navier-Stokes equations over a moving volume becomes:

$$\frac{\partial}{\partial t}\int_V \rho\phi\, dV + \int_S \rho\mathbf{n}\cdot(\mathbf{u}-\mathbf{u}_s)\,\phi\, dS - \int_S \rho\gamma_\phi\,\mathbf{n}\cdot\nabla\phi\, dS = \int_V s_\phi\, dV, \tag{3.12}$$

where $\mathbf{u}_s$ is the local velocity vector of the boundary surface S. This velocity is related to the rate of change of the volume V by the space conservation law [8]:

$$\frac{\partial}{\partial t}\int_V dV - \oint_S \mathbf{n}\cdot\mathbf{u}_s\, dS = 0. \tag{3.13}$$

3.1.4 Pressure equation

While the momentum equations determine the velocity components, there is no independent equation for the pressure in incompressible flows. It is however possible to derive an equation for the pressure in order to guarantee the satisfaction of the continuity equation. By considering the divergence of the momentum equation and using the continuity equation to simplify

the resulting equation, we obtain a Poisson equation for the pressure:

$$\frac{\partial^2 p}{\partial x_i^2} = -\rho \frac{\partial}{\partial x_i}\left(U_j \frac{\partial U_i}{\partial x_j}\right). \tag{3.14}$$

Pressure-velocity coupling

The pressure and momentum equations can be solved either simultaneously in what is known as the "coupled" approach or sequentially in the "segregated" approach. In the current study, the segregated approach is used since it is the only available solving method in *OpenFOAM* at the moment. The momentum equations are first solved by using an approximation of the pressure field. In a second step, a correction is applied on the pressure. This correction procedure is repeated for a number of iterations until the desired convergence level is achieved. There are many algorithms used for the coupling between velocity and pressure. The most common are PISO and SIMPLE and their variations. The PISO algorithm is described here since it was chosen for the current study.

PISO stands for Pressure Implicit with Splitting of Operators. The first step is called the momentum predictor. The momentum equation is solved, with the pressure gradient evaluated with the pressure field of the previous time step or iteration. Using the predicted velocities, the pressure equation can then be formulated to obtain a first estimate of the new pressure field. Finally, the velocity field is corrected explicitly using the new pressure distribution. The algorithm is represented in Fig. 3.2.

3.2 Turbulence modeling

3.2.1 Overview of approaches

There exists a large variety of approaches for the modeling of turbulence in computational fluid dynamics, each with a different level of simulation quality and computational expenses.

The most basic and accurate approach is Direct Numerical Simulation (DNS) in which all turbulent motions are directly resolved in space and time so that no empirical modeling is employed. This approach implies the full 3D spatial and temporal resolution of the smallest eddies which requires an extremely fine grid size and very fine time steps. This leads to com-

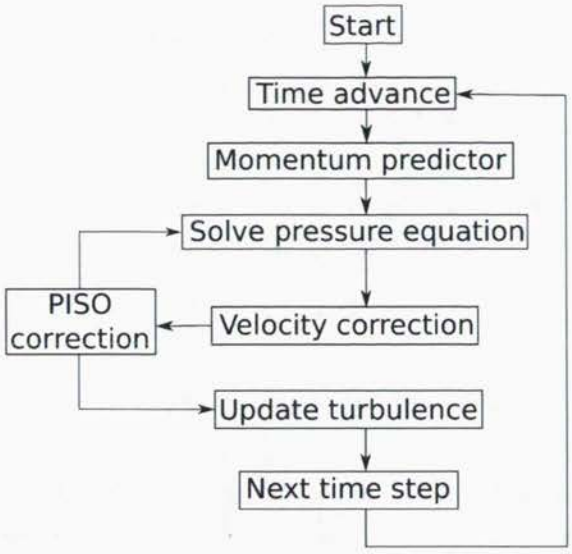

Figure 3.2: PISO solution procedure.

putational costs which greatly exceed the current computer resources for most engineering calculations at high Reynolds numbers. DNS is hence currently limited to research purposes rather than design purposes. However, it is still an extremely valuable tool to gain significant insight into the comprehension of the rich physics of turbulent flows.

The Large Eddy Simulation (LES) approach consists of the direct resolution of the larger scales of turbulent motion and the modeling of the smaller scales. This is done by applying spatial filtering, based on the grid size. The idea behind LES is based on the fact that the smaller scales of turbulent motion, those in the universal inertial range, are mostly isotropic. Hence, they are easier to model since they do not depend on the nature of the flow. This approach significantly reduces the computational cost of DNS but is still out of reach in many engineering applications since, at high Reynolds numbers, the "larger" scales which need to be resolved are still very small.

The Reynolds Averaged Navier Stokes (RANS) approach is based on the averaging of the unsteady turbulent motions. The application of the Reynolds averaging to the Navier-Stokes equations leads to the appearance of non-linear fluctuation terms, namely the Reynolds stresses, which need to be modeled. The turbulent model hence plays a very important role since it needs to predict the global effect of all scales of turbulent motion. This is why it is so difficult to develop RANS models which are very precise and applicable to a large variety of flows. The accuracy of RANS results is therefore limited compared to LES or DNS. However, the computational cost is enormously reduced since the turbulent scales are modeled and the grid can now be much coarser. Under RANS modeling, flows can even be solved in 2D and in steady state, leading to further reduction in computing requirements.

If the flow situation imposes time-varying patterns, the required temporal resolution of RANS simulations (then called URANS) is also much coarser than for LES or DNS since the time step size is now based on the time scale of the (slow) unsteadiness of the general flow patterns instead of the (fast) time scales of turbulence.

Hybrid approaches combining regions of the flow where LES is used and others where URANS is employed also exist, and will be discussed in section 3.2.4.

3.2.2 RANS/URANS

In the RANS or URANS modeling, quantities are decomposed into an average component and a fluctuating component. Applied to the velocity and pressure fields, this gives:

$$U_i = \overline{U}_i + u_i \quad \text{and} \quad p = \overline{p} + p' \,, \tag{3.15}$$

where $\overline{U}_i$ and $\overline{p}$ are the time-averaged fields, u_i is the fluctuating velocity component and p' the fluctuating pressure. This leads to the Reynolds-averaged Navier-Stokes equations:

$$\frac{\partial \overline{U}_i}{\partial x_i} = 0 \,, \tag{3.16}$$

$$\frac{\partial \overline{U}_i}{\partial t} + \overline{U}_j \frac{\partial \overline{U}_i}{\partial x_j} = -\frac{1}{\rho}\frac{\partial \overline{p}}{\partial x_i} + \frac{\partial}{\partial x_j}\left(\nu \frac{\partial \overline{U}_i}{\partial x_j} + \tau_{ij}\right) , \tag{3.17}$$

where $\tau_{ij} = -\overline{u_i u_j}$. This term is a result of the averaging process and represents the turbulent velocity fluctuation correlations, also called Reynolds stresses. The presence of this term leads to an open system of equations, since the number of unknowns now exceeds the number of equations. The role of turbulence models is to evaluate the Reynolds stresses in order to close the system.

A large variety of turbulence models are based on the concept of turbulent viscosity. This concept uses the Boussinesq's hypothesis and is expressed by the following equation:

$$\tau_{ij} + \frac{2}{3} k \, \delta_{ij} = \nu_t \left(\frac{\partial \overline{U}_i}{\partial x_j} + \frac{\partial \overline{U}_j}{\partial x_i} \right) , \tag{3.18}$$

where δ_{ij} is the Kronecker delta and ν_t is the eddy viscosity or turbulent viscosity. The turbulent kinetic energy, k, is half the trace of the Reynolds tensor:

$$k = \frac{1}{2}\overline{u_i u_j} = \frac{1}{2}(\overline{u^2} + \overline{v^2} + \overline{w^2}). \tag{3.19}$$

There are now two remaining unknowns in the system, ν_t and k. Turbulence models based on the Boussinesq's hypothesis use different means to evaluate those variables.

RANS Models

There exists a large variety of RANS turbulence models. Among these, some of the most widely known and commonly used in the aerospace community are the one-equation Spalart-Allmaras model by Spalart and Allmaras [77], the two equations $k-\omega$ SST model by Menter [40] and the $k-\epsilon$ model by Jones and Launder [27].

The Spalart-Allmaras RANS model is a one-equation eddy viscosity turbulence model formulated by Spalart and Allmaras in 1994 [77]. The model, based on a transport equation for the modified turbulent viscosity, is particularly well suited for aerodynamic flows but can also be used in a wide range of applications where resolving the near-wall region is required. The model does not have built-in transition prediction but it has a trip function that allows the user to specify a transition point. However, this function is omitted in the current implementation of *OpenFOAM* and thus, the model is not well suited to properly capture transitional boundary layers. The model equations are presented in further details in Appendice A.2.

Recently, significant progress has been made in the development of transition models for general purpose CFD codes. The $\gamma-\mathrm{Re}_\theta$ RANS model is a correlation-based transition model built on transport equations using only local variables. This is a concept which Menter *et al.* [41] describes as LCTM - Local Correlation-based Transition Model. The model has been developed by Langtry and Menter and was first presented by Menter in 2002 *et al.* [41]. Many changes were later introduced by Menter *et al.* [42] in what is known as the CFX-v-1.0 version. Later, Langtry and Menter [33] published an updated version of the model in 2009, CFX-v-1.1, releasing to the public empirical correlations that had been proprietary to ANSYS.

The model formulation uses only local variables and is not limited to 2D flows. Therefore, it can be integrated in modern 3D unstructured CFD codes. The model uses the strain-rate

Reynolds number to determine the onset of transition and adds two transport equations to the SST $k-\omega$ turbulence model [40]. The transport equation for the intermittency, γ, is used to turn on the production term of the turbulent kinetic energy downstream of the transition point in the boundary layer. The second added transport equation is solved in terms of the transition onset momentum-thickness Reynolds number ($\tilde{Re}_{\theta t}$). Its purpose is to incorporate the non-local influence of the turbulence intensity and pressure gradient in the transition prediction. The model contains three empirical correlations: one to relate the transition onset to the turbulence intensity and pressure gradient, one to relate the length of the transition zone to the transition onset momentum-thickness Reynolds number, and a third to relate the critical Reynolds number (where the intermittency starts to grow) to the transition onset momentum-thickness Reynolds number. These correlations may be expressed as:

$$Re_{\theta t} = f(Tu, \lambda_\theta), \qquad F_{length} = f(\tilde{Re}_{\theta t}), \qquad Re_{\theta t} = f(\tilde{Re}_{\theta t}) \tag{3.20}$$

The equations of this model are presented in Appendice A.3. A detailed explanation of the model formulation can be found in Langtry [32] along with numerous test cases.

Treatment of the near-wall region

The mesh requirements for RANS models depend of the type of wall treatment used. In the case of high-Reynolds models, wall functions are used, meaning that the near-wall region is modeled by the law of the wall and hence does not need to be resolved. In this case, the first cell thickness in wall coordinates (y^+) can be anywhere from 40 to 300.

So called low-Reynolds models (such as Spalart-Allmaras) require a much finer mesh near the wall since this region is now resolved. Typical recommendations consist of $y^+ \approx O(1)$ and Δx^+ and Δz^+ approximately in the range $200 \sim 400$ [7, 75].

As for transition models, the required wall resolution is similar to low-Reynolds RANS models. A value of $y^+ \lesssim 1$ along with a wall-normal expansion ratio which does not exceed $1.1 \sim 1.2$, and at least 100 streamwise nodes along the length of the boundary layer are suggested by Langtry [32].

Inlet conditions

An important and often overlooked point in RANS simulations is the inflow values of turbulence variables. As showed by Spalart and Rumsey [79], these values can have an (undesirable) impact on the turbulence model's performances. This is due to the fact that the decay

of those freestream values is often underpredicted, leading to ambient values near the airfoil much smaller than the inlet values.

For the turbulence models used in the current study, the chosen inlet conditions were based on the recommendations of the model developers. Calculations with the Spalart-Allmaras model used $\tilde{\nu} \approx 3\nu$ as suggested by Spalart and Rumsey [79].

In the case of the $\gamma - \mathrm{Re}_\theta$ RANS model, Langtry [32] recommends setting an inflow viscosity ratio of $\nu_t/\nu \sim 1-10$ and adjusting the inlet turbulence intensity to match the desired value at the airfoil leading edge. When using the SST model, it is possible to calculate the decay of turbulence intensity with the following equation:

$$Tu = \left(Tu_{inlet}^2 \left[1 + \frac{3U_\infty x \beta \, Tu_{inlet}^2}{2\nu \, (\nu_t/\nu)} \right]^{-\beta^*/\beta} \right)^{0.5} \tag{3.21}$$

where x is the streamwise distance from the inlet, $\beta = 0.09$ and $\beta^* = 0.0828$ are constants of the turbulence model. The inlet values of k and ω are then calculated from the inlet turbulence intensity and viscosity ratio as follows:

$$k_{inlet} = \frac{3}{2}(U_\infty Tu_{inlet})^2, \tag{3.22}$$

$$\omega_{inlet} = \frac{k_{inlet}}{\nu_{t,inlet}}. \tag{3.23}$$

Transition performance

Most of the conventional RANS models used in commercial CFD codes can be described as "fully turbulent" since they do not predict adequately or allow for laminar boundary layers. In some cases at low Reynolds numbers, some of these models display a behavior apparent to transition. However this behavior is rarely appropriate and it is not advised to use them for transitional flows [70, 71]. Standard RANS models cannot adequately compute transitional flows since Reynolds averaging eliminates the effects of linear disturbance growth, an important part of the transition process.

An alternative to improve transition prediction is to couple a RANS model with a method based on linear stability analysis such as the e^n method. This technique requires a boundary layer code coupled to the pressure distribution of the RANS code. The boundary layer code calculates velocity profiles which are used in the stability analysis and the results are then transfered back to the turbulence model in the RANS solver. Although this has been achieved

with success [74, 80, 91], these methods are difficult to implement in general purpose CFD codes since they often require knowledge of the geometry and grid topology, which make them very case-dependent. In addition, these transition models involve non-local operations, such as the calculation of boundary layer parameters or integration along streamlines, which are extremely difficult to carry out in unstructured parallelized CFD codes, where the body-normal grid direction is not readily available and the boundary layer region may have been split on multiple processors.

Prior to the recent development of transition models, low-Reynolds models were the only models directly applicable to general CFD codes that offered a transition prediction. In a general sense, low-Re models make use of the wall damping terms to incorporate the effects of transition. However, these terms are calibrated for the viscous sublayer damping. The transition effects captured, which Menter describes as "pseudo transition" [43], were never really built into the model. The close interaction between the viscous sublayer damping and the transition prediction is also difficult to calibrate since a modification to improve one modeling aspect often changes the performance of the other.

The authors of the transition model considered here have published various test cases to show the performances of their model. Langtry [32] showed results obtained by the $\gamma - \mathrm{Re}_\theta$ model for traditional flat plate cases, turbomachinery applications as well as external aerodynamic cases, such as the flow around a circular cylinder or wing. Ducoin *et al.* [13] also used the $\gamma - \mathrm{Re}_\theta$ for simulations of a pitching hydrofoil at $\mathrm{Re}_c = 0.75 \times 10^6$. The reported numerical results were in good agreement with experiments once the mesh resolution and temporal discretization were carefully selected.

3.2.3 LES

The original formulation of Large Eddy Simulation (LES) was proposed by Smagorinsky [73] in 1963. LES is based on the local filtering of the length scales. The filtering operation uses a filter size Δ which determines which scales are resolved and which scales are modeled. This separation of small and large turbulent structures is based on the size of the grid, hence the name of Sub-Grid Scale (SGS) for the smaller scales. Using $\tilde{U}$ which represents the filtered velocity, the Navier-Stokes and continuity equations are:

$$\frac{\partial \widetilde{U}_i}{\partial x_i} = 0 \,, \tag{3.24}$$

$$\frac{\partial \widetilde{U}_i}{\partial t} + \widetilde{U}_j \frac{\partial \widetilde{U}_i}{\partial x_j} = -\frac{1}{\rho}\frac{\partial \tilde{P}}{\partial x_i} + \frac{\partial}{\partial x_j}\left(\nu \frac{\partial \widetilde{U}_i}{\partial x_j} + \tau^s_{ij}\right), \tag{3.25}$$

where τ^s_{ij} is the sub-grid stress tensor analogous to the Reynolds stress tensor in RANS. The solution to the closure problem in LES is hence treated in a similar fashion as in RANS modeling. The eddy viscosity concept of Boussinesq is used with the tensor defined as:

$$\tau^s_{ij} = 2\nu_s \widetilde{S}_{ij} + \frac{1}{3}\tau^s_{kk}\delta_{ij}\,. \tag{3.26}$$

Sub-Grid Scale Models

Different models are used to evaluate the sub-grid viscosity ν_s. The most basic class is algebraic models. They are based on the assumption that the non-uniform component of the SGS stress tensor is locally aligned with the resolved non-uniform part of the rate of strain tensor. Among those, the first sub-grid scale model was proposed by Smagorinsky [73]. Based on a dimensional analysis, the sub-grid viscosity ν_s is defined by the mesh size Δ (typically $\Delta = (\Delta_x\Delta_y\Delta_z)^{1/3}$) and the strain-rate tensor $\widetilde{\mathbf{S}}$:

$$\nu_s = (C_S\Delta)^2|\widetilde{\mathbf{S}}|\,, \tag{3.27}$$

where C_S is a constant based on the decay of isotropic turbulence [36] and the value is given by:

$$C_S = \left(\frac{3\,C_K\,\pi^{4/3}}{2}\right)^{-3/4} \approx 0.16\,, \tag{3.28}$$

with the Kolmogorov constant $C_K \approx 1.6$. This value of C_S is formally valid in the case of isotropic turbulence. One of the main drawbacks of this model is its excessive dissipation in laminar and high shear regions, requiring a reduction of the C_S parameter. The most common solution is to use the van Driest damping function [11], which reduces the sub-grid eddy viscosity incorporating a function of wall distance. Additionally, the hypothesis that deviatoric SGS stresses and resolved strain rates are aligned is often false, producing a low correlation between the model and the actual turbulent stresses.

Dynamic models, first proposed by Germano *et al.* [18], can be viewed as a procedure to

improve previous models. The idea is that the model coefficients are determined as part of the calculation, based on the energy content of the resolved scales, instead of being constants previously chosen.

The introduction of dynamic models has been a significant progress in the sub-grid scale modeling of transitional flows and has resolved many of the problems encountered with traditional algebraic models, since the coefficients are automatically reduced in near-wall and high shear regions. It also produces the desired absence of eddy viscosity in laminar regions.

However, the dynamic models still present some limitations. In order to avoid excessive fluctuations of the computed coefficients, an averaging procedure, either in homogeneous directions, along streamlines or in local regions of the flow, is required. This is not trivial since the local averaging requires local homogeneity of the flow or a large averaging volume to obtain smooth coefficients variation. Additionally, dynamic models can produce negative dissipation, via a negative eddy viscosity. Although this backscatter can be associated with transport of energy from the unresolved to the resolved scales, in practice it can often lead to unphysical results or numerical instabilities.

The Mixed Time Scale (MTS) model of Inagaki *et al.* [23] was built in such a way to address three important defects of the Smagorinsky model, namely the need for a wall-damping function of van Driest's type, the need for the adjustment of the parameters according to the flow type and the presence of the SGS effect in laminar flow regions. The MTS model is formulated as follows:

$$\nu_s = C_{MTS} k_{es} T_S \,, \tag{3.29}$$

$$T_S^{-1} = \left(\frac{\Delta}{\sqrt{k_{es}}}\right)^{-1} + \left(\frac{C_T}{|\widetilde{\mathbf{S}}|}\right)^{-1} . \tag{3.30}$$

In the equations above, C_{MTS} and C_T with values of 0.05 and 10 respectively, were determined by different test studies. The estimated SGS turbulent energy, k_{es} is calculated as:

$$k_{es} = (\widetilde{u_k} - \hat{\widetilde{u_k}})^2, \tag{3.31}$$

where ($\hat{}$) is the filtering operator. This estimation has the purpose of guaranteeing that ν_s goes to zero in laminar flow regions as k_{es} will approach zero there. The time-scale T_S is the harmonic average of $\Delta/\sqrt{k_{es}}$ which represents the time-scale of the small-scale turbulence and $1/|\widetilde{\mathbf{S}}|$ which stands for that of the large scales. Near the wall, the time-scale approaches the value $1/|\widetilde{\mathbf{S}}|$, eliminating the need for a wall-damping function. Away from the wall, if $|\widetilde{\mathbf{S}}|$ becomes negligible, $\nu_s \approx C_{MTS}\Delta\sqrt{k_{es}}$.

Treatment of the near-wall region

The mesh requirements in the near-wall region of wall-resolved LES simulations typically found in the litterature are $y^+ \lesssim 1$, $\Delta x^+ \lesssim 50$ and $\Delta z^+ \lesssim 20$ [7, 67, 68, 95]. Although the wall-normal spacing requirement is the same as for the wall-resolving RANS models, the recommanded streamwise and spanwise spacings are much finer, which is responsible for the high computational cost of LES simulations.

Calculation of Δ

As previously mentionned, the SGS length scale or mesh size Δ is typically defined as:

$$\Delta = (\Delta_x \Delta_y \Delta_z)^{1/3}, \tag{3.32}$$

which is an appropriate definition as long as cells are roughly isotropic. In the case where cells have large aspect ratios, a different definition should be used, probably along the lines of Δ in DES discussed in section 3.2.4.

If neighboring cells have very different sizes, the change in the filter size may negatively affect the SGS model and the solution. When eddies are convected from a coarse to a finer mesh, they encounter a sudden decrease in the SGS viscosity since the length scale is smaller. This decrease is almost instantaneous compared to the SGS and resolved scale turbulent content that change more slowly, creating inaccuracies in the solution. The opposite occurs when eddies move from a fine to a coarse mesh, producing too much SGS viscosity in the larger cells. A solution to alleviate part of this problem is to smooth the SGS length scale in order to reduce sudden changes. The length scale of cells neighboring a large control volume are increased in such a way that the difference of Δ between two neighboring cells does not exceed a user-defined factor. In the present study, a factor of 1.15 was chosen.

Transition performance

Since Large Eddy Simulation requires far less computational resources than DNS and it does not make use of Reynolds averaging, its performance in transition prediction is expected to be quite good (assuming that the grid size is adequate to resolve the eddies that interact in the transition process).

Recent computations have showed the potential of large eddy simulation for flows in the

transitional Reynolds number range. Almultairi *et al.* [2] performed calculations around a NACA0012 airfoil at a Reynolds number of 50,000. The simulations were able to capture the presence and intermittent bursting of a laminar separation bubble at different angles of attack. Results were in good agreement with DNS computations.

Other recent results were reported in the works of Visbal *et al.* [86, 87], Castonguay *et al.* [6] and Uranga *et al.* [84]. Simulations were done around a SD7003 airfoil at fixed angles of attack and also undergoing a plunging motion, at Reynolds numbers ranging from 10,000 to 60,000. Results showed a good comparison with experimental PIV measurements, showing very similar flowfield structures. The computations at the higher Reynolds numbers captured important transitional effects, as laminar vortices appeared at the leading edge before breaking down into fine-scale turbulent structures due to spanwise instabilities.

Quasi-3D LES simulations of Yuan *et al.* [94] were also able to capture the most important physical behavior in the transition to turbulence on a SD7003 airfoil at a Reynolds number of 60,000. Their study showed the potential of LES for the simulation of transitional flow features even with a very limited spanwise computational domain of only 4 points. However this computational setup probably compromises the quality of the results by inhibiting the appearance of spanwise instabilities.

There are nonetheless some issues associated with LES that can have an impact in the simulation of transitional flows. One of these problems is the high sensitivity of the transition location to the choice of the Smagorinsky constant [18]. The dynamic sub-grid scale models mentioned earlier, which compute the constant locally, are supposed to improve the prediction of the transition location since the the dynamic procedure reduces the eddy viscosity to zero in laminar boundary layers.

Other problems associated with LES computations are numerical errors caused typically by grid irregularities and by the numerical schemes employed. These errors can generate artificial dissipation, leading to erroneous predictions of transitional flows. Hence, in some cases, the dynamic LES models have shown good qualitative agreement with DNS results, but noticeable differences were observed in the quantitative comparison.

In these transitional flows, the concept of LES is not necessarily associated with the existence of a full inertial spectrum which, at these low Reynolds numbers, is not expected to be present. In fact, many of the aforementioned simulations were labelled as implicit large eddy simulations (ILES), indicating that a LES type mesh was used without a sub-grid scale model. The dissipation was provided through the numerical schemes employed. The simulations thus showed the importance of not using a RANS model at such low Reynolds numbers but not necessarily the need of using a SGS model.

3.2.4 DES

DES or Detached-Eddy Simulation is a hybrid turbulence modeling approach first introduced by Spalart *et al.* [78] in 1997. The concept is to combine LES and RANS approaches in the same three-dimensional unsteady simulation through the use of a single turbulence model. The model behaves as a sub-grid scale model where the grid is fine enough for a large-eddy simulation and as a RANS model in regions where LES grid requirements are not met. In its "natural" use, attached boundary layers are entirely modeled by RANS and regions of separated flows (detached eddies) are simulated by LES. The goal is to combine the best of those two approaches. RANS models are computationally inexpensive and perform well in simple boundary layer flows. However, it is highly inaccurate in the simulation of massively separated flows. On the other hand, LES is much more accurate but the computational cost for wall-bounded high-Reynolds number flows is extremely high, making this approach impossible in many engineering applications. However, for the simulation of detached eddies far from the walls, large-eddy simulation is possible at a reasonable numerical cost.

The first formulation of this method [78] consisted of applying the concept of RANS-LES coupling to the Spalart-Allmaras RANS model [77]. As this model makes use of the wall-normal distance d, it was an ideal candidate for DES. The wall-normal distance d is replaced by the DES length scale $\tilde{d}$ which alternates between d and the LES length scale:

$$\tilde{d} = min(d, C_{DES}\Delta). \tag{3.33}$$

From this definition, we observe that near the wall, where $d < C_{DES}\Delta$, $\tilde{d} = d$ and the model formulation is identical to the S-A RANS model. Far from the wall, $C_{DES}\Delta < d$ and the LES length scale is employed, which consists of a measure of the local grid cell size, Δ, multiplied by a model constant C_{DES} which is adjusted to the solver. Δ is the LES filter width, and is defined here as the maximum cell length in each index direction $\Delta = max(\Delta_x, \Delta_y, \Delta_z)$.

Introducing the mesh size, the SA model now behaves as a one-equation sub-grid scale model. This can be shown by reducing the transport equation to an equilibrium between the production and destruction term, resulting in: $\tilde{\nu} \sim \tilde{S}d^2$. With d defined by the mesh size, this equation is a sub-grid scale model similar to the one of Smagorinsky in Eq. (3.27).

It is possible to transform any RANS model into a DES model by comparing a specific length scale to the LES length scale based on the mesh size.

A DES formulation, based on the SST RANS model of Menter [40], has been proposed

by Strelets [81]. In this case, the RANS length scale is dependent on the model variables instead of the wall-normal distance:

$$L_{RANS} = \frac{\sqrt{k}}{\beta^* \omega} \tag{3.34}$$

and is compared to the LES length scale within the F_{DES} function which multiplies the destruction term in the equation of k:

$$F_{DES} = max\left(\frac{L_{RANS}}{C_{DES}\Delta}, 1\right), \qquad \epsilon = \beta^* k \omega F_{DES}. \tag{3.35}$$

Treatment of the near-wall region

The requirements for the mesh resolution in the near-wall region are the same as RANS models, namely $y^+ \lesssim 1$, $\Delta x^+ \lesssim 200 - 400$ and $\Delta z^+ \lesssim 200 - 400$ [7], [76]. However, away from the wall, the mesh resolution should be finer than in RANS modeling since the LES model is in effect in that region.

Calculation of Δ

In DES, the recommended Δ is the maximum dimension of the cell ($\Delta = max(\Delta_x, \Delta_y, \Delta_z)$) since DES meshes are typically more anisotropic than LES meshes. However, this definition is ambiguous when cells are not hexaedrals. Other choices have therefore been proposed such as taking the longest edge of the cell, or the cube root of the cell's volume.

Transition performance

As this modeling approach normally treats the boundary layers with a RANS model, the quality of the transition prediction of DES is dependent of the RANS model used. Therefore, in cases of attached boundary layers with no separation, it can be argued that there is no real advantage of using DES over RANS. However, in cases where there are regions of attached boundary layers and also regions of separated flows, it could be interesting to use DES with a RANS model capable of transition prediction. For example, in the classical case of the drag crisis of a circular cylinder, it is well known that the movement of the separation point on the circular cylinder is highly influenced by the laminar to turbulent transition process. The use of a RANS model able to predict accurately the position of the separation point in conjunction

with the LES part of DES to resolve the separated flow region may be quite interesting in this situation.

Although the studied case of self-sustained pitch oscillations at transitional Reynolds numbers does not involve massively separated flow regions, RANS simulations have shown the presence of coherent structures in the wake region. The use of LES could help better resolve this part of the flow and maybe gain some further physical insight.

The $\gamma - \mathrm{Re}_\theta$ transition model described earlier is a good candidate for this application since the model is based on the SST RANS model which already has a DES formulation, namely DES-SST. The same formulation [81] can be used to create a transition DES model, named DES-SST $\gamma - \mathrm{Re}_\theta$.

This has been implemented in OpenFOAM, under the DDES form ("delayed DES"). The F_2 blending function shown in Eq. (A.6) is used to make sure the entire attached boundary layer is treated with the RANS model.

3.3 Fluid-Structure Interaction

3.3.1 Aeroelastic modeling

The second order equation of motion for the pitch-only case is written as a system of two first order differential equations as follows:

$$I^*_{axis}\dot{\omega} + D^*_\theta\omega + K^*_\theta\theta = M^*, \tag{3.36}$$

$$\dot{\theta} = \omega, \tag{3.37}$$

where ω is the angular velocity of the wing. The system of first order equations is then solved in time with the standard fourth order Runge-Kutta method, which was chosen because of its availability in *OpenFOAM*.

The coupling of the structural and fluid equations is enforced at each time step. At each time step, the moment around the pitching axis and the lift obtained from the fluid solver are passed to the wing; the equations of motion are then calculated to determine the dynamic response of the wing; and the kinematic information, i.e. the rotation and angular velocity as well as vertical position and velocity, is transfered back to the fluid solver which updates the

mesh position and boundary conditions accordingly and then advances to the next time step. This procedure is illustrated in Fig. 3.3.

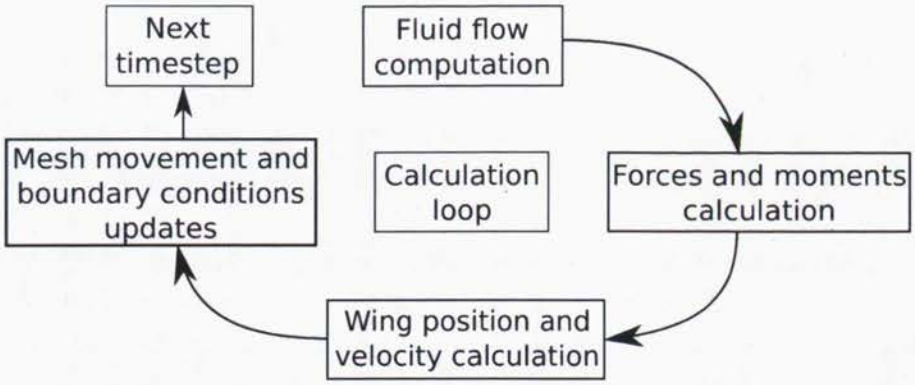

Figure 3.3: Fluid-structure interaction loop.

In the case of the two degrees of freedom pitch-heave oscillations, the two equations of motion are written as a system of four first order ordinary differential equations:

$$I^*_{axis}\,\dot{\omega} + D^*_\theta\,\omega + K^*_\theta\,\theta + m^*\dot{v}_y\,x^*_\theta\,cos(\theta) = M^*, \tag{3.38}$$

$$\dot{\theta} = \omega, \tag{3.39}$$

$$m^*\left(\dot{v}_y + x^*_\theta\,cos(\theta)\,\dot{\omega} - x^*_\theta\,sin(\theta)\,\omega^2\right) + D^*_h\,v_y + K^*_h\,y = -\mathcal{L}, \tag{3.40}$$

$$\dot{y} = v_y, \tag{3.41}$$

where v_y is the vertical velocity of the airfoil. The fluid-structure interaction loop is accomplished in a similar fashion as the pitch-only case. The vertical motion is taken into account by solving the equations in a heaving reference frame, as explained in the next subsection.

3.3.2 Mesh motion

Pitch-oscillating case

The pitch-oscillating airfoil problem is here solved in a fixed frame of reference which thus requires moving body and moving grid capabilities. There exists many possibilities to execute mesh motion in finite volume CFD calculations and different options have been considered in the current project.

In *OpenFOAM*, a non-conformal circular interface can be used in order to avoid deforming the mesh and remeshing around the airfoil. To take into account the pitching motion, the inner part of the mesh, located inside a radius of 2 chords about the pitching axis, rotates rigidly with the body while the outer part remains stationary as shown in Fig. 3.4. At the interface, interpolation is calculated by a General Grid Interface (GGI) algorithm. The approach has been thoroughly validated against several previous studies in our research group in which Fluent GGI was employed [28, 30].

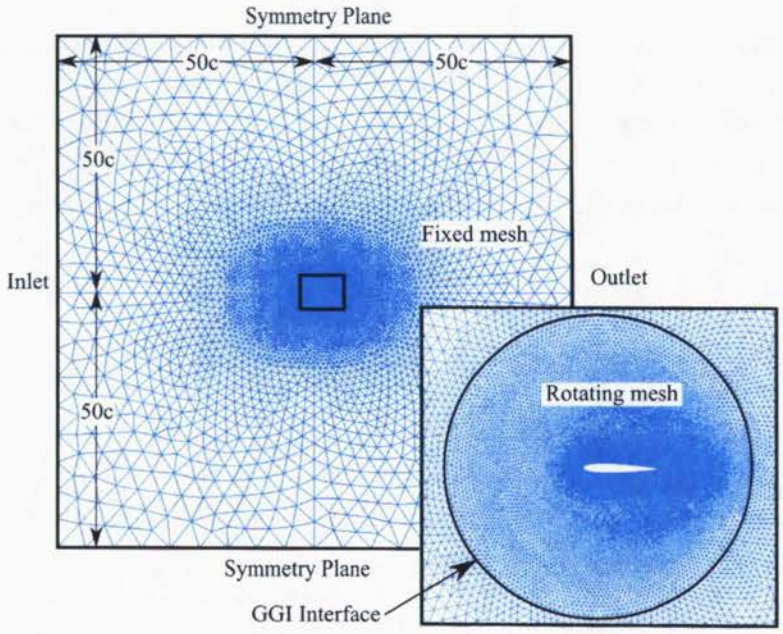

Figure 3.4: Computational domain and grid details, ~ 80,000 cells.

In the current study, this approach has been used to perform all 2D calculations. However, in 3D LES or DES simulations, the very important number of cells at the interface drastically increases computational time. Thus, another mesh handling approach has been used.

Another possible grid deformation strategy is an algebraic method, first introduced by Morton *et al.* [48] and recently used by Ou and Jameson [55] and Campbell [5]. This method has the property of preserving grid orthogonality near the surface under substantial deformation, which is very desirable for high Reynolds number viscous flow simulation where the boundary layer grid resolution is very fine. To retain the orthogonality near the surface where boundary movement starts, the grid lines perpendicular to that surface are rotated and translated as rigid bodies with the movement of the surface.

In the region close to the body, the rigid displacement of the mesh for a pitching motion

can be obtained by:

$$\begin{bmatrix} x_r \\ y_r \end{bmatrix} = \begin{bmatrix} x_i \\ y_i \end{bmatrix} + \begin{bmatrix} cos(\theta) & -sin(\theta) \\ sin(\theta) & cos(\theta) \end{bmatrix} \begin{bmatrix} x_r - x_0 \\ y_r - y_0 \end{bmatrix} \tag{3.42}$$

where (x_r, y_r) are the coordinates of the rigidly displaced mesh, (x_i, y_i) are the coordinates of the mesh in its initial condition, (x_0, y_0) is the center of rotation and θ is the angular displacement.

Far away from the moving boundary, the mesh is fixed and remains unchanged during the simulation. In the region between the rigidly displaced mesh and the stationary mesh, a blending function is used in order to obtain a smooth mesh deformation. In this study, a 5^{th} order bending polynomial, as used by Ou and Jameson [55] and Persson *et al.* [58], is used. The polynomial is given by:

$$f = 10s^3 - 15s^4 + 6s^5, \tag{3.43}$$

where $s = d/D$ is the ratio of the arc-length distance d of a point to the inner edge of the deforming region over the total width D of the deforming region. The polynomial function has a slope of zero at the end points, in order to preserve mesh orthogonality at the boundaries. The displacement of points in this region is given by:

$$\begin{bmatrix} x_d \\ y_d \end{bmatrix} = \begin{bmatrix} x_i \\ y_i \end{bmatrix} + (1 - f) \begin{bmatrix} cos(\theta) & -sin(\theta) \\ sin(\theta) & cos(\theta) \end{bmatrix} \begin{bmatrix} x_d - x_0 \\ y_d - y_0 \end{bmatrix} \tag{3.44}$$

where (x_d, y_d) are the coordinates of the deformed mesh. Figure 3.5 shows an example of a deformed mesh along with the original mesh.

Pitch-heave oscillating case

In the case of the two degrees of freedom simulations, a non-conformal interface has also been used to allow for the pitching motion of the airfoil. The grids used are thus similar as the one shown previously in Fig. 3.4. However, additional care is needed to take into account the vertical motion of the airfoil. Indeed, to avoid remeshing or deforming the mesh, the Navier-Stokes equations are solved in a heaving reference frame. This requires to update the velocity at the inlet and upper and lower boundary conditions accordingly to the airfoil's

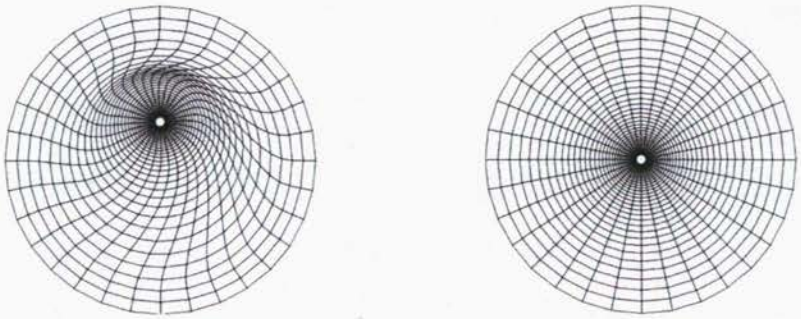

(a) Mesh with Deformation (b) Original Undeformed Mesh

Figure 3.5: Deformed and original meshes, adapted from [55].

velocity. Furthermore, a source term equal to the vertical acceleration of the airfoil is added to the Navier-Stokes equations.

Chapter 4

Test cases and validation

This chapter presents a summary of different tests cases used to validate the methodology described earlier.

4.1 Comparison of RANS models, fixed airfoil

This section presents the comparison of performances between standard, low-Reynolds and transitional RANS models for the simulation of the steady flow around a fixed airfoil. It also serves the purpose of validating our implementation of the $\gamma - \mathrm{Re}_\theta$ model in *OpenFOAM*. The chosen test case is a MS-0313 wing profile at $\mathrm{Re}_c = 2 \times 10^6$. This case was chosen because of the availability of experimental results by McGhee and Beasley [38]. Lift, drag and moment coefficients are presented for different angles of attack. Furthermore, experiments were performed with free transition and forced transition by a trip wire at the leading edge. This is of great interest here since RANS models are often reported to predict almost a fully turbulent boundary layer. In addition to experimental data, RANS models predictions have also been compared with results obtained using the XFOIL software [10] which uses the e^n method to predict transition. In this study, a criteria of $n = 9$ was used and calculations were also made with forced transition at the leading edge to simulate a fully turbulent boundary layer.

The 2D mesh used in this study has about 49 000 cells, 28 000 of hexaedral shape in the region near the airfoil and 21 000 of tetraedral shape in the freestream region. The boundaries are located 50 chords away from the airfoil. To assure adequate resolution of the boundary layer, the grid has a y^+ of approximately 1 at the first grid point off the wall. A mesh independence study showed minor discrepancies in the predicted lift, drag and moment coefficients

when using a refined mesh. All numerical results of RANS simulations were obtained in steady state with a second-order upwind discretization for all equations and convergence criteria better than 10^{-5}.

4.1.1 Forces coefficients

We begin by comparing the performance of three widely used standard RANS models, the one equation Spalart-Allmaras model [77], the $k-\omega$ SST model [40] and the $k-\omega$ model [89]. The results of lift and drag coefficients for angles of attack ranging from 0 to 20 degrees are shown in Figs. 4.1 and 4.2.

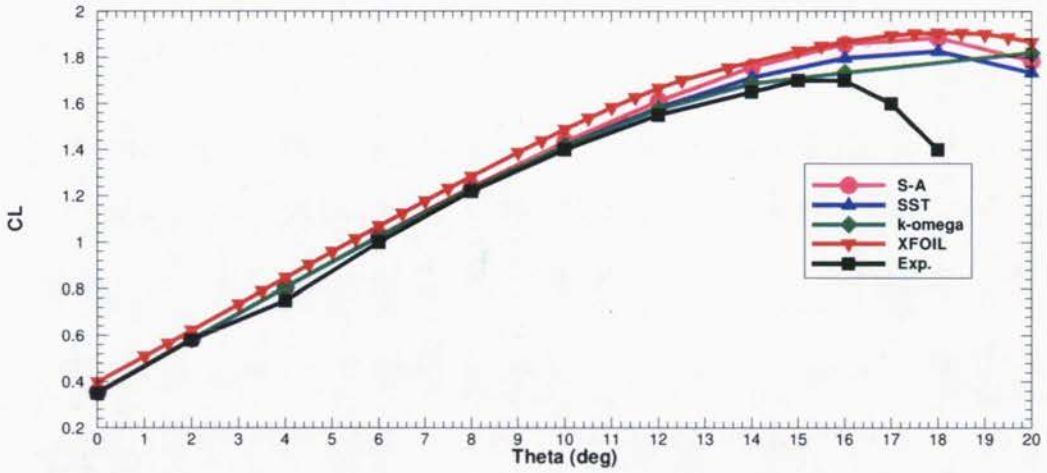

Figure 4.1: Lift coefficients obtained from RANS models, experimental data and XFOIL.

We observe that the lift prediction of all RANS models is pretty accurate at low-to-moderate angles of attack. The results are in good agreement with the experimental data and XFOIL calculations. At higher angles of attack, the RANS models overpredict the lift since the experimental stall angle is lower than the predicted one. Turning our attention to the drag coefficients, we see that all three RANS models predicted considerably higher values than the experimental data or XFOIL calculations for angles of attack below 12 degrees. This can be attributed to the important laminar part of the boundary layer which is not predicted properly by RANS models, hence the higher friction drag. This assumption is confirmed by Fig. 4.3 which shows the drag coefficients when the boundary layer is tripped at the leading edge to force transition. The experimental and XFOIL numbers, labelled as "rough" on the figure, are now in line with the RANS results.

The same cases are presented in Figs. 4.4 and 4.5 but this time, the experimental and

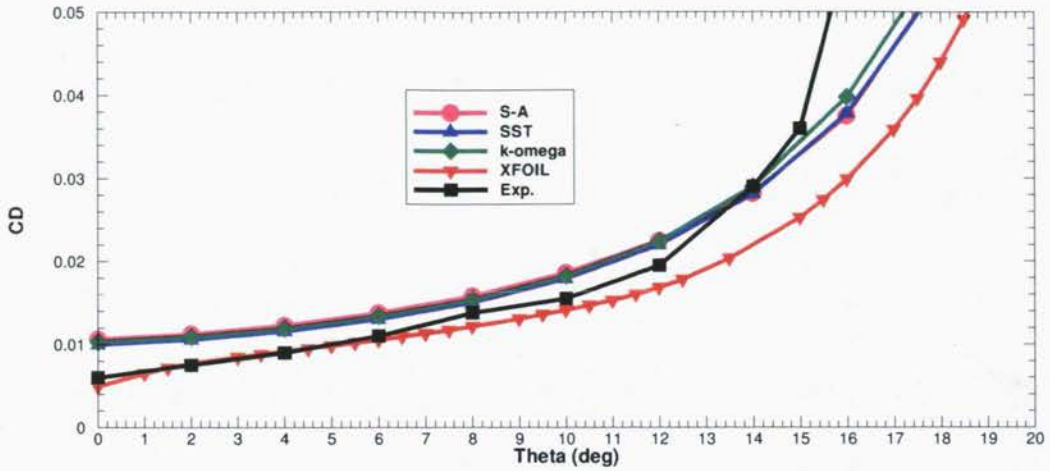

Figure 4.2: Drag coefficients obtained from RANS models, experimental data and XFOIL.

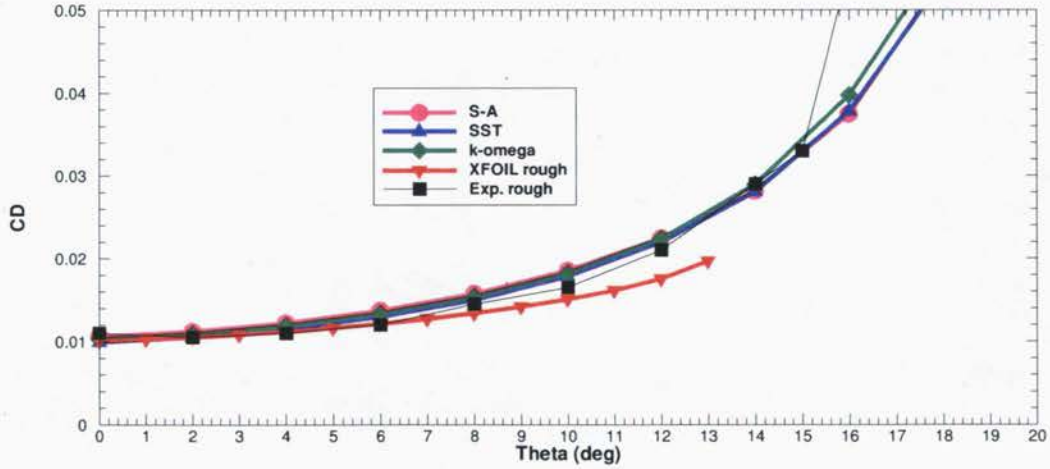

Figure 4.3: Drag coefficients obtained from RANS models, experimental data and XFOIL with forced transition at the leading edge.

XFOIL data are compared to results obtained with the $k - k_L - \omega$ model [88], the $\gamma - \mathrm{Re}_\theta$ model [33] and the $k - \omega$ SST model with the "low-Reynolds correction" applied. The simulations with the $\gamma - \mathrm{Re}_\theta$ model have been performed with both *Fluent* and *OpenFOAM*, and the results obtained were found to be very similar (less than 2% difference).

The computed lift coefficients are in good agreement with the experimental results and XFOIL calculations, remaining similar to those of the traditional RANS models. The influence of the transition models on the drag coefficient prediction is definitive. The results are very close to the free transition experimental case and XFOIL coefficients at low-to-moderate

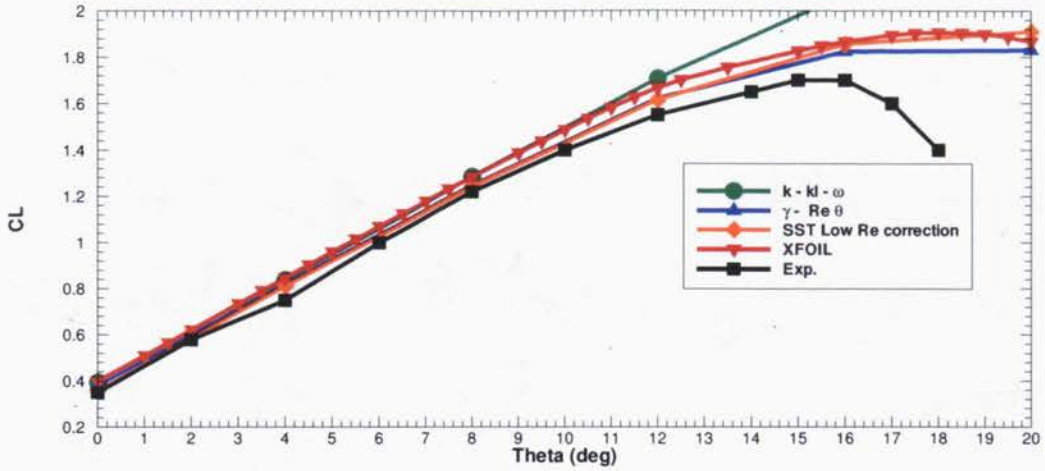

Figure 4.4: Lift coefficients obtained from transition models, experimental data and XFOIL.

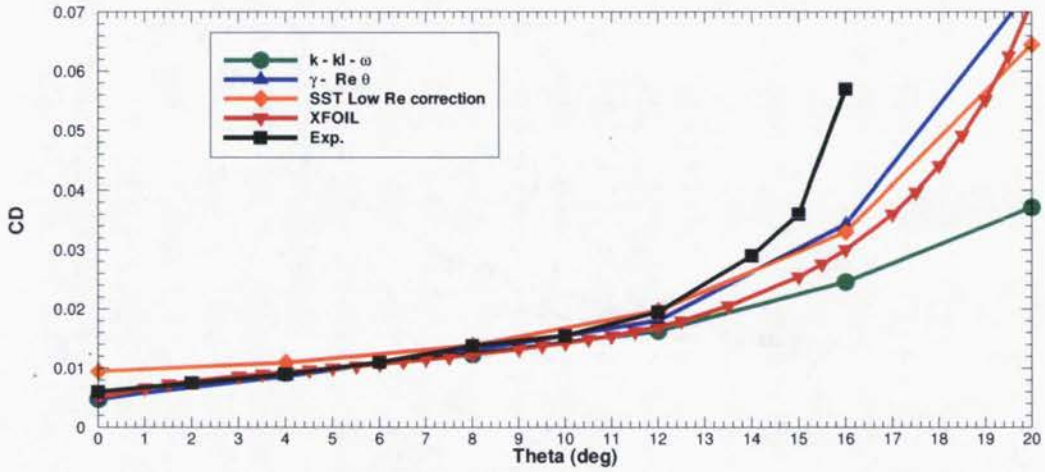

Figure 4.5: Drag coefficients obtained from transition models, experimental data and XFOIL.

angles of attack. The $k-\omega$ SST model with the "low-Reynolds correction" does not agree as well with the experimental data, giving results closer to the standard RANS models.

4.1.2 Transition position and LSB

It is also possible to compare the predicted position of laminar to turbulence transition in the boundary layer. Fig. 4.6 shows the position of transition along the chord on the suction side for angles of attack from 0 to 20 degrees, and Fig. 4.7 shows the transition location on

the pressure side. Results obtained with both transition models, the $k-\omega$ SST model with and without the "low-Reynolds correction" and XFOIL are presented. Experimental data of transition position are not available. In the RANS calculations, the positions have been estimated by identifying the location where the turbulent viscosity suddenly started to grow ($\frac{\nu_t}{\nu} > 1$).

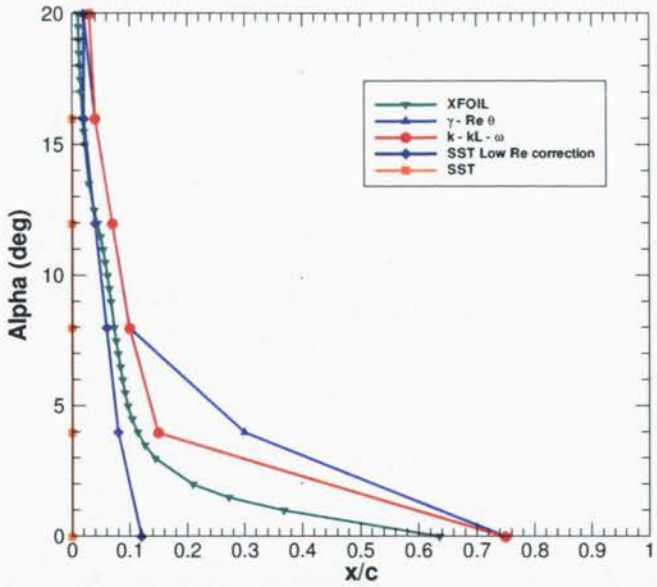

Figure 4.6: Transition position on the suction side.

Results show that the predicted transition locations of both transition models are in good agreement with XFOIL results. However, the positions obtained with the $k-\omega$ SST model with and without the "low-Reynolds correction" are quite different, predicting much larger turbulent regions, especially on the pressure side.

In addition to the good prediction of transition location, transition models are also able to simulate some interesting physical mechanisms of transition. Fig. 4.8 shows the vorticity contours and velocity vectors of the flow near the leading edge of the airfoil at an angle of attack of 12 degrees. The simulation was performed with the $\gamma - \mathrm{Re}_\theta$ model. We can observe a local separation of the laminar boundary layer, producing a small region of reversed flow. This is denoted by vectors opposite to the direction of the freestream flow and vorticity of opposite sign. The boundary layer then becomes turbulent and reattaches, hence a case of separation induced transition. Fig. 4.9 shows the presence of the laminar separation bubble by the circling streamlines and the transition to turbulence is denoted by the rapid increase in turbulent viscosity.

This test case has shown the advantages of transition models over standard RANS models

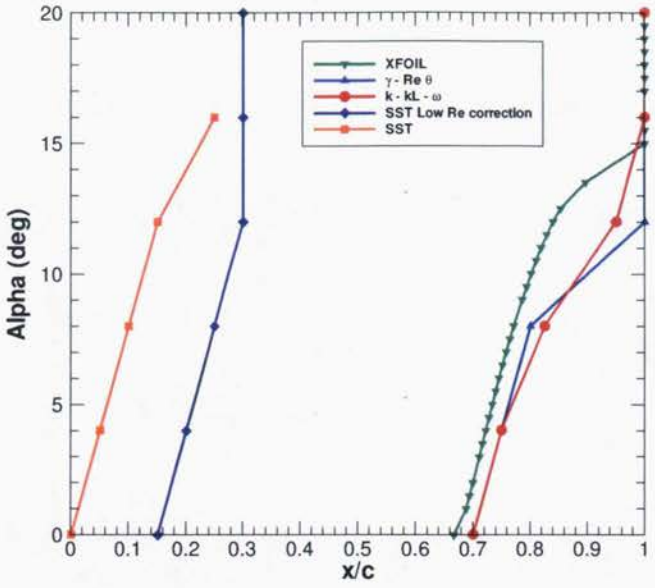

Figure 4.7: Transition position on the pressure side.

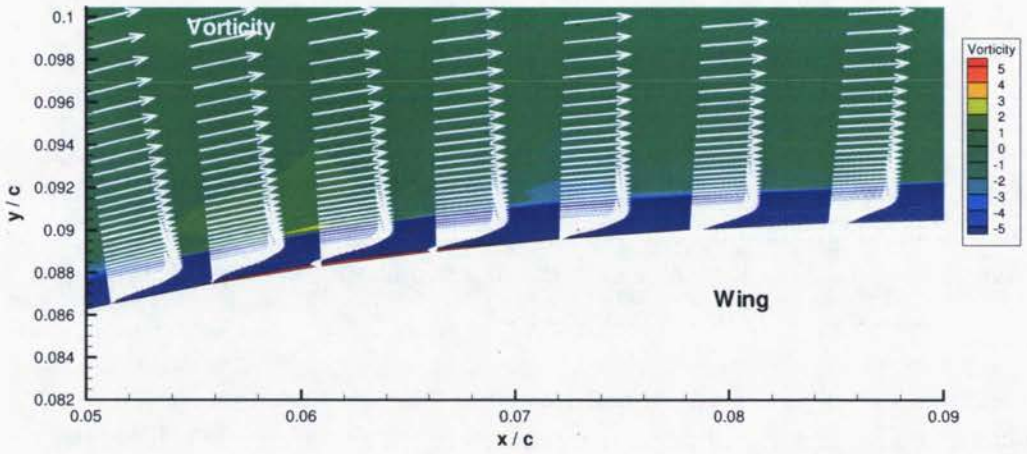

Figure 4.8: Vorticity contours and velocity vectors on the suction side, near the leading edge.

for a simple case of stationary airfoil. The lift prediction is good and the drag prediction is much improved due to a good prediction of the laminar and turbulent regions in the boundary layer. Furthermore, transition models can simulate phenomena previously outside of the scope of traditional RANS models, such as a laminar separation bubble. However, these advantages come at a higher computational cost since there are additional transport equations to solve and convergence is sometimes more difficult to reach.

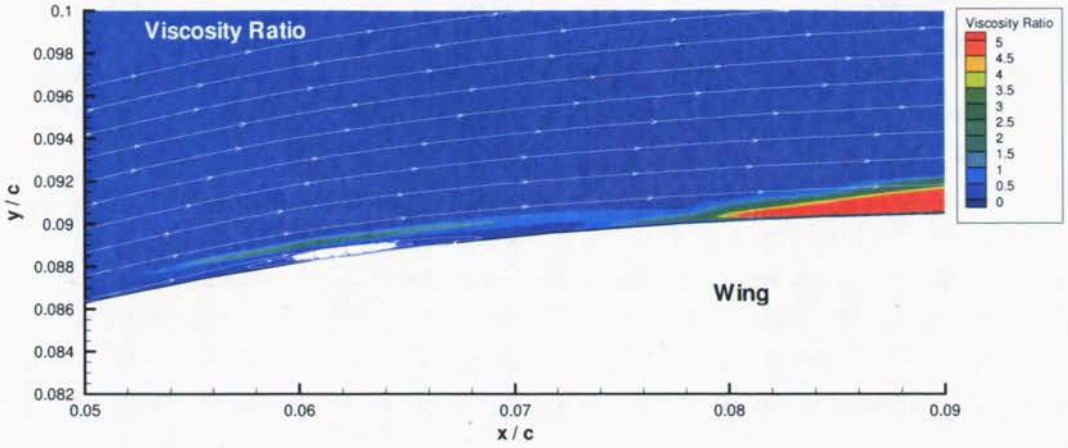

Figure 4.9: Viscosity ratio contours and streamlines on the suction side, near the leading edge.

4.2 Comparison of RANS models, moving airfoil

Since the current project involves the unsteady simulations of moving airfoils, this second test case serves as a validation of the moving mesh methodology as well as another comparison of RANS models.

The flow around an oscillating NACA0015 airfoil is computed with a non-dimensional frequency of $fc/U = 0.08$, a heaving amplitude of $H/c = 1$, and a pitching amplitude of 60 degrees at two Reynolds numbers of $\mathrm{Re}_c = 100,000$ and $\mathrm{Re}_c = 1,000,000$. This case is of interest because the frequency, the pitching amplitude and the lower Reynolds number are similar to the pitch-heave self-sustained oscillations reported by Poirel's research group [39]. It is a case where the oscillating airfoil extracts energy from the flow. The motion of the airfoil is thus described as:

$$\theta(t) = \theta_0 \sin(\gamma t), \tag{4.1}$$

$$y(t) = H \sin(\gamma t + \phi), \tag{4.2}$$

where $\gamma = 2\pi f$ and the phase-shift $\phi = 90$.

Two RANS models are used, namely the Spalart-Allmaras model and the $\gamma - \mathrm{Re}_\theta$ transition model. Simulations are performed with timestep of $\Delta t^* = 0.000625$ (20000 timesteps per cycle).

4.2.1 Evolution of force coefficients

The evolution of the vertical force (C_y), horizontal force (C_x) and moment coefficients (C_m) obtained with both turbulence models during one cycle of oscillation at a Reynolds number of 100,000 are presented in Fig. 4.10. We observe that the forces calculated with the Spalart-Allmaras model are smoother than those obtained by the transition model. There seems to be a higher level of unsteadiness (flow structures) in the latter simulation, as it can be seen in Fig. 4.11. Despite these important differences, the global mean quantities calculated over a cycle are similar. The power extraction efficiency ($\eta = \frac{\bar{P}}{\frac{1}{2}\rho U_\infty^3 d}$, where the power is defined in Eq. (4.3)) is 0.251 with the Spalart-Allmaras model and $\eta = 0.220$ with the γ–Re_θ model. The difference is due to the smaller maximum vertical forces in the calculation with the transition model.

$$P = \overbrace{F_y \cdot V_y}^{P_y} + \overbrace{M \cdot \Omega}^{P_\theta}. \tag{4.3}$$

4.2.2 Effect of Reynolds number

Instantaneous spanwise vorticity and viscosity ratio contours computed with both turbulence models at both Reynolds numbers are shown in Fig. 4.11 and Fig. 4.12 at the same instant in a cycle ($t = 4T/5$). At a Reynolds number of 100,000, there are important differences between the Spalart-Allmaras model and the $\gamma - \mathrm{Re}_\theta$ in both the vorticity and viscosity ratio contours. Looking at the vorticity contours, the S-A solution presents a large leading edge vortex while the $\gamma - \mathrm{Re}_\theta$ shows multiple smaller vortices. This difference in instantaneous vorticity flow fields can be explained by the different levels of turbulent viscosity. With the S-A model, there is a high level of viscosity ($\nu_t/\nu > 100$) over all the upper side of the airfoil while the $\gamma - \mathrm{Re}_\theta$ flow field shows a high level around the vortices but much smaller levels close to the airfoil. This lower viscosity allows for more unsteadiness in the flow and thus the smaller vortices.

At a Reynolds number of 1,000,000 however, the solutions are much closer. There are only little differences in the vorticity and viscosity ratio fields computed with both models.

This shows that, at a relatively high Reynolds number, there is not much advantage to use a transition model for the simulation of flows with large separation. A classic, fully-turbulent RANS model gives similar results at a cheaper computational cost. However, at a transitional Reynolds number, the $\gamma - \mathrm{Re}_\theta$ presents differences in the flow fields and its use could thus be justified. However, when comparing integral quantities such as power coefficients over a cycle, these differences are minor and both models return similar global values.

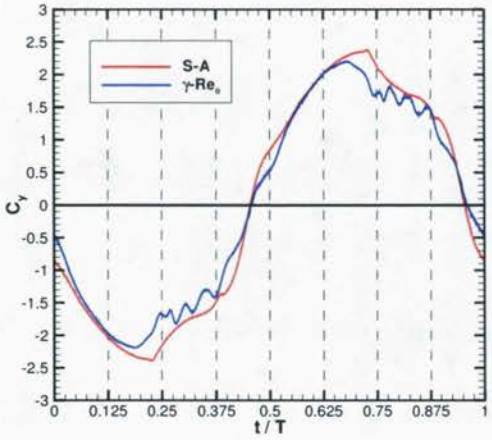

(a) Vertical force coefficient

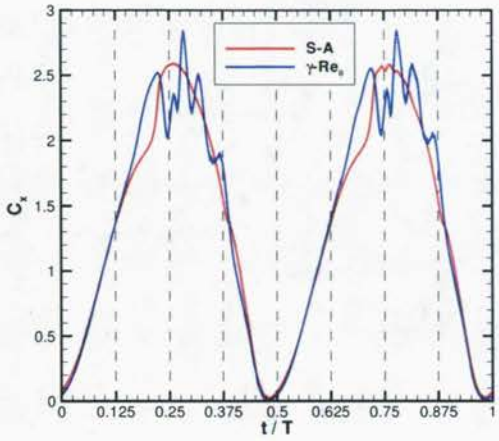

(b) Horizontal force coefficient

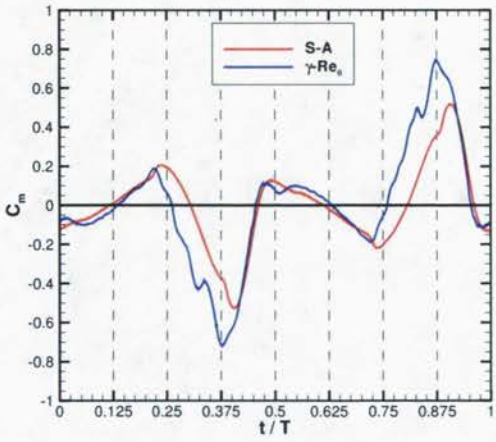

(c) Moment coefficient

Figure 4.10: Instantaneous force and moment coefficients in a cycle at Re = 100, 000.

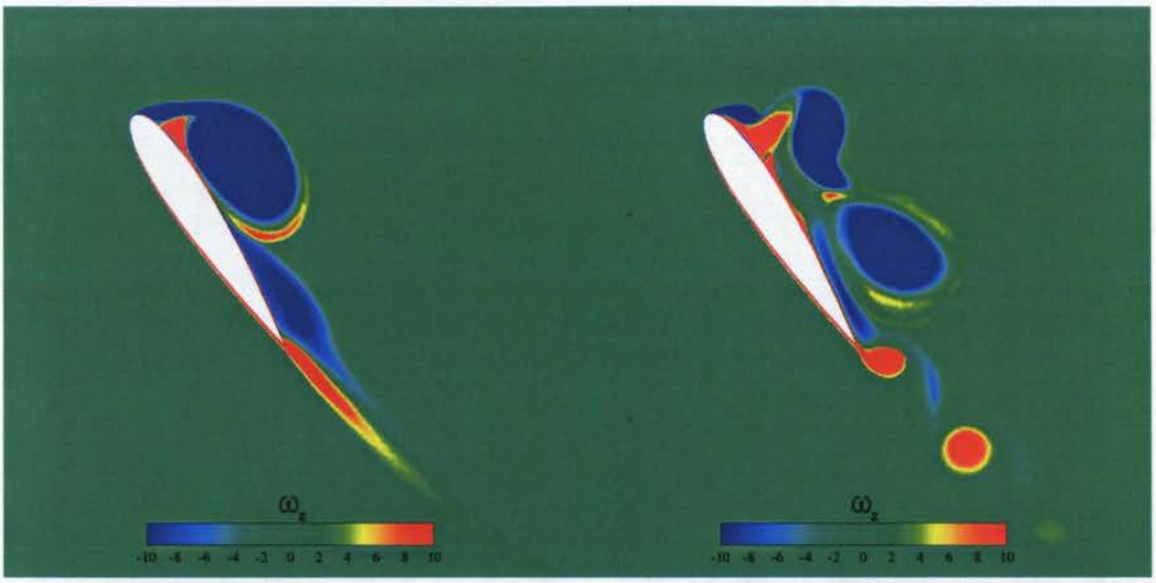

(a) $\mathrm{Re}_c = 100,000$, S-A (b) $\mathrm{Re}_c = 100,000$, $\gamma - \mathrm{Re}_\theta$

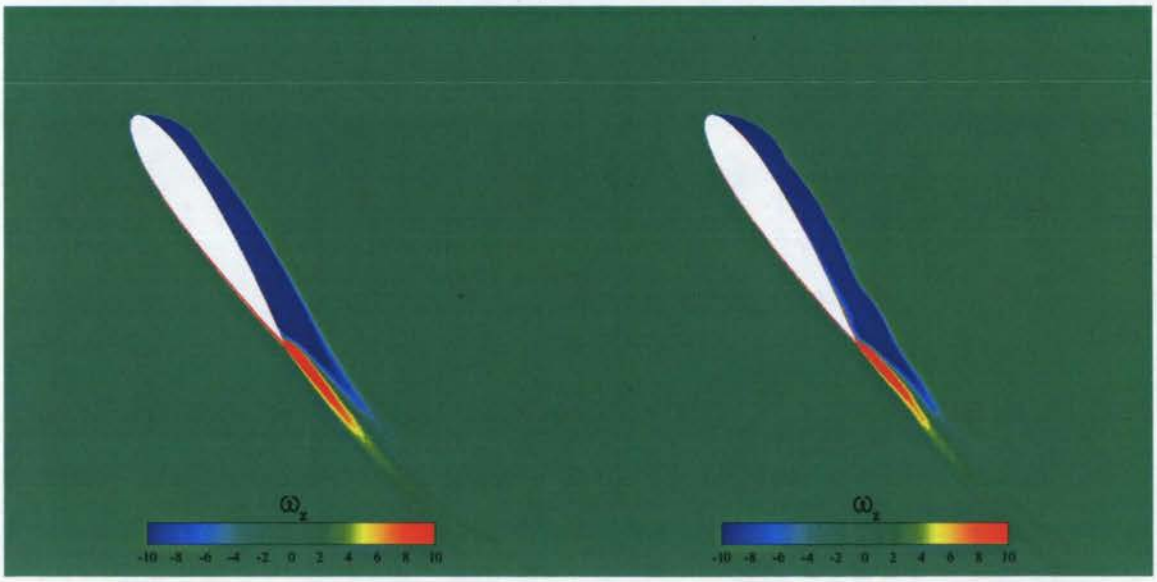

(c) $\mathrm{Re}_c = 1,000,000$, S-A (d) $\mathrm{Re}_c = 1,000,000$, $\gamma - \mathrm{Re}_\theta$

Figure 4.11: Instantaneous spanwise vorticity contours at $t/T = 0.8$ and for two Reynolds numbers.

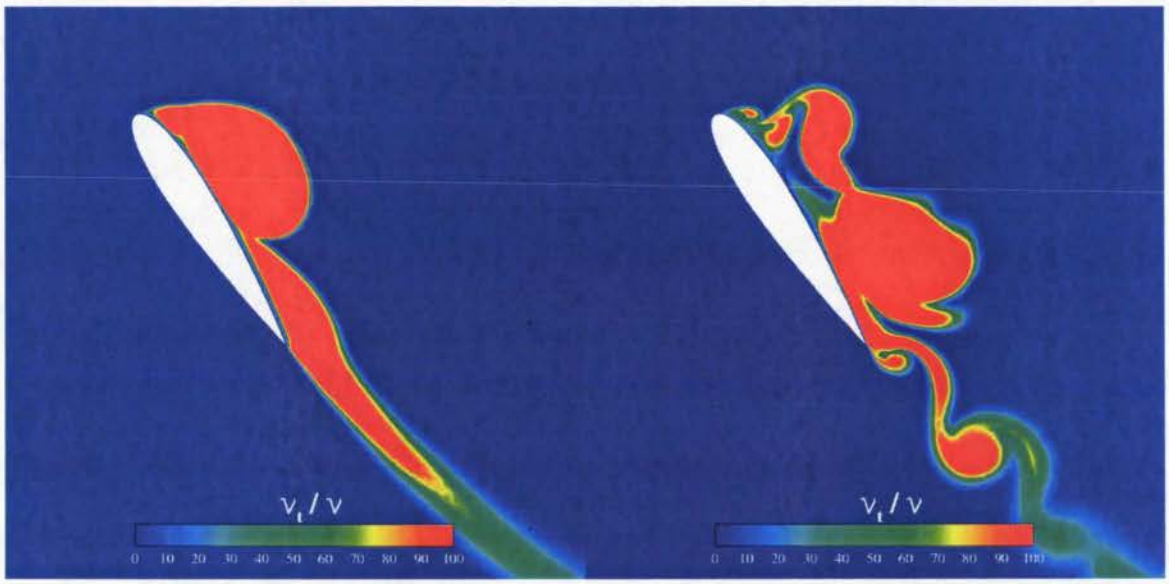

(a) $\mathrm{Re}_c = 100,000$, S-A (b) $\mathrm{Re}_c = 100,000$, $\gamma - \mathrm{Re}_\theta$

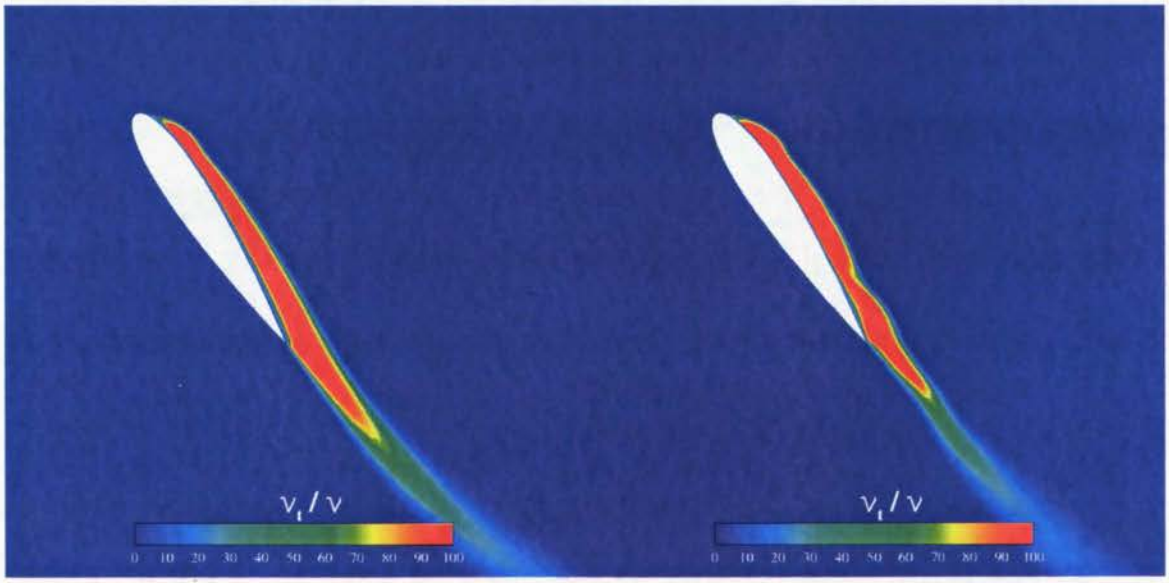

(c) $\mathrm{Re}_c = 1,000,000$, S-A (d) $\mathrm{Re}_c = 1,000,000$, $\gamma - \mathrm{Re}_\theta$

Figure 4.12: Instantaneous viscosity ratio contours at $t/T = 0.8$ and for two Reynolds numbers.

4.3 LES of transitional flows

4.3.1 References and Motivation

The objective of this part is to investigate the feasibility of a Large Eddy Simulation approach to accurately predict LSB formation and transition for low Reynolds-number airfoil applications. Additionally, this case will serve as a comparison between LES results and those obtained with transitional RANS models.

The computation of the flow over a SD7003 airfoil section, shown in Fig. 4.13b, was chosen for this validation study. This airfoil has a maximum thickness of 8.5% and a maximum camber of 1.48%. It was selected because, at low Reynolds numbers, a relatively large LSB forms on the suction side of the airfoil and high quality experimental and numerical data were available for comparison.

Experimental studies

Experimental results of high quality are always very interesting for the evaluation of computation results since they allow us to compare our numerical tools and models to "real-life" measurements. In the case of the SD7003, experiments in the Reynolds number range of interest were performed by two different groups.

Radespiel *et al.* [66] conducted Particle Image Velocimetry (PIV) experiments in both a water channel and a low-noise wind tunnel at the Technical University of Braunschweig (TU-BS). High resolution velocity and Reynolds stress measurements were recorded for a Reynolds number of 6×10^4 at angles of attack of 4 degrees in the wind tunnel and 8 and 11 degrees in the water channel. The freestream turbulence intensity was of $\sim 0.08\%$ in the wind tunnel and $\sim 0.8\%$ in the water channel.

Ol *et al.* [53] also performed PIV measurements in a water channel at the Wright Patterson Air Force Research Labs Horizontal Free-Surface Water Tunnel (HFWT) with a freestream turbulence intensity of less than 0.1%.

Numerical results

In addition to the experimental results available, this case has been studied using LES and implicit LES (ILES) simulations at multiple occasions. Among these, Galbraith [16] and Visbal *et al.* [87] performed simulations at Reynolds numbers of 10^4 to 9×10^4 and angles of attack ranging from 2 to 14 degrees using a high-order finite difference method and an ILES approach.

The particular case at $\mathrm{Re}_c = 60,000$ and $\alpha = 4$ degrees was used as a validation case for ILES by both Castonguay *et al.* [6] and Uranga *et al.* [84] using a high-order Spectral Difference method and a high-order Discontinuous Galerkin solver respectively.

Yuan *et al.* [93] also computed the flow around the SD7003 airfoil with both LES (using a subgrid scale model) and a RANS code coupled with a e^N solver.

4.3.2 Numerical considerations

Influence of grid resolution

To evaluate the required grid resolution, different C-grid type meshes were built using hexaedral cells. In all cases, a two-dimensional mesh was created and then extruded in the spanwise direction using a constant spacing. A typical mesh is shown in Fig. 4.13. Freestream and outlet boundaries are located 50 chords away from the airfoil. Uniform velocity is imposed at the inlet and constant pressure is imposed at the oulet. Periodic boundary conditions are used along the spanwise direction (which has an extent of $0.1c$ or $0.2c$ depending on the tests) and a no-slip, adiabatic wall condition is used on the surface of the airfoil.

Five different grids were built, whose parameters are presented in Table 4.1. N_x is the number of cells on the airfoil surface (the sum of both the suction and pressure sides), N_y is the number of cells in the direction normal to the airfoil surface and $\Delta z/c$ is the spacing in the spanwise direction [1]. For all these five meshes, $L_z = 0.1c$. Figure 4.14 shows the y^+, Δx^+ and Δz^+ distribution along the chord, obtained by a simulation using mesh B. The typical LES requirements of $y^+ \leq 1$, $\Delta x^+ \leq 50$ and $\Delta z^+ \leq 20$ are all respected.

In Fig. 4.15, surface pressure and skin friction distributions obtained with meshes A, B and C are presented. The distributions of meshes B and C are almost identical, however a

[1] It is more convenient to talk in terms of spacing since different spanwise sizes will be investigated later.

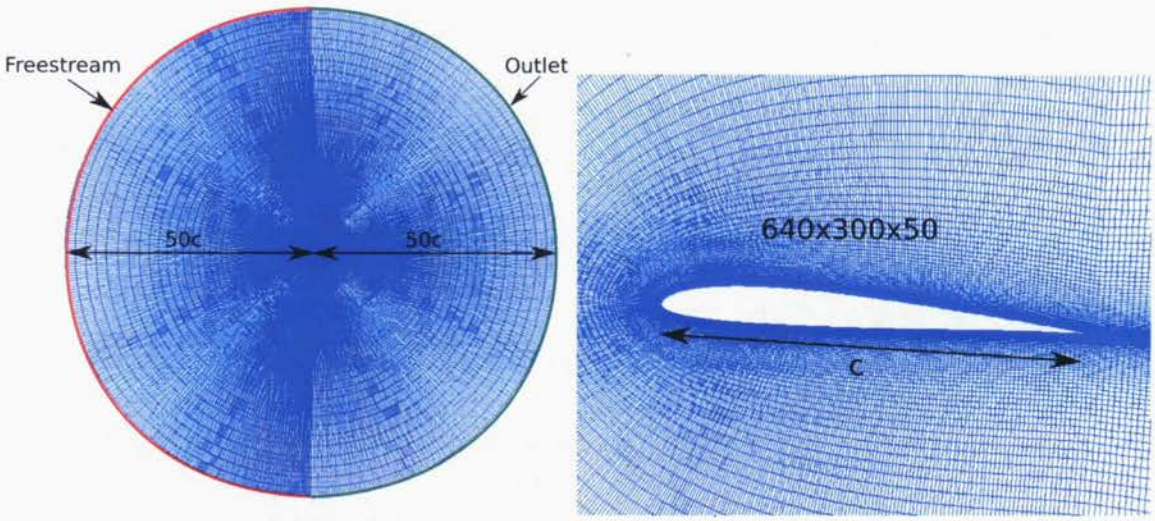

(a) Complete mesh (b) Zoom around the airfoil region

Figure 4.13: Typical mesh used in LES simulations.

Table 4.1: Parameters of different meshes used.

Mesh	N_x	N_y	$\Delta z/c$	Total cells
A	640	300	0.005	4,740,000
B	640	300	0.002	11,850,000
C	640	300	0.00125	18,960,000
D	640	400	0.002	15,800,000
E	870	300	0.002	15,300,000

longer LSB is predicted with mesh A as can be seen on both figures. Hence, it seems a spacing of $\Delta z/c = 0.002$ is sufficient since refinement does not affect the results, while $\Delta z/c = 0.005$ is too coarse.

Surface pressure and skin friction distributions presented in Fig. 4.16 were computed with meshes B, D and E in order to evaluate the required streamwise and wall-normal resolutions. Since there is no significant differences between those three meshes, we conclude that 640 cells on the airfoil and 300 cells in the wall-normal are sufficient to obtain grid independent results. Thus, in the following computations, mesh B will be used.

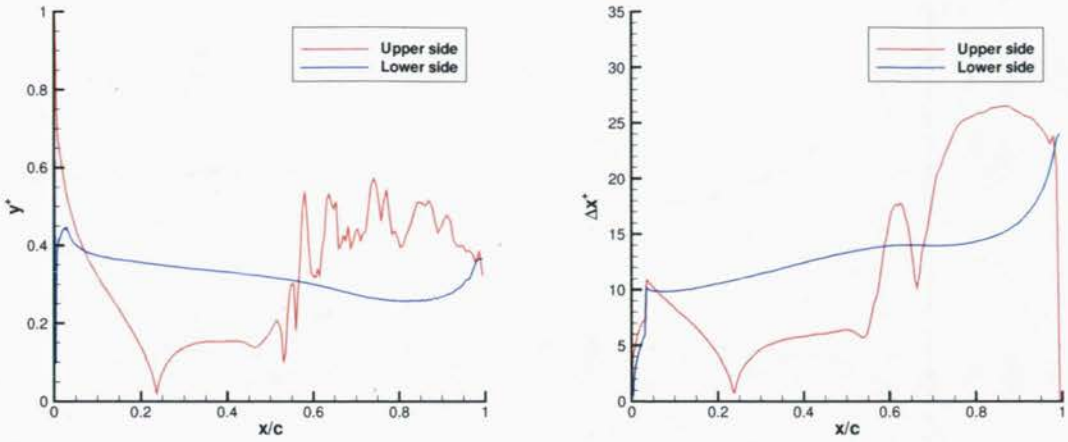

(a) y^+ (b) Δx^+

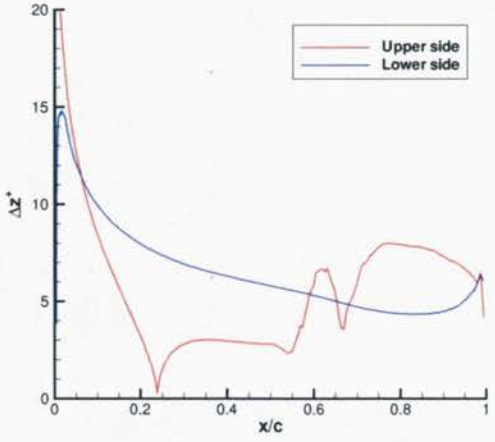

(c) Δz^+

Figure 4.14: Mesh resolution in wall units along the chord.

Influence of spatial dimension and spanwise extent

To evaluate the need for a three-dimensional domain, a two-dimensional simulation was computed and compared to a three-dimensional simulation of $AR = 0.2c$ using the same x-y mesh and a spanwise resolution of $\Delta z/c = 0.002$. Distributions of pressure and skin friction coefficients are shown in Fig. 4.17 and contours of instantaneous spanwise vorticity are shown in Fig. 4.18. The surface pressure coefficient of the 2-D simulation is quite similar to the one of the 3-D simulation although there is a significant peak at the end of the pressure plateau in 2-D which is not present in 3-D. Concerning the size of the LSB, it is slightly larger in

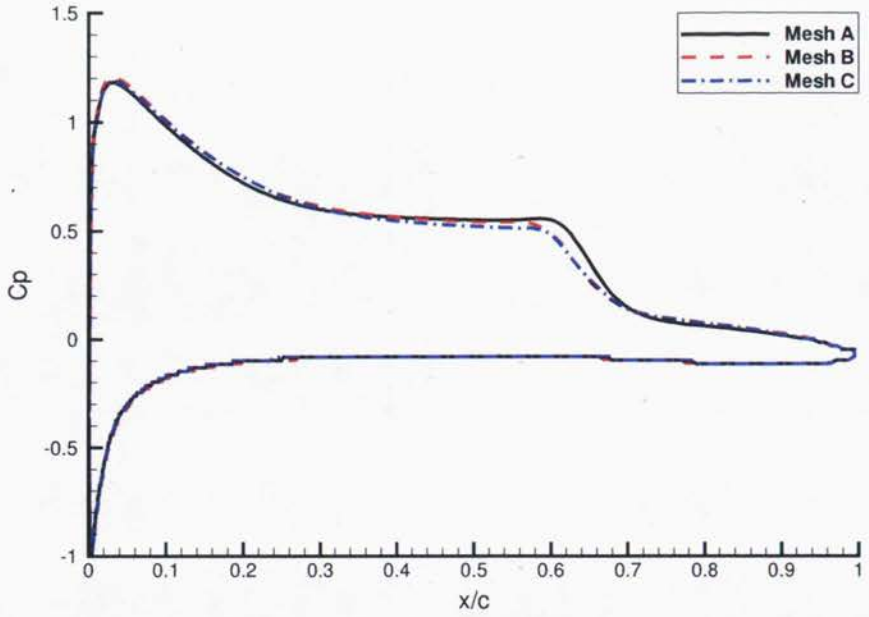

(a) Mean C_p coefficient

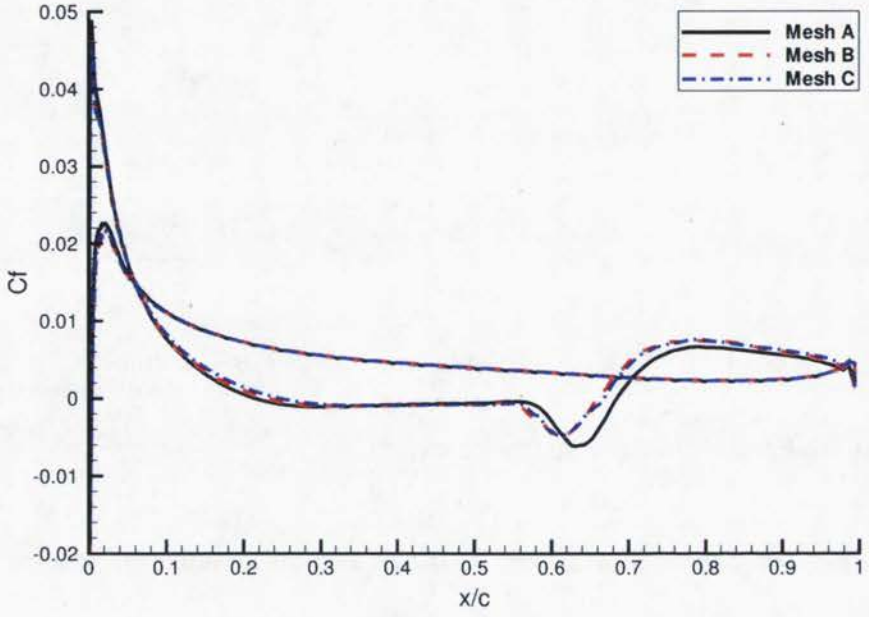

(b) Mean C_f coefficient

Figure 4.15: Comparison of spanwise grid spacing.

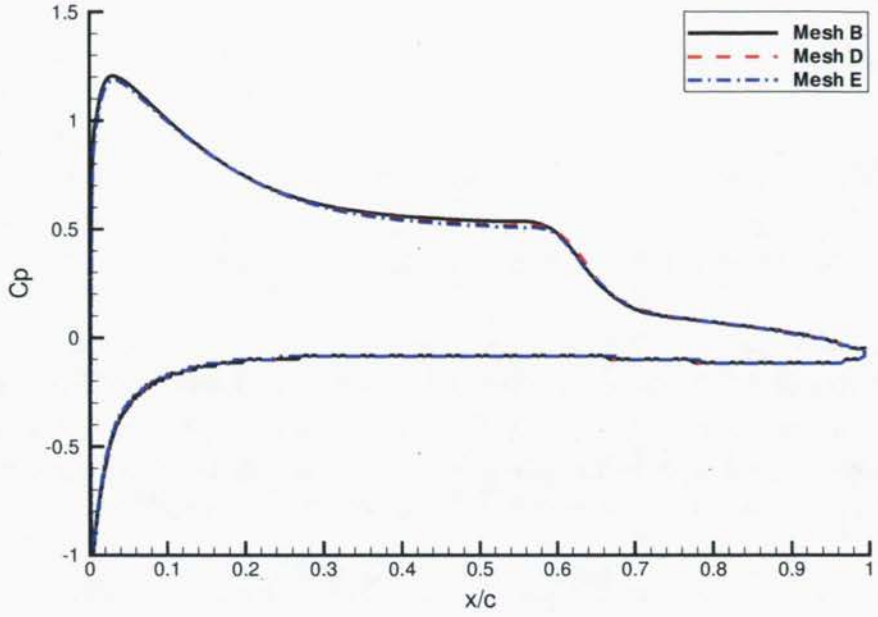

(a) Mean C_p coefficient

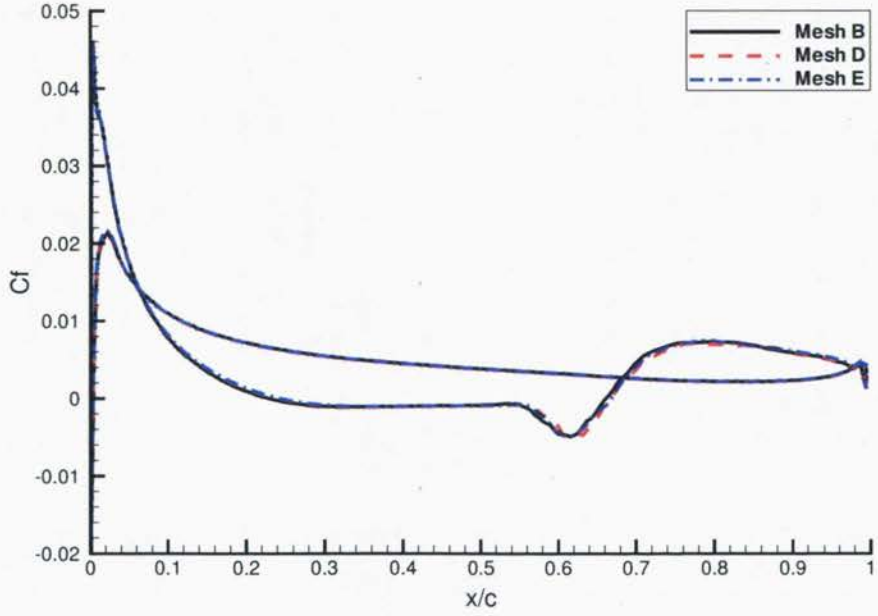

(b) Mean C_f coefficient

Figure 4.16: Comparison of streamwise and wall-normal grid resolution.

the 2-D simulation. Additionally, the skin friction coefficient from the 2-D solution does not rise to the same level as the 3-D solution downstream of the reattachment location as seen on Fig. 4.17. The most notable difference can be observed in contours of instantaneous spanwise vorticity. In the 2-D solution, the shear layer rolls up into a coherent vortex that does not diminish significantly as it travels towards the trailing edge. It is evident that the 2-D simulation restricts the decay of the vortex and the breakdown into fine-scale turbulence due to the lack of spanwise instabilities and vortex stretching. This preserved coherence of large 2-D structures has an impact on the amplitudes of the lift and drag coefficients. In the 2-D simulations, the fluctuations of the coefficients are much more important than in the 3-D case.

In the three-dimensional computations, spanwise periodic boundary conditions are used to represent a wing of infinite span. It is therefore important to choose an adequate spanwise extent since a span too short would constrain the flow structure and limit the free development of flow structures. On the other hand, a large span size would require a larger mesh size and hence a longer computation time. Spanwise domains of both $0.1c$ and $0.2c$ were tested. These were chosen based on the study of Galbraith [16] which showed that this domain size was sufficient to allow the appearance of three-dimensional flow structures while maintaining a reasonable computational cost (Galbraith [16] tested up to $AR = 0.3$ and Almutairi *et al.* [2] up to $AR = 0.5$). Similar conclusions are drawn here, as calculations with both domains produced very close results as shown in Fig. 4.19 showing the surface pressure and skin friction distributions for both calculations. To reduce computational time, the spanwise extent of $0.1c$ was used in most of this study. However, it is not a certainty that long-wavelength spanwise could not play an important role in this case. It is not impossible that a much larger spanwise domain would give different results.

Influence of SGS model

In this study, both the Mixed-Time-Scale (MTS) and the Wall Adapting Local Eddy viscosity (WALE) subgrid scale models have been used. Simulations were also realized without a subgrid scale model (implicit LES, ILES approach). Distribution of surface pressure and skin friction are presented in Fig. 4.20 and contours of Reynolds shear stresses are shown in Fig. 4.21. The differences in results obtained with both models as well as without any model are minor. While the MTS model was chosen for subsequent computations, there does not appear to be a need for an SGS model in the present case.

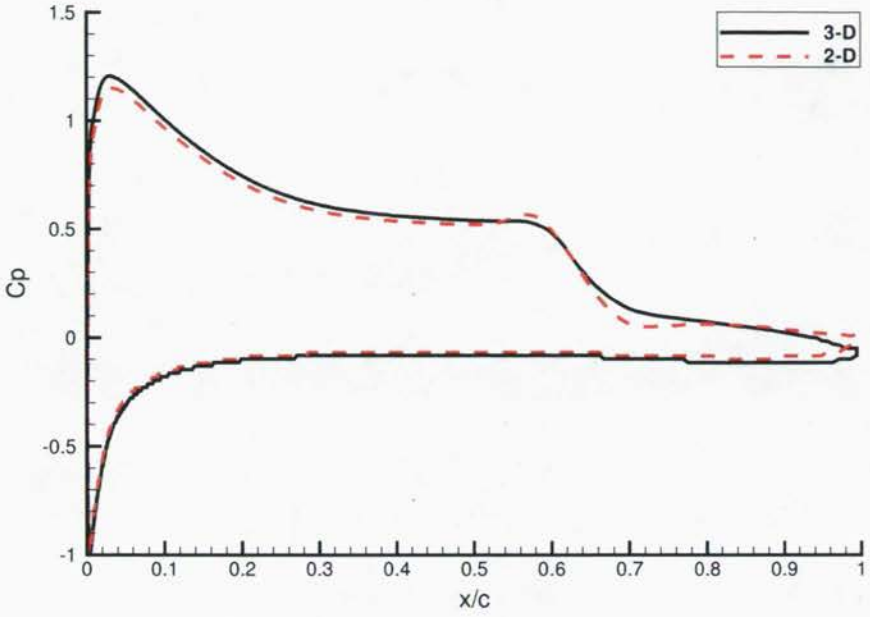

(a) Mean C_p coefficient

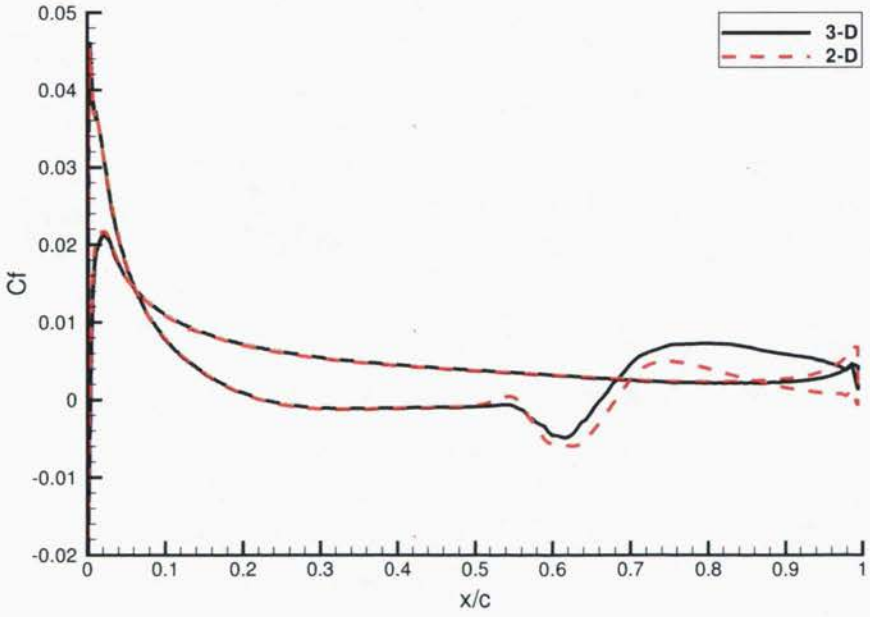

(b) Mean C_f coefficient

Figure 4.17: Comparison of spatial dimensionality.

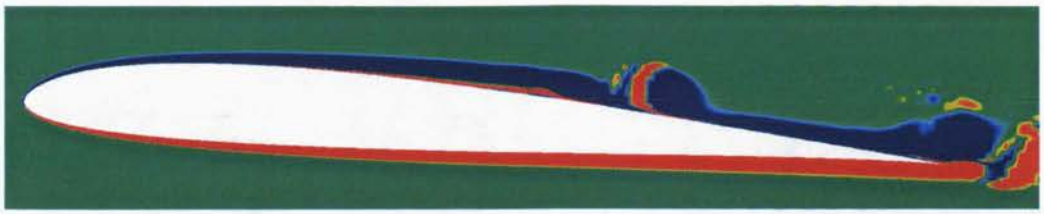

(a) 2-D

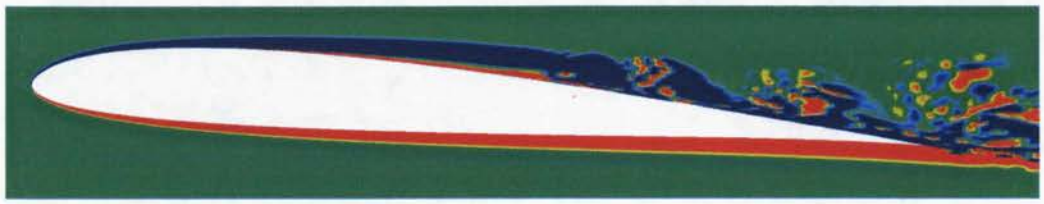

(b) 3-D

Figure 4.18: Comparison of instantaneous spanwise vorticity contours.

Influence of time discretization and simulation length

In order to assess the influence of the time discretization, non-dimensional time steps of $\Delta t^* = 2 \times 10^{-4}$ and $\Delta t^* = 1 \times 10^{-4}$ were used, leading to maximum CFL number of ~ 0.5 and ~ 0.25 respectively. No noticeable differences were observed in the instataneous flow fields and averaged quantities. Using coarser timesteps leading to CFL numbers greater than 1 negatively affected convergence.

Mean values were calculated by averaging the solution over a non-dimensional time interval of at least 10 convective units. This averaging process was started when the flow achieved a certain periodicity in order to eliminate the effect of initial transients.

4.3.3 Comparison with experimental and numerical results

Fig. 4.22 and Fig. 4.23 present the comparison of pressure coefficient and skin friction coefficient distributions of the current study with the numerical results of Visbal, Uranga and Castonguay. Discrepancies between the different distributions are small, despite the different mesh resolutions and numerical methods used. A comparison of separation, transition and reattachment positions measured from the two experimental facilities as well as numerical studies is presented in Table 4.2.

In this work as well as in other studies, the location of the separation point is taken as the

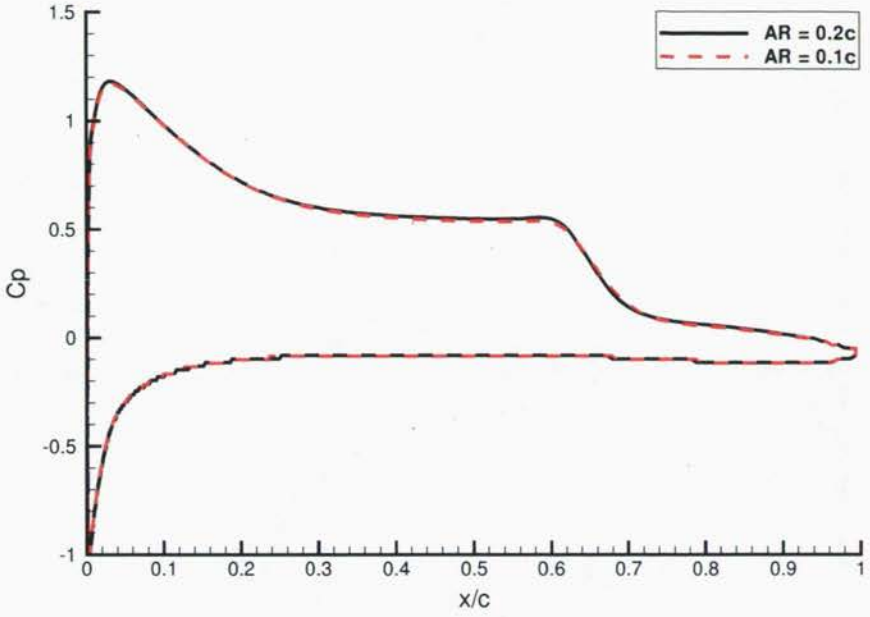

(a) Mean C_p coefficient

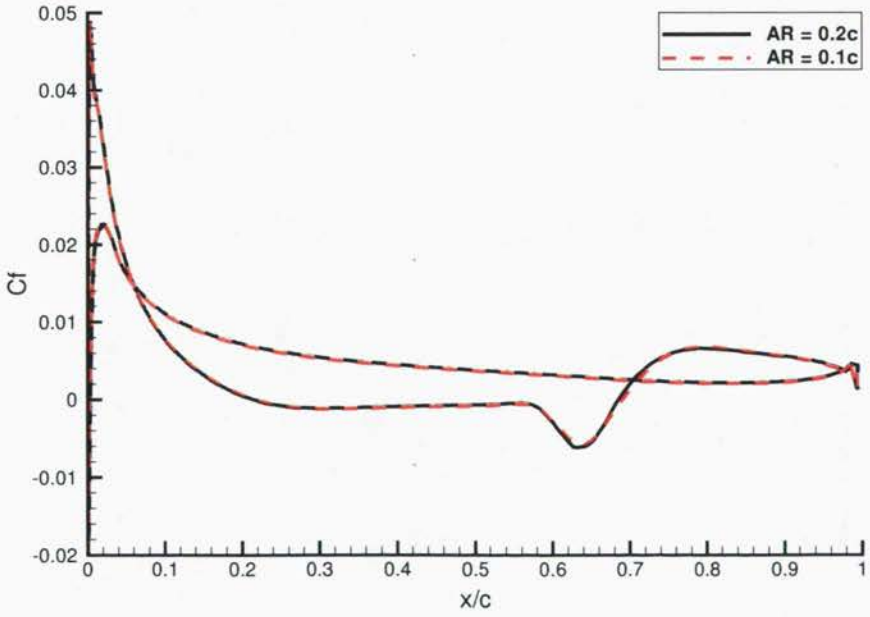

(b) Mean C_f coefficient

Figure 4.19: Comparison of spanwise domain sizes.

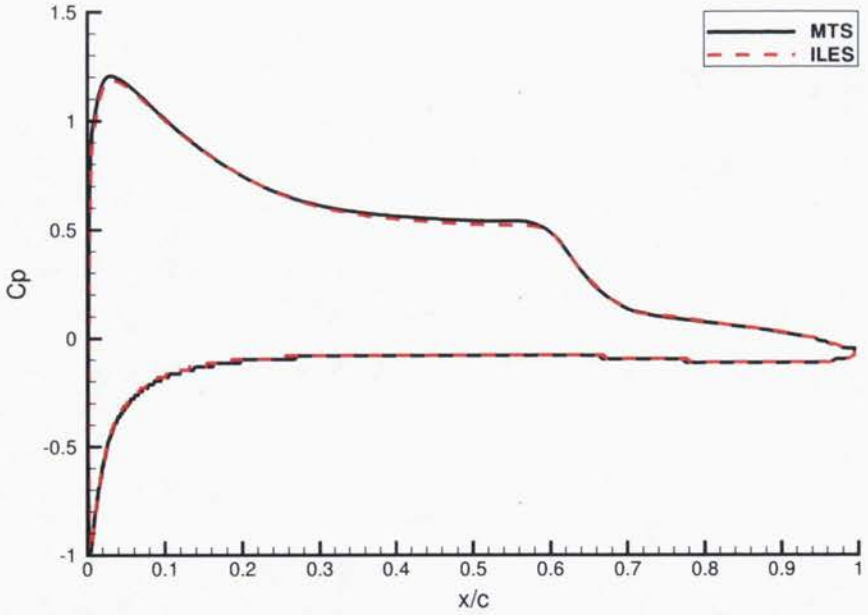

(a) Mean C_p coefficient

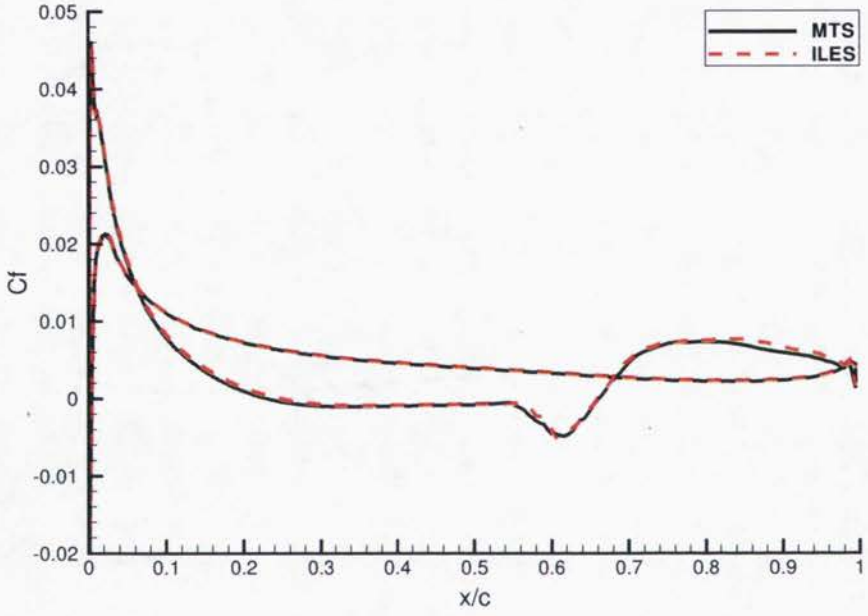

(b) Mean C_f coefficient

Figure 4.20: Comparison of subgrid scale models.

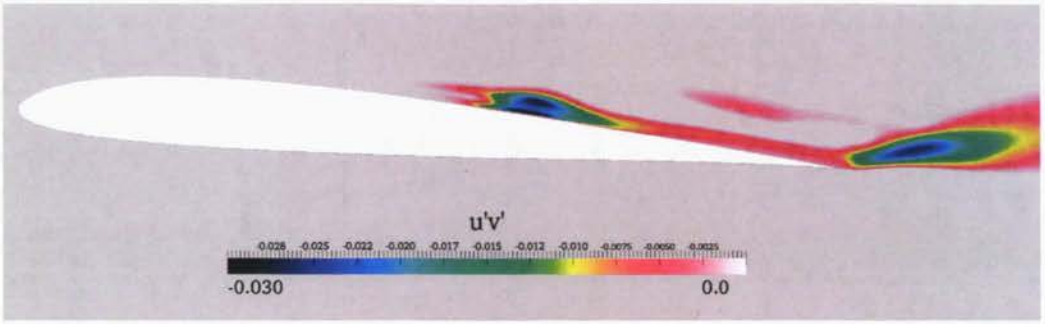

(a) MTS model

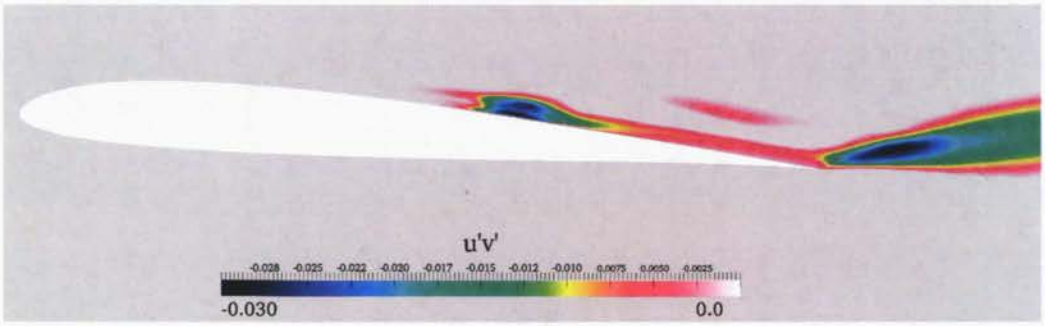

(b) WALE model

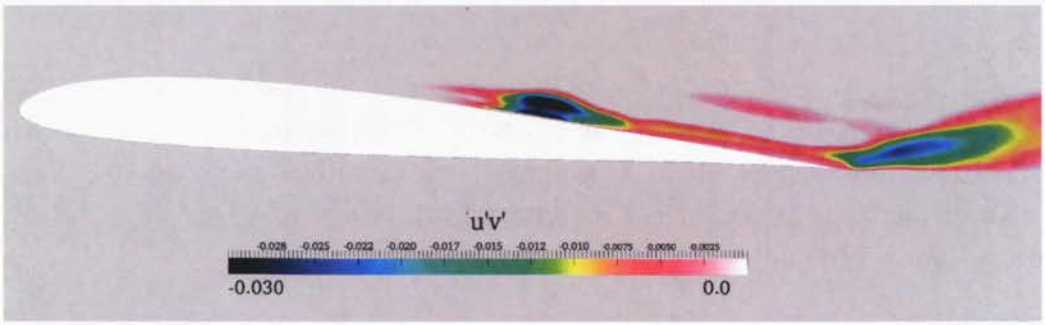

(c) No model (ILES)

Figure 4.21: Comparison of time-averaged Reynolds stresses.

point where the skin friction coefficient vanishes ($C_f = 0$) in conjunction with a plateau in the pressure coefficient distribution following a region of adverse pressure gradient. The criterion used to define the reattachment point is where the friction coefficient becomes positive and stays positive. The transition location was determined from the normalized Reynolds shear stress ($-\overline{u'v'}/U_\infty^2$) accumulated in the calculations. To allow for quantitative comparisons with the other studies, the transition location is assumed to correspond to the point where a value of $-\overline{u'v'}/U_\infty^2 > 0.1\%$ is observed along with a subsequent important rise of the Reynolds stresses.

The position of separation predicted by the current LES calculations is in between the two

Table 4.2: Measured and computed LSB properties at $\alpha = 4^{\circ}$, Re = 6×10^4.

Data Set	Freestream Turbulence [%]	Separation x_{sep}/c	Transition x_{tr}/c	Reattachment x_r/c
TU-BS [66]	0.08	0.3	0.53	0.64
HFWT [53]	0.1	0.18	0.47	0.58
Yuan SGS-LES [93]	0.1,N=8	0.21	0.49	0.60
Yuan RANS-e^N [93]	0.1,N=8	0.21	0.49	0.58
Visbal (ILES) [87]	0	0.23	0.55	0.65
Uranga (ILES) [84]	0	0.21	0.53	0.67
Castonguay (ILES) [6]	0	0.23	0.52	0.65
Present (LES)	0	0.23	0.55	0.66

experimental measurements and is in excellent agreement with all other numerical results. There is also very little difference in the prediction of both the transition and reattachment locations.

Figure 4.24 presents the time-averaged spanwise vorticity contours around the SD7003 airfoil obtained from a simulation with an aspect ratio of 0.1 and the MTS SGS model. These contours allow to see clearly the LSB as the region of positive vorticity on the upper side of the airfoil although the instantaneous vorticity field seen previously in Fig. 4.18b showed important vortex shedding.

Figure 4.25 presents the time-averaged Reynolds stress contours. A significant rise of the Reynolds stresses is noticeable close to the aft part of the laminar separation bubble, corresponding to the transition point mentionned previously.

Figure 4.26 shows the time-averaged subgrid-scale viscosity ratio contours. This underlines the low levels of subgrid-scale viscosity, remaining significantly lower than the molecular viscosity. This observation goes a long way to explain the absence of differences with simulations that did not use a subgrid-scale model. At the current Reynolds number, the mesh is probably fine enough to resolve almost all length scales (DNS type of simulation) and thus the SGS model is obsolete.

Figure 4.27 presents the instantaneous iso-surfaces of Q-criterion for a value of $Q = 500$ coloured by the Reynolds stress. This highlights the presence of small three-dimensional vortical structures following the transition to turbulence of the separated shear layer.

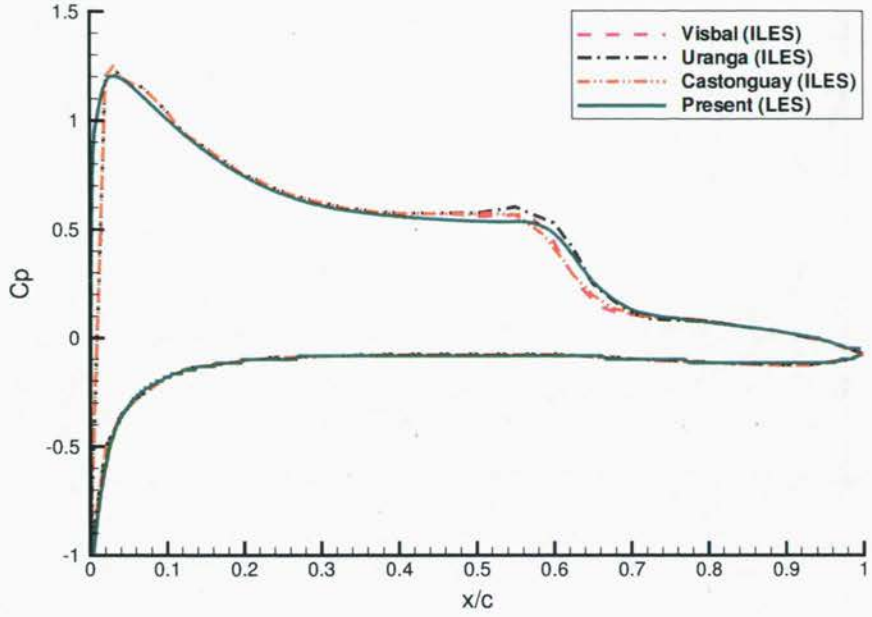

(a) Mean C_p coefficient

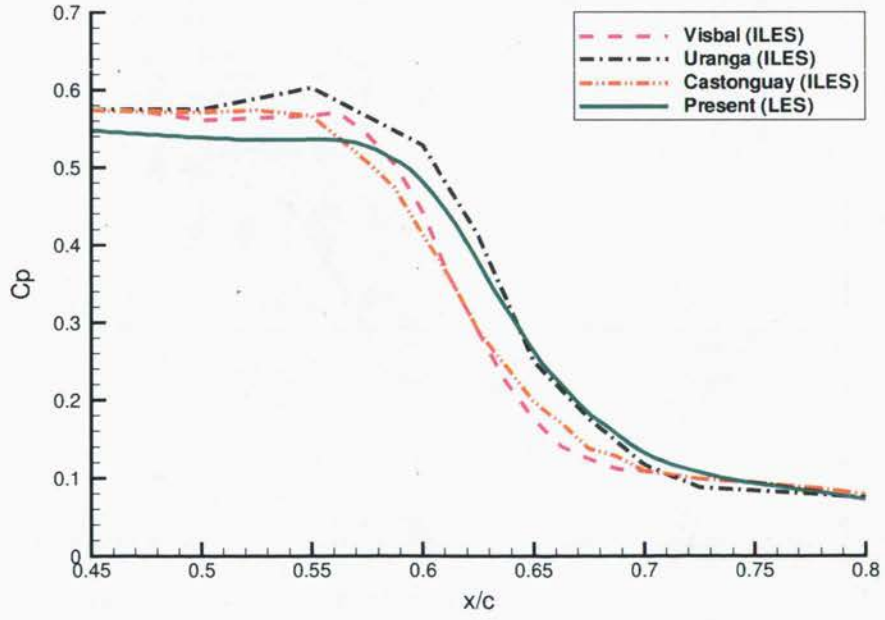

(b) Mean C_p coefficient, zoomed in

Figure 4.22: Comparison of pressure coefficient distributions.

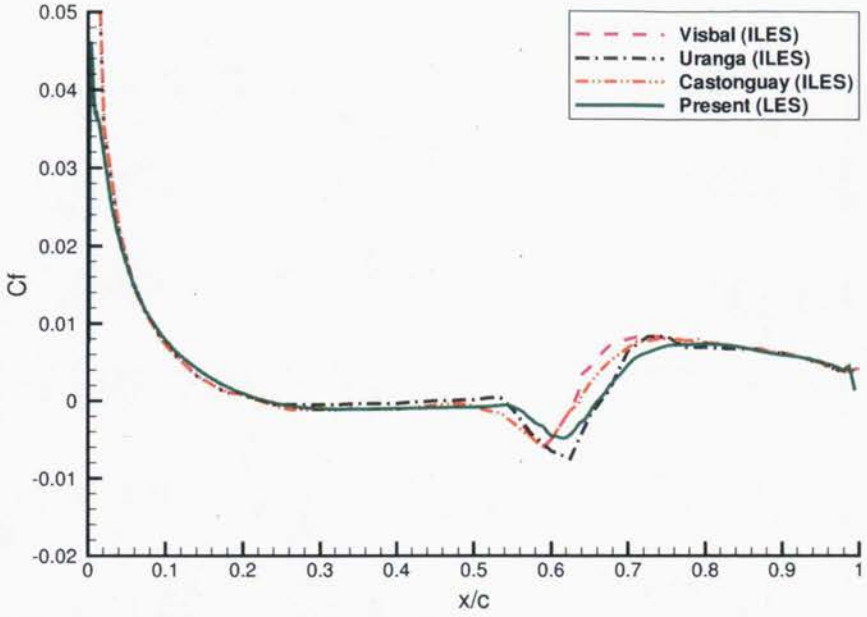

(a) Mean C_f coefficient

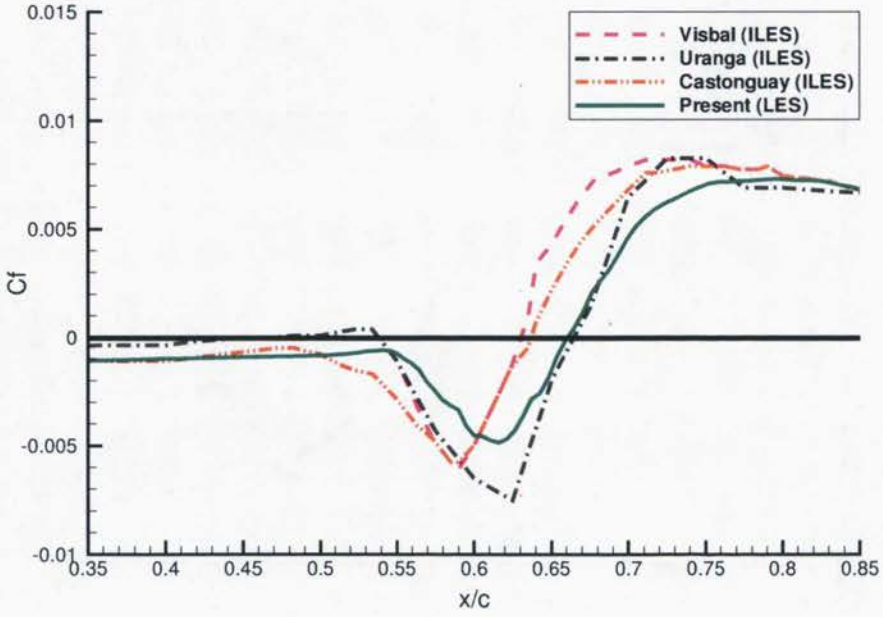

(b) Mean C_f coefficient, zoomed in

Figure 4.23: Comparison of skin friction coefficient distributions.

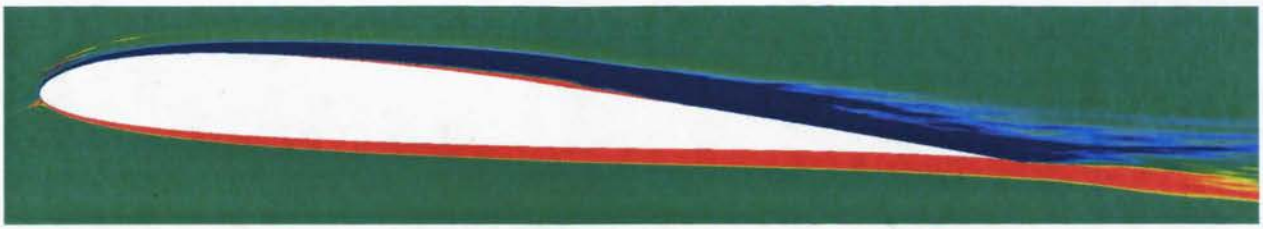

Figure 4.24: Time-averaged spanwise vorticity contours around SD7003 airfoil.

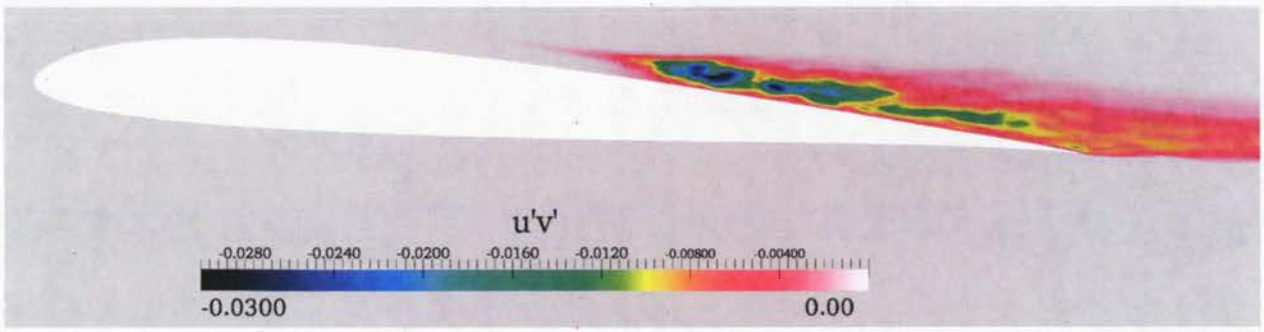

Figure 4.25: Time-averaged Reynolds stress contours around SD7003 airfoil.

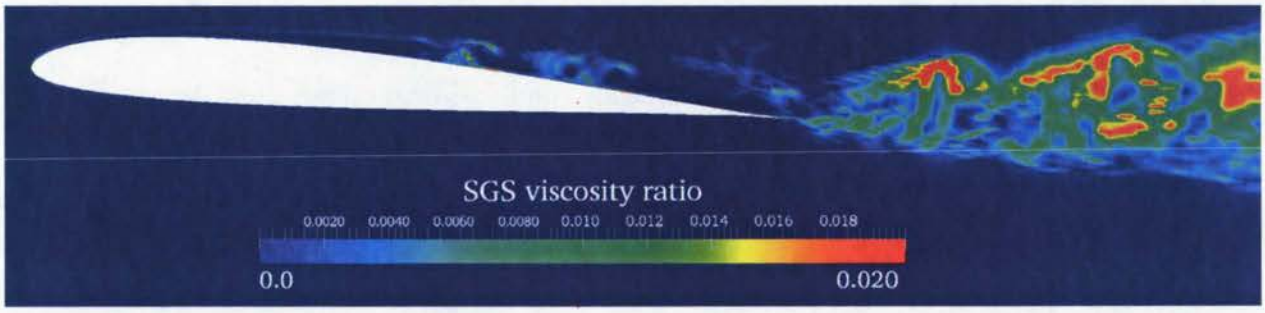

Figure 4.26: Time-averaged subgrid-scale viscosity ratio contours around SD7003 airfoil.

4.3.4 Comparison with RANS results

The test case of the SD7003 airfoil at $\mathrm{Re_c} = 60000$ was also computed using RANS models to compare with the previous results. To begin with, steady simulations were performed with both traditional RANS models (Spalart-Allmaras and $k-\omega$ SST) and the $\gamma - \mathrm{Re}_\theta$ transition model. The solutions with the S-A and $k-\omega$ SST models do not predict a laminar separation bubble. They show attached boundary layers over the whole airfoil. The steady simulation with the $\gamma - \mathrm{Re}_\theta$ model does not converge.

Unsteady simulations were also performed with the same three turbulence models using a non-dimensional time step of $\Delta t^* = 1 \times 10^{-3}$. With the S-A and $k-\omega$ SST models, there

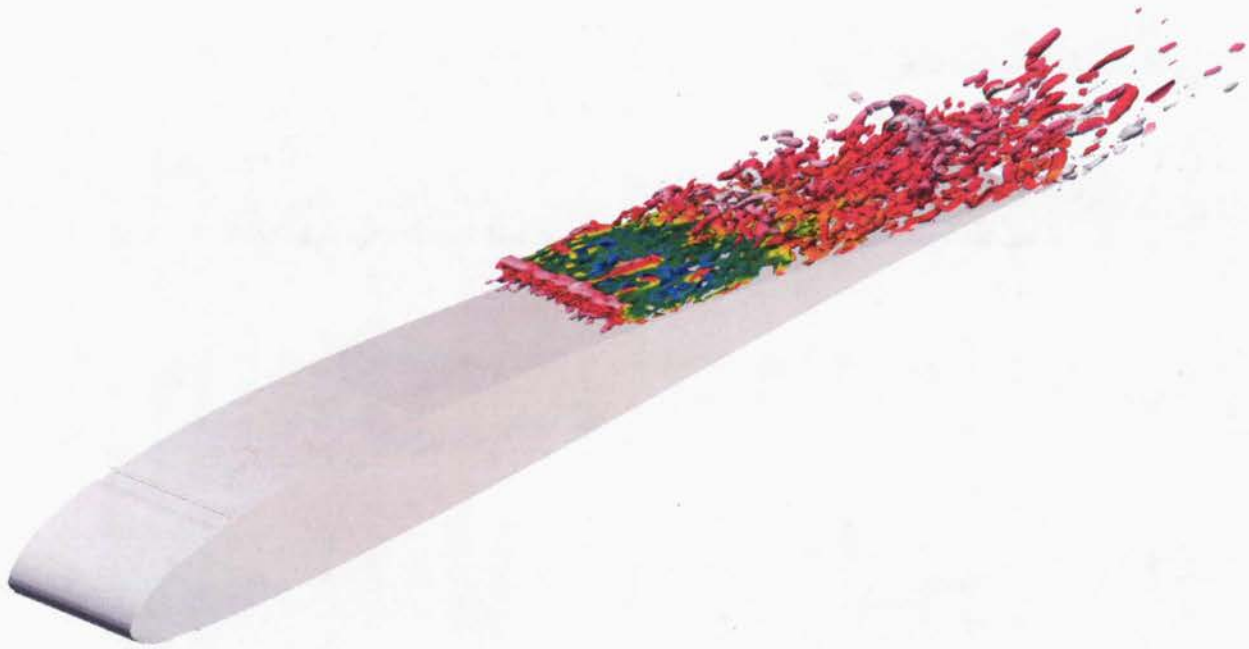

Figure 4.27: Instantaneous iso-surfaces of Q-criterion in the LES simulation around the SD7003 airfoil at Re = 60,000.

is no difference between the steady and unsteady solutions, both do not show the presence of a LSB. However, unsteady simulations with the $\gamma - \mathrm{Re}_\theta$ model capture the presence of a laminar separation bubble. The comparison between URANS and LES surface pressure and skin friction coefficients distributions are shown in Fig. 4.28. The distributions are similar but the URANS solution is characterized by a pressure increase towards the end of the LSB. This spike at the end of the pressure plateau, present in 2D URANS and quasi-3D LES simulations, was also reported by Jones 2D-DNS [26] and is in accordance with the observation of Ripley and Pauley [69]. The pressure spike corresponds to the position of the counter-rotating vortex. Its absence in 3D LES and DNS simulations is probably due to the breakdown of this vortex into fine-scale turbulent structures.

Figure 4.29 presents the time-averaged spanwise vorticity contours around the SD7003 airfoil from the 2D URANS simulation with the transition model. These contours are similar to those from the LES simulations and allow to see clearly the LSB as the region of positive vorticity on the upper side of the airfoil.

Figure 4.30 presents the time-averaged Reynolds stress contours. As in the LES simulations, there is a significant rise of the Reynolds stresses due to the transition in the laminar separation bubble. The levels are not identical to those obtained in LES but are of the same order of magnitude.

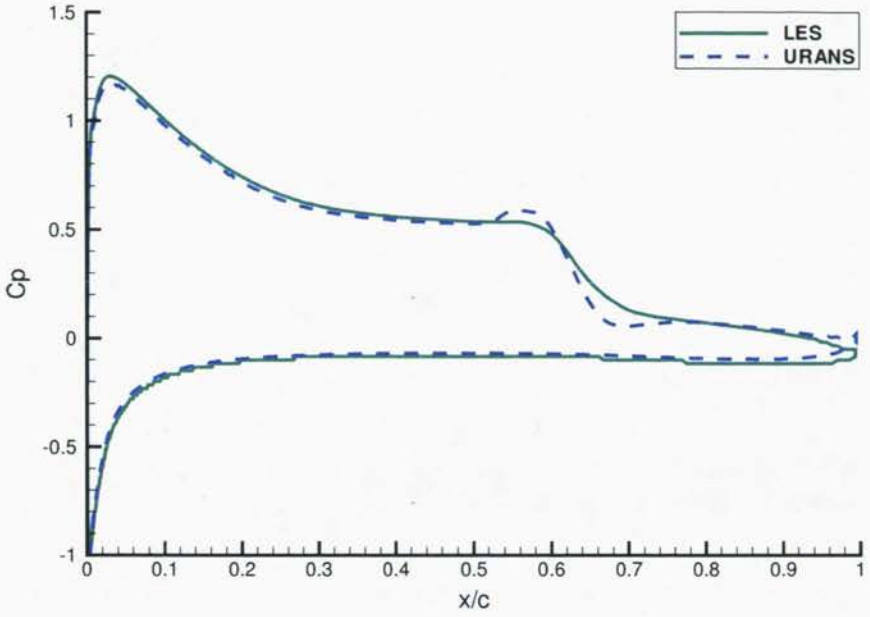

(a) Mean C_p coefficient

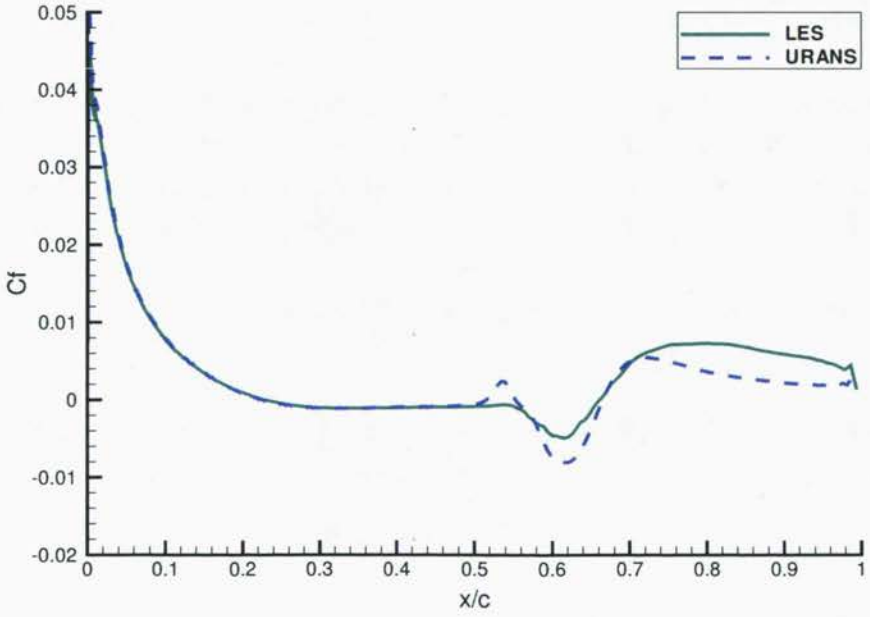

(b) Mean C_f coefficient

Figure 4.28: Comparison of surface pressure and skin friction coefficient distributions.

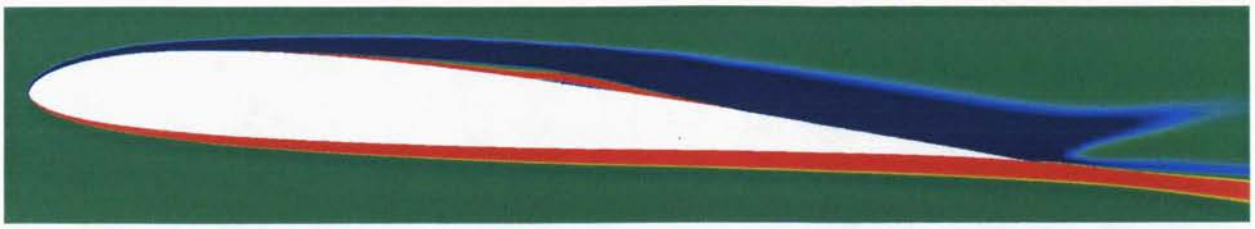

Figure 4.29: Time-averaged spanwise vorticity contours around SD7003 airfoil (URANS).

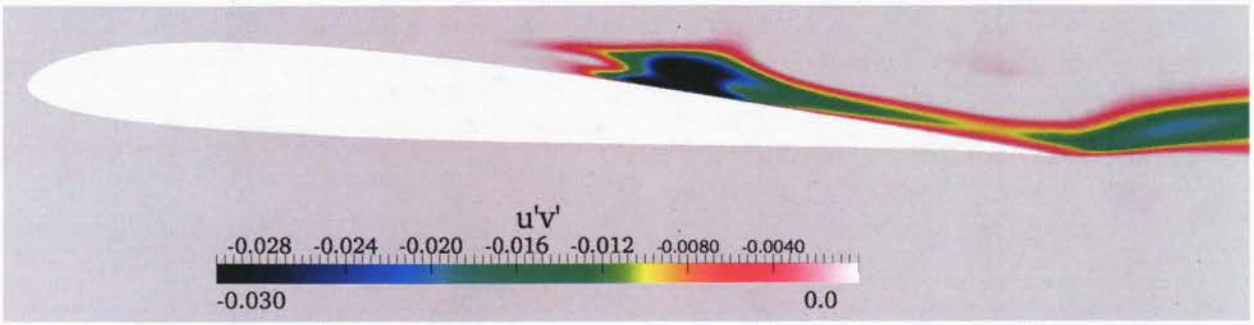

Figure 4.30: Time-averaged Reynolds stress contours around SD7003 airfoil (URANS).

Three-dimensional computations were also performed using the transition model in both URANS and DDES formulations. For those simulations, the 2D grid was extruded to a spanwise extent of $0.2c$ with 32 cells in this direction. The same time step of $\Delta t^* = 1 \times 10^{-3}$ was used. Flowfields obtained in URANS and DES are very similar, almost identical to those of the 2D URANS simulations. The DDES formulation with the F_2 blending function assures that the boundary layer is treated by RANS modeling. Since there is no important region of separated flow, the DES approach does not bring any significant improvement to URANS in this case. There are some vortical structures highlighted by the Q-criterion (iso-surface at $Q = 500$, as shown in Fig. 4.31, but the flow remains essentially two-dimensional. Thus, the superior computational cost associated with the use of DES is not justified for the simulation of airfoils at small angles of attack ($\sim$ 5 degrees) in transitional flows.

In summary, the best approach in terms of accuracy would be the ILES, i.e. a 3D unsteady simulation with no explicit turbulence modeling. The 2D URANS simulations with a transition model do produce very adequate result at a low computational cost.

4.4 Fluid-Structure interaction

In order to validate the coupling between the fluid flow and dynamics of the body, a simple test case was chosen. The oscillating cylinder with one degree of freedom is a classical case

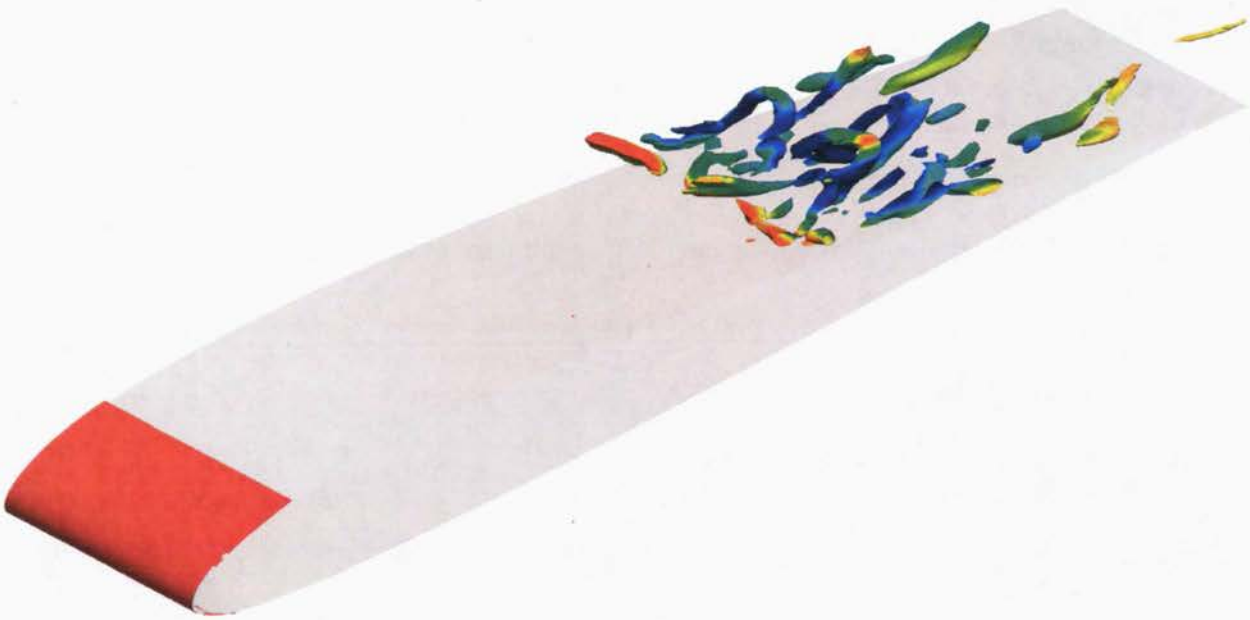

Figure 4.31: Instantaneous iso-surfaces of Q-criterion ($Q = 500$) in the DES simulation around SD7003 airfoil at Re = 60,000.

of FSI. It consists of an elastically-mounted cylinder on a vertical support, free to move in the direction perpendicular to the flow, as shown in Fig. 4.32. The oscillations are produced by the alternating vortex shedding in the wake of the cylinder, hence the name of Vortex Induced Vibrations (VIV) for this phenomenon.

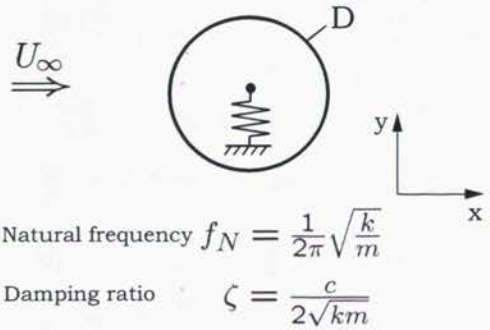

Figure 4.32: Setup of the oscillating cylinder from [47].

In *OpenFOAM*, the FSI simulation is realized by coupling the equation of motion in the y direction to the Navier-Stokes equations. The equation of motion of the spring-mass-dampener system is given by:

$$m\,\ddot{y}_c(t) + c\,\dot{y}_c(t) + k\,y_c(t) = F_y(t), \tag{4.4}$$

where m is the mass of the cylinder for a unit depth, c is the damping coefficent of the support and k is the stiffness. The position, speed and acceleration of the center of mass of the cylinder are given by y_c, $\dot{y}_c$ and $\ddot{y}_c$ respectively. The vertical force exerted by the fluid on the unit length cylinder is labelled F_y.

This problem is typically defined in a non-dimensionnal form by a mass ratio m^*, a reduced speed U^* and a damping coefficient ζ. The natural frequency of the mechanical system is given by:

$$f_N = \frac{1}{2\pi}\sqrt{\frac{k}{m}}\,. \tag{4.5}$$

The damping coefficient ζ is defined as:

$$\zeta = \frac{c}{2\sqrt{km}}\,. \tag{4.6}$$

The reduced speed is obtained by normalizing the speed of the flow U_∞ with the natural frequency and the diameter of the cylinder D:

$$U^* = \frac{U_\infty}{f_N D}\,, \tag{4.7}$$

and, finally, the mass ratio m^* is given by the ratio of the solid's density to the fluid's density:

$$m^* = \frac{\rho_s}{\rho_f}\,. \tag{4.8}$$

Considering a non-dimensional amplitude $y^* = y_c/D$, the equation of motion takes the following form:

$$\ddot{y}^* + 2\zeta\left(\frac{2\pi}{U^*}\right)\dot{y}^* + \left(\frac{2\pi}{U^*}\right)y^* = \frac{2}{\pi m^*}C_Y\,, \tag{4.9}$$

where the vertical force is expressed by the lift coefficient $C_Y = 2F_y/\rho_f U_\infty^2 Ds$ where $s = 1$.

Table 4.3 presents the physical parameters necessary to define the case studied here. These parameters lead to a lock-in regime. Namely, the oscillations reach a periodic response characterized by constant amplitudes and frequencies. They were chosen to allow a comparison with the numerical results of Yang *et al.* [92] and Leontini [35] and the previous validation of Morissette [46] and Morissette *et al.* [47] in our group. Yang *et al.*used a strongly coupled approach where an embedded-boundary method for the fluid was coupled to the dynamical equation, solved together at each timestep. Leontini used a spectral method coupled to the harmonical equation of the cylinder. Morissette *et al.*used both an in-house lagrangian vortex method and the commercial software *Fluent 6.3*.

Table 4.3: Parameters defining the VIV case.

Variable	Symbol	Value
Reynolds number	Re	200
Mass ratio	m^*	10
Damping coefficient	ζ	0.01
Reduced speed	U^*	4.5

The Reynolds number is based on the cylinder's diameter and the speed of the incoming flow, $\mathrm{Re} = \frac{U_\infty D}{\nu}$.

Simulations were done with a non-dimensionnal timestep of $\Delta t U_\infty / D = 0.005$ (the same as used in vortex and *Fluent* simulations [46, 47]) on a grid of approximately 55,000 cells. An accelerated heaving reference frame was used in order to solve in the referential of the motion of the cylinder as discussed in section 3.3.2.

In both the present simulations and those of Morissette, an initial perturbation was introduced to accelerate the appearance of the oscillations. The comparison of the vertical displacement of the cylinder obtained by the three methods is shown in Fig. 4.33. We see that the results are extremely close for both the amplitude and the frequency of the motion.

Table 4.4 presents a comparison of the maximum amplitude and lift coefficient as well as reduced frequency (compared to the f_N) obtained in the simulation with the results of Morissette [46], Leontini *et al.* [35] and Yang *et al.* [92]. Again, the results are in good agreement with previously published data, which confirms that the present fluid-structure interaction algorithm has been implemented correctly in *OpenFOAM*.

Table 4.4: Results - VIV of a cylinder at $U^* = 4.5$.

Results	A^*_{max}	$C_{L\,max}$	f^*
OpenFOAM	0.50	2.22	0.96
Vortex method	0.49	2.22	0.95
Fluent	0.49	1.90	0.96
Leontini 2006	0.47	2.37	0.95
Yang *et al.* 2008	0.42	2.25	0.95

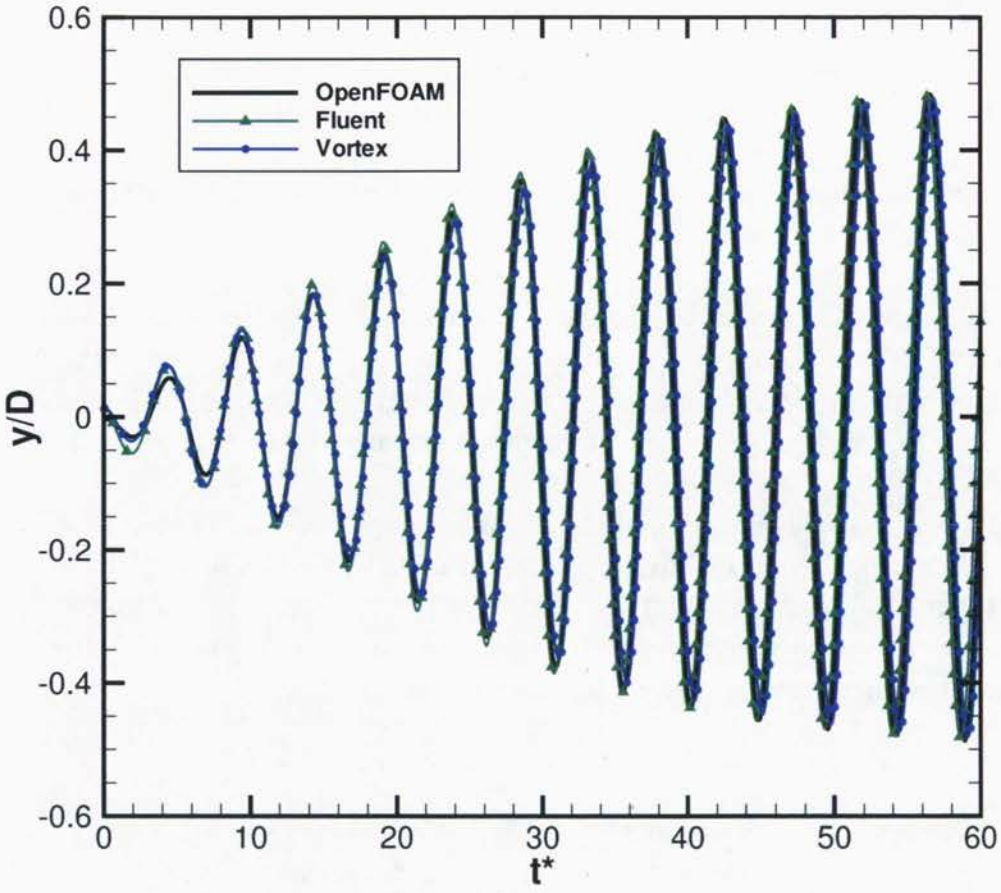

Figure 4.33: Comparison between the present *OpenFOAM* simulation and the results of [46, 47] for the vertical displacement of the cylinder at $U^* = 4.5$.

Chapter 5

NACA0012 pitch oscillations

5.1 2D simulations

5.1.1 Mesh and time discretization

Unless noted otherwise, a timestep of $\Delta t = 2\times10^{-5}$ sec ($\Delta t^* = 6\times10^{-4}$ to 2×10^{-3} depending on airspeed) has been used. This allows for about 15,000 timesteps per aeroelastic oscillation and 200 timesteps per vortex shedding period. An RMS convergence criterion of 10^{-6} on all quantities is requested at each timestep. Timestep and convergence level independence studies have shown that using a finer timestep of $\Delta t = 1\times10^{-5}$ sec or reaching a convergence level of 10^{-7} did not change the results.

All simulations of pitch-only oscillations were started with unperturbed initial conditions, namely $\theta = 0$ deg and $\dot{\theta} = 0$ deg/sec. Pitch oscillations thus develop freely in the simulations through a symmetry breaking mechanism in the flow field. In most simulations, this mechanism quickly kicks in after a transient period of approximately 1 sec as can be seen in the example of Fig. 5.2a. Fairly periodic oscillation cycles are then observed and several such periodic cycles (more than 25) are computed to allow for the production of good, stationary statistics and spectral analysis. The typical run time for a whole simulation requires about two weeks on four Intel Xeon X5560 2.8 Ghz processors.

The mesh used for these simulations was shown previously in Fig. 3.4. Constant and uniform velocity is imposed at the inlet ($50c$ upstream of the airfoil) while constant static pressure is imposed at the outlet. The inlet freestream turbulence intensity level is set to obtain $Tu \sim 0.15\%$ at the airfoil when taking into account freestream decay, a level similar

Table 5.1: Lift, drag and moment convergence according to wall-normal boundary layer resolution, $\mathrm{Re}_c = 128,000$ and $\alpha = 5$ deg.

Mesh	y^+	C_L	(%)	C_D	(%)	C_M	(%)
Coarse	~ 2	0.4982	0.79	0.01643	0.54	0.02431	6.14
Baseline	~ 0.9	0.5028	0.12	0.01632	1.21	0.02528	2.39
Fine	~ 0.4	0.5022	-	0.01652	-	0.02590	-

Table 5.2: Lift, drag and moment convergence according to streamwise boundary layer resolution, $\mathrm{Re}_c = 128,000$ and $\alpha = 5$ deg.

Mesh	N_{foil}	C_L	(%)	C_D	(%)	C_M	(%)
Coarse	170	0.4908	1.90	0.01646	0.30	0.02135	12.39
Baseline	320	0.5028	0.49	0.01632	0.55	0.02528	3.73
Fine	450	0.5004	-	0.01641	-	0.02437	-

to the experiments [61]. Far above and below the wing section, slip boundary conditions are used (symmetry plane). Adequate near-body resolution (320 cells on both the upper and lower surfaces) is used to capture accurately the vorticity gradients and to satisfy the transition model requirement for the first cell thickness, namely $y^+ \leq 1$ on the airfoil surface over the whole cycle [32].

Table 5.1 summarizes the results of the lift, drag and moment coefficients for each tested mesh in the case of a NACA0012 at $\mathrm{Re}_c = 128,000$ held at a fixed angle of attack of $\alpha = 5$ deg. Three different wall-normal resolutions are tested while maintaining the mesh structure and number of cells (320) in the streamwise direction. There is no significant differences on the lift and drag coefficients, but a difference of 6% is observed on the moment coefficient of the coarser mesh. This is not negligible because the moment coefficient prediction needs to be accurate since it will directly influence the pitching motion. The influence of the streamwise resolution has been investigated also and results are reported in Table 5.2. N_{foil} indicates the number of cells on one side of the airfoil (both the upper and lower side are identical). The wall-normal resolution is the same on all meshes, resulting in $y^+ \sim 0.9$. Once again, the differences on the lift and drag coefficients are rather small. However, there is a 12% difference on the moment coefficient of the coarser mesh. This is due to the poor capture of the shed vortices with this resolution. To make sure the baseline mesh was sufficient, aeroelastic simulations of the free-pitching airfoil were performed at a few Reynolds numbers and the predicted amplitudes and frequencies were almost identical to those obtained with the baseline mesh.

Table 5.3: Aeroelastic parameters used in the computations.

I_{axis}	0.0014 kg·m^2
D_θ	0.002 N·s/rad
K_θ	0.3 N/rad
x_{EA}	0.186c
c	0.156 m

5.1.2 Aeroelastic characteristics

Simulations were performed at twelve different Reynolds numbers corresponding to wind tunnel freestream velocities of $U_\infty = 5$ to $U_\infty = 16$ m/s using the same parameters as in the experiments [61] as shown in Table 5.3. Experimentally, it was found that no oscillations appeared below $\mathrm{Re}_c \approx 55,000$ and above $\mathrm{Re}_c \approx 140,000$. In the present numerical simulations, oscillations start to appear at $\mathrm{Re}_c = 64,000$ and are observed up to $\mathrm{Re}_c = 150,000$. At $\mathrm{Re}_c = 160,000$ and above no significant oscillations are present. If any, they are of very small amplitudes ($\theta_{max} \sim 0.1$ deg). Figure 5.1 presents the comparison of pitching amplitudes and frequencies between the wind tunnel experiments [61], the URANS aeroelastic simulations of Poirel *et al.* [62] and the numerical simulations of the current study. The results obtained with the transition model are in good agreement with the experimental results, taking into account a margin of error for the experimental results of ±0.2 deg at $\mathrm{Re}_c \leq 85,000$ and ±0.3 at $\mathrm{Re}_c \geq 85,000$ deg [61]. The calculted oscillation amplitudes and frequencies follow the trend of the experimental results, exhibiting increasing amplitudes from $\mathrm{Re}_c = 60,000$ to 85,000, and then decreasing amplitudes from $\mathrm{Re}_c = 95,000$ to 130,000.

The match with experimental results has been improved with the previous simulations compared to previous computations using the SST $k-\omega$ model with the low-Reynolds correction option activated (with the default value of $R_k = 6$ and a modified value of $R_k = 1$) as well as computations with no turbulence model (labelled as "laminar"). The simulations with the SST $k-\omega$ model ($R_k = 6$) captured the main physical features but failed to follow the trend of the experimental results at larger Reynolds numbers. Predictions were good at lower Reynolds numbers, but at $\mathrm{Re}_c = 95,000$ and higher they didn't reproduce the reduction of oscillation amplitudes. Changing the R_k constant from its default value of 6 to a lower value of 1 had for effect to improve the match with experimental results, while still overpredicting the amplitudes at higher Re numbers. Surprisingly, laminar computations carried out on the same mesh as the RANS simulations predict quite well the decreasing amplitudes but in a slightly less important fashion than with the $\gamma - \mathrm{Re}_\theta$ transition model. This similarity between laminar and transitional simulations is due to the low level of turbulent viscosity, as shown later in Fig. 5.8.

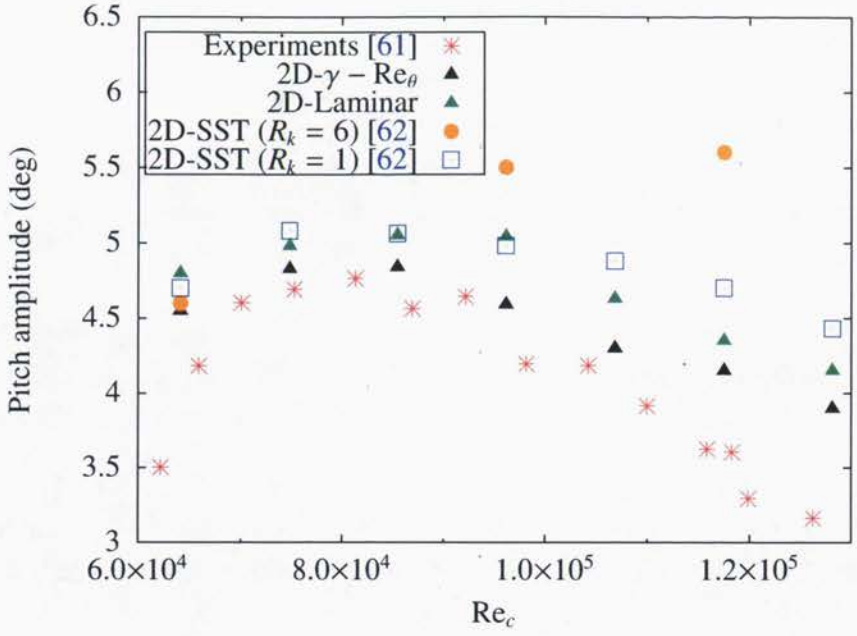

(a) Amplitudes

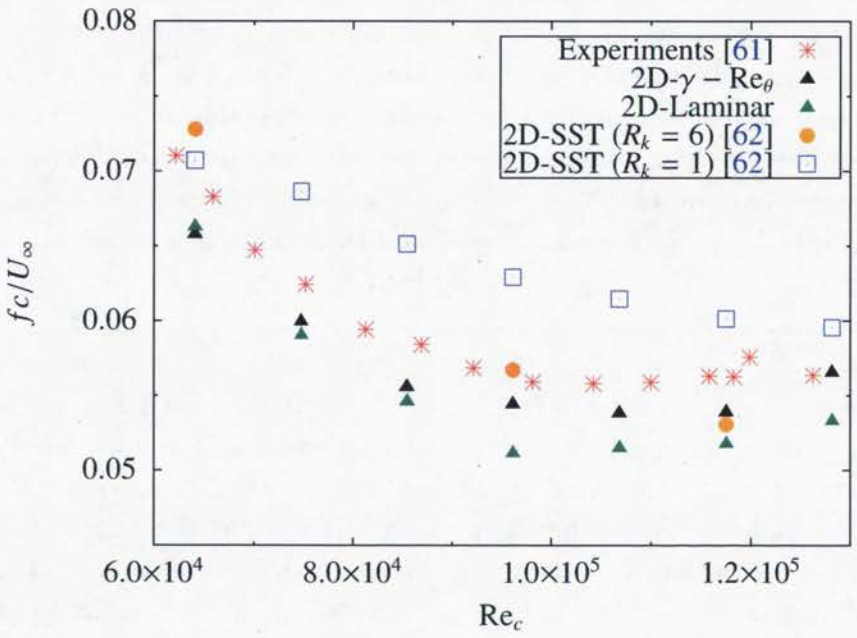

(b) Frequencies

Figure 5.1: Comparison of self-sustained oscillations characteristics from numerical simulations and experiments.

Figure 5.2 shows the pitch history and the phase plane resulting of a typical run. After a short transient period, oscillations of rather constant amplitude and speed appear. The small ripples in the phase plane are caused by the high frequency flow instabilities (Kelvin-

Helmholtz), as illustrated later in Fig. 5.7. Figure 5.3 shows the PSD of the pitch response and aerodynamic moment coefficient. With regard to the response of the wing to von Kármán vortex shedding, the pitch is not significantly influenced by this high frequency forcing which occurs at approximately 200 Hz. The frequency content of the aerodynamic moment coefficient, shown in Fig. 5.3b, displays a strong 3f super-harmonic. There is also an important energy content at higher frequencies in the vicinity of 200 Hz. This is due to the presence of the wake vortices. The wide range of the associated energy peak is caused by the non-stationary nature of the vortex shedding, since the shedding frequency varies with angle of attack.

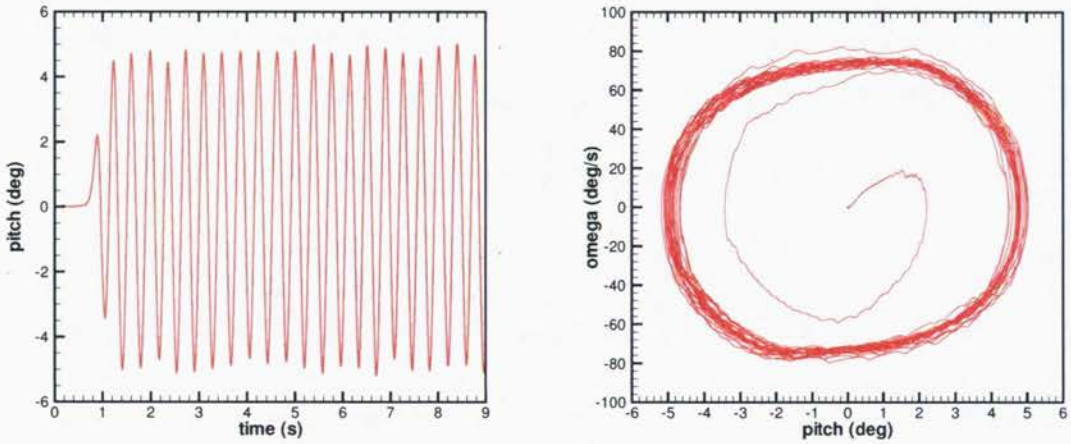

(a) Pitch history

(b) Phase plane

Figure 5.2: Airfoil pitching amplitude and speed over the whole run at $\mathrm{Re}_c = 75,000$ (model $\gamma - \mathrm{Re}_\theta$).

Figure 5.4 presents the aerodynamic moment coefficient along with the pitch response for one cycle of oscillation at three different Reynolds numbers. The important fluctuations of the moment coefficient are caused by the high-frequency flow instabilities mentionned earlier. Also shown on the figure is the filtered moment coefficient with a low-band-pass filter at a cut-off frequency of 25 Hz. This has for effect to eliminate the fluctuations caused by turbulence and the vortex shedding, while keeping the superharmonics of significant strength. At $\mathrm{Re}_c = 64,000$ and $75,000$, the moment coefficient is relatively unstable as seen by the wiggles in the filtered moment coefficient on Fig. 5.4a and Fig. 5.4b. For all cases at higher Reynolds numbers ($\mathrm{Re}_c \geq 85,000$), the behavior of the moment coefficient is more stable, similar to the one observed on Fig. 5.4c at $\mathrm{Re}_c = 117,000$. This suggests the presence of two different flow regimes.

For the case at $\mathrm{Re}_c = 117,000$, the moment coefficient, filtered at 25 Hz, is plotted in function of the pitch angle in Fig. 5.5. During the pitch-down motion (from $t/T = 0$ to

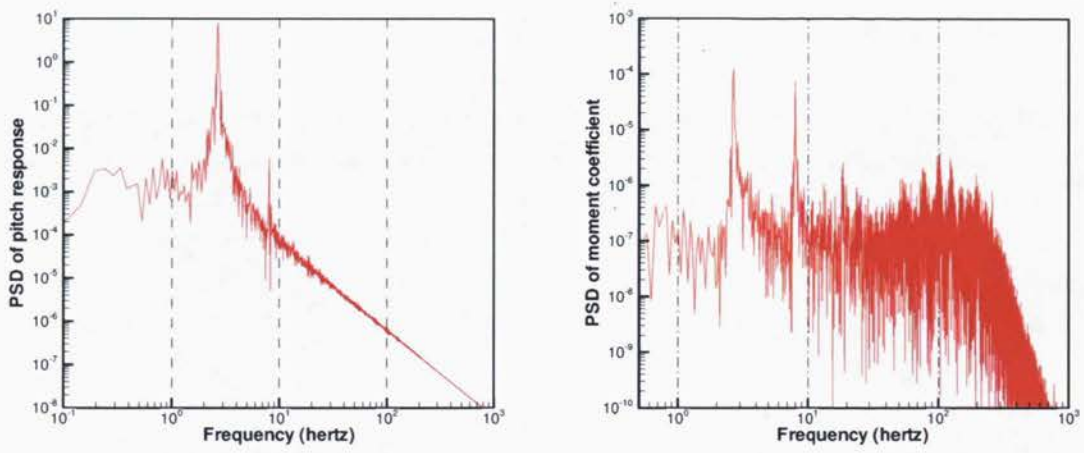

(a) PSD of pitch response

(b) PSD of aerodynamic moment

Figure 5.3: PSD of pitch response and aerodynamic moment coefficient at $\mathrm{Re_c} = 75,000$ (model $\gamma - \mathrm{Re}_\theta$).

$t/T = 0.25$), the moment coefficient increases, reaching a maximum around $t/T = 0.25$. In the next part of the cycle, the airfoil undergoes a pitch-up motion. From $t/T = 0.375$ to $t/T = 0.5$, the moment coefficient remains approximately constant while the angle of attack increases. This flattening of the moment enables the formation of the clockwise inner loop near the origin in Fig. 5.5, which is the source of the negative aerodynamic damping or, similarly, the time segment in the pitching cycle where the moment lags the pitch motion. This constant moment coefficient is caused by a decreasing length of the LSB (producing a smaller suction force) combined with a rearward motion of the LSB (creating a longer moment arm relative to the axis) during this part of the cycle. This will be made clearer in the next section.

Figure 5.6 shows the filtered aerodynamic moment coefficient as a function of the pitch angle for a cut-off frequency just above the fundamental frequency of oscillation at two Reynolds numbers. Time on the ellipses plotted in Fig. 5.6 is turning clockwise, meaning that energy is transferred from the airflow to the structure, hence sustaining the oscillations from an aeroelastic point of view. It also signifies that positive work is being done by the aerodynamic moment as the airfoil pitches. The slope of the main axis of the ellipse is also a noticeable feature and it can be interpreted as an equivalent linear static aerodynamic moment coefficient [61]. The negative of the slope, multiplied by $1/2\rho U_\infty^2 c^2 s$, is interpreted as an equivalent linear aerodynamic stiffness and is defined as:

$$K_A = -\frac{dC_{Mea}}{d\theta} 1/2\rho U_\infty^2 c^2 s. \tag{5.1}$$

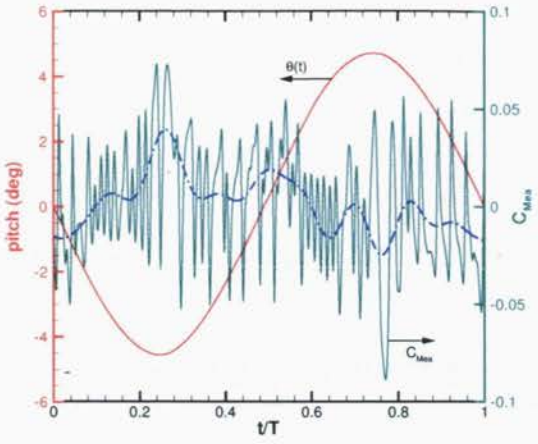

(a) $\mathrm{Re_c} = 64,000$

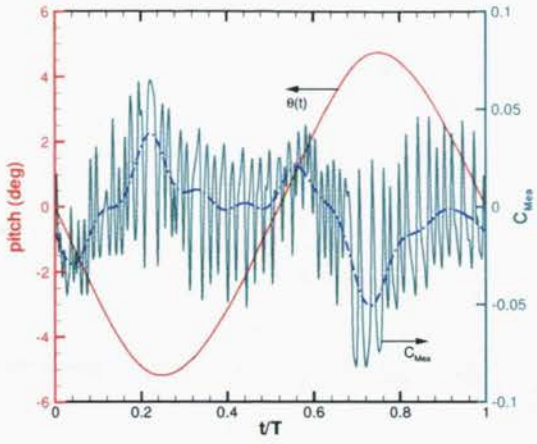

(b) $\mathrm{Re_c} = 75,000$

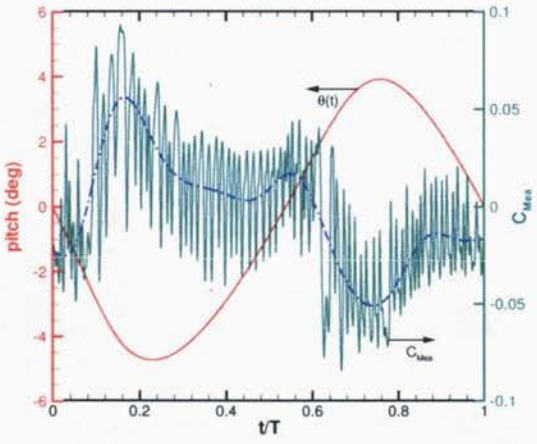

(c) $\mathrm{Re_c} = 117,000$

Figure 5.4: Pitch response (in red) and aerodynamic moment coefficient (unfiltered in green and filtered in blue) for one cycle of LCO.

A negative slope of the main axis of the ellipse means that the aerodynamic stiffness is positive which is stabilizing [61]. It acts like a restoring force. In the context of the present aeroelastic oscillations, the aerodynamic stiffness is increasing with the Reynolds number as can be seen when comparing the slopes of Fig. 5.6a and Fig. 5.6b. This corroborates findings of a recent experimental study by Poirel *et al.* [60].

Table 5.4 presents the average work done by the aerodynamic moment per cycle, computed over more than 25 LCO cycles. The positive values of the work support the observation that the flow transfers energy to the airfoil, thus the self-sustained nature of the oscillations.

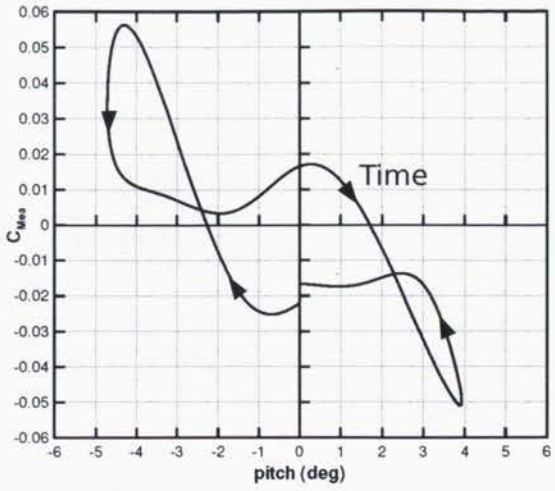

Figure 5.5: Aerodynamic moment coefficient as a function of pitch angle, f_c = 25 Hz, Re_c = 117,000.

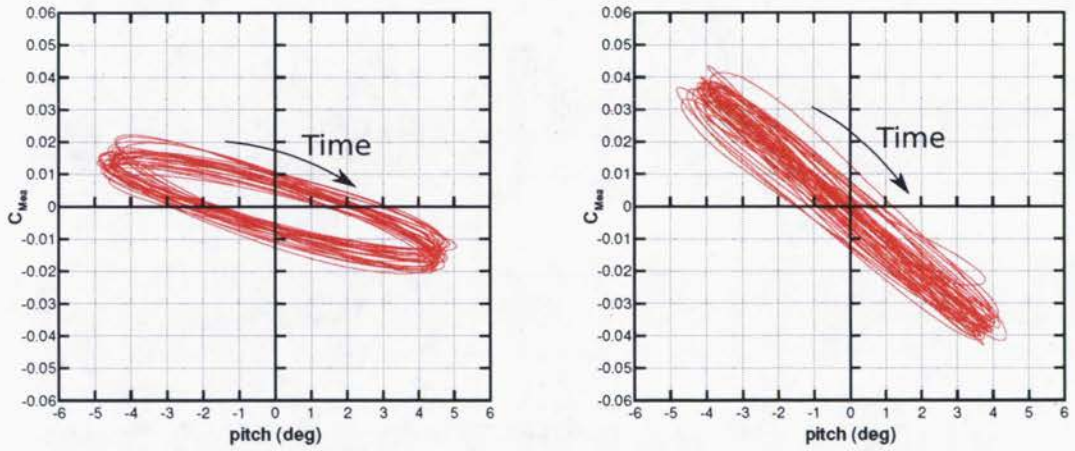

(a) Re_c = 64,000 (b) Re_c = 128,000

Figure 5.6: Aerodynamic moment coefficient as a function of pitch angle, f_c = 5 Hz.

The values are quite similar in all cases and are very close to the experimental values. Additionally, calculating the work with the filtered pitch displacement and aerodynamic moment (f_c = 25 Hz) does not significantly change the results. It is yet another observation that the low frequency content of the aerodynamics is responsible for the oscillations while the influence of the high-frequency flow structures is secondary.

Table 5.4: Average aerodynamic work per cycle and RMS moment coefficient, computed over 25 LCO cycles.

Reynolds number	W_{aero}	$C_{M,RMS}$
64,000	0.000649	0.0160
75,000	0.000739	0.0176
85,000	0.000776	0.0203
96,000	0.000787	0.0218
107,000	0.000769	0.0258
117,000	0.000775	0.0274
128,000	0.000807	0.0289
139,000	0.000834	0.0273
150,000	0.000924	0.0255

5.1.3 Flow dynamics

Figure 5.7 presents instantaneous vorticity contours around the airfoil surface at five different times in an oscillation cycle. The physics of the laminar separation bubble as well as the Kelvin-Helmholtz instability in the separated shear layer and the von Kármán vortex roll-up at the trailing edge are all captured in these simulations using a transition model.

Figure 5.8 shows contours of vorticity, viscosity ratio and intermittency at $t/T = 0.25$ at the same Reynolds number. In this case as well as in all cases where the Reynolds number is below 150,000, there is no significant appearance of turbulence in the boundary layer. This is visible in Fig. 5.8 where the viscosity ratio ν_t/ν remains very small everywhere and the intermittency γ has a value of 0 in the vicinity of the airfoil surface.

Using the low-Re correction option of the SST model and a modified constant ($R_k = 1$ instead of $R_k = 6$), Metivier [44] was able to obtain a reasonable match with the experimental results of Poirel *et al.* [61] as seen in Fig. 5.1. In those simulations, there was presence of an important level of turbulent viscosity at the trailing edge in the higher velocity cases (not in the lower ones), suggesting a possible transition of the separated shear layer followed by reattachment of the turbulent layer. This increase of ν_t concurs with the reduction of the constant R_k which triggers transition to happen sooner than with the default value. This led Metivier [44] to believe that the drop in amplitude was due to the presence of two different regimes. The first flow regime was thought to be laminar as the increase in oscillation amplitude was captured by simulations without turbulence model. The second flow regime where the oscillation amplitudes decrease was captured only with URANS simulations us-

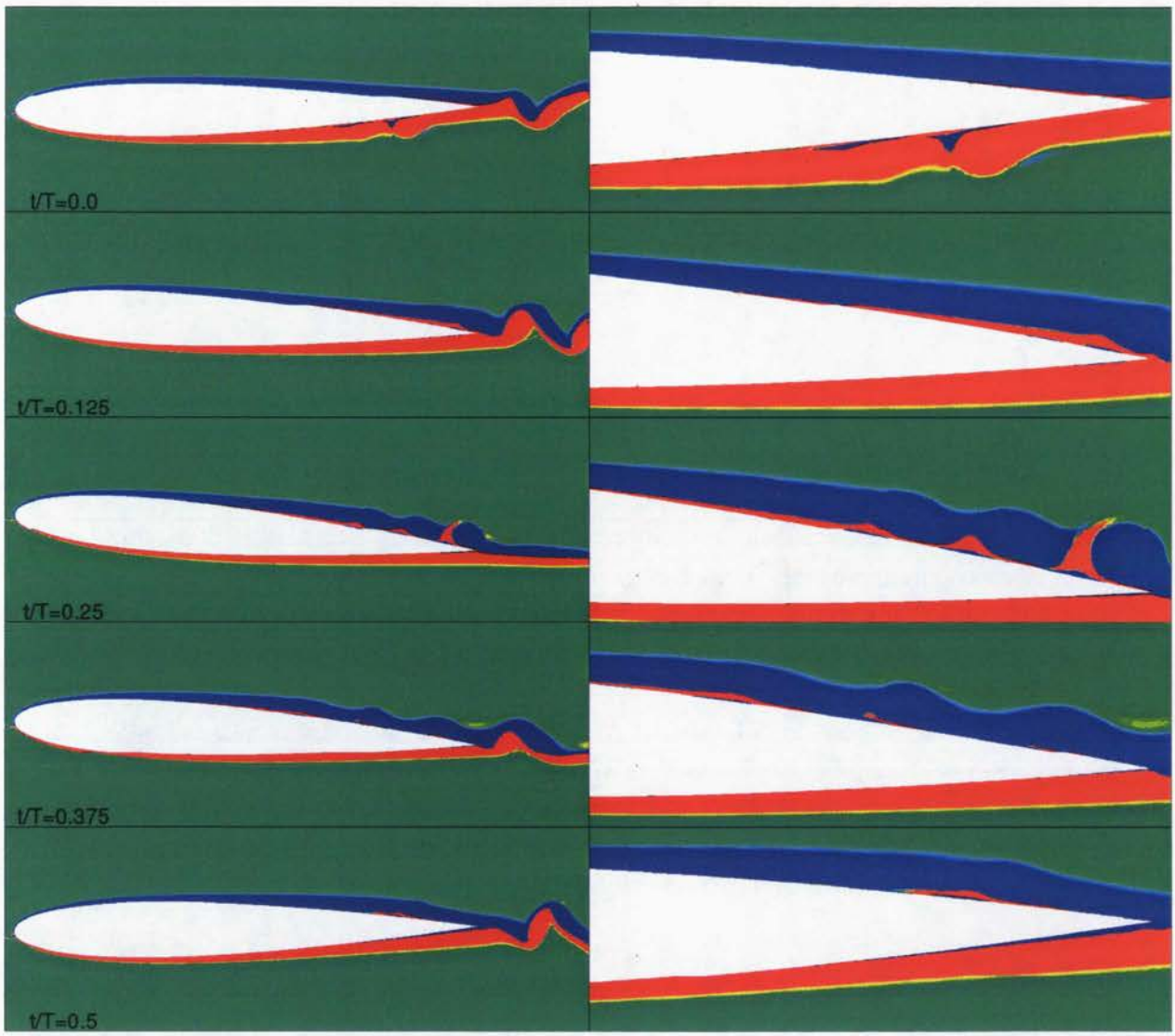

Figure 5.7: Vorticity contours around the airfoil and zoomed at the trailing edge at five times in a cycle at $\mathrm{Re_c} = 75,000$ (model $\gamma - \mathrm{Re}_\theta$).

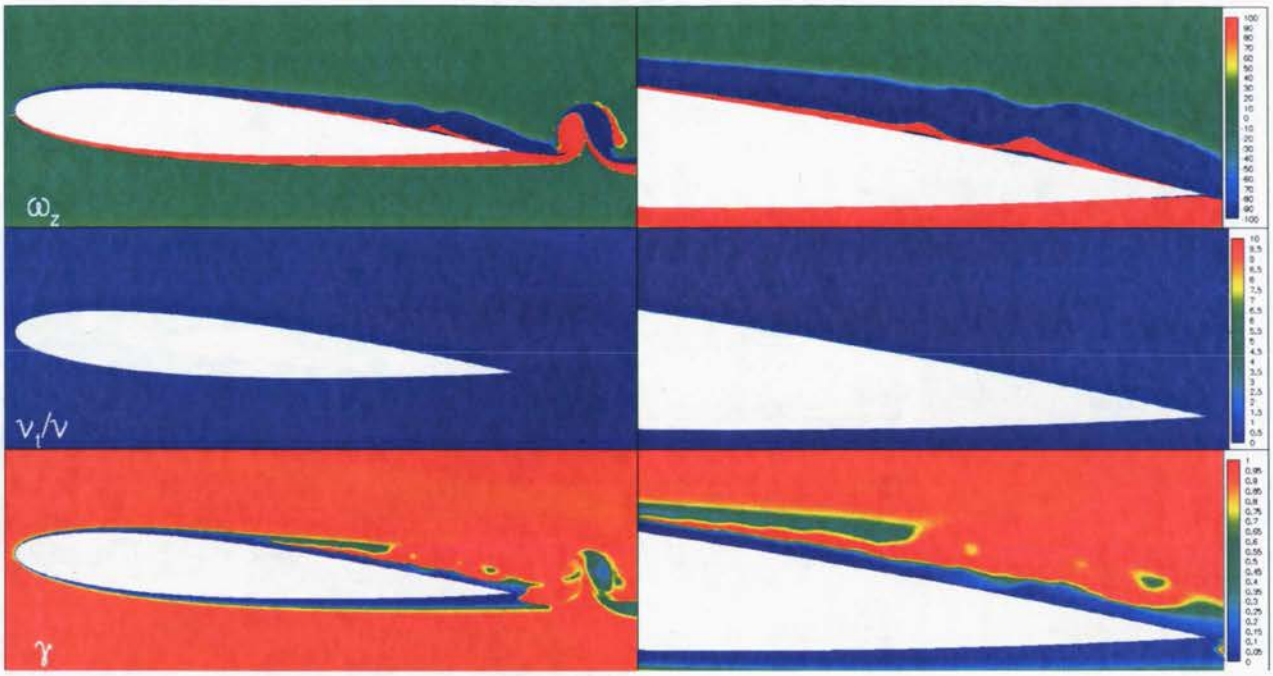

Figure 5.8: Vorticity, viscosity ratio and intermittency contours at $t = T/4$ around the airfoil and at the trailing edge at $\mathrm{Re_c} = 75,000$ (model $\gamma - \mathrm{Re}_\theta$).

ing a low-Re number correction and was thus associated with transition and boundary layer reattachement.

It is interesting that in the present study, the transition model is able to capture the trend of the experimental results as well and even better than the modified SST model without showing traces of higher turbulent viscosity at the trailing edge of cases at Reynolds numbers between 85,000 and 139,000. There is no need for higher ν_t and this will be explained later on.

At these low-Reynolds numbers, the growth rate of turbulence within the transition region from laminar to fully turbulent shear layers and the levels of shear stress around reattachment at the end of the bubble are points of major interest. It is thus pertinent to study the turbulent shear stress $\tau_{xy} = -\rho\overline{u'v'}$ since it causes transport of momentum across the boundary layer, which is responsible for the closure of the LSB.

Figures 5.9 to 5.17 presents the pressure and skin friction distribution over the airfoil as well as the contours of Reynolds stresses for the complete range of Reynolds numbers. These quantities have been phase-averaged over more than 25 LCO cycles. The present results show a very good agreement on both the C_p and C_f distributions and the contours of Reynolds stresses with the LES results of Poirel and Yuan [64] who present a similar analysis for an airfoil undergoing prescribed sinusoidal oscillations of $\theta_0 = 5.1$ deg and $f = 2.9$ Hz.

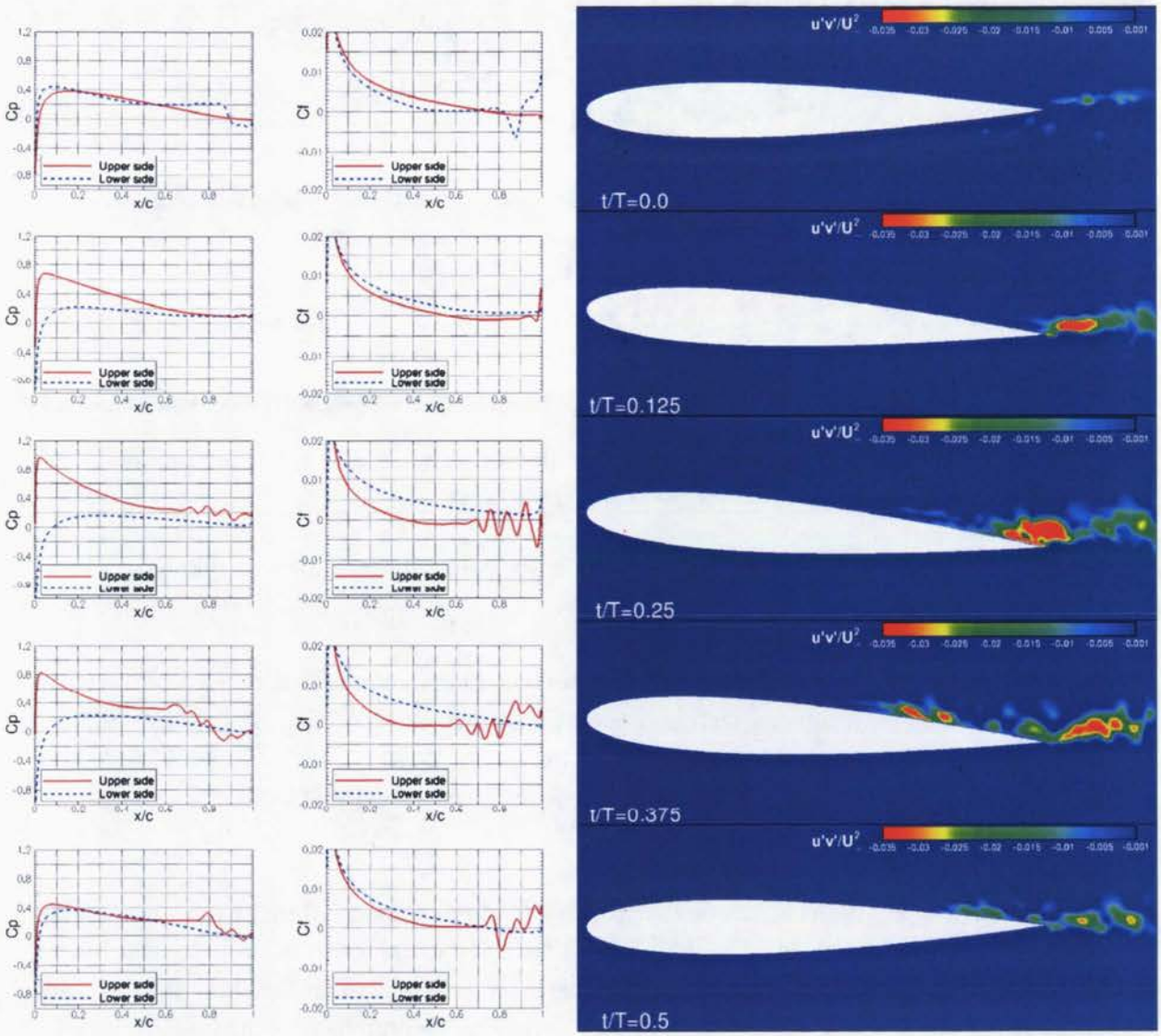

Figure 5.9: C_p and C_f distributions and contours of Reynolds stresses at five times in a cycle at $\mathrm{Re_c} = 64,000$, averaged over 25 LCO cycles (model $\gamma - \mathrm{Re}_\theta$).

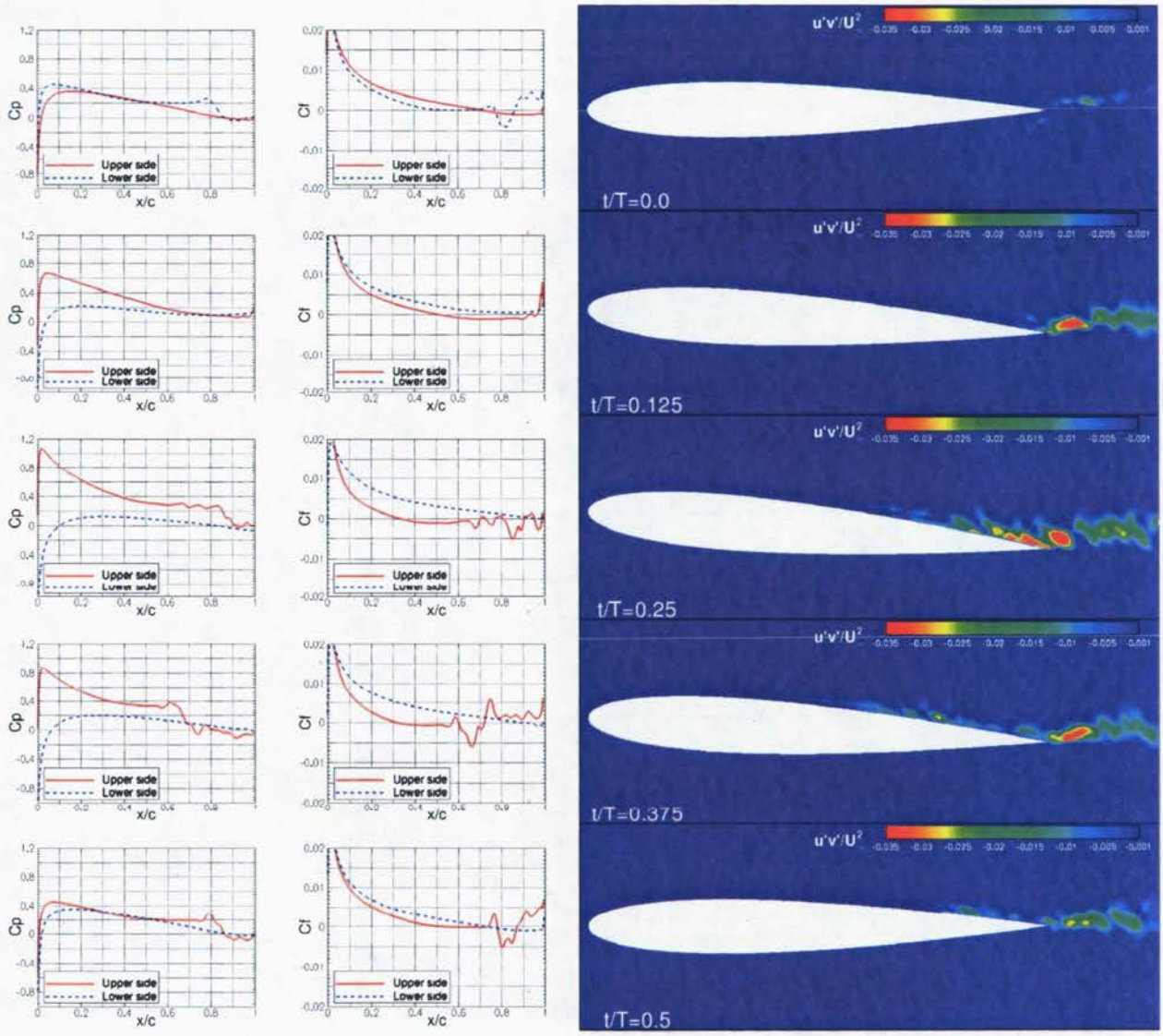

Figure 5.10: C_p and C_f distributions and contours of Reynolds stresses at five times in a cycle at $\mathrm{Re_c} = 75,000$, averaged over 25 LCO cycles (model $\gamma - \mathrm{Re}_\theta$).

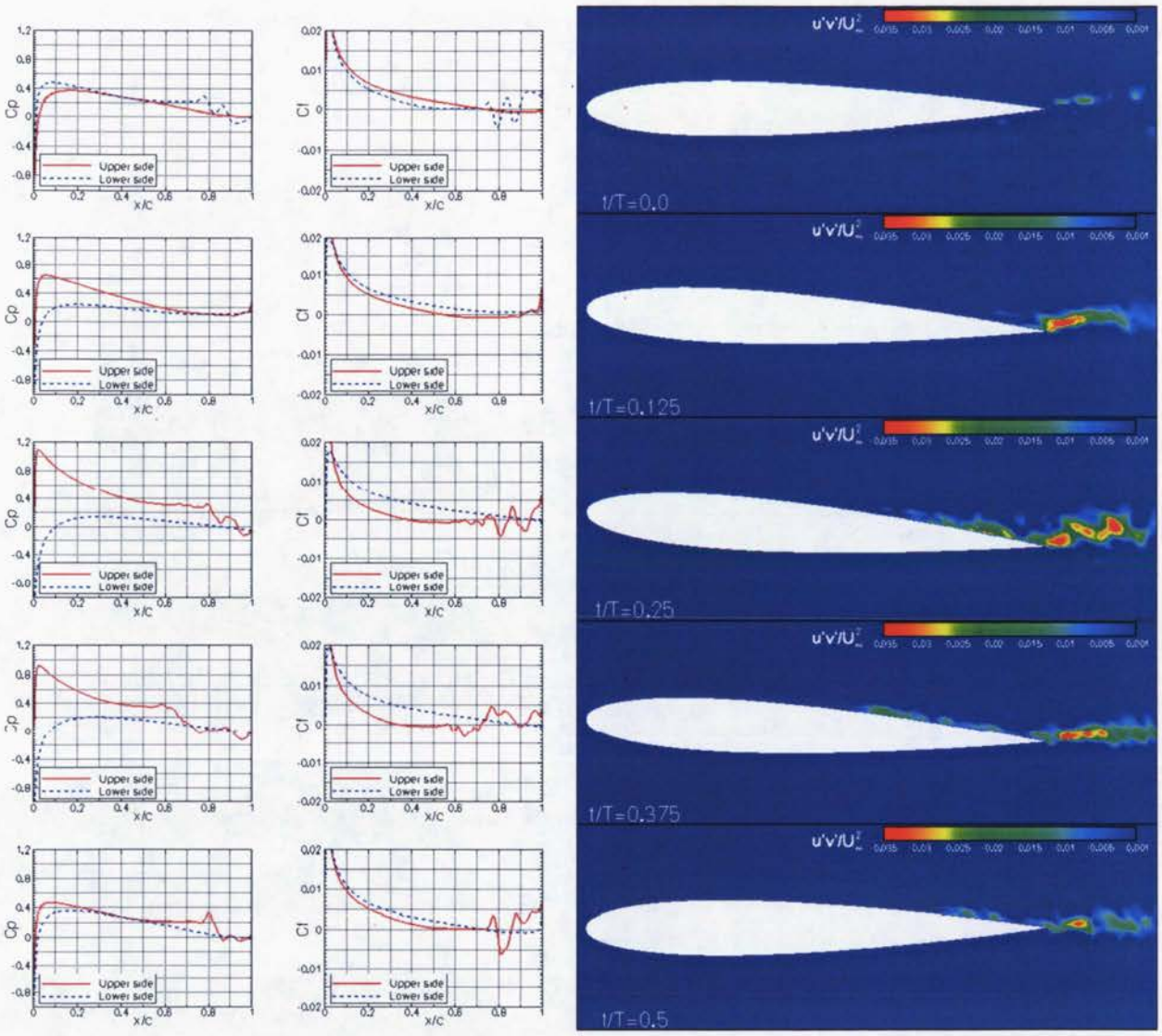

Figure 5.11: C_p and C_f distributions and contours of Reynolds stresses at five times in a cycle at $\mathrm{Re_c} = 85,000$, averaged over 25 LCO cycles (model $\gamma - \mathrm{Re}_\theta$).

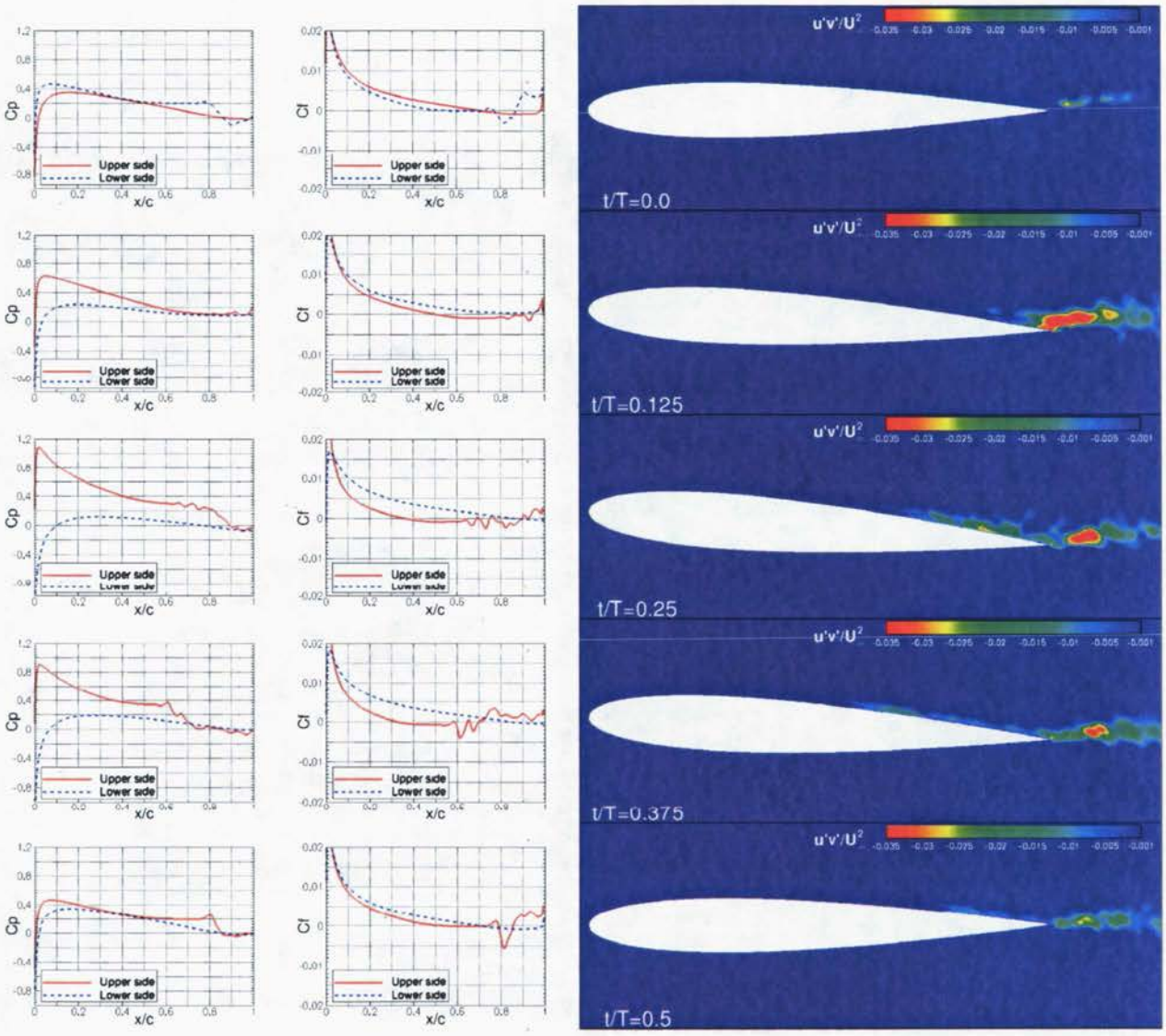

Figure 5.12: C_p and C_f distributions and contours of Reynolds stresses at five times in a cycle at $\mathrm{Re_c} = 96,000$, averaged over 25 LCO cycles (model $\gamma - \mathrm{Re}_\theta$).

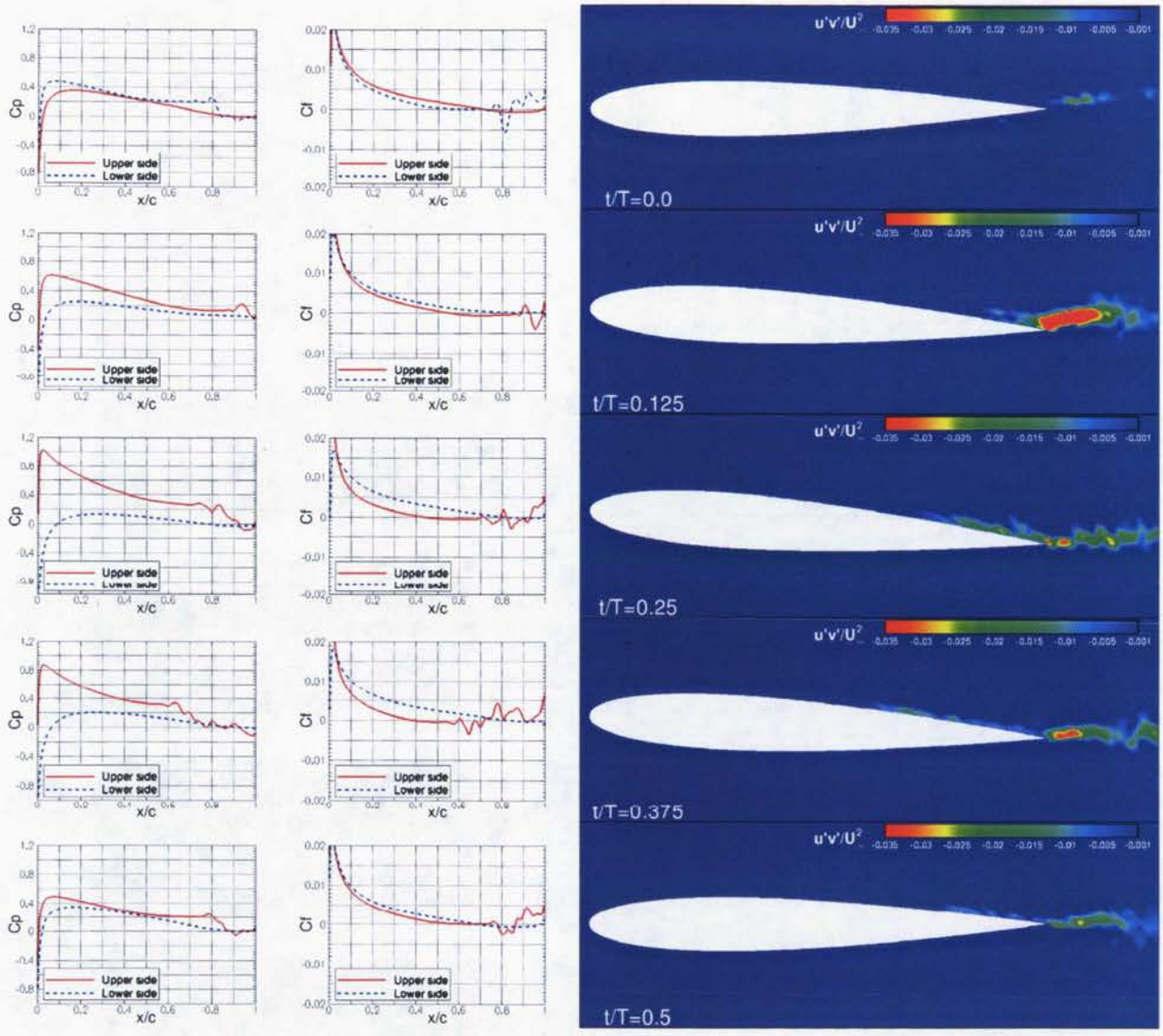

Figure 5.13: C_p and C_f distributions and contours of Reynolds stresses at five times in a cycle at $\mathrm{Re_c} = 107,000$, averaged over 25 LCO cycles (model $\gamma - \mathrm{Re}_\theta$).

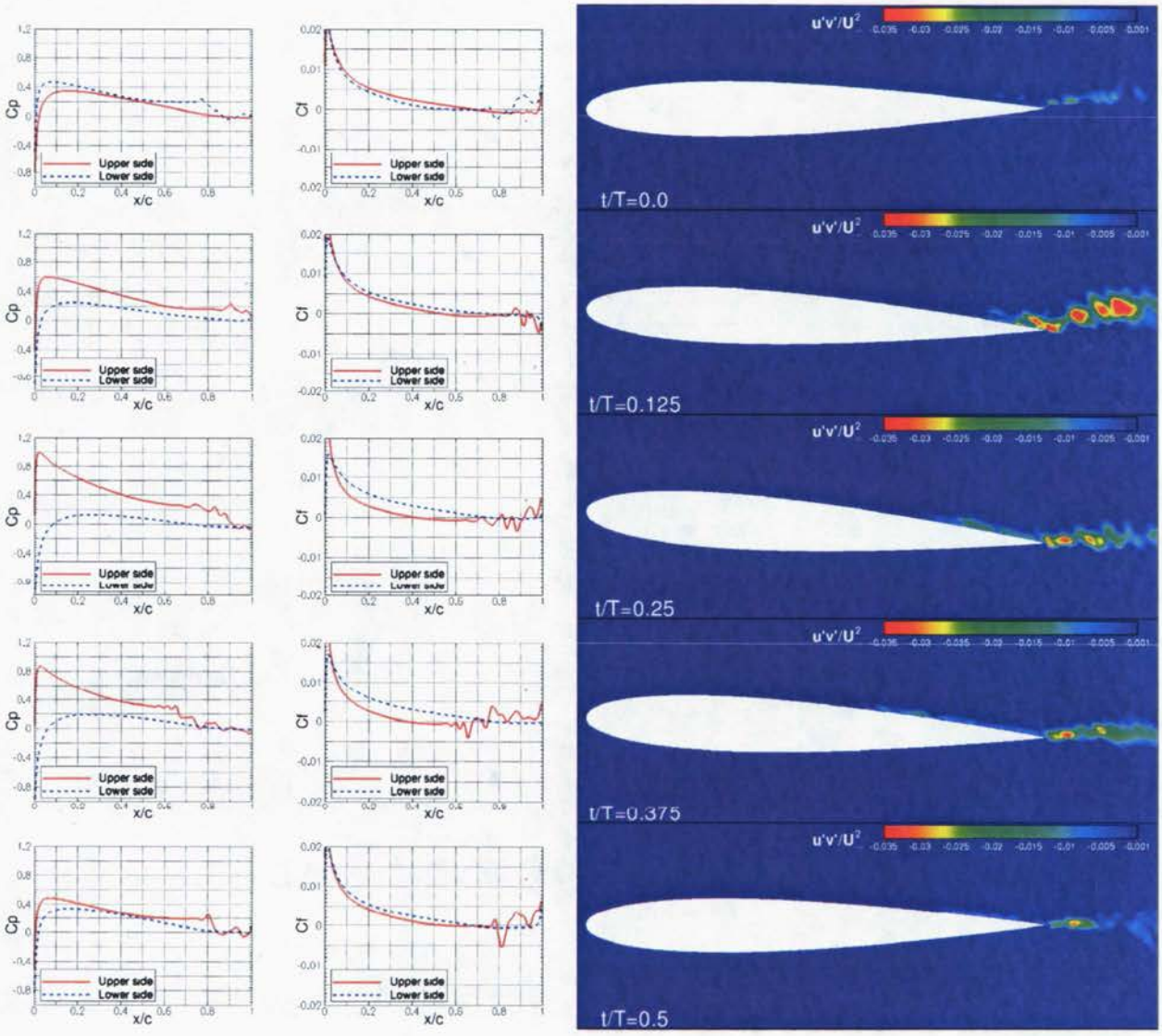

Figure 5.14: C_p and C_f distributions and contours of Reynolds stresses at five times in a cycle at $\mathrm{Re_c} = 117,000$, averaged over 25 LCO cycles (model $\gamma - \mathrm{Re}_\theta$).

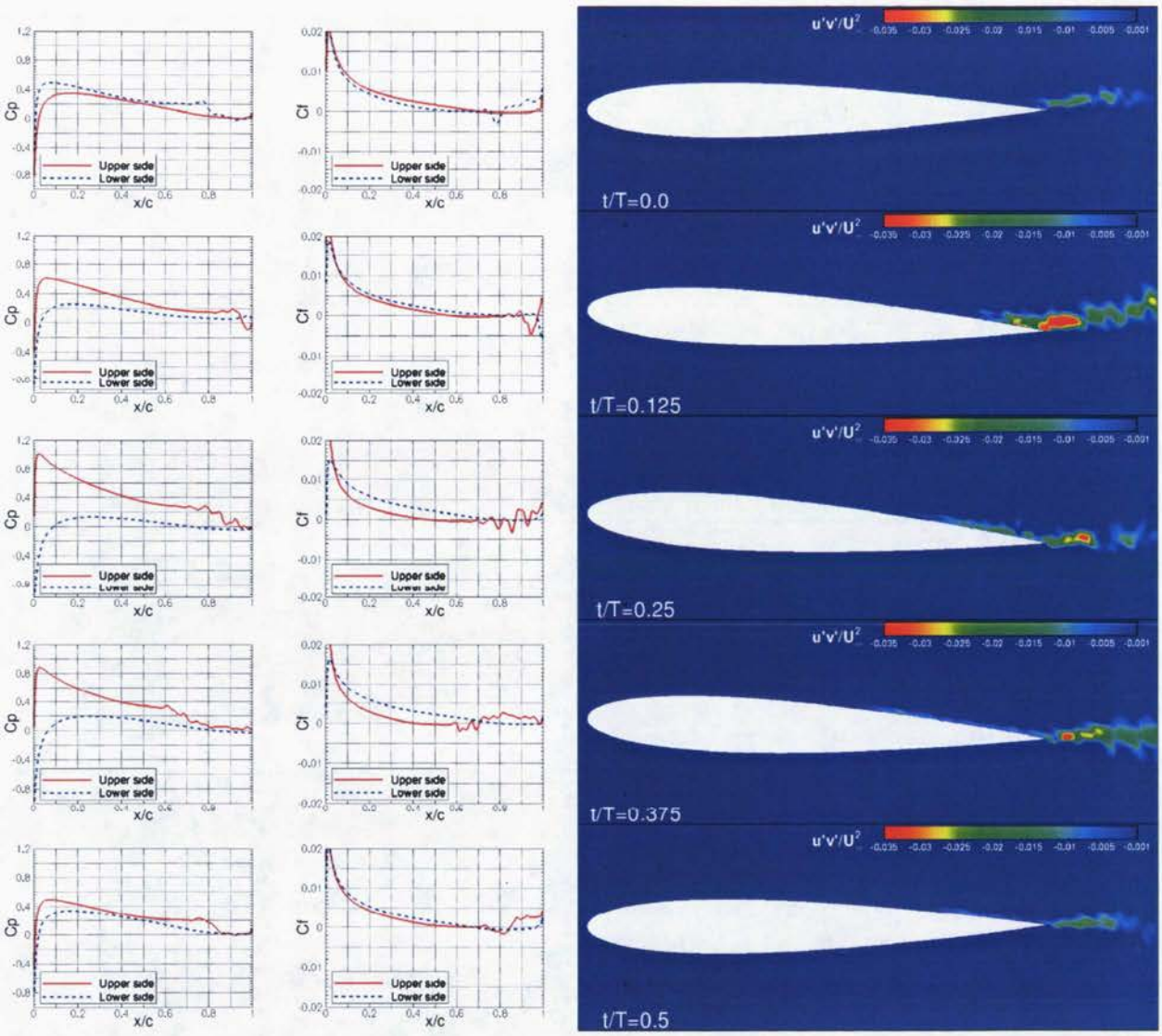

Figure 5.15: C_p and C_f distributions and contours of Reynolds stresses at five times in a cycle at $\mathrm{Re_c} = 128,000$, averaged over 25 LCO cycles (model $\gamma - \mathrm{Re}_\theta$).

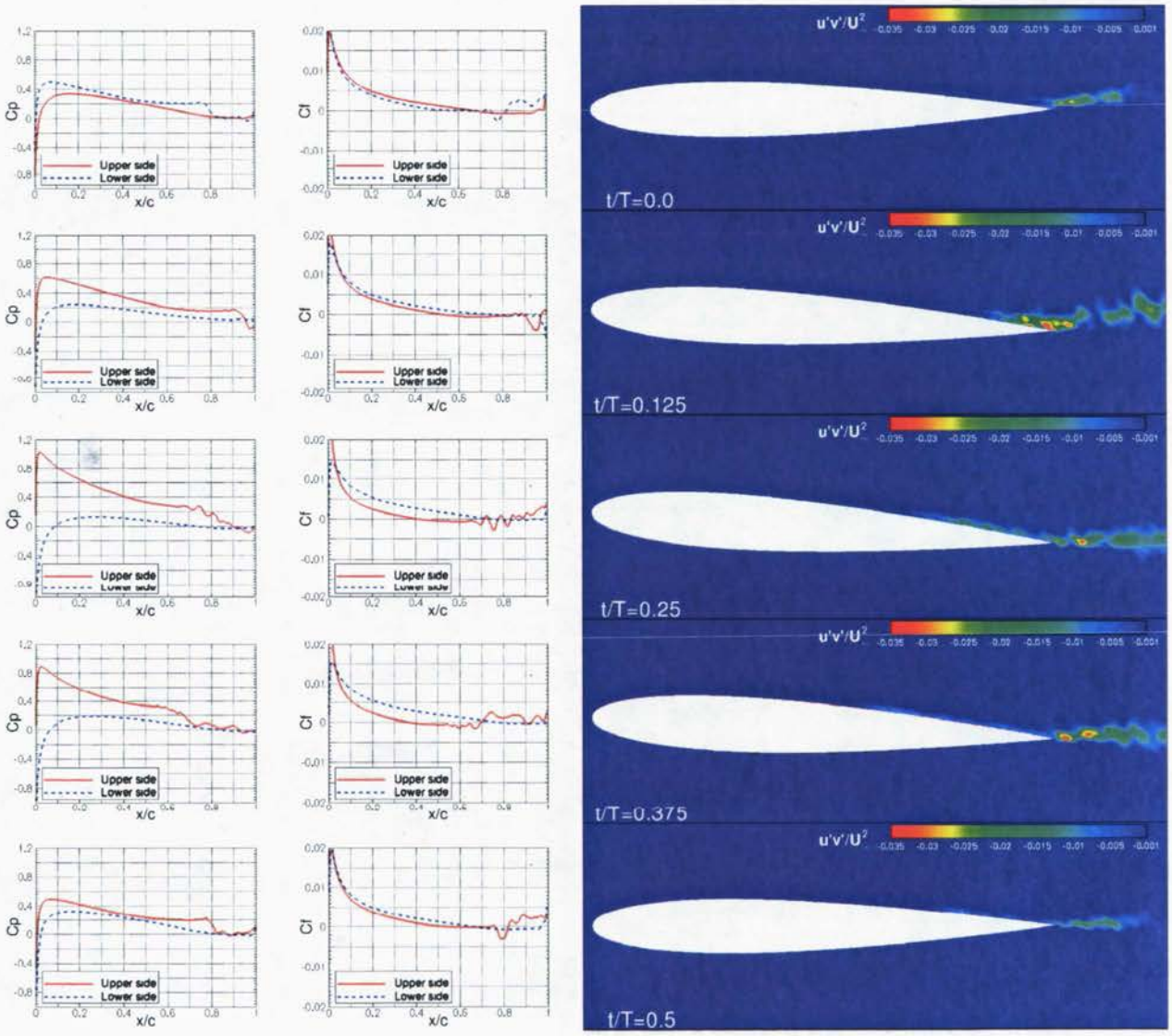

Figure 5.16: C_p and C_f distributions and contours of Reynolds stresses at five times in a cycle at $\mathrm{Re_c} = 139,000$, averaged over 25 LCO cycles (model $\gamma - \mathrm{Re}_\theta$).

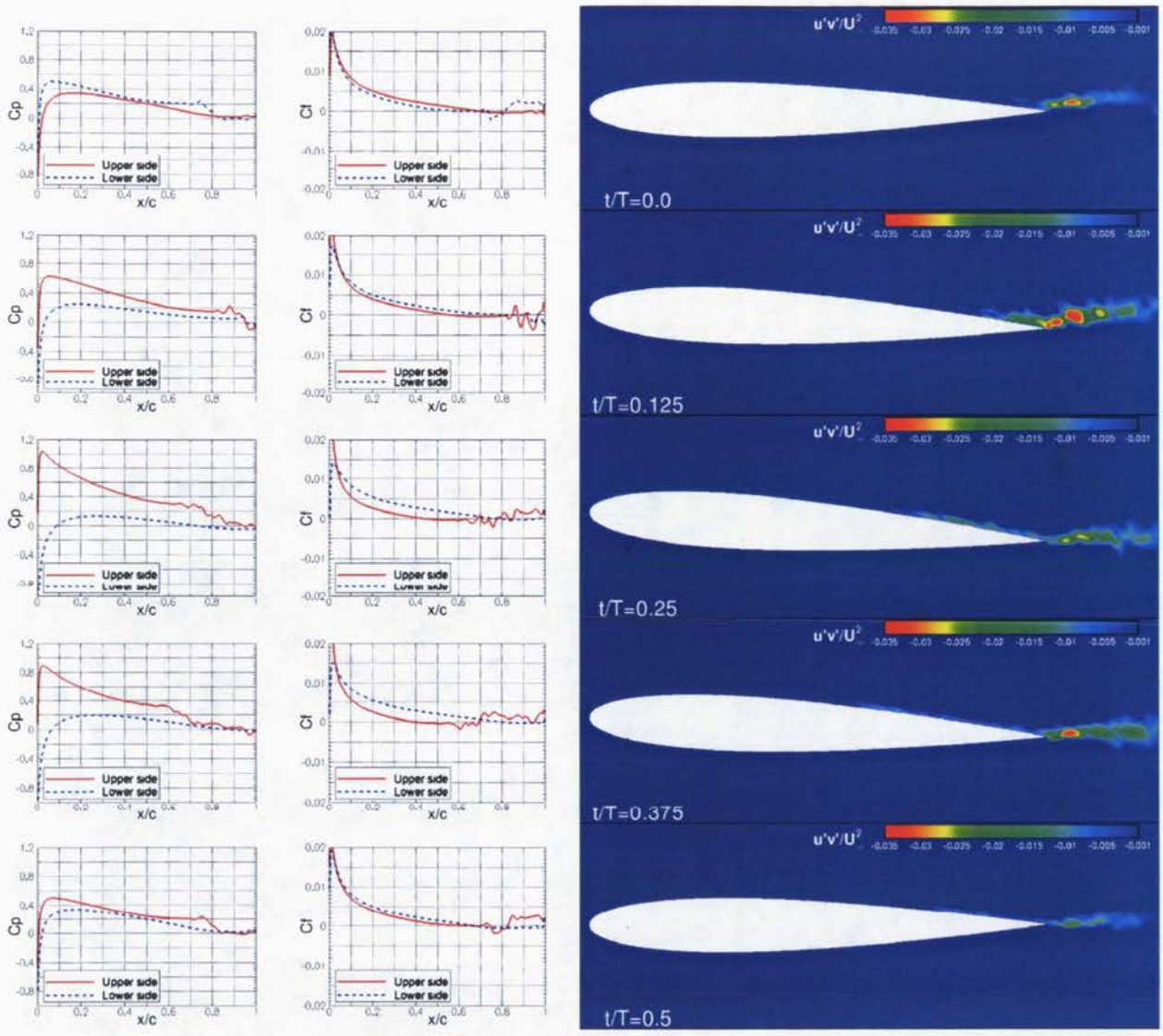

Figure 5.17: C_p and C_f distributions and contours of Reynolds stresses at five times in a cycle at $\mathrm{Re_c} = 150,000$, averaged over 25 LCO cycles (model $\gamma - \mathrm{Re}_\theta$).

From the C_f and C_p distributions, laminar boundary layer separation is observed at $t/T = 0$ and $t/T = 0.125$. In all simulations, separation occurs around $x/c \approx 0.7$ at $t/T = 0$ and around $x/c \approx 0.55$ at $t/T = 0.125$. From the Reynolds stresses, we can see that transition to turbulence occurs only in the near wake or at the trailing edge, and that there is no reattachment of the boundary layer at those two instants. The location of the separation, reattachement and transition points are determined as previously explained in section 4.3.3.

At $t/T = 0.25$ and $t/T = 0.375$, the presence of a phase-averaged laminar separation bubble is detected on the upper side of the airfoil in almost all simulations. Tables 5.5 and 5.6 present the characteristics of the LSB as well as the moment coefficient at different Reynolds numbers at $t/T = 0.25$ and $t/T = 0.375$ respectively. At $t/T = 0.25$, boundary layer separation occurs over the whole Reynolds number range and re-attachement is observed close to the trailing edge at $\mathrm{Re}_c \geq 85,000$, hence the presence of a LSB in the second flow regime. The absence of reattachment at $\mathrm{Re}_c = 64,000$ and $75,000$ might concord with the observation made earlier of the more unstable moment coefficient in those cases, suggesting a different flow regime. Over the whole range of simulations, the separation point moves toward the trailing edge with the increase in Reynolds number. This rearward motion of the LSB increases the moment arm relative to the axis and hence the (negative) moment coefficient about the elastic axis also increases with Re.

At $t/T = 0.375$, a similar behavior is observed. In all cases, there is boundary layer separation followed by transition of the shear layer and subsequent reattachment (indicating the presence of a laminar separation bubble). The length of the bubble remains relatively constant except at $\mathrm{Re}_c = 64,000$ where it is noticeably larger, corroborating the presence of a slightly different flow at lower Reynolds numbers. Again, the separation point moves toward the trailing edge with the increase in Reynolds number, causing a greater pitch moment about the axis.

At $t/T = 0.5$, there is no boundary layer separation according to the definition used here since the skin-friction coefficient goes very close to 0 around $x/c \approx 0.5$ but does not become negative. The same phenomenon was observed by Poirel and Yuan [64]. They labelled that region a "dead-air" zone and it plays essentially the same role as a laminar separation bubble. In this zone, transition to turbulence is observed and followed by an increase in skin friction ($C_f > 0$). The resulting flattened pressure plateau induces a nose-down pitching moment similarly to the previous instants where a classical LSB was present.

The increase of the negative pitch moment with the Reynolds number has for effect to accelerate the nose-down motion and hence limit the pitching motion of the airfoil. This is the cause of the decrease of oscillation amplitudes with increasing Reynolds number in the second regime, illustrated on Fig. 5.1a.

Table 5.5: Computed LSB properties at $t/T = 0.25$, phase-averaged over 25 LCO cycles.

Reynolds number	Separation x_{sep}/c	Transition x_{tr}/c	Reattachment x_r/c	Bubble length L_{LSB}/c	Moment C_{Mea}
64,000	0.36	0.69	N/A[1]	N/A	-0.026
75,000	0.36	0.63	N/A	N/A	-0.0395
85,000	0.38	0.64	0.94	0.56	-0.036
96,000	0.39	0.66	0.9	0.51	-0.0389
107,000	0.42	0.69	0.92	0.50	-0.0438
117,000	0.45	0.73	0.91	0.46	-0.0467
128,000	0.46	0.72	0.93	0.47	-0.0455
139,000	0.45	0.70	0.83	0.38	-0.0419
150,000	0.45	0.71	0.85	0.40	-0.0377

Table 5.6: Computed LSB properties at $t/T = 0.375$, phase-averaged over 25 LCO cycles.

Reynolds number	Separation x_{sep}/c	Transition x_{tr}/c	Reattachment x_r/c	Bubble length L_{LSB}/c	Moment C_{Mea}
64,000	0.33	0.57	0.83	0.5	-0.0045
75,000	0.35	0.50	0.72	0.37	-0.0043
85,000	0.35	0.54	0.72	0.37	-0.006
96,000	0.35	0.51	0.70	0.35	-0.0086
107,000	0.38	0.55	0.72	0.34	-0.015
117,000	0.4	0.57	0.75	0.35	-0.0193
128,000	0.4	0.57	0.71	0.31	-0.0189
139,000	0.4	0.59	0.70	0.3	-0.0196
150,000	0.4	0.59	0.69	0.29	-0.0189

As mentionned earlier, the amplitudes of both the experimentally and numerically simulated LCOs decrease as the Reynolds number is increased up to $Re_c \approx 150,000$. Above this Re_c, no oscillations of significant amplitude occur. A possible explanation for this phenomenon is the increase of turbulence level in the near wake of the airfoil. Figures 5.18 and 5.19 show contours of viscosity ratio and intermittency for two simulations in the upper Reynolds numbers range. At $Re_c \leq 139,000$, there is no significant turbulent viscosity around the airfoil and the intermittency doesn't show full turbulence as the level in the wake is between 0 and 1. At $Re_c = 150,000$, $160,000$ and $171,000$ however, important ratios of turbulent viscosity ($\nu_t/\nu > 10$) and an intermittency of $\gamma \sim 1$ are observed. This increase in turbulence happens early in the simulation and has a stabilizing effect on the flow. It inhibits the appearance of laminar separation which is the triggering mechanism of the oscillations.

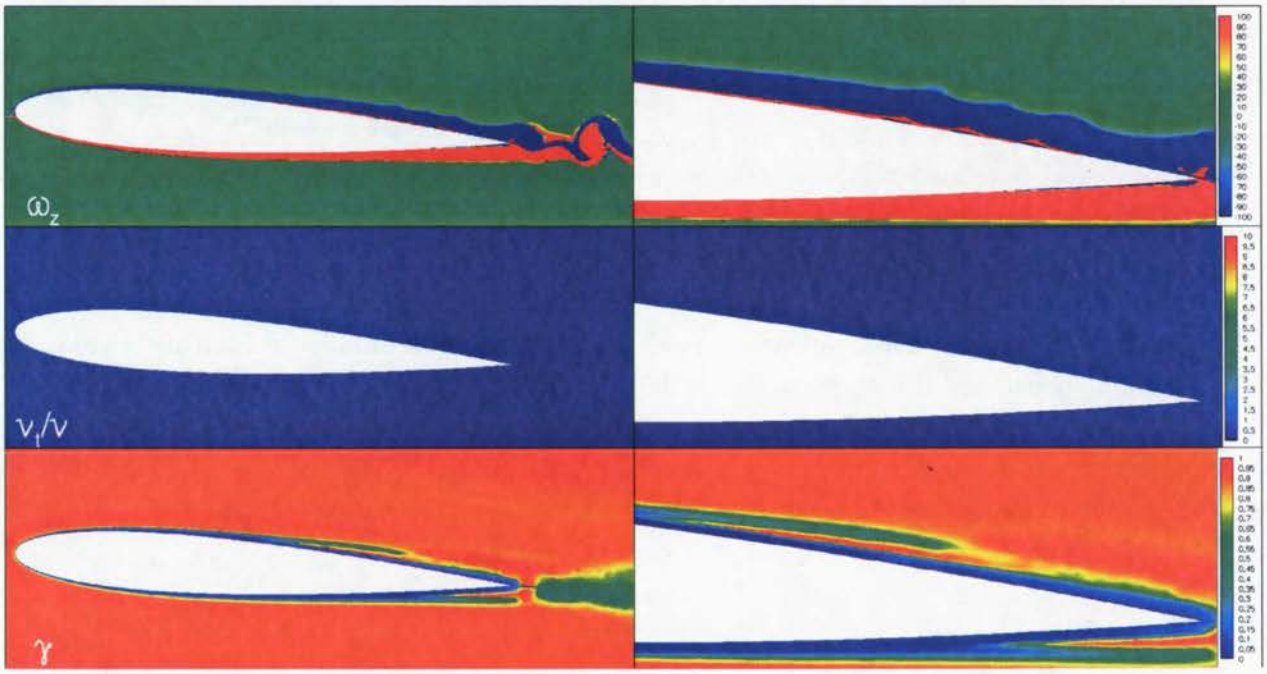

Figure 5.18: Vorticity, viscosity ratio and intermittency contours around the airfoil and at the trailing edge at $Re_c = 139,000$ (model $\gamma - Re_\theta$).

5.1.4 Effect of freestream turbulence intensity

Simulations presented up to this point have all been performed with a freestream turbulence intensity of $\sim 0.15\%$ (at the airfoil leading edge) to match the intensity in the wind tunnel experiments. In order to assess the possible influence of this parameter on the aeroelastic behavior, different intensities are now tested.

We find that there is no influence of the freestream turbulence intensity on the predicted

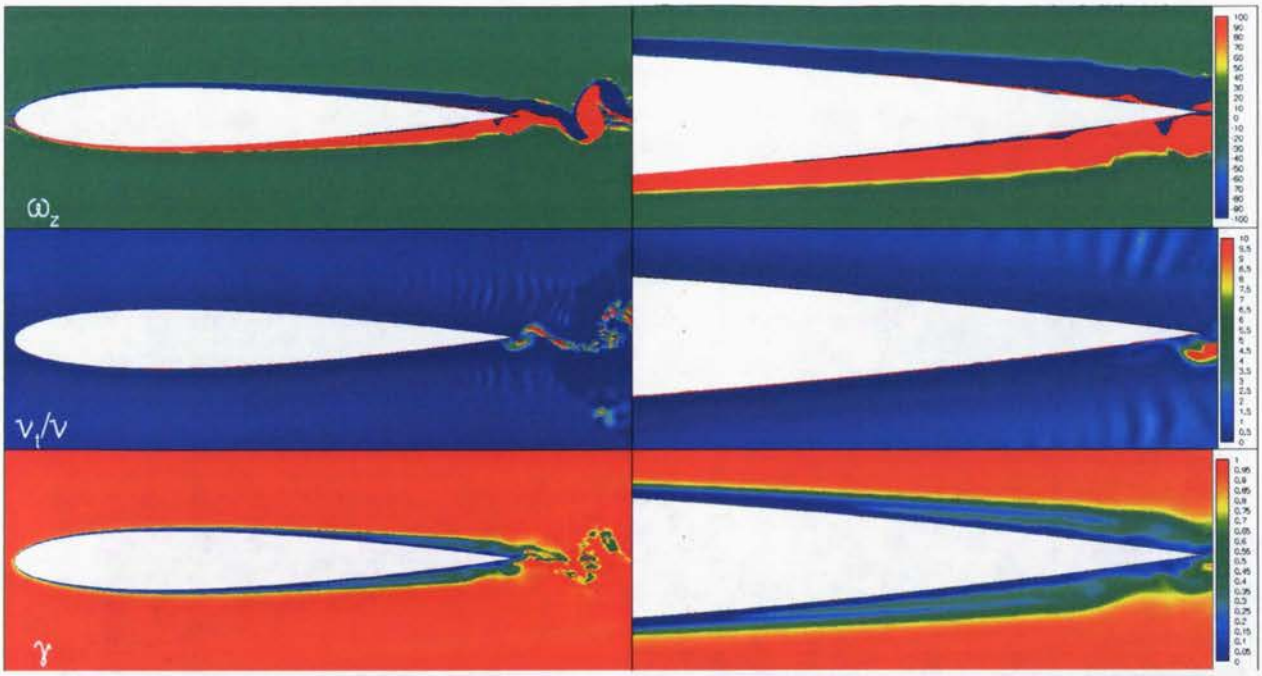

Figure 5.19: Vorticity, viscosity ratio and intermittency contours around the airfoil and at the trailing edge at $\mathrm{Re_c} = 171,000$ (model $\gamma - \mathrm{Re}_\theta$).

oscillation amplitudes and frequencies as long as a relatively low turbulence intensity is used. Simulations performed with intensities at the airfoil[2] ranging from 0.01 % to 0.3 %, all produce very similar results, showing negligible influence of Tu. This is not a surprise since turbulence is not triggered in the boundary layer at those levels. Laminar separation and the Kelvin-Helmhotz instability occur similarly in all cases in the same way as what is shown in Fig. 5.8.

Turbulence intensity is then increased to higher values of 0.7 % and 1 %. In those simulations, self-sustained oscillations do not always appear and, when they do, it is after a longer startup period and with lower oscillation amplitudes than previously obtained at lower intensities. In all those cases ($\mathrm{Re}_c = 60,000$ to $130,000$), there is important turbulent viscosity ($\nu_t/\nu > 1$) and intermittency of 1 at the airfoil trailing edge, signifying a transition to turbulence of the separated laminar boundary layer, as shown in Fig. 5.20.

At a freestream turbulence intensity of 2 %[3], no oscillation is appearing in any of the cases. The airfoil remains at zero incidence and there is evidence of boundary layer transition close to the trailing edge. This is in agreement with the experimental results of Poirel [61]

[2]Inlet turbulence intensity and viscosity ratios were adjusted to obtain the desired level of turbulence at the airfoil.

[3]In order to achieve this intensity at the airfoil, the distance between the inlet and the airfoil in the computational domain was shortened to limit freestream turbulence decay.

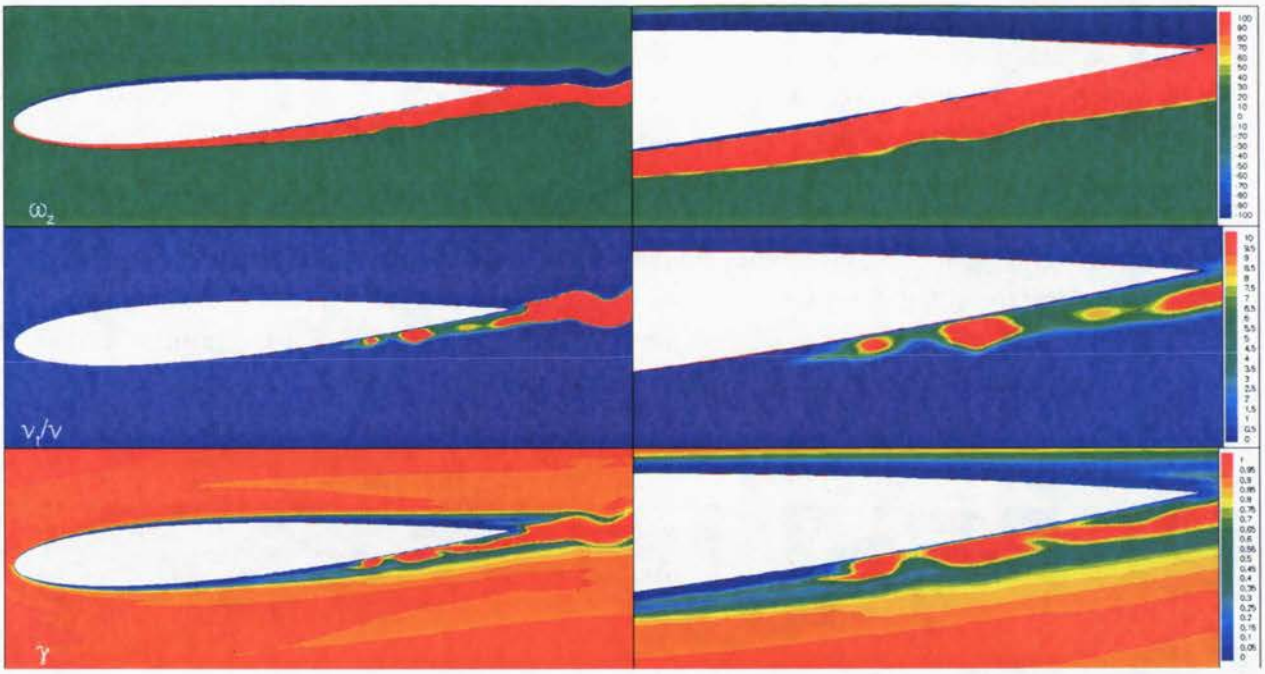

Figure 5.20: Vorticity, viscosity ratio and intermittency contours at $t = T/4$ around the airfoil and at the trailing edge at $\mathrm{Re}_c = 117,000$ and $Tu = 1\%$ (model $\gamma - \mathrm{Re}_\theta$).

where LCOs were inhibited by the use of a turbulence generating grid in the wind tunnel or by a trip-wire on the airfoil. This enhances the observation that laminar separation is essential to initiate the oscillations. When boundary layers are turbulent, either by high freestream turbulence or the use of a trip-wire, the airfoil remains at rest.

5.1.5 Effect of timestep

Improved understanding of the phenomenon can be gained by considering the impact of coarsening the timestep size in such a way to filter out more or less the highest frequencies in the flow. We have first established that a sufficiently small timestep ($\Delta t = 2 \times 10^{-5}$ sec, resulting in 12,000 to 20,000 timesteps per oscillation cycle depending on the Reynolds number) is required to obtain consistent and precise (timestep independent) results. However, Metivier *et al.* [44, 62] reported that the general behaviour of the limit-cycle oscillations was captured with much coarser timesteps ($\Delta t = 1 \times 10^{-3}$ sec). Changing the timestep to such larger values had for effect to eliminate small scale flow dynamics, in particular the high-frequency von Kármán vortex shedding. In some sense, it acted as a high-frequency filtering.

In this study, computations with the $\gamma - \mathrm{Re}_\theta$ transition model and coarse timesteps of

$\Delta t = 1 \times 10^{-3}$ and 5×10^{-4} sec predict no self-sustained oscillations at $\mathrm{Re}_c < 85,000$ and LCOs of $\theta_{max} \approx 4$ deg and $fc/U_\infty \approx 0.05$ in the higher Reynolds number range. Those simulations exhibit high levels of turbulence ($\nu_t/\nu > 1$ and $\gamma = 1$) near the trailing edge of the airfoil. Vorticity, viscosity ratio and intermittency contours are compared between the fine and coarse timesteps at $\mathrm{Re}_c = 117,000$ in Figs. 5.21 and 5.22. The aerodynamic moment coefficient is also much better behaved in the computations made with the coarser timestep, as shown in Fig. 5.23. Indeed, it becomes similar to the filtered moment coefficient ($f_c = 25$ Hz) obtained from the simulations with the fine timestep. This suggests that the high-frequency flow instabilities (Kelvin-Helmholtz and von Kármán shedding) are not the primary LCO mechanism since self-sustained oscillations are observed despite their absence.

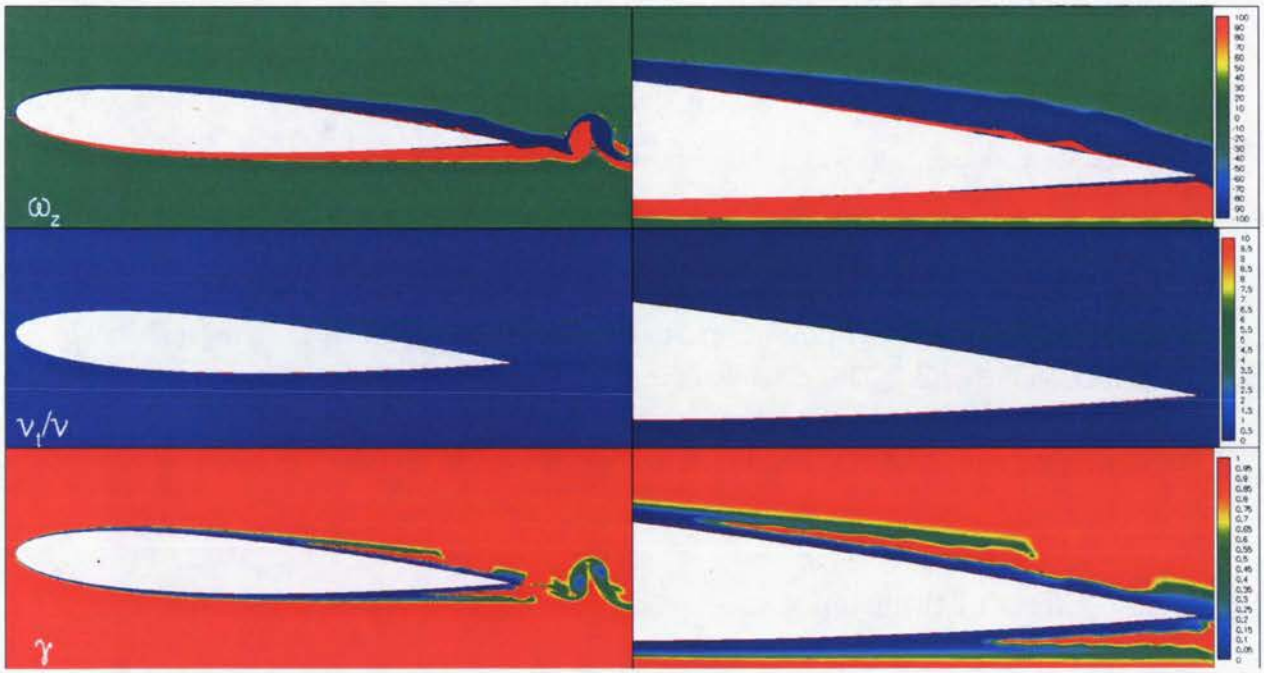

Figure 5.21: Vorticity, viscosity ratio and intermittency contours at $t = T/4$ around the airfoil and at the trailing edge at $\mathrm{Re}_c = 117,000$ with a fine timestep of $\Delta t = 2 \times 10^{-5}$ sec (model $\gamma - \mathrm{Re}_\theta$).

As already mentionned, there is no apparent vortex roll-up with the coarse timestep, hence turbulent dissipation is produced solely by the rise of the turbulent viscosity. With a fine timestep, the level of turbulent viscosity is much smaller since dissipation is enhanced by the high-frequency flow structures. This can be visualized in the form of the correlation of the velocity fluctuations $\overline{u'v'}$ as shown in Fig. 5.24. From the RANS computations using eddy-viscosity models based on the Boussinesq approximation, those can be recovered by Eq. (5.2)

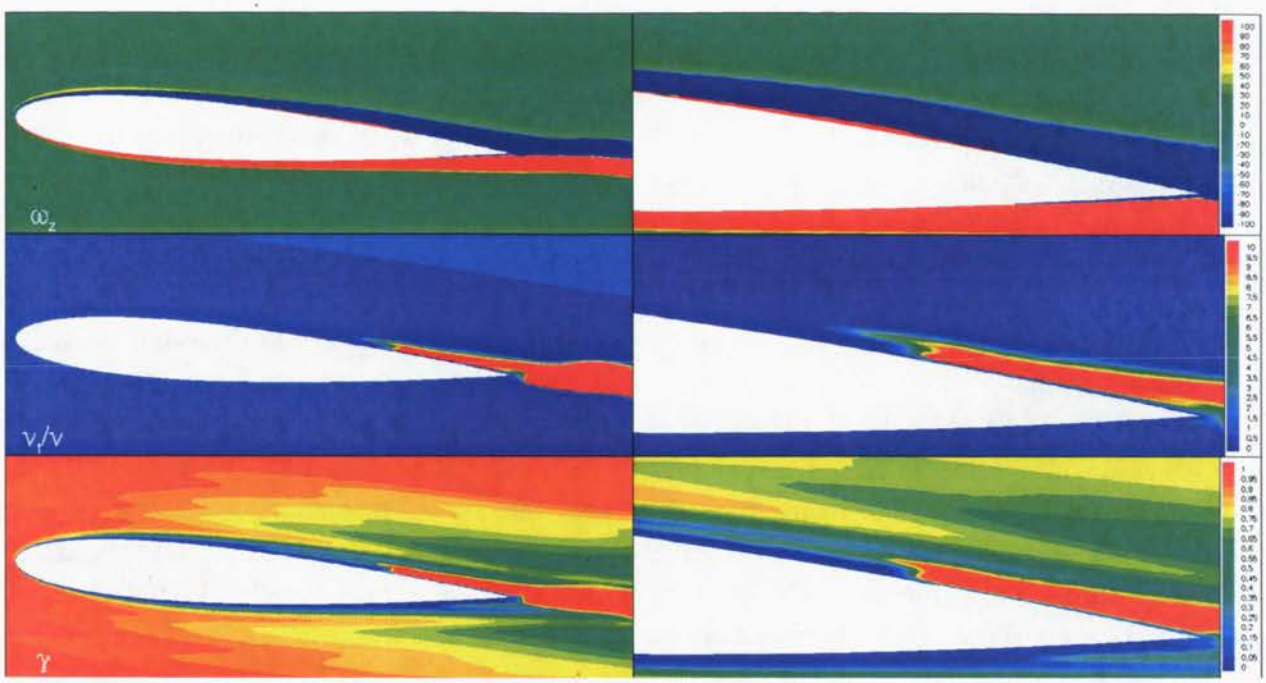

Figure 5.22: Vorticity, viscosity ratio and intermittency contours at $t = T/4$ around the airfoil and at the trailing edge at $\mathrm{Re_c} = 117,000$ with a coarse timestep of $\Delta t = 1 \times 10^{-3}$ sec (model $\gamma - \mathrm{Re}_\theta$).

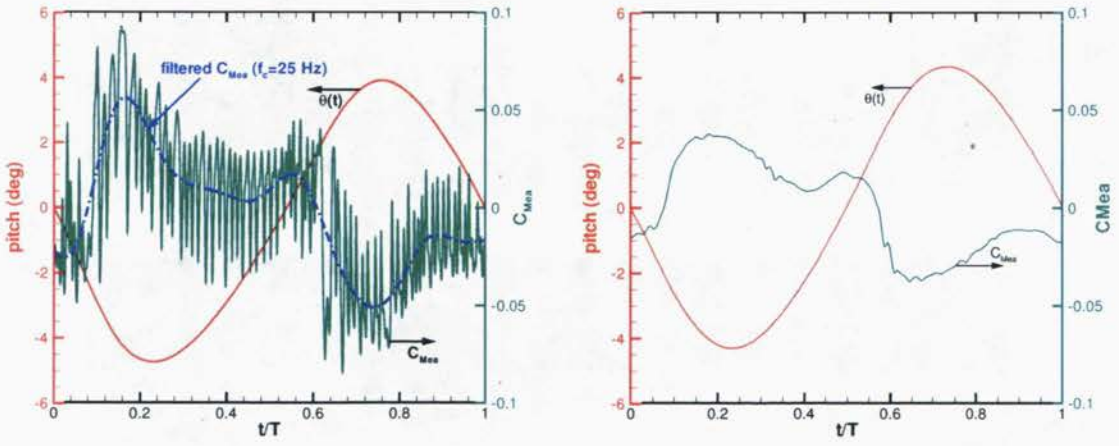

(a) $\Delta t = 2 \times 10^{-5}$ sec

(b) $\Delta t = 1 \times 10^{-3}$ sec

Figure 5.23: Pitch response and aerodynamic moment coefficient for one cycle of LCO at $\mathrm{Re_c} = 117,000$ with both a fine and a coarse timestep (model $\gamma - \mathrm{Re}_\theta$).

below as proposed by Windte *et al.* [91]:

$$\overline{u'v'} = -\tilde{\nu}_t \left(\frac{\partial \tilde{u}}{\partial y} + \frac{\partial \tilde{v}}{\partial x} \right) + \left(\overline{\tilde{u}\tilde{v}} - \bar{u}\bar{v} \right), \tag{5.2}$$

where $\tilde{u}$ and $\bar{u}$ denote the ensemble-averaged (corresponding to the computed URANS values) and phase-averaged values, respectively. The second term on the right hand side takes into account the mean flow fluctuations that are encountered in some of the calculations in the form of rolled-up vortices at the aft part of the bubble, in other words these are the variations from cycle to cycle present in the URANS solution. Note that for unsteady flows Eq. (5.2), is an approximation, as not all velocity correlations necessary for a full account of $\overline{u'v'}$ are given by the URANS solution.

When the timestep is much increased, the shed vortices are not captured by the simulation and hence, the second term approaches zero. The turbulent velocity fluctuations are then essentially modelled by the first term, creating an higher level of turbulent viscosity than in the case with the fine timestep where the second term is dominant. Looking at Fig. 5.24, we observe that even though there are some differences, the order of magnitude of the Reynolds stresses at the same instant, averaged over 25 cycles, is similar but about three times smaller than with the large timestep. The use of a coarser timestep is thus associated with a rise of turbulent viscosity which creates a similar level of turbulent dissipation, allowing for the appearance of the limit-cycle oscillations. This was also the case with the simulations of Metivier *et al.* [44, 62] who used the low-Re correction option of the SST model.

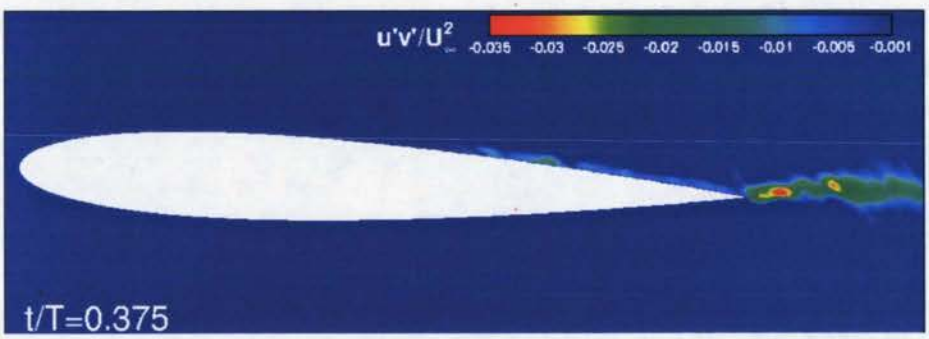

(a) $\Delta t = 2 \times 10^{-5}$ sec

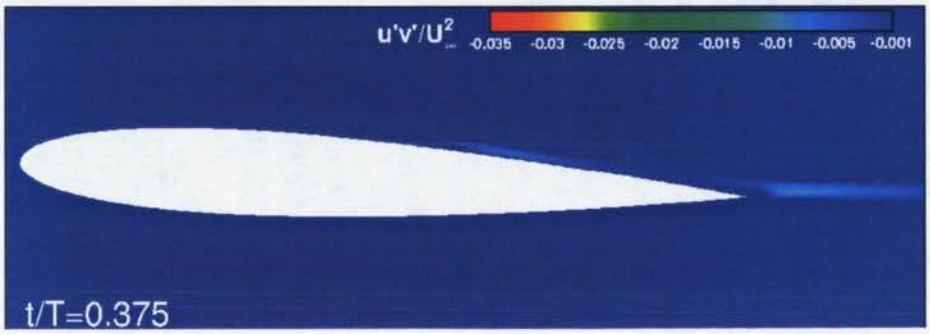

(b) $\Delta t = 1 \times 10^{-3}$ sec

Figure 5.24: Contours of Reynolds stress at one instant in a cycle at $\mathrm{Re_c} = 117,000$ using respectively a fine and a coarse timestep, averaged over 25 LCO cycles (model $\gamma - \mathrm{Re}_\theta$).

5.2 3D simulations

5.2.1 Mesh and time discretization

A 3D LES simulation has been performed for the same free-pitching NACA0012 airfoil at $\mathrm{Re_c} = 64,000$. As in the 2D URANS calculations, the same aeroelastic parameters as in the wind tunnel experiments were used. A spanwise extent of $0.1c$ was chosen based on the SD7003 test case presented earlier in order to limit the computational time and resources required. Contrary to the 2D simulations that have used the non-conformal GGI interface to take into account the pitching motion of the airfoil, the present 3D calculations make use of the algebraic grid deformation approach presented in section 3.3.2 to reduce simulation time since the GGI in *OpenFOAM* becomes quite slow on large 3D meshes.

A very fine timestep of $\Delta t = 1 \times 10^{-5}$ sec ($\Delta t^* = 4 \times 10^{-4}$) has been used to ensure that the maximum Courant number never exceeds a value of $\sim O(1)$. This allows for about 30,000 timesteps per aeroelastic oscillation and 400 timesteps per vortex shedding period. An RMS convergence criterion of 10^{-6} on all quantities is enforced at each timestep. Timestep and convergence level independence studies have shown that using a finer timestep of $\Delta t = 5 \times 10^{-6}$ sec or reaching a convergence level of 10^{-7} did not change the results.

The computation was started from unperturbed initial conditions, namely $\theta = 0$ deg and $\dot{\theta} = 0$ deg/s. Pitch oscillations thus develop freely in the simulations through a symmetry breaking mechanism in the flow field. The oscillations grow slowly over a period of a few seconds, as shown on Fig. 5.25a. Fairly periodic oscillation cycles are then observed and several such periodic cycles are computed to allow for the production of good, stationary statistics and spectral analysis. The typical run time for a whole simulation requires about four weeks on 128 Intel Xeon X5560 2.8 Ghz processors.

5.2.2 Aeroelastic characteristics

The self-sustained oscillations observed here have a maximal amplitude of approximately 5.3 degrees and a frequency of 2.57 Hz. This is in good agreement with the experimental values of 4 degrees and 2.7 Hz and the results of 2D URANS simulations (4.61 degrees and 2.53 Hz). The oscillations amplitude in the LES simulation is slightly higher than in the experimental and URANS computations. A possible explanation for this difference is the absence of freestream turbulence intensity in the LES calculation. Indeed, it was shown earlier in the URANS simulations that an increase in turbulence intensity produces a decrease

in the oscillations amplitude. Another cause could be the relatively small spanwise extent used, as will be discussed later. The average work done by the aerodynamic moment per cycle is 0.00092 Nm, close to the values of 0.00080 Nm and 0.00065 Nm obtained by the experiments and 2D URANS simulations, respectively. These positive values of the work indicate that, in average over one cycle of oscillation, the flow is transferring energy to the airfoil thus sustaining the aeroelastic LCOs.

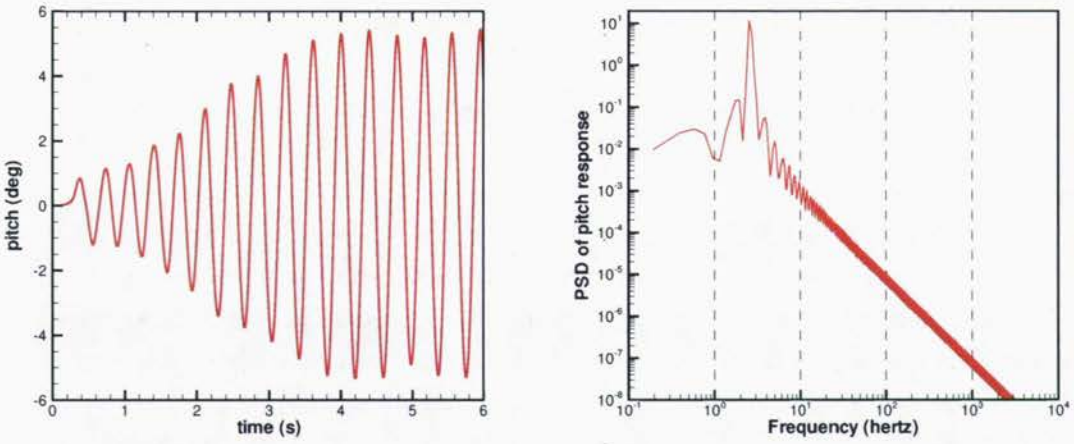

(a) Pitch history

(b) PSD of pitch response

Figure 5.25: Airfoil pitching amplitude and frequency over the whole run at $\mathrm{Re}_c = 64,000$ (LES).

The evolution of the aerodynamic moment coefficient and pitch angle during one cycle is presented in Fig. 5.26. The important fluctuations of the moment coefficient are caused by the small, high-frequency von Kármán vortices as mentioned earlier. Also shown on the figure is the filtered moment coefficient with a low-band-pass filter at a cut-off frequency of 25 Hz. Recall that the filter has for effect to eliminate the fluctuations caused by turbulence and the vortex rolling, while keeping the super harmonics of significant strength. As the airfoil is moving pitching up at the beginning of the cycle, the moment coefficient is positive but decreasing. Around $t/T = 0.125$, it becomes negative and keeps going down until around $t/T = 0.25$. From $t/T = 0.25$ to 0.5, the moment remains negative and relatively constant and thus induces the downward motion of the airfoil. The opposite is observed in the second half of the cycle. The aeroelastic behavior reported here is similar to what was obtained in the 2D URANS simulations using the $\gamma - \mathrm{Re}_\theta$ transition model in section 5.1.2.

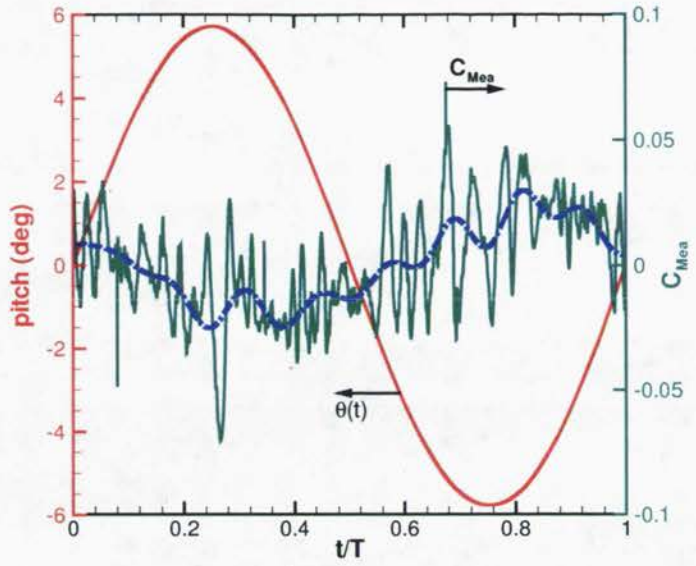

Figure 5.26: Pitch response and aerodynamic moment coefficient for one cycle of LCO at $Re_c = 64,000$ (LES). Blue dashed curve is the filtered (25 Hz) moment coefficient.

5.2.3 Flow dynamics

Figure 5.27 shows the instantaneous spanwise vorticity contours at midspan at five times during a LCO cycle. The boundary layer separation followed by the Kelvin-Helmholtz instability in the separated shear layer is clearly visible on the upper side at $t/T = 0$, 0.125 and 0.25. The iso-surfaces of Q-criterion [12] are shown in Fig. 5.28. The analysis of the flow field reveals the 3D distortion of the two-dimensional shear layer and the presence of three-dimensional turbulent structures over the airfoil. This breakdown of the 2D flow to 3D is characteristic of the transition from laminar to turbulent flow. This corroborates the results of the 2D URANS simulations shown in Fig. 5.9 where transition (denoted by the rise of the Reynolds stresses) was observed following the separation of the boundary layer.

In the first half of the cycle, the separated flow produces a flattened pressure plateau on the upper side of the airfoil. This flattened pressure plateau contributes to a nose-down pitching moment, as observed earlier on Fig. 5.26. While the boundary layer remains separated following transition at $t/T = 0$, 0.125 and 0.25, the situation is different at $t/T = 0.375$ and 0.5. Indeed, in that point of the cycle the turbulent boundary layer reattaches at the trailing edge, forming a LSB in a time-averaged sense. This is in agreement with both the results obtained by URANS simulations using the $\gamma - Re_\theta$ transition model and the LES results of an airfoil undergoing prescribed oscillations [64]. The presence of the laminar separation bubble is responsible for the relatively constant pitch moment in the second part of the half cycle as

noted previously [34, 64], thus playing an important role in the LCO phenomenon.

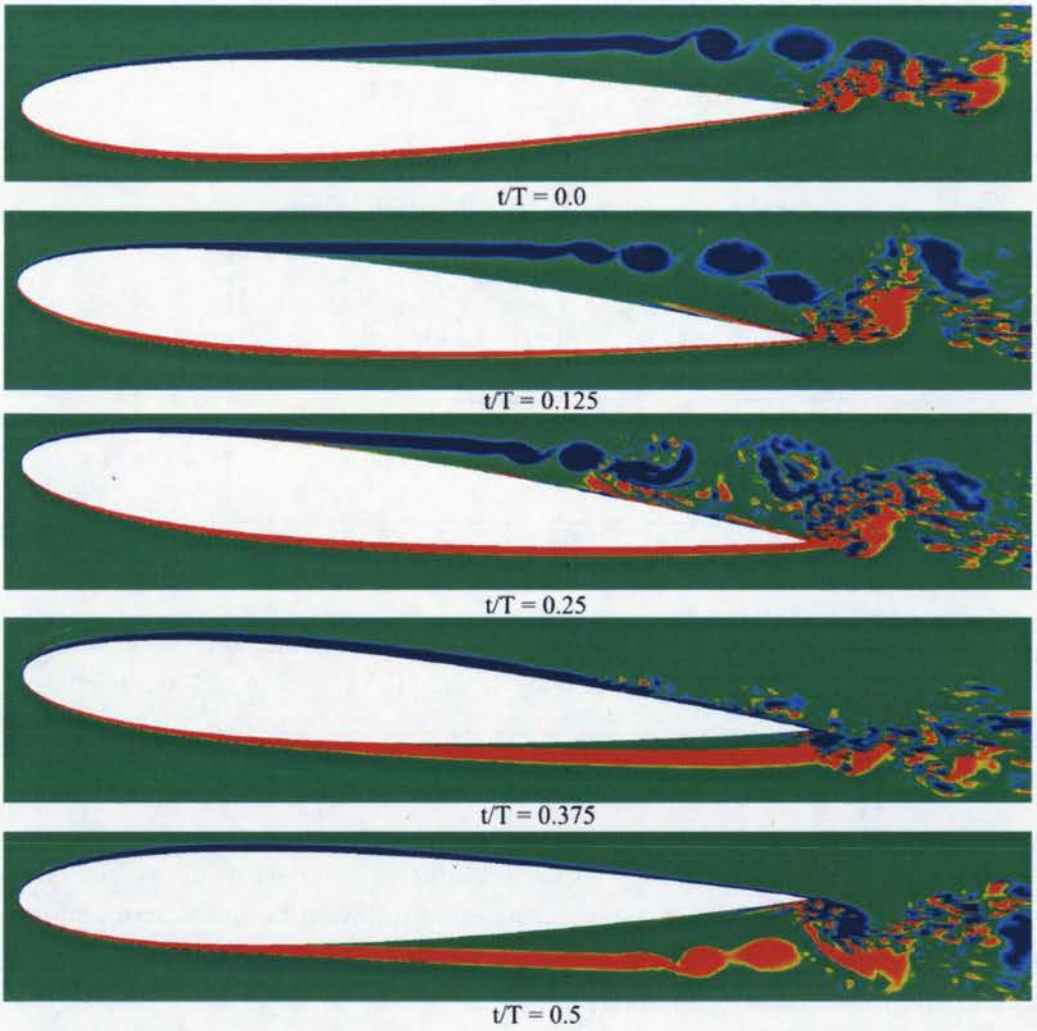

Figure 5.27: Instantaneous spanwise vorticity ω_z at fives times in a LCO cycle at $\mathrm{Re_c} = 64,000$ (LES).

In retrospect, it appears that the spanwise extent used here might not be sufficient and that could explain the difference observed in the predicted oscillation amplitude. The proper size of spanwise extent L_z should depend on the thickness of the boundary layer at the separation point δ_s. This will be the scale of the Kelvin-Helmoltz wave length and the 3D instabilities would also scale on that dimension. In the present case, with a spanwise extent of $0.1c$, $\delta_s \approx 0.02c$ meaning that $L_z = 5\delta_s$ which might be a little short. This small spanwise extent is probably constraining the flow structures and delaying the transition process. Increasing the spanwise extent to $L_z \approx 20\delta_s$ might be a solution, although this would increase the computational cost of the simulation.

The LES simulation has confirmed that the previous URANS computations with the tran-

sition model performed well at capturing quite well the physics involved at a much cheaper cost. Despite the 2D assumption of the flow, the main features such as the separation of the boundary layer and formation of a LSB are present and the oscillations amplitudes and frequencies are predicted with acceptable accuracy.

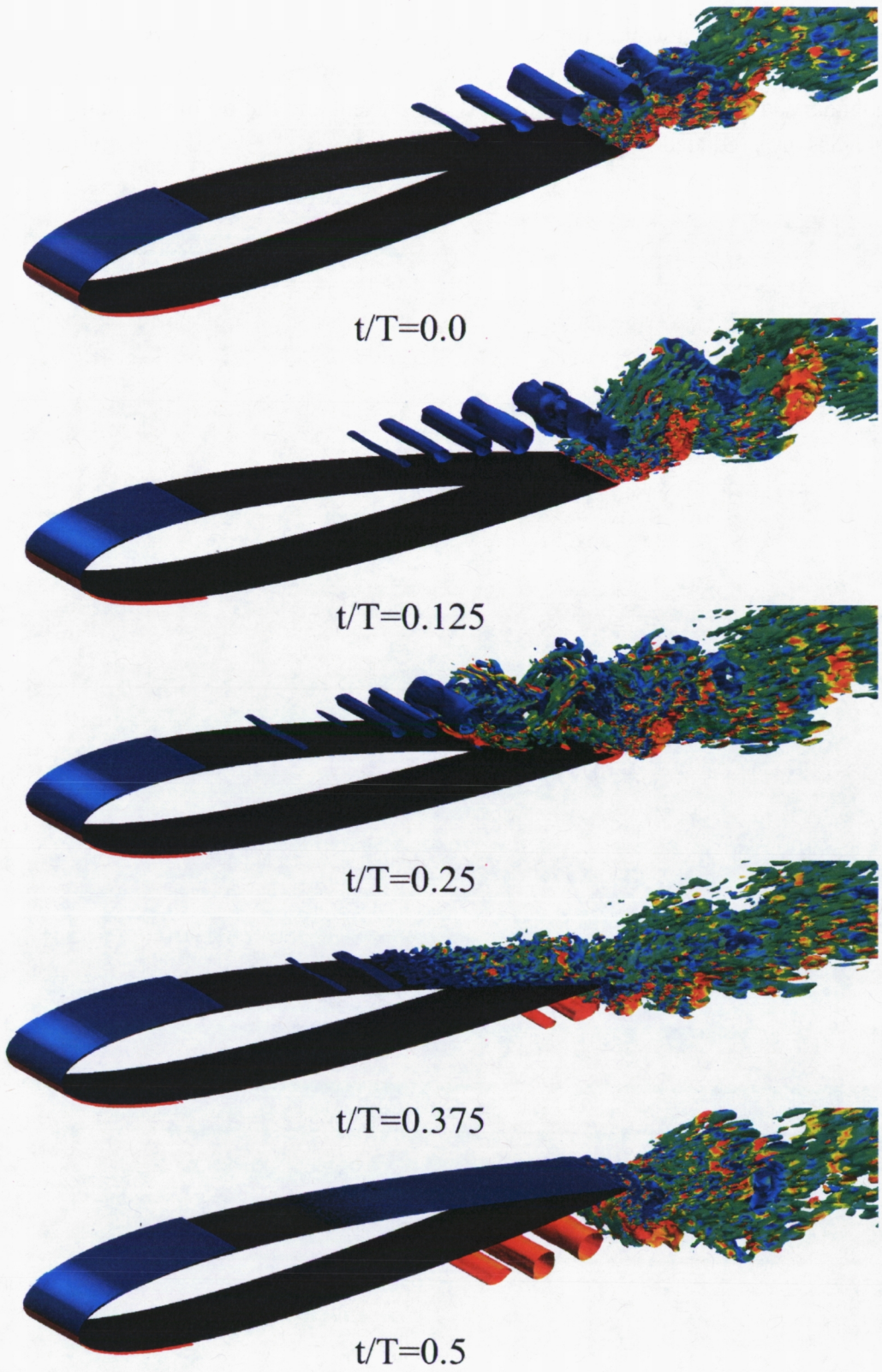

Figure 5.28: Instantaneous iso-surfaces of Q-criterion, colored by spanwise vorticity at Re_c = 64,000 (LES).

Chapter 6

NACA0012 pitch-heave oscillations

Simulations with both free pitching and heaving motions are presented in this chapter. The methodology described in section 3.3.1 is used to perform the computations and the results are compared with the available wind tunnel experiments of Poirel's group presented earlier in section 1.2. Force coefficients and flow fields are analyzed and, to relate this application to hydrokinetic turbine design, the power extraction efficiencies of the oscillating airfoil are also presented.

6.1 Mesh and time discretization

The mesh used in these simulations is the same as the baseline mesh in the pitch-only simulations. Following mesh convergence studies, the mesh was deemed fine enough around the airfoil and in the wake region to properly compute even the massively separated flows that may occur in some cases in these two DOF LCOs.

The timestep of $\Delta t = 2 \times 10^{-5}$ sec ($\Delta t^* = 6 \times 10^{-4}$ to 2×10^{-3} depending on airspeed) is kept constant in all simulations.

6.2 Aeroelastic characteristics

Simulations have been performed to demonstrate the capability of modern CFD to capture these pitch-heave limit cycle oscillations at transitional Reynolds numbers and to compare

I_{axis}	0.0014	kg·m^2
D_θ	0.0020	N·m·s/rad
K_θ	0.3000	N·m/rad
m	0.7710	kg
K_h	75 - 371	N/m
D_h	3.5	N·s/m
x_{EA}	0.186c	
x_θ	0.1c	
c	0.156	m

Table 6.1: Aeroelastic parameters used in the 2-DOF computations.

the predictions with the preliminary experimental results of Mendes *et al.* [39]. Based on the scarce available data (conference paper [39]), parameters have been chosen to match as best as possible those of the experiments concerning the inertia, mass, rotation damping, rotational stiffness and heaving stiffness as shown in Table 6.1. The heaving damping was first set at $D_h = 3.5$ N·s/m ($\zeta = 0.1$) which was established as an educated guess following a personal communication with Poirel. The effect of this parameter is investigated later.

Turbulence modeling is done using the $\gamma - \mathrm{Re}_\theta$ transition model and the Spalart-Allmaras RANS model. In the cases where large pitching amplitudes occur, the transition phenomena are expected to have a lesser impact on the physics which could justify the use of a traditional RANS model such as Spalart-Allmaras. A series of simulations without a turbulence model (laminar) is also performed.

If we recall the experimental results described in section 1.2, both small and large oscillations were measured using a high plunge stiffness while only relatively small oscillation amplitudes were observed when a low plunge stiffness was used. To obtain the large amplitude oscillations, an external perturbation had to be provided.

In the present computations, to start with, no initial perturbations were imposed. The wing was initially at an angle of attack of zero degree with no angular or heaving velocity. Using these initial conditions, no large LCOs were obtained. The pitching amplitudes reported are very similar to the cases of one DOF where only the pitching motion is allowed. The plunging amplitudes were very small, almost negligible. Changing the heaving stiffness from small (75 N/m) to large (371 N/m) did not influence the results.

The second step was to give the wing an initial perturbation. Providing the wing with an initial heaving velocity, the results obtained are very different. Using the higher heaving

stiffness, LCOs of large pitching and heaving amplitudes are obtained. However, when the smaller heaving stiffness is used, no oscillations of significant heaving amplitude occur. The focus here will be on the large amplitude oscillations. Figure 6.1 presents the pitching and heaving amplitudes as well as frequencies of the LCOs predicted. Results do not show a very good quantitative agreement with the experimental measurements of Mendes *et al.* [39] but similar observations are made. Large pitching amplitudes are obtained over the whole Reynolds number range with both turbulence models as well as for the laminar simulations. The numerical simulations also present a decrease in pitching amplitudes at Reynolds numbers higher than 90,000, a trend also present in the experiments. However the simulations tend to predict higher maximal angles of attack than the experimental measurements. This discrepancy is attributable to the turbulence modeling and the bi-dimensionnality of the simulations, as 2D URANS simulations have a tendency to overestimate the lift due to the artificial vortex coherence, but mainly to the difference between the structural and geometric parameters used in the present computations and those used in the experiments. Recent discussions with the experimental team have informed us that the experimental setup had distinct heaving and rotating masses and that the heaving stiffness used was higher than in the present computations.

On the other hand, frequencies obtained from the computations are quite close to the experiments, albeit slightly higher.

Figures 6.2 and 6.3 show the airfoil's pitching and heaving amplitudes over the whole run along with the power spectral density of the responses. In both cases the oscillations are periodic and they have the same dominating frequency. This is typical of all cases over the range of Reynolds numbers of interest.

Figure 6.4 shows both the pitching and heaving responses for one LCO cycle at two Reynolds numbers. This shows that there is a phase-shift between the pitching and heaving motions as the wing does not reach its higher angle of attack when it is at the highest vertical position. To quantify this phenomenon, ϕ is defined as the phase-shift between the pitching and heaving motions. It is expressed in degrees to compare with previous studies [28–30] of oscillating wings turbines even though, in the present case, the motions are not necessarily purely sinusoidal. Hence, for example, $\phi = 90$ degrees corresponds to a shift of a quarter cycle between pitching and heaving which is typical for the turbine applications.

At $\mathrm{Re_c} = 75,000$, the phase-shift is $\phi = 40$ degrees ($\sim 1/10$ cycle) while at $\mathrm{Re_c} = 117,500$ it is $\phi = 97$ degrees ($\sim 1/4$ cycle). Looking over the range of Reynolds numbers, the phase-shift increases with the Reynolds number, from $\phi = 24$ degrees at $\mathrm{Re_c} = 64,000$ to $\phi = 117$ degrees at $\mathrm{Re_c} = 139,000$. These results are presented in Table 6.2 at the end of this section.

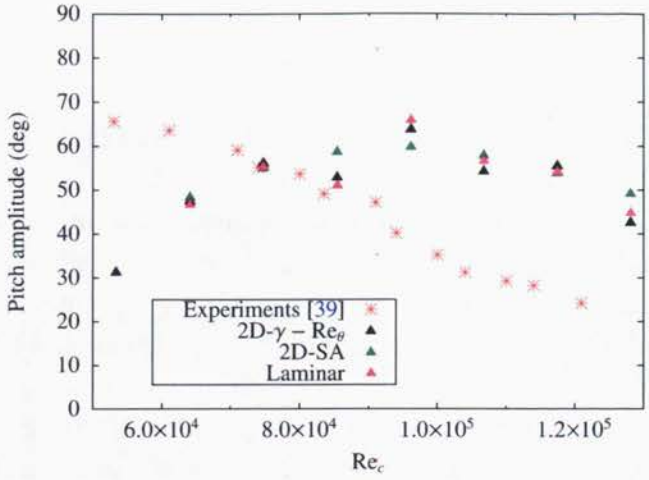

(a) Pitching amplitudes

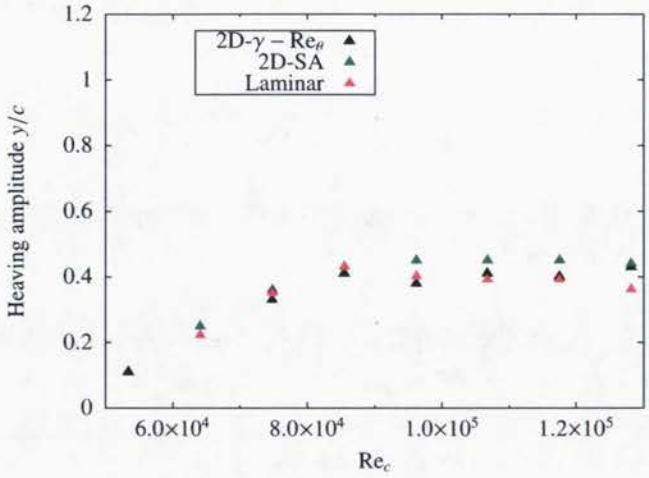

(b) Heaving amplitudes

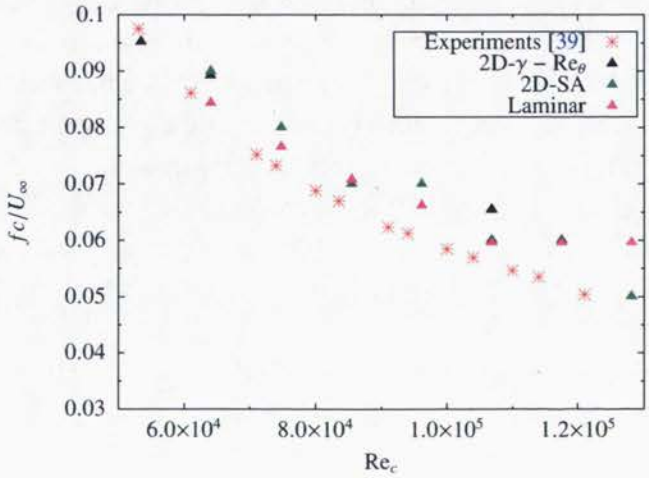

(c) Frequencies

Figure 6.1: Comparison of self-sustained 2 DOF oscillations characteristics from the present numerical simulations with different turbulence models and available experimental data.

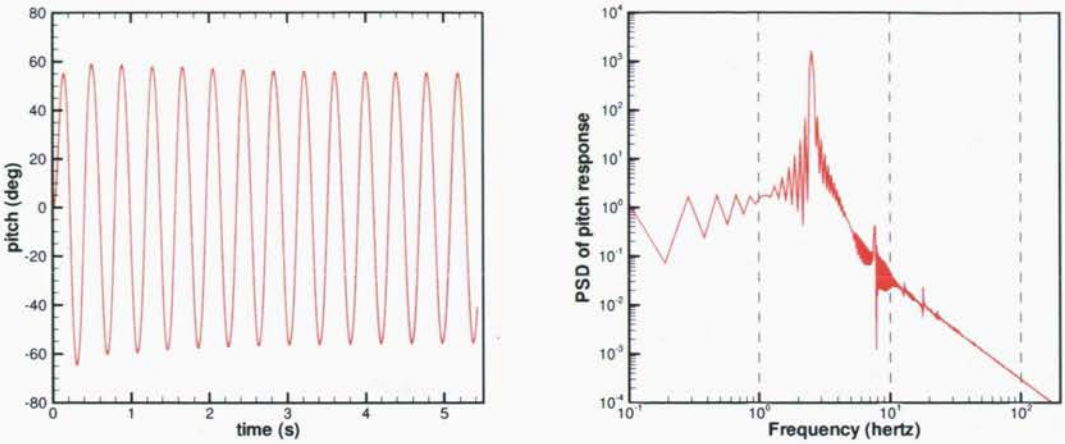

(a) Pitch history

(b) PSD of pitch response

Figure 6.2: Airfoil pitching amplitude and frequency over the whole run at $\mathrm{Re_c} = 64,000$ (2 DOF).

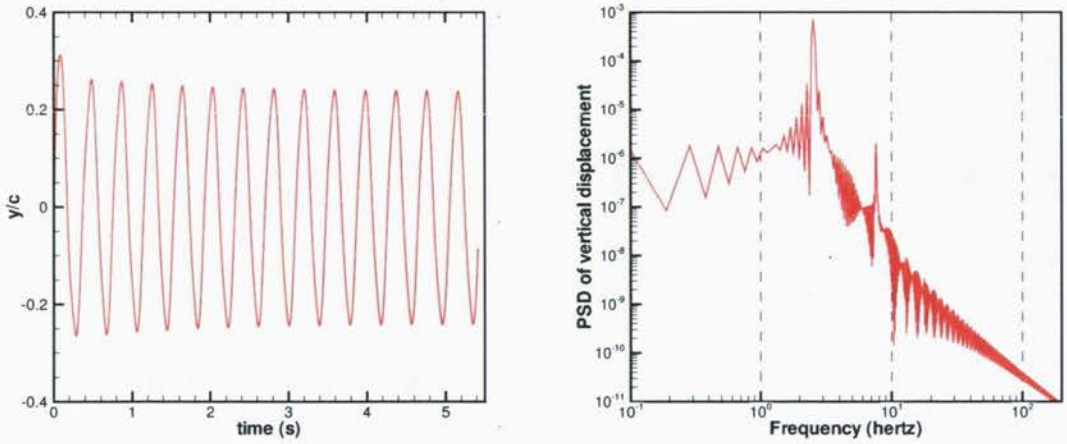

(a) Heaving history

(b) PSD of heaving motion

Figure 6.3: Airfoil heaving amplitude and frequency over the whole run at $\mathrm{Re_c} = 64,000$ (2 DOF).

The evolution of the vertical force coefficient C_y and the aerodynamic moment coefficient C_m in one LCO cycle is shown in Fig. 6.5 at the same two Reynolds numbers.

Looking first at C_y, it increases rapidly from $t/T = 0$ to $t = T/8$. Then follows a sharp decrease (up to $t = 3T/8$ at $\mathrm{Re_c} = 75,000$ and up to $t = T/4$ at $\mathrm{Re_c} = 117,500$) succeeded by

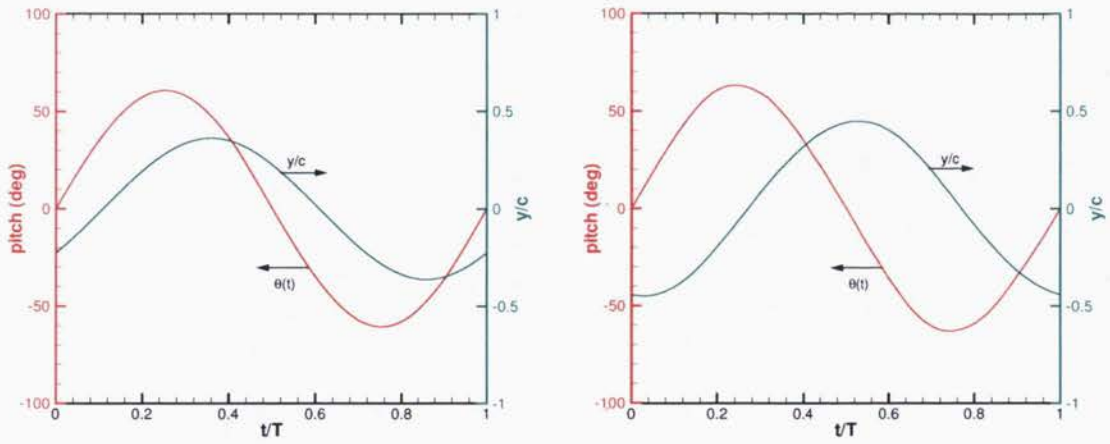

(a) $\mathrm{Re_c} = 75,000$ (b) $\mathrm{Re_c} = 117,500$

Figure 6.4: Pitching and heaving response for one cycle of LCO at two Reynolds numbers (2 DOF).

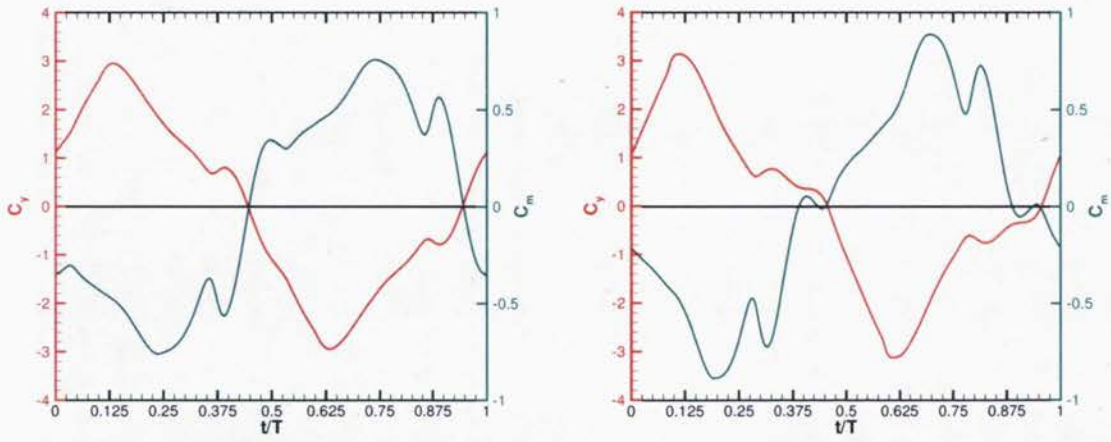

(a) $\mathrm{Re_c} = 75,000$ (b) $\mathrm{Re_c} = 117,500$

Figure 6.5: Vertical force and moment coefficients for one cycle of LCO at two Reynolds numbers (2 DOF).

a short plateau slightly above 0 around $t = 3T/8$ and then another decrease to a negative value. The moment coefficient has a somewhat opposite behavior. It is negative and decreasing at the beginning of the cycle and reaches its lower value shortly after C_y reaches its peak. It then increases and goes through a small plateau similar to C_y before increasing to a positive value. For both coefficients the opposite behavior is observed in the second half of the cycle.

6.3 Flow dynamics

The instantaneous spanwise vorticity and pressure contours at eight times in a half-cycle are shown in Figs. 6.6 and 6.7 at $\mathrm{Re_c} = 75,000$ and $\mathrm{Re_c} = 117,500$[1]. The flow dynamics is somewhat similar at both Reynolds numbers. The wing begins its cycle by pitching up, which causes the increase in C_y and decrease of C_m shown in Fig. 6.5. The pivot point being relatively close to the leading edge, the high angle of attack creates an important negative moment. C_y reaches its peak value around $t = T/8$, when a leading edge vortex starts to appear. This separation of the flow causes deep stall and the rapid decrease of lift from $t = T/8$ to $t = 3T/8$ or $t = T/4$ depending on the Reynolds number. C_m reaches its lowest value around $t = T/4$ when the wing is at its highest angle of attack and then increases as the wing starts to pitch down. The small plateau observed in both lift and moment coefficients is caused by a trailing edge vortex that forms around $t = 3T/8$ at $\mathrm{Re_c} = 75,000$ and $t = T/4$ at $\mathrm{Re_c} = 117,500$. This vortex is bigger at $\mathrm{Re_c} = 117,500$ and thus has a sligthly larger impact on the force and moment.

6.3.1 Physical mechanism

Contrary to the pitch-only oscillations, laminar separation of the boundary layer is not the triggering phenomenon of the self-sustained pitch-heave oscillations. The large pitch-heave oscillations have been obtained numerically with a fully turbulent model (Spalart-Allmaras) and experimentally even when placing a trip wire close to the leading edge, revealing the secondary role of the boundary layer regime. The large oscillations reported here are thus not associated with laminar separation flutter as it is the case with the pitch-only oscillations. The LCOs observed here are thus described as coalescence flutter [63]. The instability causing coalescence flutter is due to the coupling between the vertical and torsional degrees of freedom of the airfoil. If the center of gravity of the wing coincided with the pivot point ($x_\theta = 0$ in Eqs. (2.15) and (2.16)), then the equations of motion would not be coupled and, indeed, simulations performed with this parameter ($x_\theta = 0$) did not produce any oscillations. It is also of interest to note that increasing the value of x_θ increases the frequency of the oscillations observed. A possible explanation for this behavior is that increasing x_θ increases (or excites) the coalescence and thus produces higher flutter speeds.

Figures 6.8, 6.9 and 6.10 compare the contours of vorticity and turbulent viscosity ratio (ν_t/ν) between simulations with the Spalart-Allmaras model, the transition model and no turbulence model (laminar) at the same instant in a cycle at $\mathrm{Re_c} = 75,000$. There are some differences in the turbulent viscosity levels between these three simulations as the results

[1]Note that field data exceeding the min/max values of the color maps are coloured by that min/max value.

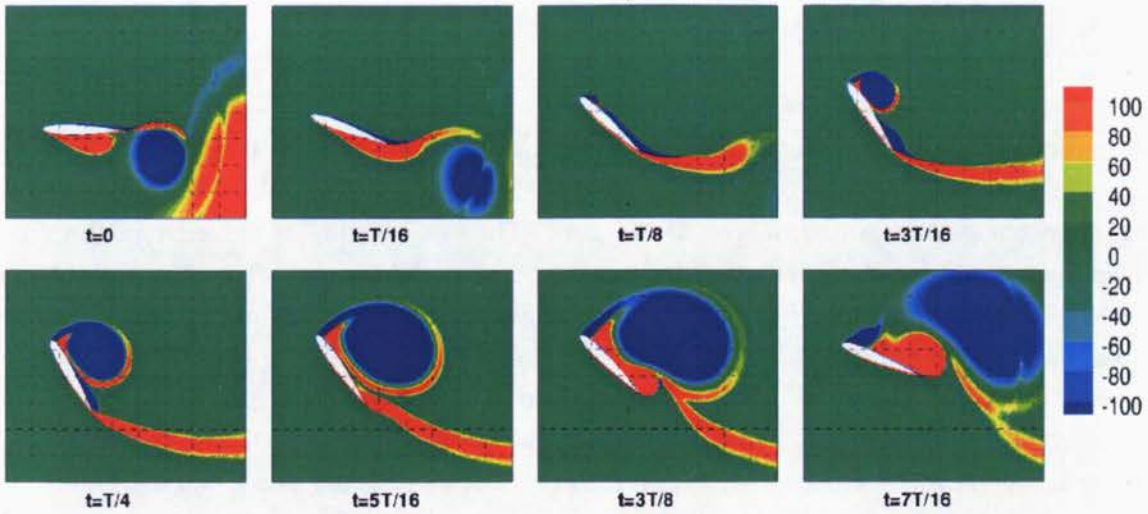

(a) Vorticity contours

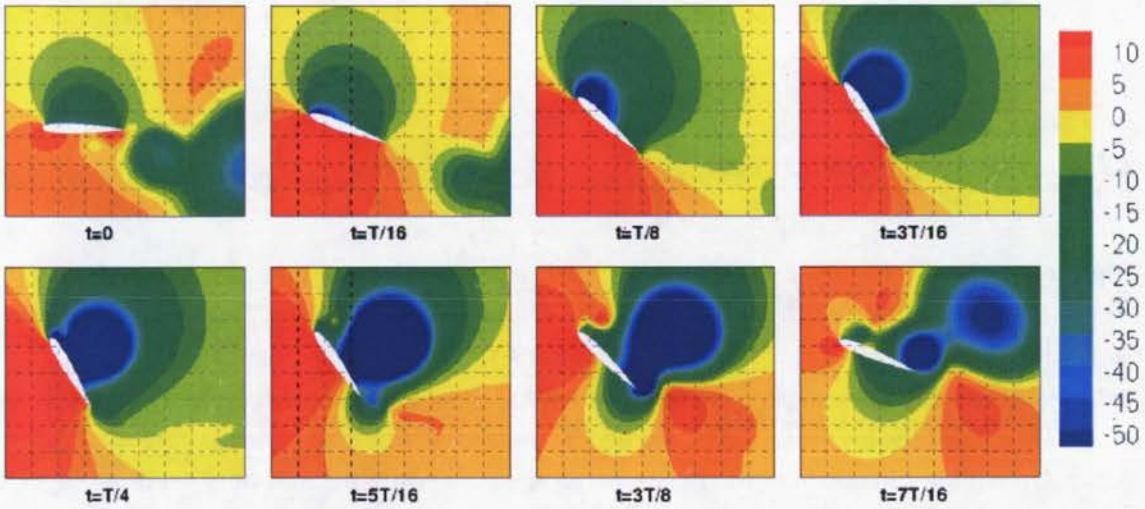

(b) Pressure contours

Figure 6.6: Instantaneous vorticity and pressure contours at $\mathrm{Re_c} = 75,000$, $\zeta = 0.1$ (2 DOF).

obtained with the transition model present lower levels of turbulent viscosity close to the airfoil and in the wake. The flow dynamics observed are somewhat in between those of a laminar simulation and those of the fully-turbulent S-A model. This is reflected in the vorticity contours which show more unsteadiness in the solution computed with the $\gamma - \mathrm{Re}_\theta$ model but less than in the laminar simulation. This is very similar to what was observed in the test case shown in section 4.2.

Despite this difference in the instantaneous flow fields, the global results are very similar. All three models predict comparable pitching and heaving amplitudes and frequencies as well as power extraction efficiencies (shown in section 6.5).

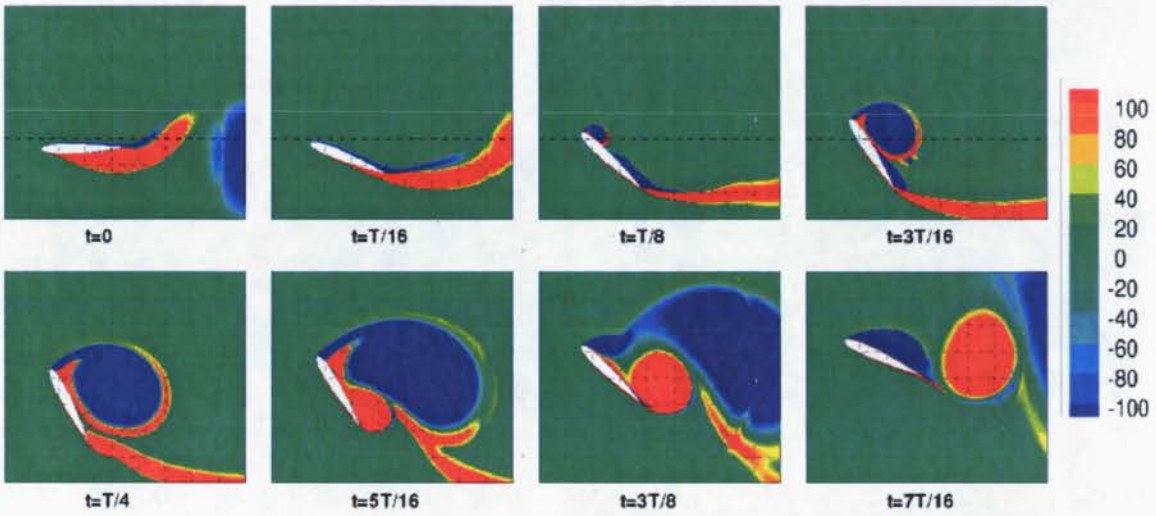

(a) Vorticity contours

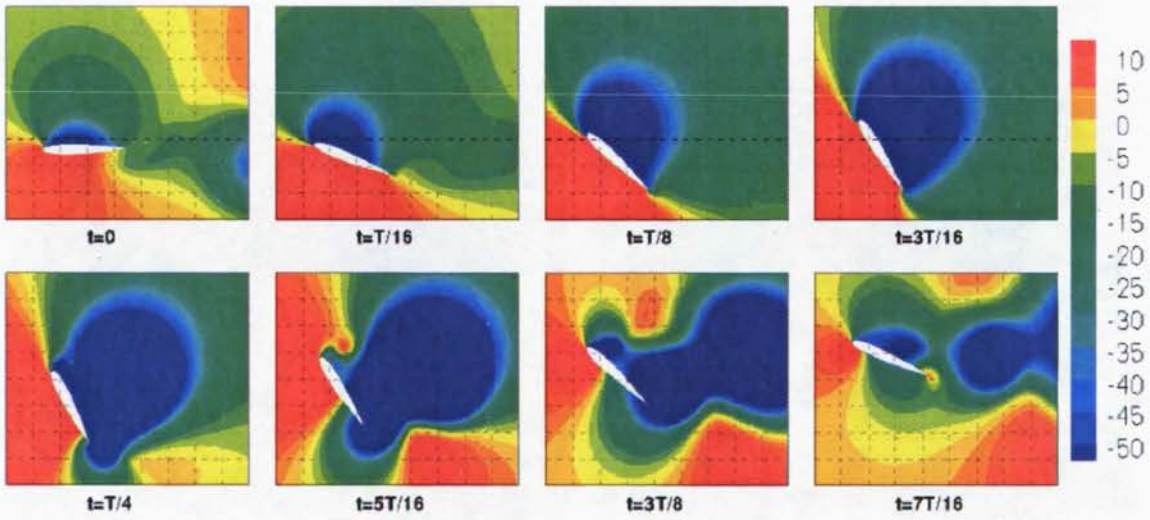

(b) Pressure contours

Figure 6.7: Instantaneous vorticity and pressure contours at $\mathrm{Re_c} = 117,500$, $\zeta = 0.1$ (2 DOF).

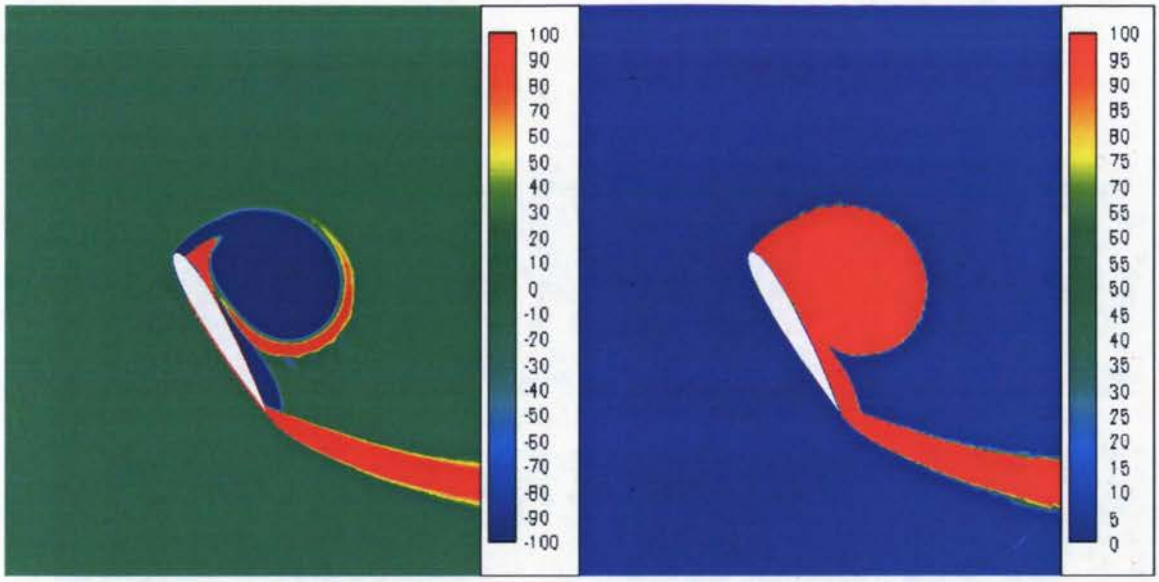

(a) Vorticity contours (b) Viscosity ratio contours

Figure 6.8: Instantaneous vorticity and viscosity ratio contours at $\mathrm{Re}_c = 75,000$, $\zeta = 0.1$, Spalart-Allmaras (2 DOF).

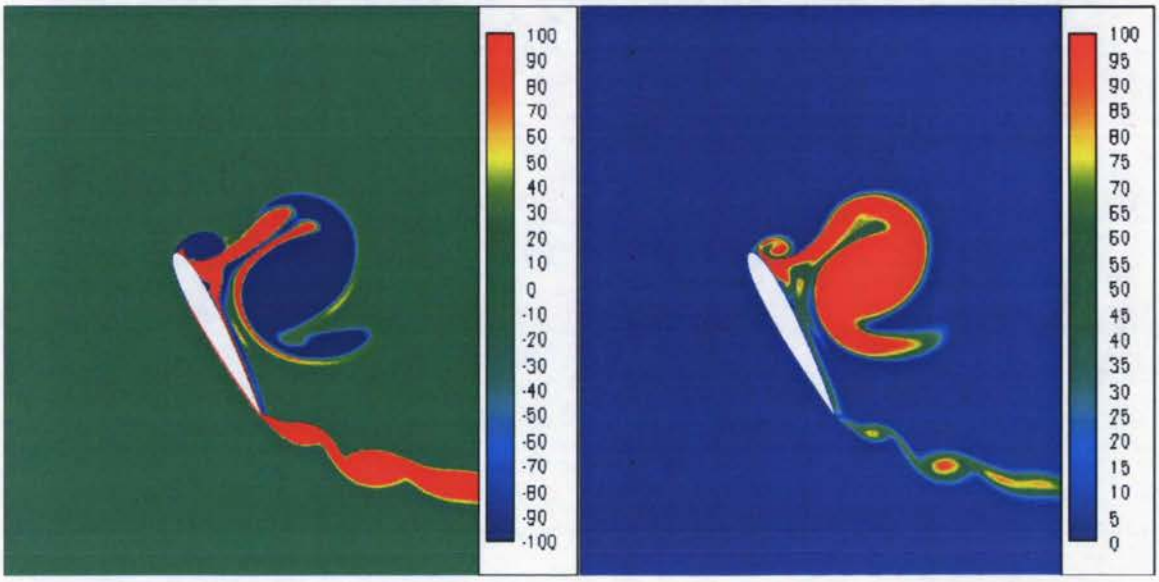

(a) Vorticity contours (b) Viscosity ratio contours

Figure 6.9: Instantaneous vorticity and viscosity ratio contours at $\mathrm{Re}_c = 75,000$, $\zeta = 0.1$, $\gamma - \mathrm{Re}_\theta$ (2 DOF).

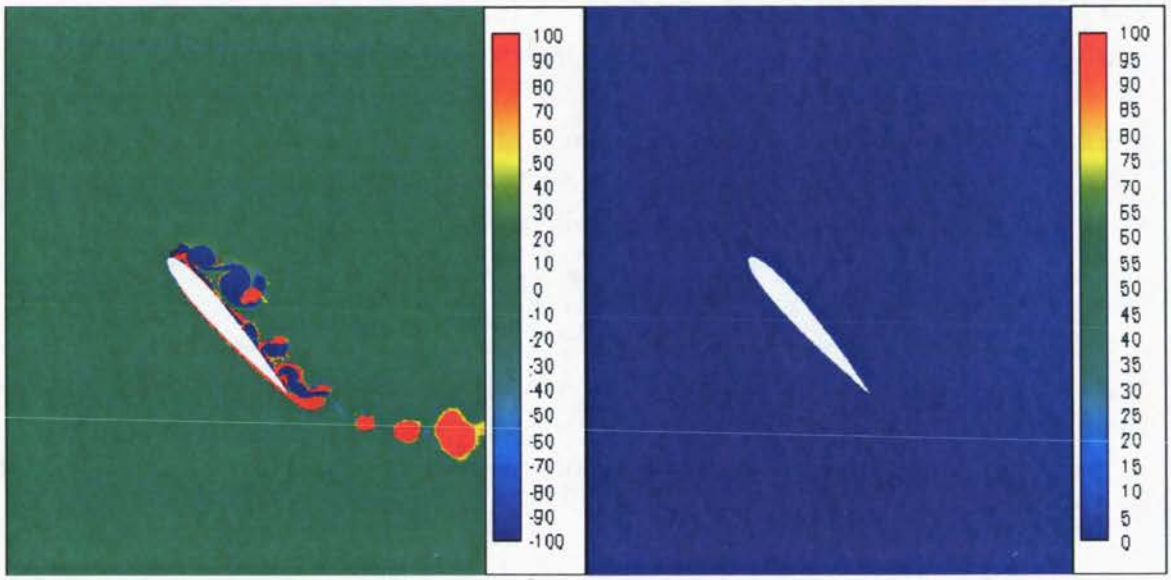

(a) Vorticity contours (b) Viscosity ratio contours

Figure 6.10: Instantaneous vorticity and viscosity ratio contours at $\mathrm{Re}_c = 75,000$, $\zeta = 0.1$, laminar (2 DOF).

6.4 Effect of vertical damping, stiffness, mass and inertia

In order to gain a better insight on the influence of other parameters on the oscillations, simulations with different values of vertical stiffness, mass and inertia have been performed.

Figure 6.11 presents the pitching and heaving amplitudes and frequencies for five different vertical damping coefficients. Oscillations were obtained in all cases except with the higher damping ($\zeta = 0.3$) at Reynolds numbers lower than 80,000. A decrease in both the pitching and heaving amplitudes is observed when higher damping coefficients are used. The frequencies appear to be only slightly influenced by the changes in vertical damping.

Figure 6.12 presents the pitching and heaving amplitudes and frequencies for two additional values of vertical stiffness (k_0 is the standard value used in the previous computations). All simulations were performed on the same range of Reynolds numbers but no oscillations have been obtained with the higher stiffness value at Reynolds lower than 90,000. The high stiffness value leads to slightly higher pitching and heaving amplitudes as well as frequencies, while the smaller value leads to lower amplitudes and frequencies.

Figure 6.13 presents the pitching and heaving amplitudes and frequencies for two additional values of the airfoil's mass (m_0 is the standard value used in the previous computations). At the smaller mass value, oscillations have only been obtained at the highest Reynolds number and were of higher amplitudes than with the standard mass value. Using a larger mass, both pitching and heaving amplitudes are reduced significantly while the frequency is only slightly decreased.

Figure 6.14 presents the pitching and heaving amplitudes and frequencies for two additional values of the airfoil's pitching inertia (I_0 is the standard value used in the previous computations). The higher value of inertia only predicted oscillations at Reynolds numbers higher than 80,000 and these oscillations are of higher pitching and heaving amplitudes and lower frequencies. The smaller value of inertia reduces both the pitching and heaving amplitudes, the latter significantly, and also increases greatly the frequency of oscillations.

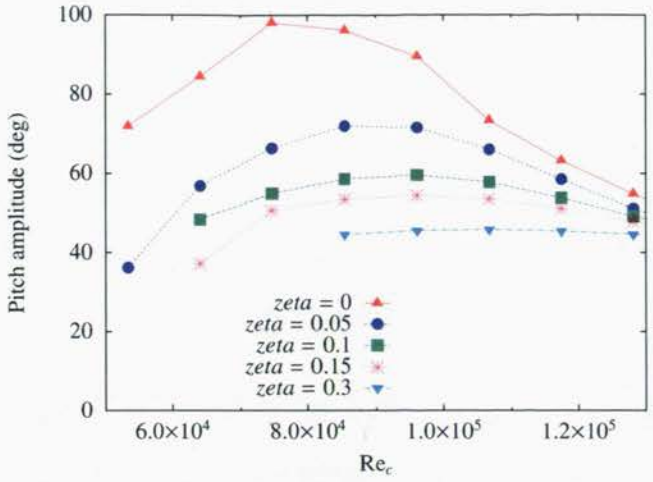

(a) Pitching amplitudes

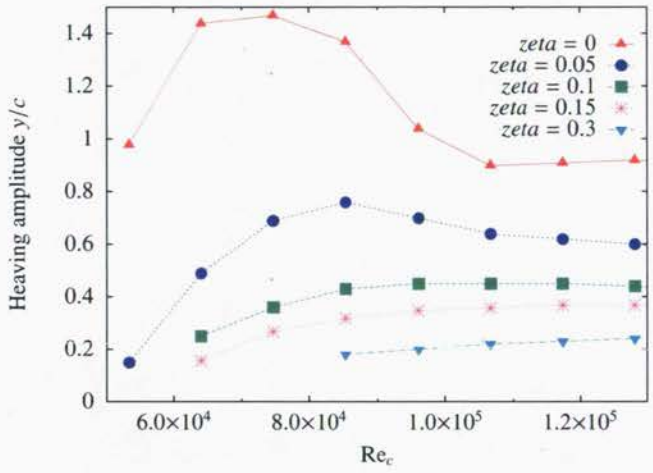

(b) Heaving amplitudes

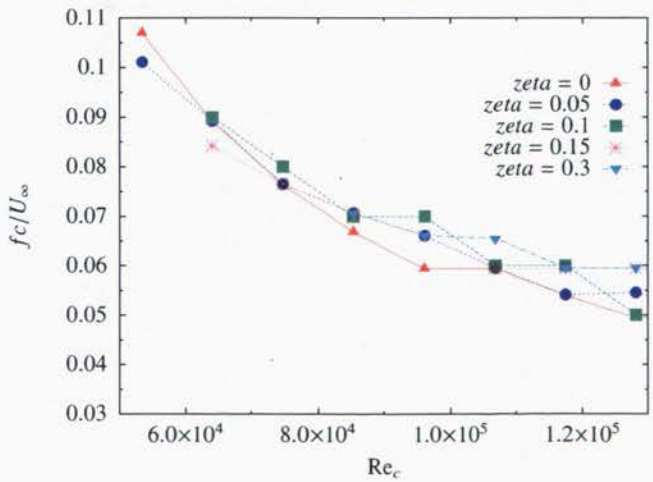

(c) Frequencies

Figure 6.11: Comparison of self-sustained 2 DOF oscillations characteristics for different vertical damping coefficients.

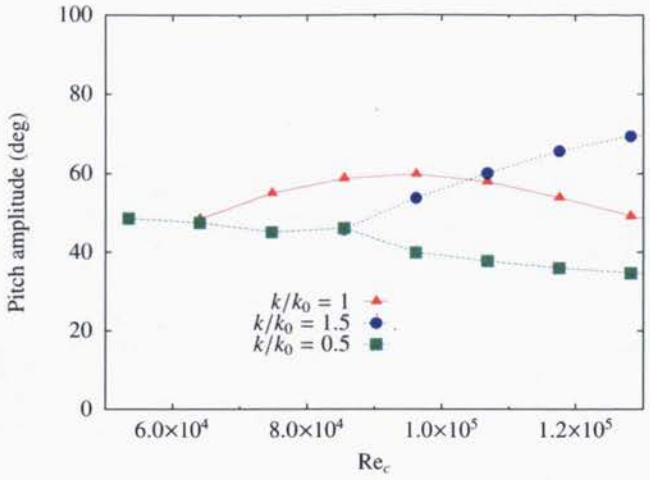

(a) Pitching amplitudes

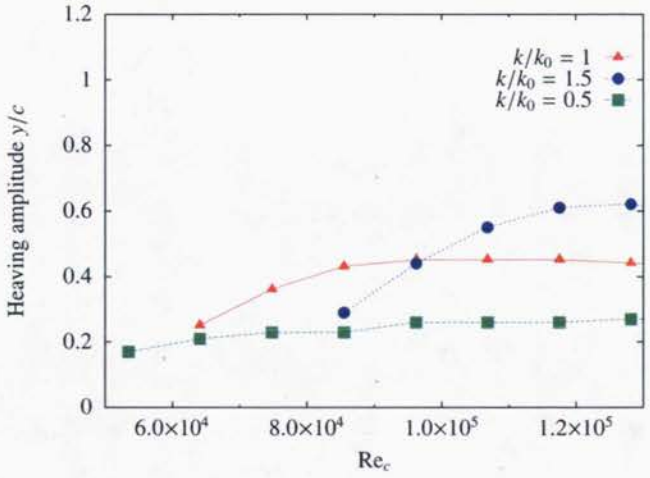

(b) Heaving amplitudes

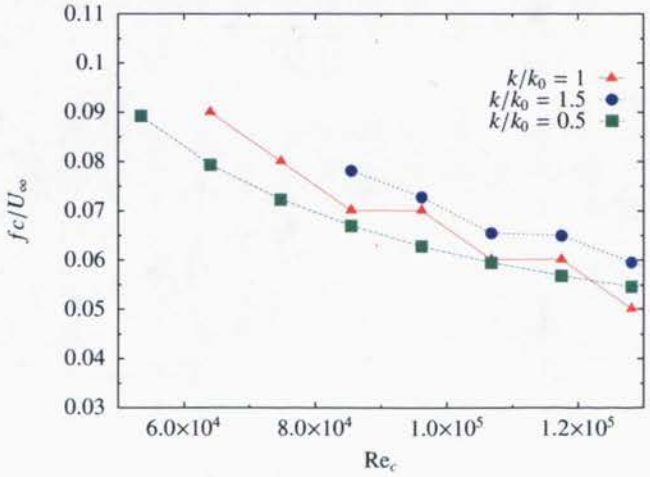

(c) Frequencies

Figure 6.12: Effect of heaving stiffness on self-sustained 2 DOF oscillations characteristics.

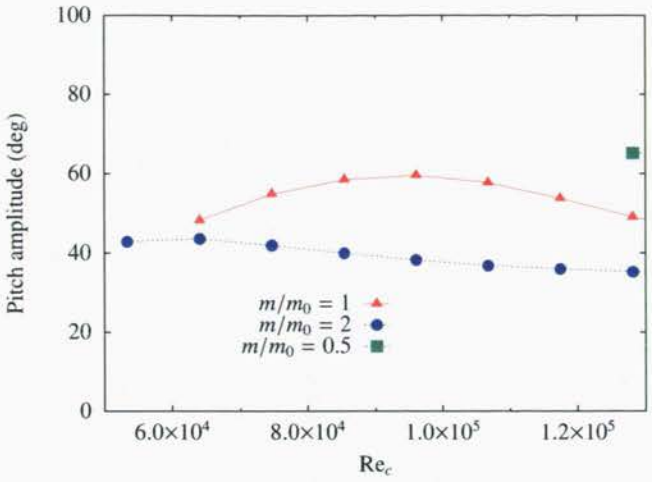

(a) Pitching amplitudes

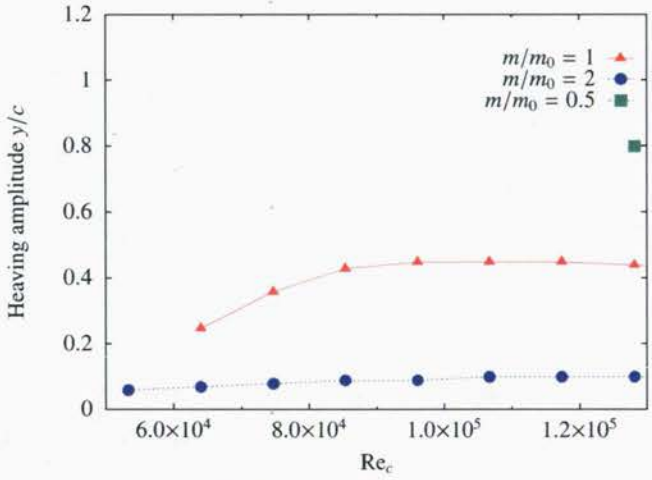

(b) Heaving amplitudes

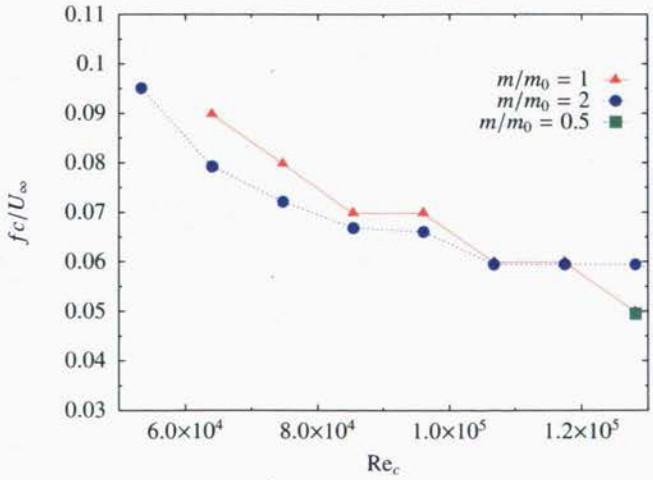

(c) Frequencies

Figure 6.13: Effect of heaving mass on self-sustained 2 DOF oscillations characteristics.

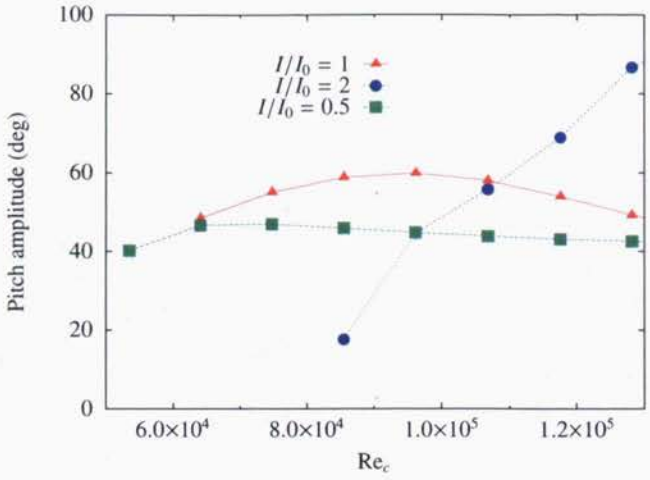

(a) Pitching amplitudes

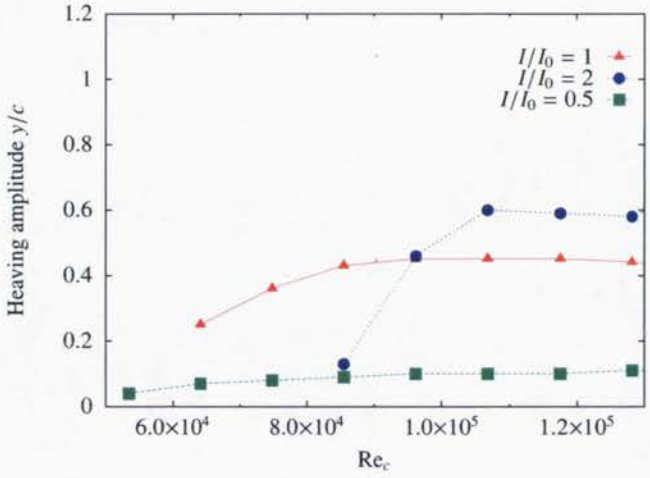

(b) Heaving amplitudes

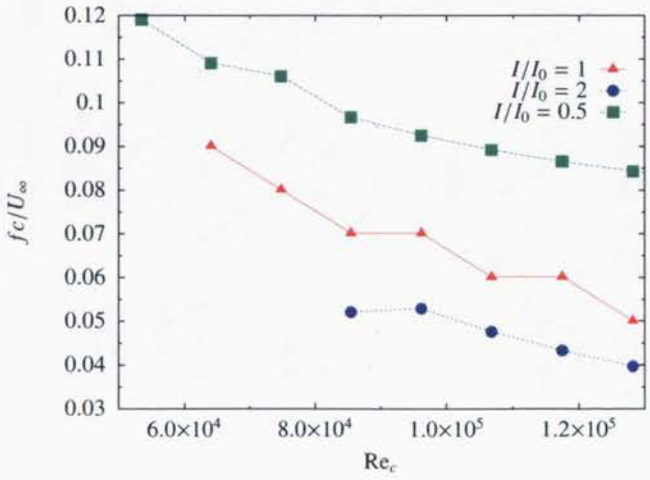

(c) Frequencies

Figure 6.14: Effect of pitching inertia on self-sustained 2 DOF oscillations characteristics.

6.5 Potential for energy harvesting

The present thesis was not meant to be a parametric study to optimize the energy harvesting performances of the self-sustained oscillating airfoil. Nonetheless, the energy extraction performances of the simulated cases may be presented and compared. A discussion about the actual potential of the present set-up follows along with suggestions of modification to improve the performances. This is a topic of interest since previous studies have shown that oscillating wing turbines [29] or oscillating cylinders [3,4] can be used to produce energy.

The results shown here have been obtained with the Spalart-Allmaras model. The efficiencies calculated from simulations with both the $\gamma - \mathrm{Re}_\theta$ transition model and no turbulence model (laminar) are very similar.

Efficiencies may be expressed with three different quantities, $\bar{C}_P$ defined in Eq. (6.1), C_P^* defined in Eq. (6.2) and η defined in Eq. (6.3). Both C_P^* and η represent the ratio of the mean power extracted ($\bar{P}$) per unit depth in a cycle to the incoming power available in a certain window of upstream flow while $\bar{C}_P$ is normalized by the chord and thus independant of the solution. For C_P^*, this window is defined as $2y_{max}$ which is the distance between the highest and lowest positions of the pivot point in a cycle. In the definition of η, d is the distance between the highest and lowest positions reached by any point of the airfoil in a cycle [29]. Thus d represents the actual flow window and is slightly larger than $2y_{max}$, which explains why η is always smaller than C_P^*. The power P is the aerodynamic power as previously defined in section 4.2.1.

$$\bar{C}_P = \frac{\bar{P}}{\frac{1}{2}\rho U_\infty^3 c}, \tag{6.1}$$

$$C_P^* = \frac{\bar{P}}{\frac{1}{2}\rho U_\infty^3 (2y_{max})}, \tag{6.2}$$

$$\eta = \frac{\bar{P}}{\frac{1}{2}\rho U_\infty^3 d}. \tag{6.3}$$

Tables 6.2 and 6.3 present the oscillation characteristics and power extraction efficiencies at different Reynolds numbers and two values of the vertical damping coefficient. In both cases ($\zeta = 0.1$ and $\zeta = 0$) the efficiency generally decreases as the Reynolds number and phase-shift increase. The highest efficiences are thus observed around $\mathrm{Re}_c \approx 60,000$ and are around 15%. These results should not be interpreted only as a Reynolds number effect as other non-dimensional parameters are changing.

The difference in efficiencies at different Reynolds numbers and damping coefficients presented in tables 6.2 and 6.3 can be better understood by looking at the separate contributions

Re	θ_{max}	y/c_{max}	fc/U	ϕ	$\bar{C}_P$	C_P^*	η
64000	48	0.25	0.089	26	0.122	0.244	0.141
75000	55	0.36	0.076	40	0.161	0.224	0.156
85500	59	0.43	0.071	52	0.161	0.187	0.124
96000	60	0.45	0.066	72	0.135	0.150	0.086
107000	58	0.45	0.059	83	0.107	0.119	0.060
117500	54	0.45	0.059	97	0.086	0.095	0.044
128000	49	0.44	0.055	108	0.068	0.077	0.035
139000	45	0.42	0.055	117	0.054	0.064	0.029

Table 6.2: Two DOF self-sustained oscillations characteristics and efficiencies, $\zeta = 0.1$.

Re	θ_{max}	y/c_{max}	fc/U	ϕ	$\bar{C}_P$	C_P^*	η
53000	72	0.98	0.107	10	0.399	0.204	0.174
64000	85	1.44	0.089	9	0.420	0.146	0.129
75000	98	1.47	0.076	10	0.197	0.067	0.060
85500	96	1.37	0.067	17	0.148	0.054	0.048
96000	90	1.04	0.059	49	0.062	0.030	0.025
107000	73	0.90	0.059	94	0.022	0.012	0.008
117500	63	0.91	0.054	112	0.015	0.008	0.005
128000	55	0.92	0.050	122	0.009	0.005	0.003
139000	47	0.90	0.050	128	0.004	0.002	0.001

Table 6.3: Two DOF self-sustained oscillations characteristics and efficiencies, $\zeta = 0$.

of the pitching and heaving motions. As mentionned previously in section 4.2.1, the power coefficient C_P is the sum of the heaving (or vertical) power coefficient C_{Py} and the pitching power coefficient $C_{P\theta}$. Figure 6.15 presents the power coefficients and their respective contributions (C_y and V_y for C_{Py} and C_m and ω for $C_{P\theta}$) in a cycle at a Reynolds number of 75,000 and $\zeta = 0.1$. The same analysis is made at $\mathrm{Re_c} = 117,500$ in Fig. 6.16.

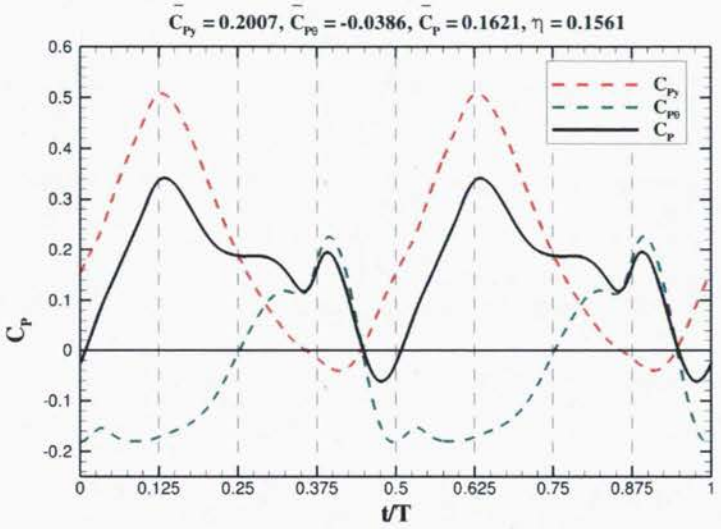

(a) Power coefficients

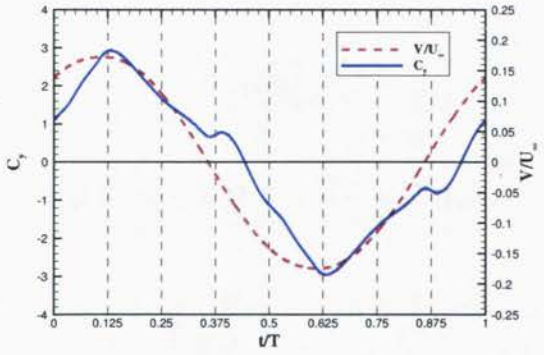

(b) Vertical force and speed

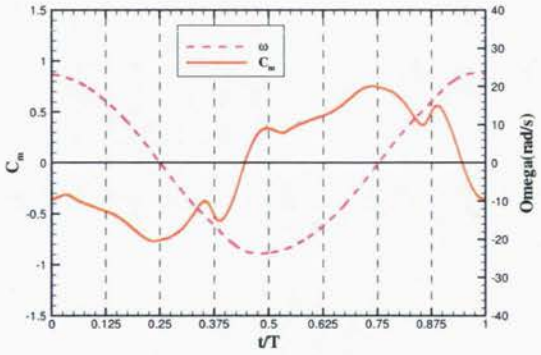

(c) Angular moment and speed

Figure 6.15: Evolutions of power coefficients in a cycle at $\mathrm{Re_c} = 75,000$, $\zeta = 0.1$ (2 DOF).

The difference in the efficiencies of these cases may now be made clearer. C_{Py} is mostly positive in both cases and larger at $\mathrm{Re_c} = 75,000$, while $C_{P\theta}$ is mostly negative in both and has a greater negative impact on efficiency at $\mathrm{Re_c} = 117,500$. The lower value of C_{Py} at $\mathrm{Re_c} = 117,500$ is explained by a lack of synchronization between C_y and V_y. As seen on Fig. 6.18b, the velocity reaches its peak when C_y is rather small due to the separated flow as opposed to the case at $\mathrm{Re_c} = 75,000$ (see Fig. 6.17b) where C_y and V_y are at their highest and lowest values at the same time, increasing the power extracted.

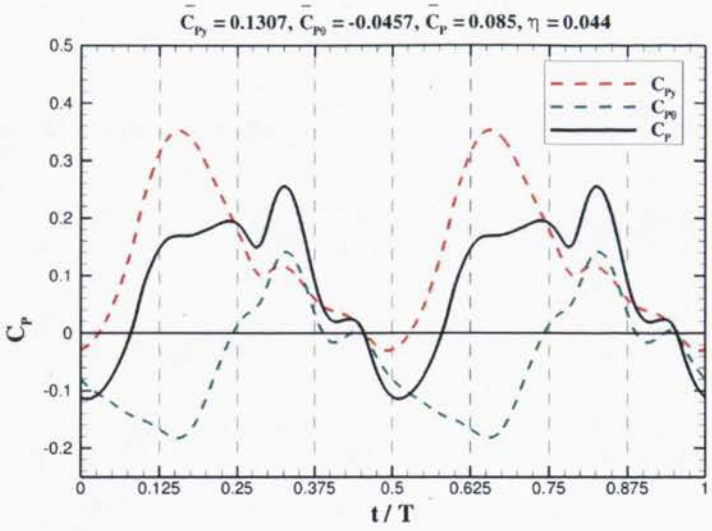

(a) Power coefficients

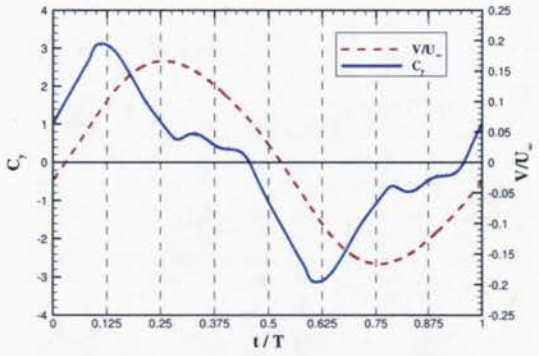

(b) Vertical force and speed

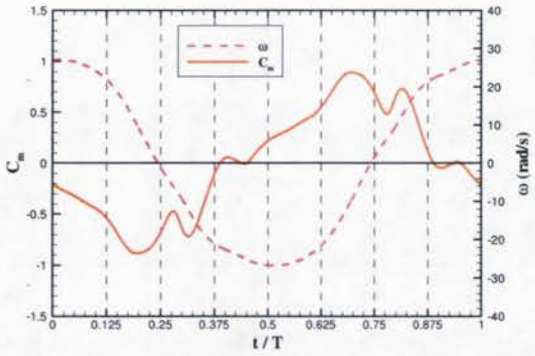

(c) Angular moment and speed

Figure 6.16: Evolutions of power coefficients in a cycle at $\mathrm{Re_c} = 117,500$, $\zeta = 0.1$ (2 DOF).

The evolution of the power coefficients at the same two Reynolds numbers is presented in Figs. 6.17 and 6.18 for the cases with $\zeta = 0$ which all have a larger heaving amplitude. However, this higher amplitude does not translate into greater efficiencies, but it does produce higher power coefficients $\bar{C}_P$.

At $\mathrm{Re_c} = 75,000$, there are significant portions of the cycle where C_{Py} is negative due to a positive C_y combined with a negative V_y, at $t = 7T/16$ and the opposite at $t = 15T/16$. The second peak of positive C_y at $t = 7T/16$ is due to the presence of a large trailing edge vortex coming over the upper side of the airfoil as it is moving down. It is clearly seen in Fig. 6.19 which presents the vorticity and pressure contours at different instants in a cycle.

At $\mathrm{Re_c} = 117,000$ the low power extraction is due in part to a weak coordination of

C_y and V_y as C_y almost vanishes when the wing is at its highest velocity. $C_{P\theta}$ also has an important negative contribution as the moment coefficient reaches its highest absolute values at times when the angular velocity is also high but of opposite sign. This happens at $t = T/8$ and $t = 5T/8$ when the airfoil is at a large angle of attack and there is not yet a leading edge vortex to counteract the moment applied by the incoming flow on the airfoil. This is seen in Fig. 6.20.

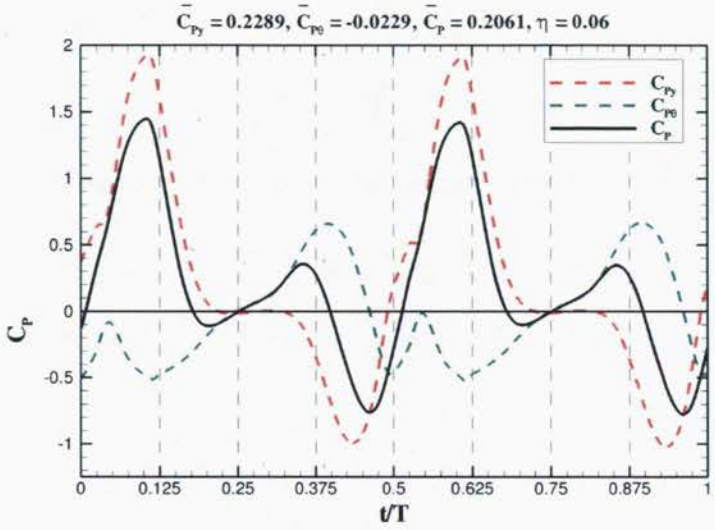

(a) Power coefficients

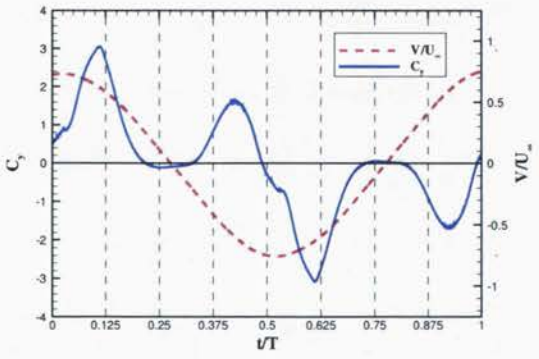

(b) Vertical force and speed

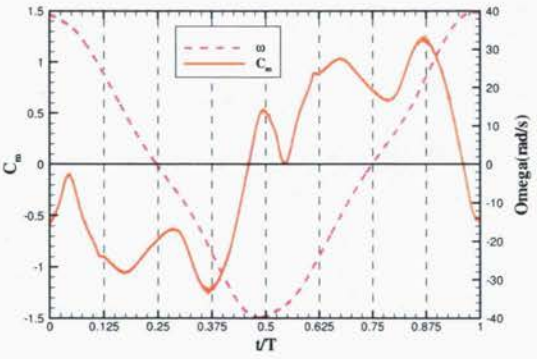

(c) Angular moment and speed

Figure 6.17: Evolutions of power coefficients in a cycle at $\mathrm{Re_c} = 75,000$, $\zeta = 0$ (2 DOF).

Discussion

As seen previously, the combination of large pitching amplitudes and a relatively low frequency lead to strong dynamic stall and thus massively separated flows. This limits the

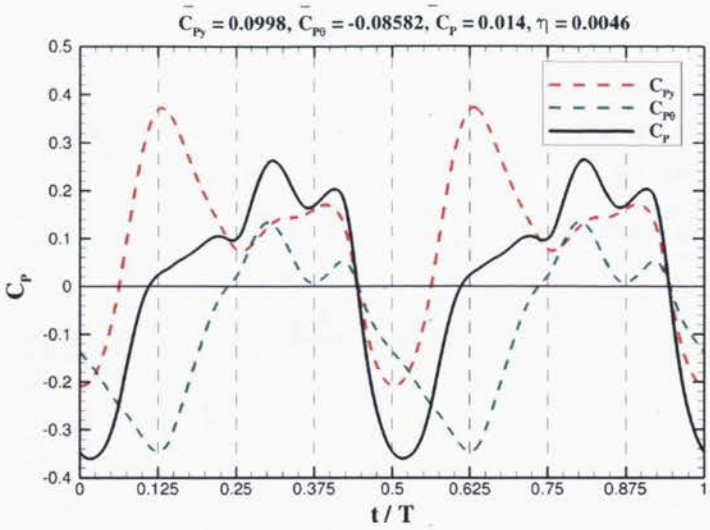

(a) Power coefficients

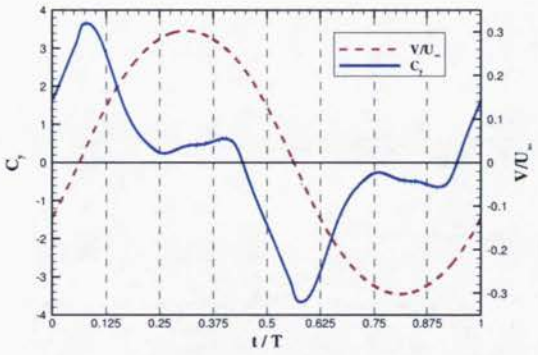

(b) Vertical force and speed

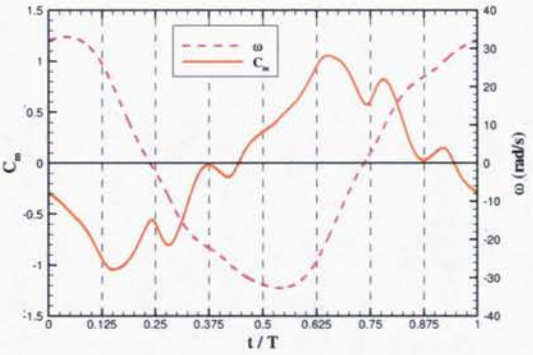

(c) Angular moment and speed

Figure 6.18: Evolutions of power coefficients in a cycle at $Re_c = 117,500$, $\zeta = 0$ (2 DOF).

energy extracted as the vertical force drops rapidly following separation. Hence, the efficiencies are lower than those of optimized and controlled oscillating airfoils motions presented by Kinsey [29]. However, the performances of the current oscillating airfoils are similar to those of the VIVACE turbine of Bernitsas *et al.* [3, 4] which is constituted of an oscillating cylinder. This is logical since the flow around a bluff body such as a cylinder produces large alternate vortex shedding, somewhat similarly to what was shown in the present study with the free oscillating wing.

There is also a close resemblance between the current study and the recent results of Peng and Zhu [57]. In the latter, the authors investigated the dynamics of a foil mounted on a rotational spring and a heaving damper. The motion was passively generated by flow-induced instability and periodic oscillations were obtained for certain parameters (position of

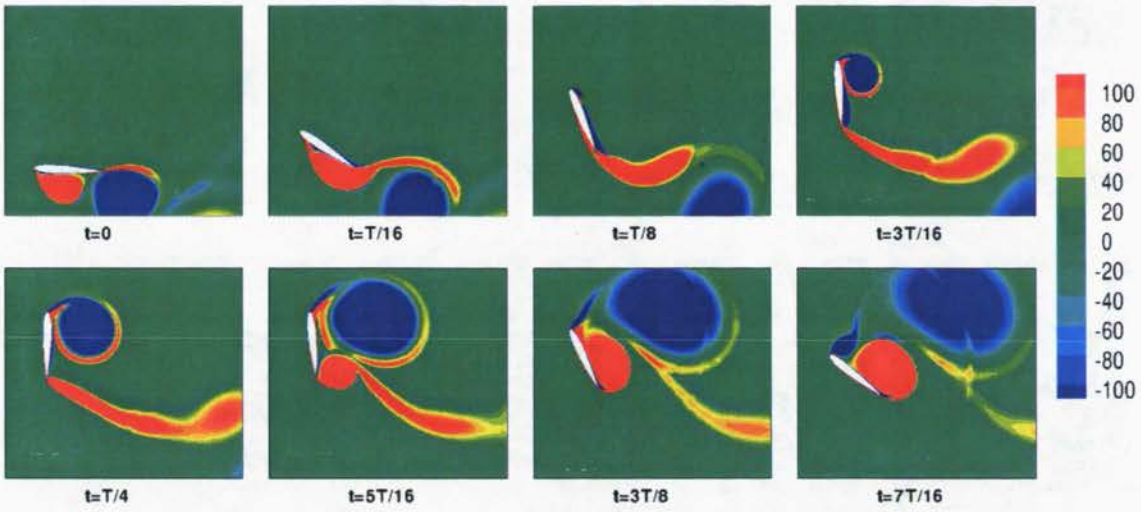

(a) Vorticity contours

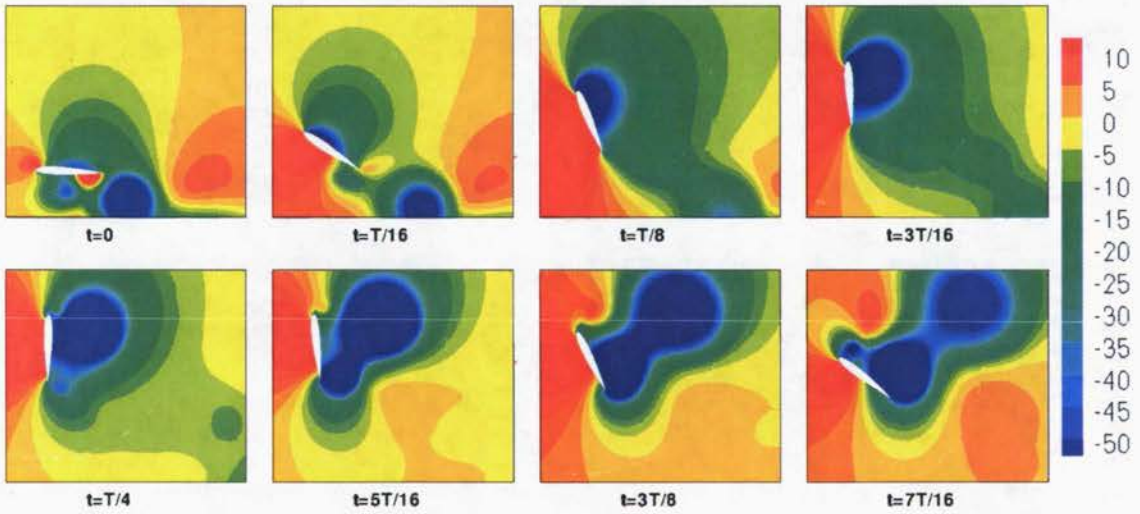

(b) Pressure contours

Figure 6.19: Instantaneous vorticity and pressure contours at $\mathrm{Re_c} = 75,000$, $\zeta = 0$ (2 DOF).

pitching axis and rotational spring). In optimal conditions, they reported an energy harvesting efficiency of 20% (defined as η) along with large pitching amplitudes (around 60 degrees for the most efficient cases), a total vertical flow window of $\sim 1.5c$ and frequencies between 0.08 and 0.15.

Possible improvements

Based on the current results, there appears to be many interesting possibilities to further optimize the power extraction efficiencies of a free oscillating airfoil.

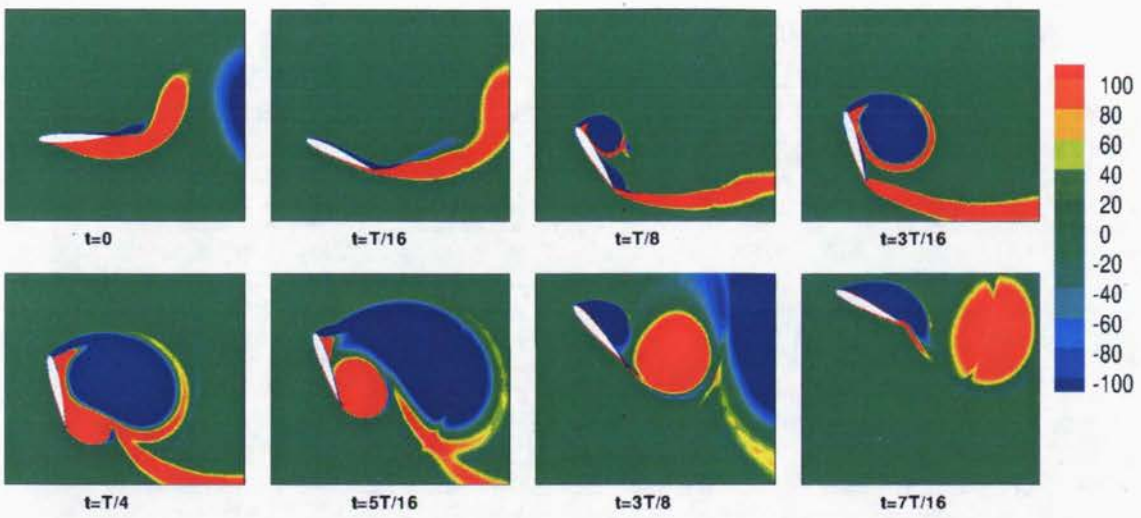

(a) Vorticity contours

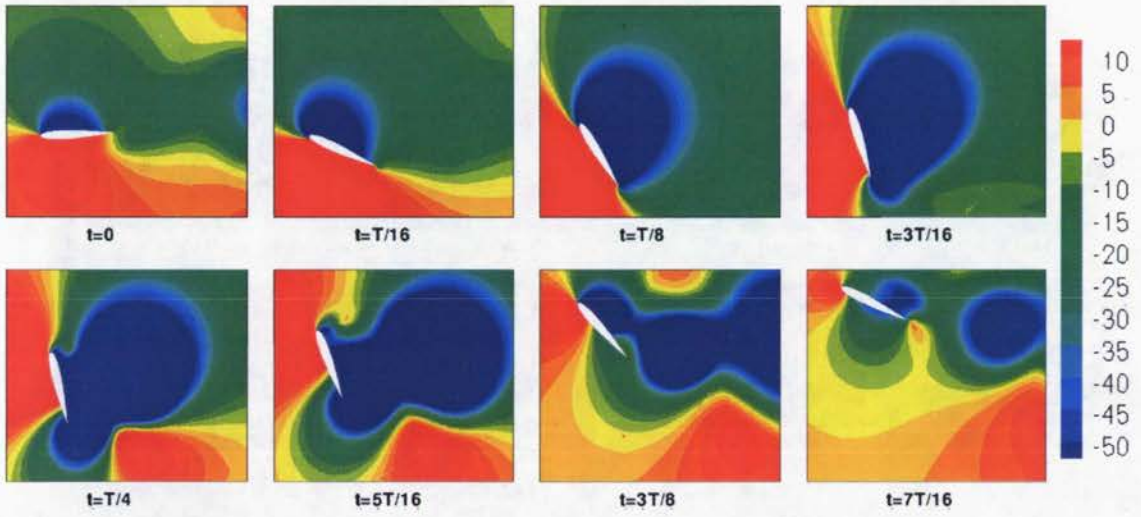

(b) Pressure contours

Figure 6.20: Instantaneous vorticity and pressure contours at $Re_c = 117,500$, $\zeta = 0$ (2 DOF).

Following the results of Kinsey [29] and Zhu [96], one can infer that maximal efficiencies are obtained at higher frequencies than those found in the current study. There are multiple parameters that can have an effect on the frequency of the oscillations. Indeed, either a reduction of the inertia or an increase in the stiffness of the vertical spring or in the distance between the pitching axis and the center of mass all lead to an increase in the frequency of the oscillations.

We have also shown in the present study that the heaving amplitude can be modified solely by changing the vertical damping. A modification of the vertical stiffness also affects the heaving amplitude as seen previously in Fig. 6.12. The pitching amplitude is also influ-

enced by vertical damping as seen previously, but also directly by the rotational stiffness and rotational damping.

Therefore, it seems feasible to conceive a combination of the positive effects of a few changes in the parameters to obtain greater power extraction efficiencies.

Chapter 7

Conclusion

The present master's thesis has focused on the numerical simulation of self-sustained aeroelastic oscillations of an airfoil at transitional Reynolds numbers. Both pitch-only and pitch-heave oscillations have been studied through computational fluid dynamics.

The free and open-source software *OpenFOAM* has been used to perform the numerical simulations and different turbulence modeling strategies were employed. Two-dimensional simulations combined with RANS models have been performed as well as three-dimensional LES simulations. Particular attention has been paid to the use of the $\gamma - \mathrm{Re}_\theta$ transition model and its improved performance over classical RANS models for the present aeroelastic problem.

Results summary

Pitch-only oscillations

First, the self-sustained pitch-only oscillations of a NACA0012 airfoil at transitional Reynolds numbers have been studied. Computations of the flow have been performed using the $\gamma - \mathrm{Re}_\theta$ transition model. The predicted amplitudes and frequencies of the self-sustained oscillations obtained are found to be in good agreement with previous experimental measurements and show an improvement compared to previous numerical predictions. It is shown that the amplitude of the LCOs is mainly dictated by the laminar separation of the boundary layer and the possible transition and reattachment of the shear layer, forming a laminar separation bubble. At all Reynolds numbers where oscillations are observed, laminar separation occurs. It was found to be the triggering effect of the phenomenon since no oscillations are observed in

the presence of turbulent boundary layers (created either by high freestream turbulence or the use of a trip wire). In the first flow regime ($Re_c \leq 85,000$), the aerodynamic moment is rather noisy and the separated shear-layer reattaches during a short part of the oscillation cycle. The second flow regime ($Re_c \geq 85,000$), where the amplitude is decreasing and the frequency is approximately constant, is characterized by the presence of a laminar separation bubble over a longer part of the cycle. The bubble creates a greater suction on the aft part of the airfoil and hence a greater pitch moment causing the decrease in amplitude. It was also shown that at higher Reynolds numbers ($Re_c > 150,000$), the turbulence level in the near-wake of the airfoil increases which produces more robust boundary layers. There is no laminar separation and hence no aeroelastic oscillations at those Reynolds numbers. It is also found that the freestream turbulence intensity has a stabilizing effect on the oscillations, suppressing them completely at high levels. Oscillations have also been reproduced using both a fine and a coarse timestep, the latter filtering out the high-frequency flow structures. The computational timestep size is thus shown to have an unanticipated and interesting impact on the results.

Large Eddy Simulations of transitional flows have also been performed to gain a deeper insight in the flow physics and to determine if 2D URANS computations are adequate. The LES methodology was first validated by computing the flow over a steady SD7003 airfoil at $Re_c = 60,000$. The computed separation, transition and reattachment locations were in good agreement with previously published experimental and computational results. Thereafter, the flow around the NACA 0012 airfoil undergoing self-sustained aeroelastic pitch oscillations have been computed at $Re_c = 64,000$. The predicted oscillations amplitude and frequency are found to compare well with previous experimental results as well as with the numerical calculations using a RANS transition model. Analysis of the flow fields obtained by LES shows separation of the boundary layer followed by transition to turbulence in the separated shear layer, highlighted by the appearance of three-dimensional structures. This transition can lead to reattachment of the shear layer, forming a laminar separation bubble. The presence of the separation zone and this bubble has a significant influence on the moment coefficient of the airfoil and is thus responsible for the self-sustained nature of the oscillations. In this case, it appears that 2D URANS and laminar computations are accurate and do not suffer from significant limitations as they compare favorably to the LES results.

Pitch-heave oscillations

Self-sustained pitch-heave oscillations of an airfoil have also been studied to gain an understanding of the phenomenon and to lead the way for future studies. Two-dimensional URANS simulations have been performed using both the Spalart-Allmaras and the $\gamma - Re_\theta$ models. Predicted oscillations frequencies are found to be quite close to the experimental values but pitching amplitudes have opposite slops than the measurements from wind tun-

nel experiments. However, they still showed comparable trends. Discrepancies between the numerical and experimental values are believed to be caused by differences in structural and inertial parameters and perhaps also by the 2D assumption of the flow which may have more important limitations in the case of massively separated flows.

As opposed to the pitch-only simulations which are caused by laminar separation of the boundary layer, these large oscillations are caused by an instability occuring through the coupling between the pitching and heaving motions and are thus labelled as coalescence flutter. The analysis of the flow fields shows important boundary layer separation at both the leading and trailing edges, causing large vortex shedding.

The potential of these self-sustained oscillations for power extraction applications such as turbines has also been studied. It is found that the present oscillations are not optimal as the best cases featured efficiencies slightly above 15%, which is quite low compared to optimized oscillating airfoils turbines [29], but comparable to other self-sustained devices [3]. The deep stall present in all simulations is found to be in part responsible for the relatively low efficiencies. Indeed, it creates rapid decreases of the lift coefficient which reduces significantly the power extracted.

Future works

The present master's thesis has opened the door to interesting possibilities for future works, mainly in the potential of energy harvesting by two-degrees-of-freedom self-sustained oscillations.

In the current study, the parameters were chosen to reproduce experimental wind tunnel experiments and thus were probably not optimized in the context of power extraction. It would be of interest to pursue a parametric study to determine which values could lead to more efficient oscillations. The airfoil's mass, inertia, position of the center of gravity as well as spring stiffness and damping are some of the parameters that have an important impact on the aeroelastic behavior. Additionally, different spring placement configurations could be used. Instead of a vertical and rotational spring, two vertical springs could be considered [85].

Furthermore, the present study of pitch-heave oscillations has only been conducted through 2D URANS computations. As this methodology is known to have serious limitations in the simulation of massively separated flows, it would be of interest to investigate the possible 3D effects by performing 3D simulations using DES or LES modeling approaches.

Bibliography

[1] Alam, M. and Sandham, N.D. *Direct numerical simulation of 'short' laminar separation bubbles with turbulent reattachment*. Journal of Fluid Mechanics, **410**:1–28, 2000. *Page 19*

[2] Almutairi, J.H., Jones, L.E., and Sandham, N.D. *Intermittent Bursting of a Laminar Separation Bubble on an Airfoil*. AIAA Journal, **48**(2):414–426, 2010. *Pages 44 and 70*

[3] Bernitsas, M.M., Ben-Simon, Y., Raghavan, K., and Garcia, E.M.H. *VIVACE (Vortex Induced Vibration Aquatic Clean Energy): A New Concept in Generation of Clean and Renewable Energy from Fluid Flow*. Journal of Offshore Mechanics and Arctic Engineering, **130**:041 101, 2008. *Pages 137, 142, and 149*

[4] Bernitsas, M.M., Ben-Simon, Y., Raghavan, K., and Garcia, E.M.H. *The VIVACE Converter: Model Tests at High Damping and Reynolds Number around* 10^5. Journal of Offshore Mechanics and Arctic Engineering, **131**:011 102, 2009. *Pages 137 and 142*

[5] Campbell, R.L. *Fluid-Structure Interaction and Inverse Design Simulations for Flexible Turbomachinery*. Ph.D. thesis, Department of Mechanical Engineering and Nuclear Engineering, College of Engineering, The Pennsylvania State University, 2010. *Page 49*

[6] Castonguay, P., Liang, C., and Jameson, A. *Simulation of Transitional Flow over Airfoils using the Spectral Difference Method*. AIAA Paper 2010-4626, 2010. *Pages 44, 65, and 76*

[7] de Villiers, E. *The Potential of Large Eddy Simulation for the Modeling of Wall Bounded Flows*. Ph.D. thesis, Department of Mechanical Engineering, Imperial College of Science, Technology and Medicine, 2006. *Pages xv, 11, 38, 43, and 46*

[8] Demirdzić, I. and Perić, M. *Space conservation law in finite volume calculations of fluid flow*. Internation Numerical Methods in Fluids, **8**:1037–1050, 1988. *Page 33*

[9] Dowell, E.H. and Tang, D. *Nonlinear Aeroelasticity and Unsteady Aerodynamics*. AIAA Journal, **40**(9):1697–1707, 2002. *Page 1*

[10] Drela, M. and Yungren, H. *XFOIL 6.9 User guide*. MIT Aero and Astro, 30th november 2001. *Page 53*

[11] Driest, E.R. Van. *On turbulent flow near a wall*. Journal of Aerospace Sciences, **23**:1007–1011, 1956. *Page 41*

[12] Dubief, Y. and Delcayre, F. *On coherent-vortex identification in turbulence*. Journal of Turbulence, **1**:1–22, 2000. *Pages 14 and 117*

[13] Ducoin, A., Astolfi, J.A., Deniset, F., and Sigrist, J-F. *Computational and experimental investigation of flow over a transient pitching hydrofoil*. European Journal of Mechanics B/Fluids, 2009. *Page 40*

[14] Eca, L., Hoekstra, M., Hay, A., and Pelletier, D. *A Manufactured Solution for a Two-Dimensional Steady Wall-Bounded Incompressible Turbulent Flow*. International Journal of Computational Fluid Dynamics, **21**:175–188, 2007. *Page 162*

[15] Fung, Y.C. *An Introduction to the Theory of Aeroelasticity*. Dover Phoenix, dover edition, 1955. *Page 26*

[16] Galbraith, M.C. *Implicit Large Eddy Simulation of Low-Reynolds-Number Transitional Flow Past the SD7003 Airfoil*. Master's thesis, Department of Aerospace Engineering and Engineering Mechanics, University of Cincinnati, 2009. *Pages 65 and 70*

[17] Gaster, M. *The structure and behavior of laminar separation bubbles. AGARD CP-4*. Technical report, 1966. *Page 19*

[18] Germano, M., Piomelli, U., Moin, P., and Cabot, W.H. *A Dynamic Subgrid-Scale Eddy Viscosity Model*. Physics of Fluids, **A3**:1760–1765, 1991. *Pages 41 and 44*

[19] Harris, Y. *The Aeroelastic Dynamics of a NACA 0012 Airfoil Oscillating in Pitch at Transitional Reynolds Numbers*. Master's thesis, Department of Mechanical Engineering, Royal Military College, 2007. *Pages xv, 1, and 3*

[20] Horton, H.P. *A semi-empirical theory for the growth and bursting of laminar separation bubbles*. 1967. *Page 19*

[21] Horton, H.P. *Laminar separation bubbles in two- and three-dimensional incompressible flow*. Ph.D. thesis, University of London, 1968. *Pages xv and 18*

[22] Hunt, J.C.R, Wray, A.A., and Moin, P. *Eddies, stream and convergence zones in turbulent flows*. Technical report, CTR-S88, Center for turbulence Research, 1988. *Page 14*

[23] Inagaki, M., Kondoh, T., and Nagano, Y. *A Mixed-Time-Scale SGS Model With Fixed Model-Paramaters for Practical LES*. Journal of Fluids Engineering, **127**:1–13, 2005. *Page 42*

[24] Jasak, H. *Error Analysis and Estimation for the Finite Volume Method with Applications to Fluid Flows*. Ph.D. thesis, Imperial College, 1996. *Page 32*

[25] Jeong, J. and Hussain, F. *On the identification of a vortex*. Journal of Fluid Mechanics, **285**:69–94, 1995. *Page 14*

[26] Jones, L.E., Sandberg, R.D., and Sandham, N.D. *Direct numerical simulations of forced and unforced separation bubbles on an airfoil at incidence*. Journal of Fluid Mechanics, **602**:175–207, 2008. *Pages 1 and 80*

[27] Jones, W.P. and Launder, B.E. *The prediction of laminarisation with a two-equation model for turbulence*. Int. J. Heat and Mass Tranfer, **15**:301–314, 1972. *Pages 37 and 159*

[28] Julien, S., Dumas, G., and Métivier, V. *URANS Simulations of High Amplitude Flapping Airfoils*. 15th Annual Conference of the CFD Society of Canada, Toronto, Canada, may 2007. *Pages 49 and 123*

[29] Kinsey, T. *Analysis, Optimization and Demonstration of a new concept of hydrokinetic turbine based on oscillating hydrofoils*. Ph.D. thesis, Department of Mechanical Engineering, Laval University, 2011. *Pages 123, 137, 142, 144, and 149*

[30] Kinsey, T. and Dumas, G. *Parametric Study of an Oscillating Airfoil in Power-Extraction Regime*. AIAA Journal, **46**(6):1318–1330, 2008. *Pages 49 and 123*

[31] Kolmogorov, A. *The local structure of turbulence in incompressible viscous fluid for very large reynolds numbers*. Dokl. Akad. Nauk SSSR, **30**:299–303, 1941. *Page 10*

[32] Langtry, R.B. *A Correlation-Based Transition Model using Local Variables for Unstructured Parallelized CFD codes*. Ph.D. thesis, Institute of Thermal Turbomachinery and Machinery Laboratory, University of Stuttgart, 2006. *Pages 38, 39, 40, and 88*

[33] Langtry, R.B. and Menter, F.R. *Correlation-Based Transition Modeling for Unstructured Parallelized Computational Fluid Dynamics Codes*. AIAA Journal, **47**(12):2894–2906, 2009. *Pages 37, 55, and 162*

[34] Lapointe, S. and Dumas, G. *Improved Numerical Simulations of Self-Sustained Oscillations of a NACA0012 with Transition Modeling*. AIAA Paper 2011-3258, 2011. *Page 118*

[35] Leontini, J.S., Thompson, M.C., and Hourigan, K. *The beginning of branching behaviour of vortex-induced vibration during two-dimensional flow*. Journal of Fluids and Structures, **22**:857–864, 2006. *Pages 84 and 85*

[36] Lilly, D.K. *The representation of small-scale turbulence in numerical simulation experiments*. In *IBM Scientific Computing Symposium on Environmental Sciences*, page 195. 1967. *Page 41*

[37] Mayle, R.E. *The Role of Laminar-Turbulent Transition in Gas Turbine Engines*. Journal of Turbomachinery, **113**:509–537, 1991. *Page 17*

[38] McGhee, R.J. and Beasley, W.D. *Low-Speed Aerodynamic Characteristics of a 13-Percent-Thick Medium-Speed Airfoil Designed for General Aviation Applications*. Technical report, NASA Langley Research Center, 1979. *Page 53*

[39] Mendes, F., Poirel, D., and Benaissa, A. *Experimental Investigation of Self-Sustained Pitch-Heave Aeroelastic Oscillations of a NACA0012 Airfoil at Transitional Reynolds Numbers*. CASI 2011, Montreal, Canada, 2011. *Pages xv, 2, 3, 5, 6, 59, 122, 123, and 124*

[40] Menter, F.R. *Two-equation Eddy-viscosity turbulence models for engineering applications*. AIAA Journal, **32**(8):1598–1605, 1994. *Pages 7, 37, 38, 45, and 54*

[41] Menter, F.R., Esch, T., and Kubacki, S. *Transition modelling based on local variables*. 5th International Symposium on Turbulence Modeling and Measurements, Mallorca, Spain, 2002. *Page 37*

[42] Menter, F.R., Langtry, R.B., Likki, S.R., Suzen, Y.B., and Huang, P.G. *A Correlation Based Transition Model Using Local Variables Part 1: Model Formulation*. Journal of Turbomachinery, **128**(3):413–422, 2006. *Page 37*

[43] Menter, F.R., Langtry, R.B., and Völker, S. *Transition Modelling for General Purpose CFD Codes*. Flow, Turbulence and Combustion, **77**:277–303, 2006. *Page 40*

[44] Metivier, V. *Étude des oscillations auto-excitées d'un profil d'aile NACA 0012 à des nombres de Reynolds transitionnels*. Master's thesis, Department of Mechanical Engineering, Laval University, 2012. *Pages 7, 95, 111, and 114*

[45] Mockett, C. *A comprehensive study of detached-eddy simulation*. Ph.D. thesis, Technischen Universität Berlin, 2009. *Pages xv and 13*

[46] Morissette, J.-F. *Simulations aéroélastiques d'ailes oscillantes multi-segments par méthode vortex*. Master's thesis, Département de Génie Mécanique, Université Laval, 2010. *Pages xvi, 84, 85, and 86*

[47] Morissette, J.-F. and Dumas, G. *A Meshless Approach for Fluid-Structure Interactions Analysis in Flapping-Wing Flyers*. 17th Annual Conference of the CFD Society of Canada, Ottawa, Canada, may 2009. *Pages xvi, 83, 84, 85, and 86*

[48] Morton, S.A., Melville, R.B., and Visbal, M.R. *Accuracy and Coupling Issues of Aeroelastic Navier Stokes Solutions on Deforming Meshes*. Journal of Aircraft, 1998. *Page 49*

[49] Mueller, T.J. and DeLaurier, J.D. *Aerodynamics of Small Vehicles*. Annual Review of Fluid Mechanics, **35**:89–111, 2003. *Page 1*

[50] Métivier, V., Dumas, G., and Poirel, D. *Simulations of Self-Excited Pitch Oscillations of a NACA 0012 Airfoil in the Transitional Reynolds Number Regime*. CSME/SCGM Conference, Ottawa, Canada, june 2008. *Pages 5 and 7*

[51] Métivier, V., Dumas, G., and Poirel, D. *Aeroelastic Dynamics of a NACA 0012 Airfoil at Transitional Reynolds Numbers*. 39th AIAA Fluid Dynamics Conference, San Antonia, Texas, june 2009. *Pages xv, 2, 3, and 4*

[52] Métivier, V., Dumas, G., and Poirel, D. *Effects of Inertia and Boundary Layer Tripping on Aeroelastic, Self-Excited Pitch Oscillations of an Airfoil*. Canadian Aeronautics and Space Institute AERO'09 Conference, Ottawa, Canada, may 2009. *Pages xv and 4*

[53] Ol, M.V., McAuliffe, B.R., Hanff, E.S., Scholz, U., and Kahler, C. *Comparison of Laminar Separation Bubble Measurements on a Low Reynolds Number Airfoil in Three Facilities*. AIAA Paper 2005-5149, 2005. *Pages 64 and 76*

[54] OpenCFD. *OpenFOAM - The Open Source CFD Toolbox - User's Guide*. OpenCFD Ltd., United Kingdom, 1.5 edition, 1st august 2008. *Pages xv and 31*

[55] Ou, K. and Jameson, A. *Flow Induced Cylinder Oscillations and its Control with High Order Spectral Difference Method on Deformable Mesh*. ASME Paper FEDSM-ICNMM2010-30577, 2010. *Pages xv, 49, 50, and 51*

[56] Pauley, L.L., Moin, P., and Reynolds, W.C. *The structure of two-dimensional separation*. Journal of Fluid Mechanics, **220**:397–411, 1990. *Page 19*

[57] Peng, Z. and Zhu, Q. *Energy harvesting through flow-induced oscillations of a foil*. Physics of Fluids, **21**, 2009. *Page 142*

[58] Persson, P.O., Peraire, J., and Bonet, J. *Discontinuous Galerkin solution of the Navier-Stokes equations on deformable domains*. AIAA Paper 2007-0513, 2007. *Page 50*

[59] Poirel, D. *Wing LCO at Transitional Re Numbers. NATO RTO-AVT-152*. Technical report, 2008. *Page 1*

[60] Poirel, D., Benaissa, A., Yuan, W., and Khalid, M. *Self-Excited Oscillations of a NACA 0012 Airfoil in the Transitional Re Regime*. CASI 2007, Toronto, Canada, 2007. *Page 93*

[61] Poirel, D., Harris, Y., and Benaissa, A. *Self-sustained aeroelastic oscillations of a NACA0012 airfoil at low-to-moderate Reynolds numbers*. Journal of Fluids and Structures, **24**(5):700–719, 2008. *Pages xv, 1, 2, 4, 5, 7, 28, 88, 89, 90, 92, 93, 95, and 110*

[62] Poirel, D., Métivier, V., and Dumas, G. *Computational Aeroelastic Simulations of Self-Sustained Pitch Oscillations of a NACA0012 at Transitional Reynolds Numbers*. Journal of Fluids and Structures, **27**:1262–1277, 2011. *Pages 2, 5, 89, 90, 111, and 114*

[63] Poirel, D. and Price, S.J. *Random binary (coalescence) flutter of a two-dimensional linear airfoil*. Journal of Fluids and Structures, **18**(1):23–42, 2003. *Pages 5 and 127*

[64] Poirel, D. and Yuan, W. *Aerodynamics of laminar separation flutter at a transitional Reynolds number*. Journal of Fluids and Structures, **26**(7-8):1174–1194, 2010. *Pages 97, 107, 117, and 118*

[65] Pope, S. *Turbulent Flows*. Cambridge University Press, 2000. *Page 12*

[66] Radespiel, R., Windte, J., and Scholz, U. *Numerical and Experimental Flow Analysis of Moving Airfoils with Laminar Separation Bubbles*. AIAA Paper 2006-501, 2006. *Pages 19, 64, and 76*

[67] Raverdy, B., Mary, I., Sagaut, P., and Liamis, L. *High-resolution large-eddy simulation of the flow around a low pressure turbine blade*. AIAA Journal, **41**:390–397, 2003. *Page 43*

[68] Richez, F., Mary, I., Gleize, V., and Basdevant, C. *Near stall simulation of the flow around an airfoil using zonal RANS/LES coupling method*. Computers and Fluids, **37**:857–866, 2008. *Page 43*

[69] Ripley, M.D. and Pauley, L.L. *The Unsteady Structure of Two-Dimensional Steady Laminar Separation*. Physics of Fluids, **5**:3099–3106, 1993. *Page 80*

[70] Rumsey, C.L. *Apparent transition behavior of widely-used turbulence models*. International Journal of Heat and Fluid Flow, **28**:1460–1471, 2007. *Pages 39 and 162*

[71] Rumsey, C.L. and Spalart, P.R. *Turbulence Model Behavior in Low Reynolds Number Regions of Aerodynamic Flowfiels*. 38th Fluid Dynamics Conference and Exhibit, paper AIAA-2008-4403, Seattle, Washington, june 2008. *Page 39*

[72] Schlichting, H. and Gersten, K. *Boundary Layer Theory*. Springer, eighth edition, 2000. *Pages xv and 17*

[73] Smagorinsky, J. *General circulation experiments with the primitive equations*. Mon. Weather Rev., **91**, 1963. *Pages 40 and 41*

[74] Sousa, J.M.M. and Silva, L.M.G. *Transition prediction in infinite swept wings using Navier-Stokes computations and linear stability theory*. Computers and Structures, **82**:1551–1560, 2004. *Page 40*

[75] Spalart, P.R. *Strategies for turbulence modeling and simulation*. Int. J. Heat and Fluid Flow, pages 252–263, 2000. *Page 38*

[76] Spalart, P.R. *Young-Person's Guide to Detached-Eddy Simulation Grids*. Technical report, Boeing Commercial Airplanes, 2001. *Page 46*

[77] Spalart, P.R. and Allmaras, S.R. *A one-equation turbulence model for aerodynamic flows*. La recherche aérospatiale, **1**:5–21, 1994. *Pages 37, 45, 54, and 161*

[78] Spalart, P.R., Jou, W.-H., Strelets, M., and Allmaras, S.R. *Comments on the feasibility of LES for wings, and on a hybrid RANS/LES approach*. In *Advances in DNS/LES, by Liu and Liu*. 1997. *Page 45*

[79] Spalart, P.R. and Rumsey, C.L. *Effective Inflow Conditions for Turbulence Models in Aerodynamic Calculations*. AIAA Journal, **45**(10):2544–2553, 2007. *Pages 38 and 39*

[80] Stock, H.W. and Haase, W. *Navier-Stokes Airfoil Computations with Transition Prediction Including Transitional Flow Regions*. AIAA Journal, **38**(11):2059–2066, 2000. *Page 40*

[81] Strelets, M. *Detached eddy simulation of massively separated flows*. AIAA Paper 2001-0879, 2001. *Pages 46 and 47*

[82] Tani, L. *Low-speed flows involving bubble separations*. Progress in Aerospace Sciences, **5**:70–103, 1964. *Page 18*

[83] Tennekes, H. and Lumley, J.L. *A First Course in Turbulence*. MIT Press, Cambridge, 1972. *Page 10*

[84] Uranga, A., Persson, P., Drela, M., and Peraire, J. *Implicit Large Eddy Simulation of transition to turbulence at low Reynolds numbers using a Discontinuous Galerkin method*. International Journal for Numerical Methods in Engineering, 2010. *Pages 44, 65, and 76*

[85] Veilleux, J.-C. *Dynamique de pilonnement-tangage d'une aile portante montée sur des supports élastiques*. Technical report, Université Laval, 2011. *Page 149*

[86] Visbal, M.R. *High-Fidelity Simulation of Transitional Flows past a Plunging Airfoil*. AIAA Journal, **47**(11):2685–2697, 2009. *Page 44*

[87] Visbal, M.R., Gordnier, R.E., and Galbraith, M.C. *High-fidelity simulations of moving and flexible airfoils at low Reynolds numbers*. Experiments in Fluids, **46**:903–922, 2009. *Pages 1, 44, 65, and 76*

[88] Walters, D.K. and Cokljat, D. *A Three-Equation Eddy-Viscosity Model for Reynolds-Averaged Navier-Stokes Simulations of Transition Flow*. Journal of Fluids Engineering, **130**:121 401.1–121 401.14, 2008. *Page 55*

[89] Wilcox, D.C. *Turbulence modeling for CFD*. Technical report, DCW Industries, 1993. *Pages 54 and 159*

[90] Wilcox, D.C. *Turbulence Modeling for CFD*. DCW Industries, second edition, 2002. *Page 7*

[91] Windte, J., Scholz, U., and Radespiel, R. *Validation of the RANS-simulation of laminar separation bubbles on airfoils*. Aerospace Science and Technology, **10**:484–494, 2006. *Pages 40 and 113*

[92] Yang, J., Preidikman, S., and Balaras, E. *A strongly coupled, embedded-boundary method for fluid-structure interactions of elastically mounted rigid bodies*. Journal of Fluids and Structures, **24**:167–182, 2008. *Pages 84 and 85*

[93] Yuan, W., Khalid, M., Xu, H., and Radespiel, R. *An Investigation of Low-Reynolds-number Flows past Airfoils*. AIAA Papaer 2005-4607, 2005. *Pages 65 and 76*

[94] Yuan, W., Xu, H., Khalid, M., and Radespiel, R. *A parametric study of LES on laminar-turbulent transitional flows past an airfoil*. International Journal of Computational Fluid Dynamics, **20**(1):45–54, 2006. *Page 44*

[95] Zang, T. *Numerical simulation of the dynamics of turbulent boundary layers: perspectives of a transition simulator*. Philosophical Transactions Royal Society of London, **336**:95–102, 1991. *Page 43*

[96] Zhu, Q. *Optimal frequency for flow energy harvesting of a flapping foil*. Journal of Fluid Mechanics, **675**:495–517, 2011. *Page 144*

Appendix A

Turbulence model formulations

A.1 $k-\omega$ SST RANS model

The $k-\omega$ SST model is a two equation RANS turbulence model. It is based on the $k-\omega$ model of Wilcox [89] and the $k-\epsilon$ model of Jones and Launder [27]. Historically, the $k-\omega$ model has been reported to perform well in cases with separated boundary layers, adverse pressure gradients and surface curvature. However, it is very sensitive to free stream turbulence values which makes the model unstable in some cases. On the other hand, the $k-\epsilon$ model is efficient to resolve the free stream zones and the external part of the boundary layer, but does not predict well boundary layer separation. The $k-\omega$ SST model was built to take profit of the advantages of both this model. By the introduction of blending functions, it is designed to act as a $k-\omega$ model in the near-wall region and as a $k-\epsilon$ model in the free stream region. The equations of the model are presented below:

$$\overbrace{\frac{\partial k}{\partial t}}^{\text{Change rate}} + \overbrace{U_j\frac{\partial k}{\partial x_j}}^{\text{Convection}} = \overbrace{\tilde{P}_k}^{\text{Production}} - \overbrace{\beta^* k\omega}^{\text{Destruction}} + \overbrace{\frac{\partial}{\partial x_j}\left((\nu+\sigma_k\nu_t)\frac{\partial k}{\partial x_j}\right)}^{\text{Diffusion}}, \tag{A.1}$$

$$\overbrace{\frac{\partial \omega}{\partial t}}^{\text{Change rate}} + \overbrace{U_j\frac{\partial \omega}{\partial x_j}}^{\text{Convection}} = \overbrace{\alpha S^2}^{\text{Production}} - \overbrace{\beta\omega^2}^{\text{Destruction}} + \overbrace{\frac{\partial}{\partial x_j}(\nu+\sigma_\omega\nu_t)\frac{\partial \omega}{\partial x_j}}^{\text{Diffusion}} + \underbrace{2(1-F_1)\sigma_{\omega 2}\frac{1}{\omega}\frac{\partial k}{\partial x_j}\frac{\partial \omega}{\partial x_j}}_{\text{Cross diffusion term}}, \tag{A.2}$$

the turbulent kinematic viscosity is defined as:

$$\nu_t = \frac{a_1 k}{\max(a_1\omega,\ S F_2)}\,, \tag{A.3}$$

where $S = \sqrt{2S_{ij}S_{ij}}$ is the absolute value of the strain rate tensor $S_{ij} = \frac{1}{2}\left(\frac{\partial \overline{U}_i}{\partial x_j} + \frac{\partial \overline{U}_j}{\partial x_i}\right)$ and F_2 is a blending function.

The F_1 blending function is used to switch between the $k-\omega$ and $k-\epsilon$ formulations and is defined as:

$$F_1 = \tanh\left\{\left(\min\left[\max\left(\frac{\sqrt{k}}{\beta^*\omega y},\ \frac{500\nu}{y^2\omega}\right),\ \frac{4\rho\sigma_{\omega 2}k}{CD_{k\omega}y^2}\right]\right)^4\right\}\,, \tag{A.4}$$

where y is the wall-normal distance and $CD_{k\omega}$ is the positive part of the cross diffusion term of Eq. (A.2). $CD_{k\omega}$ is defined as following, to avoid a division by zero:

$$CD_{k\omega} = \max\left(2\rho\sigma_{\omega 2}\frac{1}{\omega}\frac{\partial k}{\partial x_j}\frac{\partial \omega}{\partial x_j},\ 10^{-10}\right)\,. \tag{A.5}$$

The second blending function F_2 is

$$F_2 = \tanh\left\{\left[\max\left(\frac{2\sqrt{k}}{\beta^*\omega y},\ \frac{500\nu}{y^2\omega}\right)\right]^2\right\}\,. \tag{A.6}$$

A limiter is applied to the production term of the kinetic energy transport equation to avoid the artificial production of turbulence in stagnation regions:

$$P_k = \nu_t\frac{\partial U_i}{\partial x_j}\left(\frac{\partial U_i}{\partial x_j} + \frac{\partial U_j}{\partial x_i}\right) \longrightarrow \tilde{P}_k = \min(P_k,\ 10\epsilon)\,. \tag{A.7}$$

The constants of the model are calculated from a blending, by Eq. (A.8) between the constants of both the $k-\epsilon$ and $k-\omega$ standard models given below:

$$\alpha = \alpha_1 F_1 + \alpha_2(1 - F_1)\,, \tag{A.8}$$

Constants of the $k-\epsilon$ model:

$\beta^* = 0.09,\ \alpha_1 = 5/9,\ \beta_1 = 3/40,\ \sigma_{k1} = 0.5,\ \sigma_{\omega 1} = 0.5$

Constants of the $k-\omega$ model:

$\beta^* = 0.09,\ \alpha_2 = 0.44,\ \beta_2 = 0.0828,\ \sigma_{k2} = 1,\ \sigma_{\omega 2} = 0.856$

A.2 Spalart-Allmaras RANS model

The one-equation Spalart-Allmas RANS model is described here. The original version of Spalart [77] is presented and it solves one transport equation for the modified turbulent viscosity $\tilde{\nu}$.

The model is based on the following transport equation for the modified kinematic turbulent viscosity $\tilde{\nu}$.

$$\frac{D\tilde{\nu}}{Dt} = \underbrace{c_{b1}(1-f_{t2})\tilde{S}\,\tilde{\nu}}_{Production} + \underbrace{\frac{1}{\sigma}[\nabla((\nu+\tilde{\nu})\nabla\tilde{\nu}) + c_{b2}(\nabla\tilde{\nu})^2]}_{Diffusion} - \underbrace{\left(c_{w1}f_w - \frac{c_{b1}}{\kappa^2}f_{t2}\right)\left[\frac{\tilde{\nu}}{d}\right]^2}_{Destruction} + \underbrace{f_{t1}\Delta U^2}_{Trip} \quad \text{(A.9)}$$

The eddy viscosity ν_t is related to $\tilde{\nu}$ according to

$$\nu_t = \tilde{\nu} f_{v1} \quad \text{(A.10)}$$

$$f_{v1} = \frac{\chi^3}{\chi^3 + c_{v1}^3} \quad \text{(A.11)}$$

where f_{v1} is a function constructed so that $\tilde{\nu}$ equals ν_t except in the viscous region and $\chi \equiv \tilde{\nu}/\nu$.

In the production term, $\tilde{S}$ is defined by

$$\tilde{S} \equiv S + \frac{\tilde{\nu}}{\kappa^2 d^2} f_{v2} \quad \text{(A.12)}$$

$$f_{v2} = 1 - \frac{\chi}{1+\chi f_{v1}} \quad \text{(A.13)}$$

where S is defined as the vorticity magnitude [1]. The function f_{v2} serves a similar purpose as f_{v1}, assuring that $\tilde{S}$ respects the log-layer behavior up to the wall.

[1] Another alternative is to define S as the strain rate [77].

In the destruction term, f_w is a function calibrated to decrease the production term in the outer region of the boundary layer and to increase it in the near-wall region. The function equation is

$$f_w = g\left[\frac{1 + c_{w3}^6}{g^6 + c_{w3}^6}\right]^{1/6} \tag{A.14}$$

where g is defined by

$$g = r + c_{w2}(r^6 - r) \tag{A.15}$$

and r is inspired by the mixing length definition in algebraic models.

$$r \equiv \frac{\nu_t}{S\kappa^2 d^2} \tag{A.16}$$

The trip term is used to initiate transition at a specified trip point. The f_{t1} function is defined as

$$f_{t1} = c_{t1} g_t exp\Big(- c_{t2}\frac{\omega_t^2}{\Delta U^2}[d^2 + g_t^2 d_t^2]\Big) \tag{A.17}$$

where $g_t = min(0.1, \delta U/\omega_t \Delta x_t)$. The function f_{t2} present in the production and destruction terms is also linked to transition and the trip term. It is a numerical fix that makes zero a stable solution, which ultimately results in delaying transition so that the trip term can be activated appropriately. The term trip and the f_{t2} function are often left out because the model is mostly used for fully turbulent calculations. Some studies [14, 70] have shown that the omission of these terms makes very little difference at reasonably high Reynolds numbers.

Constants of the Spalart-Allmaras model:

$c_{b1} = 0.1355$, $c_{b2} = 0.622$, $c_{w2} = 0.3$, $c_{w3} = 2$, $c_{v1} = 7.1$, $c_{v2} = 5$, $\sigma = 0.666$, $\kappa = 0.41$

A.3 $\gamma - Re_\theta$ transition RANS model

The $\gamma - Re_\theta$ transition model is a RANS model with four transport equations, based on the $k - \omega$ SST RANS model. In addition to the transport equations for k and ω, there is a transport equation for the intermittency, γ, and for the transition momentum-thickness Reynolds number, $\tilde{Re}_{\theta t}$. The version of the model presented here is referred to as CFX-v.1.1 [33].

The transport equation for the intermittency is:

$$\overbrace{\frac{\partial \gamma}{\partial t}}^{\text{Change rate}} + \overbrace{U_j \frac{\partial \gamma}{\partial x_j}}^{\text{Convection}} = \overbrace{P_\gamma}^{\text{Production}} - \overbrace{E_\gamma}^{\text{Destruction}} + \overbrace{\frac{\partial}{\partial x_j}\left((\nu + \frac{\nu_t}{\sigma_f})\frac{\partial \gamma}{\partial x_j}\right)}^{\text{Diffusion}}, \tag{A.18}$$

and the one for the transition momentum-thickness Reynolds number:

$$\overbrace{\frac{\partial \tilde{Re}_{\theta t}}{\partial t}}^{\text{Change rate}} + \overbrace{U_j \frac{\partial \tilde{Re}_{\theta t}}{\partial x_j}}^{\text{Convection}} = \overbrace{P_{\tilde{Re}_{\theta t}}}^{\text{Production}} + \overbrace{\frac{\partial}{\partial x_j}\left((\sigma_{\theta t}(\nu + \nu_t))\frac{\partial \tilde{Re}_{\theta t}}{\partial x_j}\right)}^{\text{Diffusion}}. \tag{A.19}$$

In Eq. (A.18), the production source term is defined as:

$$P_\gamma = F_{length} c_{a1} \rho S [\gamma F_{onset}]^{0.5} (1 - c_{e1}\gamma), \tag{A.20}$$

where S is the strain-rate magnitude, F_{length} is an empirical correlation to determine the length of the transition region and F_{onset} is a function controlling the transition onset location.

The intermittency destruction source term is defined as:

$$E_\gamma = c_{a2} \rho \Omega \gamma F_{turb} (c_{e2}\gamma - 1), \tag{A.21}$$

where Ω is the vorticity magnitude and F_{turb} a function used to disable the source term in fully turbulent flow. The empirical correlation and the different functions used in the intermittency transport equations are defined below:

$$Re_V = \frac{y^2 S}{\nu}, \tag{A.22}$$

$$F_{onset1} = \frac{Re_V}{2.193 \cdot Re_{\theta C}}, \tag{A.23}$$

$$F_{onset2} = min(max(F_{onset1}, F_{onset1}^4), 2), \tag{A.24}$$

$$R_T = \frac{k}{\nu \omega}, \tag{A.25}$$

$$F_{onset3} = max\left(1 - \left(\frac{R_T}{2.5}\right)^3, 0\right), \tag{A.26}$$

$$F_{onset} = max(F_{onset2} - F_{onset3}, 0), \tag{A.27}$$

$$F_{length} = \begin{cases} 39.189 - (119.27 \cdot 10^{-4})\tilde{Re}_{\theta t} - (132.567 \cdot 10^{-6})\tilde{Re}_{\theta t}^2, & \tilde{Re}_{\theta t} < 400 \\ 263.404 - (123.939 \cdot 10^{-2})\tilde{Re}_{\theta t} + (194.548 \cdot 10^{-5})\tilde{Re}_{\theta t}^2 & \\ -(101.695 \cdot 10^{-8})\tilde{Re}_{\theta t}^3, & 400 \leq \tilde{Re}_{\theta t} < 596 \\ 0.5 - (\tilde{Re}_{\theta t} - 596) \cdot 3 \cdot 10^{-4}, & 596 \leq \tilde{Re}_{\theta t} < 1200 \\ 0.3188, & \tilde{Re}_{\theta t} \geq 1200 \end{cases} \tag{A.28}$$

$$F_{sublayer} = e^{-(\frac{R_\omega}{0.4})^2}, \tag{A.29}$$

$$R_\omega = \frac{y^2 \omega}{500\nu}, \tag{A.30}$$

$$F_{length} = F_{length}(1 - F_{sublayer}) + 40 \cdot F_{sublayer}, \tag{A.31}$$

$$F_{turb} = e^{-(\frac{R_T}{4})^4}, \tag{A.32}$$

$$Re_{\theta c} = \begin{cases} \tilde{Re}_{\theta t} - (396.035 \cdot 10^{-2} - (120.656 \cdot 10^{-4}\tilde{Re}_{\theta t} + (868.23 \cdot 10^{-6})\tilde{Re}_{\theta t}^2 & \\ -(696.056 \cdot 10^{-9})\tilde{Re}_{\theta t}^3 + (174.105 \cdot 10^{-12})\tilde{Re}_{\theta t}^4), & \tilde{Re}_{\theta t} \leq 1870 \\ \tilde{Re}_{\theta t} - (593.11 + (\tilde{Re}_{\theta t} - 1870) \cdot 0.482), & \tilde{Re}_{\theta t} > 1870 \end{cases} \tag{A.33}$$

and the constants are:

$$c_{a1} = 2,\ c_{a2} = 0.06,\ c_{e1} = 1,\ c_{e2} = 50,\ \sigma_f = 1.$$

The production source term in the transport equation of $\tilde{Re}_{\theta t}$ is defined as follows:

$$P_{\tilde{Re}_{\theta t}} = c_{\theta t}\frac{\rho}{t}(Re_{\theta t} - \tilde{Re}_{\theta t})(1 - F_{\theta t}), \tag{A.34}$$

where t is a time scale and $F_{\theta t}$ is a blending function necessary to turn off the source term in the boundary layer. The formulation of those functions and them empirical correlation for transition onset are given below:

$$t = \frac{500}{\nu U^2}, \tag{A.35}$$

$$F_{\theta t} = min\left(max\left(F_{wake} \cdot e^{-(\frac{y}{\delta})^4}, 1 - \left(\frac{\gamma - 1/c_{e2}}{1 - 1/c_{e2}}\right)^2\right), 1\right), \tag{A.36}$$

$$\theta_{BL} = \frac{\tilde{Re}_{\theta t}}{\nu U}, \tag{A.37}$$

$$\delta_{BL} = \frac{15}{2}\theta_{BL}, \tag{A.38}$$

$$\delta = \frac{50\Omega y}{U}\delta_{BL}, \tag{A.39}$$

$$Re_{\omega} = \frac{\omega y^2}{\nu}, \tag{A.40}$$

$$F_{wake} = e^{-(\frac{Re_{\omega}}{1E+5})^2}, \tag{A.41}$$

$$\lambda_{\theta} = \frac{\theta^2}{\nu}\frac{dU}{ds}, \tag{A.42}$$

where $\frac{dU}{ds}$ is the acceleration along the streamwise direction,

$$Tu = 100\frac{\sqrt{2k/3}}{U}, \tag{A.43}$$

$$Re_{\theta t} = \begin{cases} \left[1173.51 - 589.428Tu + \frac{0.2196}{Tu^2}\right] F(\lambda_{\theta}), & Tu \leq 1.3 \\ 331.5\,(Tu - 0.5658)^{-0.671}\, F(\lambda_{\theta}), & Tu > 1.3 \end{cases} \tag{A.44}$$

$$F(\lambda_{\theta}) = \begin{cases} 1 - (-12.986\lambda_{\theta} - 123.66\lambda_{\theta}^2 - 405.689\lambda_{\theta}^3)e^{-(\frac{Tu}{1.5})^{1.5}}, & \lambda_{\theta} \leq 0 \\ 1 + 0.275(1 - e^{-35\lambda_{\theta}})e^{-(\frac{Tu}{0.5})}, & \lambda_{\theta} > 0 \end{cases} \tag{A.45}$$

and the constants are:

$$c_{\theta t} = 0.03,\ \sigma_{\theta t} = 2$$

Finally, the transition model interacts with the SST model by modifying the production and destruction source terms of in the transport equation of k Eq. (A.1) seen precedently. The modified source terms are:

$$\tilde{P}_k = \gamma_{eff} P_k, \tag{A.46}$$

$$\tilde{D}_k = min(max(\gamma_{eff}, 0.1), 1) D_k, \tag{A.47}$$

with P_k and D_k the original source terms. The γ_{eff} function is used to take into account a modification to the intermittency to predict separation induced transition and is calculated as follows:

$$\gamma_{eff} = max(\gamma, \gamma_{sep}), \tag{A.48}$$

$$\gamma_{sep} = min\left(s_1 max\left[0, \left(\frac{Re_V}{3.235 Re_{\theta c}}\right) - 1\right] F_{reattach}, 2\right) F_{\theta t}, \tag{A.49}$$

$$F_{reattach} = e^{-(\frac{R_T}{20})^4}, \tag{A.50}$$

where the constant $s_1 = 2$. The F_1 blending function of the SST model is also modified as follows:

$$F_1 = max(F_{1orig}, F_3), \tag{A.51}$$

$$F_3 = e^{-(\frac{R_y}{120})^8}, \tag{A.52}$$

$$R_y = \frac{y\sqrt{k}}{\nu}. \tag{A.53}$$